

Chasing the Rare Decay $K^+ \rightarrow \pi^+ \nu\bar{\nu}$

Robert A. McPherson

A DISSERTATION

PRESENTED TO THE FACULTY

OF PRINCETON UNIVERSITY

IN CANDIDACY FOR THE DEGREE

OF DOCTOR OF PHILOSOPHY

RECOMMENDED FOR ACCEPTANCE

BY THE DEPARTMENT OF

PHYSICS

NOVEMBER 1995

UMI Number: 9541194

**UMI Microform 9541194
Copyright 1995, by UMI Company. All rights reserved.**

**This microform edition is protected against unauthorized
copying under Title 17, United States Code.**

UMI
300 North Zeeb Road
Ann Arbor, MI 48103

© Copyright 1995 by Robert A. McPherson.

All rights reserved.

Abstract

In the Standard Model, the experimental fact that the quark weak interaction eigenstates are not the mass eigenstates permits a set of otherwise forbidden processes, including flavour changing neutral currents (FCNC) and CP violation. This is the phenomenology of the quark-mixing matrix, V_{CKM} . While it, together with the fact that quarks have differing masses, allows these processes to occur, they are by no means encouraged. This strong Standard Model suppression allows relatively significant contributions from the host of theories of physics at higher energy scales. Such contributions may not make any single processes inconsistent with the Standard Model, but their different contributions to processes with related V_{CKM} dependencies may leave a picture inconsistent with the current theory. Exploring V_{CKM} is an important part of the near-term program of particle physics, especially at the two new B -factories under construction. A measurement of the branching ratio of the rare kaon decay $K^+ \rightarrow \pi^+ \nu \bar{\nu}$ is a theoretically clean measurement of the product of V_{CKM} elements $V_{ts}^* V_{td}$, currently the poorest known elements of the mixing matrix,

constrained primarily by the unitarity of V_{CKM} demanded by the theory. The dependence of $K^+ \rightarrow \pi^+ \nu \bar{\nu}$ on various types of new physics is complementary to that of the measurements that will be made at the B -factories, so $K^+ \rightarrow \pi^+ \nu \bar{\nu}$ will remain of interest into the future. Experiment 787 at Brookhaven National Lab is a dedicated search for $K^+ \rightarrow \pi^+ \nu \bar{\nu}$, expected in the Standard Model to have a branching fraction of $(0.3 - 3) \times 10^{-10}$; the range is due to the uncertainties in the V_{CKM} parameters themselves. This thesis is a complete analysis of our existing data set, yielding no candidate events. A 90% CL upper limit of 2.43×10^{-9} on the $K^+ \rightarrow \pi^+ \nu \bar{\nu}$ branching fraction is inferred. A simultaneous search for the processes $K^+ \rightarrow \pi^+ X^0$, where X^0 is any massless, weakly interacting particle, results in a 90% CL upper limit on the branching fraction of 5.18×10^{-10} .

Acknowledgements

“Absolutely,” Stew Smith said. It was January 1990, and I was in the middle of asking him about possibly doing my thesis on his rare kaon decay experiment. He didn’t actually let me finish my question. His style set the tone for much of my stay at graduate school. With the next problem beating down the door and as many facts at hand as there were ever likely to be, just make the damn decision and get on with it. And no hand-wringing afterwards. While you will occasionally make the wrong decision, I’ve come to believe that this is the only way to move ahead. I hate hand-wringing.

Stew sent me to work with the most gifted and productive group of people I’ve ever met. Mark Ito was first, trying to tease precise information out of data that had been mortally wounded. His level of detailed attention to an almost intractable task made the impossible just barely conceivable. Somehow, the patient lived. Dan Marlow was next, on a project that started out as an assignment, and then a challenge, and then an obsession. Although I’m not in the same league, I think my style was mostly learned from Dan: just make it work. If someone else says it’s impossible, so much

the worse for them. Lately, Peter Meyers has been my watchdog more than anyone else. He might be the brightest person I've ever met. His un-compromising attitude towards physics demands that average work be made good, and that good work be made better. He's even tried to make me wring my hands from time-to-time: I like to think I've met him half way. Frank Shoemaker has become my sounding-board, and counsellor of last resort. When all else has failed and no more information is available: get Frank's best guess on how to proceed. Somehow, this almost always seems to work.

Particle Physics experiments are team efforts, requiring a skilled and dedicated technical group. No one is skilled enough to build what physicists actually ask for, but Bill Sands, Bob Klemmer, Bill Groom, Alan Nelson and Sam Morreale always seem to manage to design and build what we really need. Stan Chidzik, Dick Rabberman, and Carl Bopp are always near by to design and assemble the electronics to read out what we've built, and Ken Kazlauskis maintains the computers we use to transform what we actually did into what we wish we had done. Together with the more recent addition of the skills and experience of Bob Wixted, the strength of this technical group is truly formidable.

Working with other students has taught me more than I'd care to admit. Mark Convery has a demanding attention to detail that I marvel at. I think he worries too much. I suspect that he thinks I don't worry enough. Mehran Ardebili has

a singularly unwavering belief in his viewpoint that can sway almost anyone. His determination is to be marvelled at. Jesse Stone is one of the more interesting people I've ever come across. Somehow, he manages to combine heavy-metal trivia with productive physics research (clearly leaving no room for the basic knowledge the rest of us take for granted). Sometimes, he scares me.

At home, I've missed too much of Lisa, Katie, and Michael growing up. I've missed Freya growing old. I miss Nana. Somehow, my mother kept me in touch with my whole family, and when I'm home it's like I never left. That, at least, kept it all bearable.

Contents

| | |
|---|------------|
| Abstract | iii |
| Acknowledgements | v |
| 1 Introduction | 1 |
| 1.1 The Standard Model and the Quark Mixing Matrix | 2 |
| 1.2 Measuring V_{CKM} | 7 |
| 1.3 Measuring V_{td} : Getting into the Loop(s) | 10 |
| 1.4 The decay $K^+ \rightarrow \pi^+ \nu \bar{\nu}$ | 16 |
| 1.5 Unless There's Something Else Out There | 20 |
| 1.6 Current Experimental Status | 25 |
| 2 The E787 Experiment | 27 |
| 2.1 Overview | 27 |
| 2.2 The K^+ Beam Instrumentation. | 32 |
| 2.3 The K^+ Stopping Target | 37 |

| | | |
|------------|--|-----------|
| 2.4 | The Drift Chamber | 38 |
| 2.5 | The Range Stack | 38 |
| 2.6 | The γ-Veto | 39 |
| 2.7 | The $K^+ \rightarrow \pi^+ \nu\bar{\nu}$ Trigger | 41 |
| 2.7.1 | Level 0 Trigger | 41 |
| 2.7.2 | Level 1 Refined Range and Hextant Veto | 43 |
| 2.7.3 | Level 1.5 Energy Trigger | 43 |
| 2.7.4 | Online TD $\pi^+ \rightarrow \mu^+$ Finder | 44 |
| 2.8 | Monitor Triggers | 44 |
| 2.9 | The Data | 46 |
| 3 | The Offline Analysis | 47 |
| 3.1 | Offline Software | 47 |
| 3.2 | Basic Track Reconstruction and Kinematic Calculations | 48 |
| 3.2.1 | Kinematic Scaling | 53 |
| 3.3 | Offline Cuts | 58 |
| 3.3.1 | Reconstruction | 62 |
| 3.3.2 | Beam line Elements | 63 |
| 3.3.3 | Drift Chamber | 67 |
| 3.3.4 | Kaon Stopping Target | 68 |
| 3.3.5 | Range Stack Track Analysis | 72 |

| | | |
|----------|---|------------|
| 3.3.6 | Delayed Coincidence and Timing Consistency Checks | 81 |
| 3.3.7 | TD Particle Identification | 82 |
| 3.3.8 | INTIME γ Veto | 88 |
| 3.3.9 | Kinematics | 90 |
| 3.4 | Background Studies | 93 |
| 3.4.1 | π scats | 97 |
| 3.4.2 | $K^+ \rightarrow \mu^+ \nu_\mu$ | 105 |
| 3.4.3 | $K^+ \rightarrow \pi^+ \pi^0$ | 111 |
| 3.5 | The $K^+ \rightarrow \pi^+ \nu\bar{\nu}$ Search | 115 |
| 3.5.1 | Pass 1 | 115 |
| 3.5.2 | Pass 2 | 115 |
| 3.5.3 | Pass 3 | 117 |
| 4 | The Sensitivity | 121 |
| 4.1 | The UMC-based acceptance measurements | 127 |
| 4.1.1 | The online trigger, A_{trig} | 128 |
| 4.1.2 | The offline fiducial region cuts, A_{umc} | 132 |
| 4.1.3 | Nuclear interactions and decay-in-flight, A_{nivid} | 132 |
| 4.2 | $K^+ \rightarrow \mu^+ \nu_\mu$ based measurements | 137 |
| 4.2.1 | Reconstruction losses, A_{recon} | 137 |
| 4.2.2 | Photon veto, beam, target, and accidental losses, $A_{K_{\mu 2}}$ | 144 |

| | |
|---|------------|
| 4.2.3 Accidental losses in the LAY14 cut, $A_{\text{L14}}^{\text{acc}}$ | 145 |
| 4.2.4 Delayed coincidence and related losses, A_{DC} | 148 |
| 4.3 π scat measurements | 150 |
| 4.3.1 TD $\pi^+ \rightarrow \mu^+$ fitter and related losses, A_{TD} | 150 |
| 4.3.2 Tracking losses in the range stack, $A_{\pi\text{scat}}$ | 155 |
| 4.4 $K^+ \rightarrow \pi^+\pi^0$ measurements | 161 |
| 4.4.1 Particle-type dependent losses in the target, $A_{K_{\pi^2}}$ | 161 |
| 4.4.2 Level 1.5 energy trigger, $A_{\text{L1.5}}$ | 162 |
| 4.5 The beam kaon flux, $N_{KT\text{live}}$ | 165 |
| 4.6 The $K^+ \rightarrow \mu^+\nu_\mu$ branching ratio and kaon stopping fraction, f_S | 170 |
| 4.7 The $K^+ \rightarrow \pi^+\pi^0$ branching ratio | 175 |
| 4.8 Putting it all together | 180 |
| 5 Conclusions | 184 |
| 5.1 Establishing Branching Ratio Upper Limits | 184 |
| 5.1.1 The $K^+ \rightarrow \pi^+\nu\bar{\nu}$ Upper Limit | 186 |
| 5.1.2 The $K^+ \rightarrow \pi^+X^0$ Upper Limit | 187 |
| 5.2 The Future | 187 |
| References | 193 |
| A The E787 Collaboration | 197 |

| | |
|---|-----|
| A.1 The E787 collaboration, participating in data taking or analysis for this thesis | 197 |
| B The Home of the Offline Analysis 199 | |
| B.1 KOFIA | 199 |
| B.2 UMC | 200 |
| C The Straw Chamber Electronics 201 | |
| C.1 Overview | 201 |
| C.2 Front End Electronics | 204 |
| C.3 Cables | 207 |
| C.4 External Electronics | 208 |
| C.5 Calibration sources | 214 |
| C.6 Where, and what, to ground | 216 |

List of Tables

| | |
|---|----|
| 2.1 Decay mode branching ratios and end points for K^+ decays with a final state μ^+ or π^+ , along with the rare decay modes of interest | 28 |
| 3.1 Target energy scale factors, the slopes from linear fits to energy vs. visible target energy expected from range. The correction for 1990 data is particularly large. | 54 |
| 3.2 Kinematic scale factors for data. | 56 |
| 3.3 Kinematic scale factors and smearing for UMC. | 56 |
| 3.4 Peak positions and widths (from gaussian fits with no background) before and after corrections for both data and UMC. Momentum is correct with TG+IC Range. | 57 |
| 3.5 Part 1: the complete list of the offline cuts. | 58 |
| 3.5 Part 2: the complete list of the offline cuts, continued. | 61 |
| 3.6 Č _π Cut half window and time offset $t_{RS} - t_{C_\pi}$ | 64 |
| 3.7 BWPC Cut half window and time offset. | 65 |
| 3.8 Maximum allowed RPRFIT stopping position. | 78 |

| | |
|---|----|
| 3.9 RSDEDX σ 's used in χ^2_{RSDEDX} calculation. | 80 |
| 3.10 Some FITPI output variables and derivatives. | 83 |
| 3.11 Variable central values and sigmas used in the TDACC χ^2 . The quantity z_{dc}^{nsec} is the expected stopping range stack z position based on a DC track extrapolation calibrated in nsec of end-to-end-time. | 84 |
| 3.12 Variables, weights, and pion offsets for DFA. The quantity ELASTRS is the stopping counter energy. | 85 |
| 3.13 INTIME half window, time offset, and prompt energy thresholds. . . . | 90 |
| 3.14 Summary of the background study results arrived at in the following sections. The π scat background is split into two parts: the “two-beam-particle” background is defined to have a second beam particle in coincidence with the range stack time TRS, while the “one-beam-particle” background does not. | 96 |
| 3.15 Cuts removed from analysis for π scat study setup. The PBGLASS cut was used only in 1991, while B4TDEDX was used only for 1989 and 1990. | 98 |

| | |
|--|-----|
| 3.16 Sample selection and rejection estimates for the two-beam-particle background study. In 1991, the several cuts were inadvertently not used in “setup” stage of the PICER and PISCAT_BW rejection measurements, resulting in increased statistics but possibly with a sample not representative of the background. “Selection” refers to the inverted PISCAT_BW cut described in the text, resulting in N survivors in the figure. | 101 |
| 3.17 Sample selection and rejection estimates for the one-beam-particle background study. “Selection” refers to the inverted B4DEDX cut, resulting in N survivors in the figure. | 104 |
| 3.18 $K^+ \rightarrow \mu^+ \nu_\mu$ kinematic and TD cuts removed from setup. | 107 |
| 3.19 Numerical results of the $K^+ \rightarrow \mu^+ \nu_\mu$ background studies. A local version of the ELVETO cut (Section 3.3.7) was applied in the 1989 Pass 1, reducing both the number surviving the kinematic selection and TD rejection. | 109 |
| 3.20 Cross check of the $K^+ \rightarrow \mu^+ \nu_\mu$ study, by predicting the number of surviving events after inverting the RBOX cut. | 110 |

| | |
|---|-----|
| 3.21 Numerical results of the $K^+ \rightarrow \pi^+\pi^0$ background studies. The “33cm” entries refer to a range box cut with a lower bound of 33 cm which was considered for this analysis, but replaced with a 34 cm cut based on this study. | 113 |
| 3.22 Cross check of the $K^+ \rightarrow \pi^+\pi^0$ study, by predicting the number of events expected in the “High Range” ($100 \text{ MeV} < E_{\text{tot}}^{\text{new}} < 115 \text{ MeV}$ and $R_{\text{tot}}^{\text{new}} > 33 \text{ cm}$) and “High Energy” ($28 \text{ cm} < R_{\text{tot}}^{\text{new}} < 33 \text{ cm}$ and $E_{\text{tot}}^{\text{new}} > 115 \text{ MeV}$) tails of the $K^+ \rightarrow \pi^+\pi^0$ peak. The agreement is fairly good. | 114 |
| 3.23 Summary of the various Pass 1 analyses from 89-91 data. | 116 |
| 3.24 The Pass 2 analysis. During Pass 1, under certain conditions no photon veto was applied. The cut GAMVETP1 forces the re-application of the full Pass 1 photon veto. | 118 |
| 3.25 The Pass 3 analysis. The GOOD_RUN cut removes events from duplicate runs, and is used consistently during the scaler counting in Chapter 4. | 120 |
| 4.1 UMC-based $K^+ \rightarrow \pi^+\nu\bar{\nu}$ trigger acceptance factors. | 130 |
| 4.2 UMC-based $K^+ \rightarrow \pi^+X^0$ trigger acceptance factors. | 131 |
| 4.3 UMC-based fiducial volume acceptance for $K^+ \rightarrow \pi^+\nu\bar{\nu}$ | 132 |
| 4.4 UMC-based fiducial volume acceptance for $K^+ \rightarrow \pi^+X^0$ | 133 |

| | | |
|------|--|-----|
| 4.5 | UMC-based nuclear interactions and decay-in-flight analysis for $K^+ \rightarrow \pi^+ \nu\bar{\nu}$.134 | |
| 4.6 | UMC-based nuclear interactions and decay-in-flight analysis for $K^+ \rightarrow \pi^+ X^0$.134 | |
| 4.7 | $K^+ \rightarrow \pi^+ \nu\bar{\nu}$ nuclear interaction and decay-in-flight acceptance. The errors are purely statistical, and the true errors due to uncertainties in the nuclear interaction simulation are likely somewhat larger. | 135 |
| 4.8 | $K^+ \rightarrow \pi^+ X^0$ nuclear interaction and decay-in-flight acceptance. The errors are purely statistical, and the true errors due to uncertainties in the nuclear interaction simulation are likely somewhat larger. | 135 |
| 4.9 | Reconstruction efficiency method 1: assume all $K_{\mu 2}(1)$ events passing the online delayed coincidence are reconstructible. | 141 |
| 4.10 | Reconstruction efficiency method 2: assume $K_{\mu 2}(1)$ events passing the online delayed coincidence and with $E_{RS} > 100$ MeV are reconstructible. | 142 |
| 4.11 | Reconstruction efficiency method 3: assume $K_{\mu 2}(1)$ events passing the online delayed coincidence and with $100 \text{ MeV} < E_{RS} < 160 \text{ MeV}$ are reconstructible. | 142 |
| 4.12 | Reconstruction efficiency method 4: Using the events from method 3, use the area of a gaussian fit to E_{RS} to count the events (the actual fit is a gaussian plus flat background). | 143 |

| | |
|--|-----|
| 4.13 The RS-TRK algorithm efficiency. The “RS-TRK” entry is the number of events that pass the momentum-selection that are reconstructed by RS-TRK with $E_{RS} > 100$ MeV/c. | 144 |
| 4.14 The final reconstruction efficiency calculation. | 144 |
| 4.15 The basic $K^+ \rightarrow \mu^+ \nu_\mu$ efficiency measurement. | 146 |
| 4.16 Accidental losses in the LAY14 cut for $K^+ \rightarrow \pi^+ \nu\bar{\nu}$ | 147 |
| 4.17 Accidental losses in the LAY14 cut for $K^+ \rightarrow \pi^+ X^0$ | 148 |
| 4.18 Delayed coincidence and related acceptances. | 148 |
| 4.19 Selection cuts applied to π scat triggers for the TD efficiency calculation. | 151 |
| 4.20 The TD fitter efficiency, A_{tdfit} | 155 |
| 4.21 The acceptance of the remaining TD cuts, A_C . ONLTD is the online $\pi^+ \rightarrow \mu^+$ finder described in chapter 2. | 156 |
| 4.22 The complete TD $\pi^+ \rightarrow \mu^+$ cuts acceptance. | 156 |
| 4.23 Selection cuts applied to $K^+ \rightarrow \pi^+ \nu\bar{\nu}$ triggers for the DC/RS efficiency calculation, $A_{\pi scat}$ | 157 |
| 4.24 The acceptance of the RS analysis, assuming stopping layer independence. | 159 |
| 4.25 The acceptance of the RS analysis weighted by $K^+ \rightarrow \pi^+ \nu\bar{\nu}$ stopping layer distribution. Error is inferred by varying the box cut used for selection as described in the text. | 160 |

| | |
|--|-----|
| 4.26 The acceptance of the RS analysis weighted by $K^+ \rightarrow \pi^+ X^0$ stopping layer distribution. Error is inferred by varying the box cut used for selection as described in the text. | 160 |
| 4.27 The pion dependent target cuts, $A_{K_{\mu 2}}$ | 162 |
| 4.28 The $K^+ \rightarrow \pi^+ X^0$ level 1.5 trigger efficiency measurement. | 164 |
| 4.29 The $K^+ \rightarrow \pi^+ \nu\bar{\nu}$ level 1.5 trigger efficiency measurement. | 165 |
| 4.30 The run ranges analyzed, and the kaon flux into the target with the detector “live.” | 170 |
| 4.31 The $K^+ \rightarrow \mu^+ \nu_\mu$ branching ratio analysis. | 171 |
| 4.32 The UMC $K^+ \rightarrow \mu^+ \nu_\mu$ analysis efficiency, for assumed range stack layer thicknesses 1.905 cm and 1.95 cm. The total efficiency of the analysis is $A_{K_{\mu 2}}^{\text{umc}}$. The reconstruction efficiency, $A_{\text{recon}}^{\text{umc}}$, for UMC data is the fraction of events passed by ISKCODE, and will be used in the branching ratio calculation below. | 173 |
| 4.33 The KT_{live} calculation for the $K^+ \rightarrow \mu^+ \nu_\mu$ branching ratio calculation. | 174 |
| 4.34 The f_S calculation. In 1991, changes in the beam instrumentation may be responsible for the lower stopping fraction that year. | 175 |
| 4.35 The $K^+ \rightarrow \pi^+ \pi^0$ branching ratio analysis. | 176 |

| | |
|--|-----|
| 4.36 The UMC $K^+ \rightarrow \pi^+\pi^0$ analysis efficiency, for assumed range stack layer thicknesses 1.905 cm and 1.95 cm (the PNNSTOP cut introduces the scintillator thickness dependency). $A_{\text{recon}}^{\text{umc}}$ is the basic reconstruction efficiency for the UMC data. | 177 |
| 4.37 The $KTlive$ calculation for the $K^+ \rightarrow \pi^+\pi^0$ branching ratio calculation. | 178 |
| 4.38 The KOFIA reconstruction efficiency for UMC $K^+ \rightarrow \pi^+\pi^0$ under various conditions. The range stack scintillator thickness parameter was set to 1.905 cm for all trials. The corresponding $A_{\text{recon}}^{\text{umc}}$ for $K^+ \rightarrow \mu^+\nu_\mu$ is 0.979 ± 0.001 | 179 |
| 4.39 The $K^+ \rightarrow \pi^+\pi^0$ branching ratio measurement. The accepted value is 0.2116 ± 0.0014 , so the measurement is about 3% low (a 0.75σ discrepancy). | 181 |
| 4.40 The complete $K^+ \rightarrow \pi^+\nu\bar{\nu}$ efficiency. | 182 |
| 4.41 The complete $K^+ \rightarrow \pi^+X^0$ efficiency. | 182 |
| 4.42 The complete $K^+ \rightarrow \pi^+\nu\bar{\nu}$ sensitivity. The errors on A_{tot} and f_S have been adjusted, removing common factors that will cancel in the product. | 183 |
| 4.43 The complete $K^+ \rightarrow \pi^+X^0$ sensitivity. The errors on A_{tot} and f_S have been adjusted, removing common factors that will cancel in the product. | 183 |
| C.1 Custom surface mount parts for HV distribution and blocking. | 207 |

| | |
|--|-----|
| C.2 Cables used for custom signal cable assemblies, and HV distribution. | |
| Each cable is actually 16 feet long. | 208 |
| C.3 Tests performed end-to-end time readout circuit. | 212 |
| C.4 Key parts used on the external electronics boards. | 214 |

List of Figures

| | | |
|-----|--|----|
| 1.1 | Constraints from $B^0 - \overline{B}^0$ mixing, ϵ , and $ V_{ub}/V_{cb} $ in the (ρ, η) plane. Central values of the various parameters (see text) result in the solid lines, with the $\pm 1\sigma$ values dashed. The allowed region is shaded. | 15 |
| 1.2 | The prototype unitarity triangle. $K^+ \rightarrow \pi^+ \nu \bar{\nu}$ and tree-level B decays measure the length of its sides, while CP violation in the B system will measure the angles α, β , and γ | 22 |
| 1.3 | A hypothetical perfect $K^+ \rightarrow \pi^+ \nu \bar{\nu}$ measurement of $B = 1 \times 10^{-10}$ superimposed onto the (ρ, η) plane constraints, along with the unitarity triangle. The solid line is the $K^+ \rightarrow \pi^+ \nu \bar{\nu}$ allowed curve for the central parameter values, and the dotted lines are the $\pm 1\sigma$ bounds. | 23 |
| 2.1 | Common K^+ Decay mode spectra, along with $K^+ \rightarrow \pi^+ \nu \bar{\nu}$ | 29 |
| 2.2 | 3-D Perspective view of the E787 detector. | 33 |
| 2.3 | Side view of the E787 detector. | 34 |

| | |
|---|----|
| 2.4 Transient digitizer data showing a complete $\pi^+ \rightarrow \mu^+ \rightarrow e^+$ sequence for a pion passing through layer 11 and stopping in layer 12. About 40 nsec later it decayed into a muon which stayed in layer 12. 220 nsec later, the muon decayed into a positron, which penetrates deeper into the range stack. | 40 |
| 3.1 Range, energy, and momentum peaks for data and reconstructed monte carlo from 1991. | 59 |
| 3.2 Range, energy, and momentum peaks for data and reconstructed monte carlo from 1991. | 60 |
| 3.3 The target dE/dX cut for $K^+ \rightarrow \pi^+\pi^0$ pions in the $K^+ \rightarrow \pi^+\nu\bar{\nu}$ data after the Pass 1 photon cuts. The top plot is for events in the peak, centre is for pions with typical $K^+ \rightarrow \pi^+\pi^0$ total energy but a high total range measurement, and the bottom is for pions with typical $K^+ \rightarrow \pi^+\pi^0$ total range but a high energy. | 71 |
| 3.4 Target kaon energy vs. drift chamber extrapolated kaon decay position for 1990 $K^+ \rightarrow \mu^+\nu_\mu$ monitor triggers. | 72 |
| 3.5 The RS stopping z cut, ZFRF. The plots are labeled with effective RS layer, corresponding to physical layers 11-21. Events with high stopping $ z $ are cut. | 77 |

| | |
|--|----|
| 3.6 Range stack dE/dX χ^2 per degree of freedom. Pions from the π scat trigger are solid lines, and $K^+ \rightarrow \mu^+ \nu_\mu$ background events from the background study in Section 3.4.2 are dashed. The distributions are normalized to unit area, and there are numerous overflows in the $K^+ \rightarrow \mu^+ \nu_\mu$ sample. The top plot is all events passing the $K^+ \rightarrow \mu^+ \nu_\mu$ background “setup” (see the $K^+ \rightarrow \mu^+ \nu_\mu$ background study, Section 3.4.2), the centre is events passing everything except the box, and the bottom is for events in the box. | 79 |
| 3.7 The Fisher variable, F , for 1989 $K^+ \rightarrow \mu^+ \nu_\mu$ background events passing the rest of the TD analysis from the $K^+ \rightarrow \mu^+ \nu_\mu$ background study (Section 3.4.2), plotted along with pions from π scats after the same cuts. Cut events with $F < -1$ | 86 |
| 3.8 The final photon veto, part 1: the energy threshold. After applying the full Pass 1 photon veto, the prompt energy in each sub-system in narrow time windows around TRS is plotted for residual $K^+ \rightarrow \pi^+ \pi^0$ in the $K^+ \rightarrow \pi^+ \nu \bar{\nu}$ data and $K_{\mu 2}(1)$ monitors. The energy threshold is set by inspection of these distributions, shown with solid lines in the plots for the RS, BV, EC, IC, and VC. The energy cuts off on the high side due to photon veto applied at Pass 1. | 91 |

| | | |
|------|---|-----|
| 3.9 | The final photon veto, part 2: the INTIME time windows. Using the energy threshold found above, the time of the hit nearest TRS with energy above threshold in each subsystem is plotted, and the time window is set by eye. The distributions are made after the full Pass 1 γ -veto, which makes the “notch” near $t = 0$ corresponding the Pass 1 windows. $K^+ \rightarrow \pi^+\pi^0$ lines are solid, and $K^+ \rightarrow \mu^+\nu_\mu$ lines are dashed. | 92 |
| 3.10 | A prototype background study. The full $K^+ \rightarrow \pi^+\nu\bar{\nu}$ data set is analyzed with all but two selected cuts. These cuts should have high rejections for the background under study, and be uncorrelated. Using this technique of factoring the rejections of multiple cuts allows estimates of less than one expected event to be inferred from the study. | 95 |
| 3.11 | Two-beam-particle π scat study. | 100 |
| 3.12 | One-beam-particle π scat study. PROMPT requires that the target TIMEPI be within 2 nsec of TIMEK. | 103 |
| 3.13 | $K^+ \rightarrow \mu^+\nu_\mu$ background study outline. The inverted RNGMOM cut was not applied to 1990 data, because a version of RNGMOM was applied at Pass 1. | 108 |
| 3.14 | $K^+ \rightarrow \pi^+\pi^0$ background study outline. | 112 |
| 3.15 | The final range/energy spectrum after the total momentum cut. The range/energy box is overlaid. No events are observed in the final sample. | 119 |

| | | |
|-----|--|-----|
| 4.1 | The UMC-based acceptance calculations. | 129 |
| 4.2 | Range vs. Energy spectra for $K^+ \rightarrow \pi^+ \nu\bar{\nu}$, before and after the PBOX cut, showing the RBOX/EBOX cuts, using the nuclear interactions and decay-in-flight enabled sample. | 136 |
| 4.3 | Range vs. Energy spectra for $K^+ \rightarrow \pi^+ X^0$, before and after the PBOX cut, showing the RBOX/EBOX cuts, using the nuclear interactions and decay-in-flight enabled sample. | 136 |
| 4.4 | The $K^+ \rightarrow \mu^+ \nu_\mu$ based acceptance calculations. The “layer 15 veto” refers to effective layer 15, which is the outer RS layer (physical layer 21).138 | |
| 4.5 | The RS energy of the track found by RS_TRK nearest 130 MeV for all 1990 $K_{\mu 2}(1)$ triggers (top), plus the online delayed coincidence (middle), plus a veto on the outer RS layer (bottom), plotted on linear (left) and log (right) scales. The final reconstruction efficiency measurement will assume that all events above 100 MeV (the vertical line) are reconstructible. | 139 |

| | |
|--|-----|
| 4.6 Target TIMEPI-TIMEK for the 1990 $K_{\mu 2}(1)$ selected sample used to measure the delayed coincidence efficiency. The sample has no significant decay-in-flight contamination. TIMEPI-TIMEK is fit to an exponential from 0 to 40 nsec resulting in a kaon lifetime $\tau_K = 12.2 \pm 0.2$ nsec, in good agreement with the accepted value of 12.371 ± 0.0029 nsec. | 149 |
| 4.7 Pion lifetime fits over various fit ranges for 1990 data. The parameter "P2" is the τ_π (in nsec) fit result, and changes significantly with different fit ranges. Zero-bins are included in the fit. | 153 |
| 4.8 The TD fitter acceptance calculation. | 154 |
| 4.9 Total range vs. energy distributions for π scats from the $K^+ \rightarrow \pi^+ \nu \bar{\nu}$ trigger, before and after the PBOX cut. The range-energy box is overlaid. The sample in-the-box is used for the $A_{\pi scat}$ efficiency measurement. | 159 |
| 4.10 Regions in the level 1.5 energy trigger efficiency calculation. | 164 |
| C.1 Comparison of old range stack chambers to new straw chambers. | 202 |
| C.2 Detailed view of the new straw chambers, drawn by William Sands, Princeton High Energy Physics group. | 203 |
| C.3 RSSC readout electronics. | 205 |
| C.4 Comparator threshold adjust and signal path for one straw pair. | 211 |

| | |
|--|-----|
| C.5 The time stretcher schematic. The design is adapted from a Lecroy time-of-flight TDC. "Vref" is about 9 volts. | 213 |
| C.6 ^{55}Fe calibration data from the inner straw chamber in RS sector 1, channel 1. There are two peaks per straw, or 4 per channel. The ordinate is counts, and the abscissa is the pulse width in stretched nsec. The complete system has 1248 such channels, or 2496 straws. . | 215 |

Chapter 1

Introduction

For much of my career as a student, I found physics to be somewhat fickle. As one professor was insisting on the fundamental importance of some “law”, another would be teaching that it was more of a guideline, really. It was relatively recently that I realized I was simply observing the evolution of a living field. New results seem to transform “elementary” particles into “composite” ones, but it takes a few years to fix all the text books and a few decades to rewrite all the introductory lectures. Finally, it dawned on me that physics itself doesn’t change: it is our best current approximation to, quite simply, everything, along with quantitative measurements of just how bad that approximation could be.

Admittedly, “everything” sounds a little grandiose. A good place to start might be to figure out the most basic bits and pieces that make up “everything,” and all the ways in which these components can interact. This is Elementary Particle Physics, and its current best approximation to the basic constituents of matter and the forces

and rules that govern their interactions is called the Standard Model.

1.1 The Standard Model and the Quark Mixing Matrix

While elementary particle theory has a rich and complex history, here I will only emphasize the details important to this work.¹ Fundamental particles seem to come in two groups: firstly, quarks and leptons make up what can be thought of as *matter* – spin 1/2 particles obeying Fermi-Dirac statistics, commonly called *fermions*; secondly, the photon, the intermediate vector bosons, the gluon and possibly the graviton mediate the *forces* – integer spin particles obeying Bose-Einstein statistics, commonly called the *gauge bosons*.

Both quarks and leptons apparently come in three generations of doublets, usually presented something like this:

quarks

$$\begin{pmatrix} u \\ d \end{pmatrix}, \begin{pmatrix} c \\ s \end{pmatrix}, \begin{pmatrix} t \\ b \end{pmatrix},$$

¹Commins and Bucksbaum [1] is the principal reference for this section, and has a detailed presentation of Weak interactions in general.

leptons

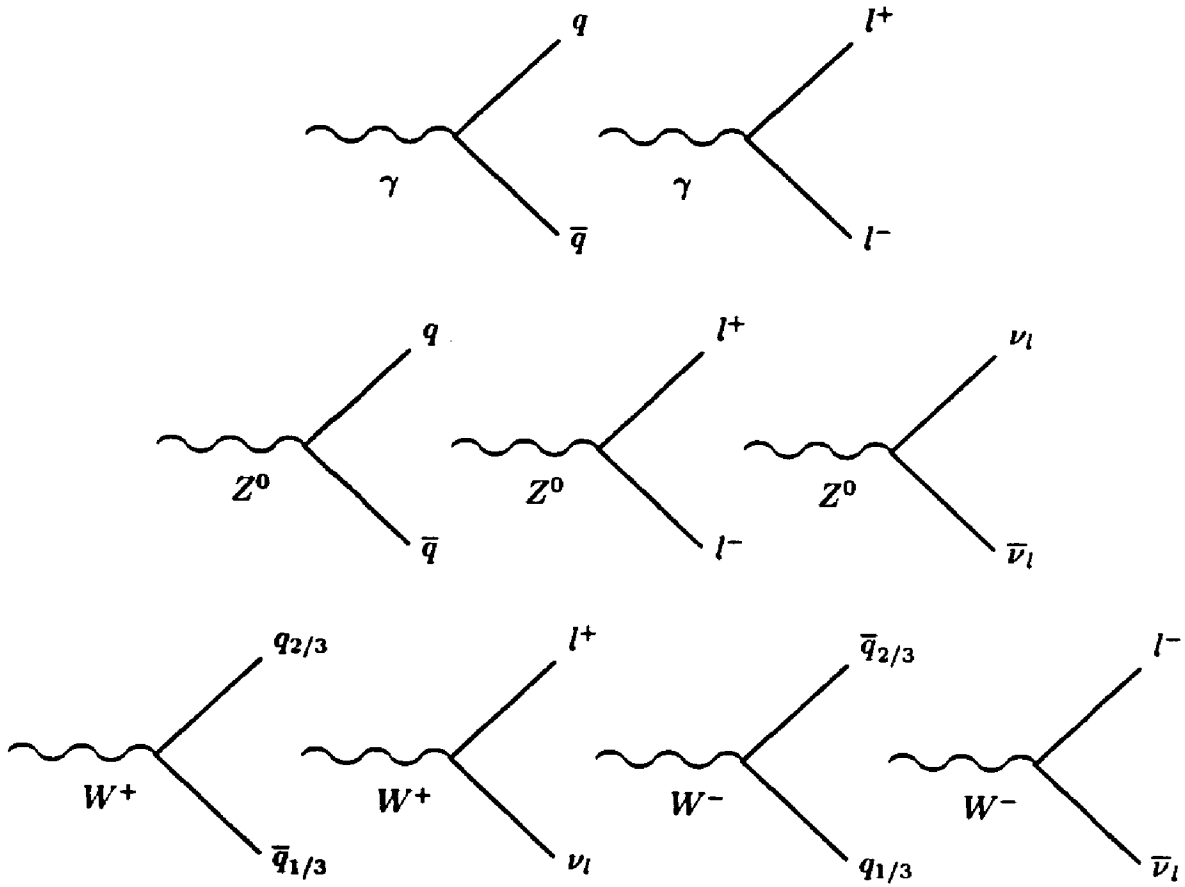
$$\begin{pmatrix} \nu_e \\ e^- \end{pmatrix}, \begin{pmatrix} \nu_\mu \\ \mu^- \end{pmatrix}, \begin{pmatrix} \nu_\tau \\ \tau^- \end{pmatrix}.$$

In addition, each of the above particles has an “anti-particle” partner, which is represented either with an opposite charge sign (eg e^+) or an over-bar (eg \bar{u}). The charged leptons can be referred to generically as l^- , the neutral leptons as ν_l , quarks as simply q , or the $+2/3$ charged u, c, and t quarks as $q_{2/3}$ and the $-1/3$ charge d, s, and b quarks as $q_{1/3}$.

This piece of paper consists of only the up (u) and down (d) quarks (which are bound together by gluons to make up the familiar protons and neutrons), and the electron (e). Since we’re all in favour of literacy, the existence of the first generation seems well motivated; however, the theoretical case for the second and third generations is less sound. Experimentally, they simply exist.²

The gauge bosons that concern us here mediate the “Weak Force” and are called the intermediate vector bosons, W^\pm and Z^0 , and their sibling from electromagnetism the photon, γ . Their interactions with matter can be represented by a set of basic vertices which can be represented pictorially:

²Actually, while the tau neutrino, ν_τ , has most likely been observed as missing momentum in τ lepton decays, it has not been directly demonstrated to be different than ν_e and ν_μ .



The above diagrams represent the decay modes of the gauge bosons, with time running horizontally. With appropriate rotations, they include all the primary interaction vertices of the γ , W^\pm and Z^0 with quarks and leptons.

A feature of the quark sector is that the quantum mechanical eigenstates of the electroweak interaction, q' , are not the same as the physical mass eigenstates, q ; they are related by a unitary transformation of the form

$$q_{2/3}^j = \sum_{k=1}^3 U_{2/3}^{jk} q'^k_{2/3}, \quad q_{1/3}^j = \sum_{k=1}^3 U_{1/3}^{jk} q'^k_{1/3}.$$

or, more commonly, using matrix notation

$$q_{2/3} = U_{2/3} q'_{2/3}, \quad q_{1/3} = U_{1/3} q'_{1/3}.$$

Since the quantum mechanical amplitude, T , for a process can be written in terms of the particle currents, J_μ , the effect of these different eigenstates on physical phenomena is contained in the current itself ($T \propto \int J_\mu A^\mu d^4x$, where A^μ is the interaction potential or field). So, write out the basic quark electro-magnetic and weak currents in this basis and see what they look like in the physical mass basis (frequently exploiting the fact $U^\dagger U = I$ for a unitary matrix):

$$\begin{aligned} J_\mu^{\text{EM}} &= \bar{q}' \gamma_\mu Q q' \\ &= \bar{q}' \gamma_\mu Q U_Q^\dagger U_Q q' \\ &= (U_Q q')^\dagger \gamma_\mu Q (U_Q q') \\ &= \bar{q} \gamma_\mu Q q, \end{aligned}$$

where Q is the charge operator and U_Q is either $U_{2/3}$ or $U_{1/3}$, appropriate to the quark charge. It is apparent that J_μ^{EM} is invariant under the transformation U_Q . The same is true of the weak neutral current:

$$\begin{aligned} J_\mu^{\text{NC}} &= \bar{q}' \gamma_\mu 1/2(c_V - c_A \gamma^5) q' \\ &= \bar{q}' \gamma_\mu 1/2(c_V - c_A \gamma^5) U_Q^\dagger U_Q q' \\ &= (U_Q q')^\dagger \gamma_\mu 1/2(c_V - c_A \gamma^5) (U_Q q') \\ &= \bar{q} \gamma_\mu 1/2(c_V - c_A \gamma^5) q \end{aligned}$$

where the factors c_V and c_A are the vector and axial vector components of the weak neutral current calculable from the standard model, and the factor of $1/2$ is added for the conventional normalization.

The weak charged current, however, will make matters more interesting. Consider the charge raising weak current:

$$\begin{aligned}
 J_\mu^{\text{CC}} &= \bar{q}'_{2/3} \gamma_\mu 1/2(1 - \gamma^5) q'_{1/3} \\
 &= \bar{q}'_{2/3} \gamma_\mu 1/2(1 - \gamma^5) U_{2/3}^\dagger U_{2/3} U_{1/3}^\dagger U_{1/3} q'_{1/3} \\
 &= (U_{2/3} q'_{2/3})^\dagger \gamma_\mu 1/2(1 - \gamma^5) U_{2/3} U_{1/3}^\dagger (U_{1/3} q'_{1/3}) \\
 &= \bar{q}_{2/3} \gamma_\mu 1/2(1 - \gamma^5) U_{2/3} U_{1/3}^\dagger q_{1/3} \\
 &= \bar{q}_{2/3} \gamma_\mu 1/2(1 - \gamma^5) V_{\text{CKM}} q_{1/3}
 \end{aligned}$$

where $V_{\text{CKM}} = U_{2/3} U_{1/3}^\dagger$ is the product of two unitary matrices and is therefore itself unitary. Note that the two separate transformations ($U_{2/3}$ and $U_{1/3}$) become physically equivalent to a single transformation, which is conventionally applied to $-1/3$ charge quarks. V_{CKM} is called the Cabibbo-Kobayashi-Maskawa, or quark-mixing, matrix.

It is important to comment on precisely what parts of the theory require that V_{CKM} be unitary. It is widely believed that all interactions can be described by quantum field theories which are invariant under local gauge transformations. For the Standard Model, this includes the $SU(2)$ transformation $\psi \rightarrow \psi' = e^{ia(x) \cdot \tau/2} \psi$, where ψ is the $SU(2)$ wave-function, τ are the familiar Pauli Matrices in weak-isospin space, and

$\alpha(x)$ is a vector in weak-isospin space. With a bit of effort, requiring invariance under this transformation can be shown to require that *all* fermion doublets have the *same* weak coupling [2] (this did not need to be true – for example, the $U(1)$ invariance of electromagnetism does not require that all particles have the same charge). If the different doublets were allowed to have different weak couplings, V_{CKM} would have to reflect this and would not necessarily be unitary; the theory would, however, lose its coveted “re-normalizability,” and would be completely ruined.

1.2 Measuring V_{CKM}

Next, let’s analyze the mixing matrix in a little more detail.³ An arbitrary 3×3 complex matrix has 18 parameters. Unitarity ($V^\dagger V = I$) provides 9 independent equations, leaving 9 free parameters which can be the 3 real Euler rotation angles and 6 complex phases. For further simplification, use the fact that the absolute phase of each quark is not observable and may be arbitrary redefined. Returning to J_μ^{CC} , redefine the quark phases:

$$J_\mu^{\text{CC}} = \bar{q}_{2/3} P_1^\dagger \gamma_\mu 1/2(1 - \gamma^5) V P_2 q_{1/3}$$

³This discussion closely follows Meyers’ course notes [3].

where

$$P_1 = \begin{pmatrix} e^{i\delta_1} & 0 & 0 \\ 0 & e^{i\delta_2} & 0 \\ 0 & 0 & e^{i\delta_3} \end{pmatrix} \text{ and } P_2 = \begin{pmatrix} e^{i\delta_4} & 0 & 0 \\ 0 & e^{i\delta_5} & 0 \\ 0 & 0 & e^{i\delta_6} \end{pmatrix},$$

with the δ_i 's arbitrary. Remove an overall phase from each P_1 , P_2 , and V :

$$J_\mu^{CC} = e^{i\delta_{OV}} \bar{q}_{2/3} \begin{pmatrix} 1 & 0 & 0 \\ 0 & e^{i\delta_2-\delta_1} & 0 \\ 0 & 0 & e^{i\delta_3-\delta_1} \end{pmatrix}^\dagger \gamma_\mu 1/2(1-\gamma^5) V' \begin{pmatrix} 1 & 0 & 0 \\ 0 & e^{i\delta_5-\delta_4} & 0 \\ 0 & 0 & e^{i\delta_6-\delta_4} \end{pmatrix} q_{1/3},$$

where $e^{\delta_{OV}}$ is an unobservable overall phase term which ate up one phase from V (thus the V'), leaving 5 free phases left in V_{CKM} . The four arbitrary relative phase terms ($e^{i\delta_2-\delta_1}$, $e^{i\delta_3-\delta_1}$, $e^{i\delta_5-\delta_4}$ and $e^{i\delta_6-\delta_4}$) can now be used to eliminate four more V_{CKM} phases; thus, V_{CKM} has one remaining unspecified phase, or four free parameters in total.

In principle, the task now at hand seems straight-forward. Pick any four processes that depend independently on elements of V_{CKM} , and measure them well enough to measure the four free parameters. Subsequent measurements will then over-constrain and test the theory.

In practice, however, nature has played a small trick on us which is nicely illustrated by the approximate V_{CKM} parametrization of Wolfenstein [4]:

$$V = \begin{pmatrix} V_{ud} & V_{us} & V_{ub} \\ V_{cd} & V_{cs} & V_{cb} \\ V_{td} & V_{ts} & V_{tb} \end{pmatrix} \simeq \begin{pmatrix} 1 - \lambda^2/2 & \lambda & A\lambda^3(\rho - i\eta) \\ -\lambda & 1 - \lambda^2/2 & A\lambda^2 \\ A\lambda^3(1 - \rho - i\eta) & -A\lambda^2 & 1 \end{pmatrix}$$

with $\lambda = 0.22$ and $A = 0.8 \pm 0.1$. This parameterization takes advantage of the highly diagonally dominant nature of V_{CKM} as well as the approximate unitarity of the upper 2×2 sub-matrix, with the 90% confidence level lower and upper limits on the magnitudes of the components (assuming three quark generations and unitarity)

[6]

$$\begin{pmatrix} (0.9747, 0.9759) & (0.218, 0.224) & (0.002, 0.005) \\ (0.218, 0.224) & (0.9738, 0.9752) & (0.032, 0.048) \\ (0.004, 0.015) & (0.032, 0.048) & (0.9988, 0.9995) \end{pmatrix}.$$

Considerable experimental effort has gone into the above numbers:⁴ $|V_{ud}|$ from nuclear beta decay and μ decay; $|V_{us}|$ from analysis of $K^+ \rightarrow \pi^0 e^+ \nu_e$ and $K^0 \rightarrow \pi^\pm e^\mp \nu_e$; $|V_{cd}|$ from lepto-production of charm and charmed-meson decays; $|V_{cs}|$ from charmed-meson decays; $|V_{cb}|$ from B meson decays; $|V_{ub}/V_{cb}|$ from B meson decays. The remaining elements, V_{td} , V_{ts} and V_{tb} are constrained principally by unitarity; this is a relatively good constraint for V_{tb} , a fair one for V_{ts} , but almost no constraint on V_{td} (it is constrained to be small, but the fractional error from unitarity is large compared

⁴See the Review of Particle Properties [6] and the references within.

to the expected value).

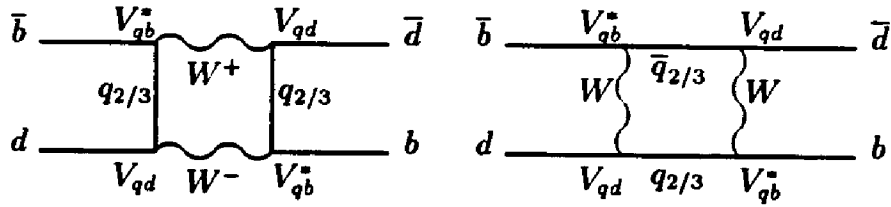
Nature's trick is in the way that the information (in the form of the physical Wolfenstein parameters) gets distributed in V_{CKM} . Notice that two of the four parameters (ρ and η) only play a significant role in V_{ub} and V_{td} , which must be extracted by measuring processes with large $u - b$ or $t - d$ contributions. Put another way, the four "independent" processes must include at least one with a $u - b$ vertex and another with a $t - d$ vertex.⁵ Such processes are highly suppressed and very difficult to see. Detecting the direct decay $b \rightarrow u$ is just barely possible, resulting in the $|V_{ub}/V_{cb}|$ measurement mentioned above. For V_{td} , even if a large sample of t decays is someday available, it seems unlikely that the direct decay $t \rightarrow d$ could ever be detected over the favoured $t \rightarrow b$ process. A direct measurement of V_{td} , now or in the future, is extremely unlikely.

Fortunately, there is another way.

1.3 Measuring V_{td} : Getting into the Loop(s)

Rather than look for direct $t \rightarrow d$ decays, one can look for processes that would be suppressed or forbidden without a $t - d$ vertex. For example, $B^0 - \bar{B}^0$ mixing takes place via the second order "box" diagrams

⁵Of course, this fact is not dependent upon any particular parametrization; rather, it results from the highly diagonally dominant nature of V_{CKM} which is the foundation of the Wolfenstein parametrization, making the conclusions more apparent.



and is suppressed in the Standard Model due to partial cancelations of the various $q_{2/3} = u, c$ or t diagrams. Theoretically, any internal t quark contribution (present if V_{td} is nonzero) would be greatly enhanced by the large t mass. B^0 mixing is usually parameterized in terms of the parameter $x_d = \Delta m_{B^0}/\Gamma$, where Γ is the total B^0 width and Δm_{B^0} is magnitude of the difference of the B^0 decay eigenstate masses. Neglecting any c quark contributions, a Standard Model calculation yields [7]

$$\begin{aligned} x_d &= \frac{G_F^2}{6\pi^2} f_{B_d}^2 B_{B_d} \tau_B m_B M_W^2 \eta_t S(x_t) |V_{td} V_{tb}^*|^2 \\ &\simeq \frac{G_F^2}{6\pi^2} f_{B_d}^2 B_{B_d} \tau_B m_B M_W^2 \eta_t S(x_t) A^2 \lambda^6 [(1 - \rho)^2 + \eta^2], \end{aligned}$$

where $x_t = (m_t/M_W)^2$, $S(x_t)$ is calculable from the loop integrals

$$S(x) = \frac{x}{4(1-x)^2} (4 - 11x + x^2) - \frac{3x^3}{2(1-x)^3} \ln x,$$

$\eta_t \approx 0.85$ is a calculable QCD correction to the four quark operator, and most of the rest is either known or measurable. Thus, a measurement of x_d is almost a measurement of $|V_{td}|$; unfortunately, the two parameters f_{B_d} and B_{B_d} are not known at all. A few years ago, ranges for $f_{B_d}^2 B_{B_d}$ of $(150 \pm 50 \text{ MeV})^2$ were popular [7], while lately heavier reliance on lattice QCD suggests ranges more like $(200 \pm 30 \text{ MeV})^2$.

The above expression for x_d can be written

$$(1 - \rho)^2 + \eta^2 = R^2,$$

forming a circle in the (ρ, η) plane centred at $(1, 0)$ with radius squared

$$R^2 = \frac{6\pi^2 x_d}{G_F^2 f_{B_d}^2 B_{B_d} \tau_B m_B M_W^2 \eta_t S(x_t) A^2 \lambda^6} = (0.0876 \text{ GeV}^2 \text{ psec}) \frac{x_d}{f_{B_d}^2 B_{B_d} A^2 \tau_B S(x_t)}$$

where I have substituted the book values [6] for the relatively well known quantities.

The primary theoretical uncertainty in $f_{B_d}^2 B_{B_d}$ is difficult to reduce.

Another constraint comes from the neutral kaon system. While $K^0 - \bar{K}^0$ mixing is dominated by the CP conserving u and c quark contributions, internal t loops appear as a small correction causing the “indirect” CP violation observed in 1964.

The familiar ϵ parameter is almost calculable [7]:

$$\begin{aligned} \epsilon &= \frac{G_F^2 f_K^2 m_K M_W^2 B_K}{6\pi^2 \sqrt{2} \Delta m_K} \text{Im}[V_{ts}^* V_{td}] \\ &\quad (Re[V_{cs}^* V_{cd}] (\eta_3 S(x_c, x_t) - \eta_1 S(x_c)) + Re[V_{ts}^* V_{td}] \eta_2 S(x_t)) \\ &\simeq \frac{G_F^2 f_K^2 m_K M_W^2 B_K}{6\pi^2 \sqrt{2} \Delta m_K} A^2 \lambda^{10} \eta \\ &\quad \left(\frac{1}{\lambda^4} (\eta_3 S(x_c, x_t) - \eta_1 S(x_c)) + \eta_2 (1 - \rho) A^2 S(x_t) \right), \end{aligned}$$

where $\eta_1 \approx 0.7$, $\eta_2 \approx 0.6$, and $\eta_3 \approx 0.3$ are calculable QCD corrections [7], and

$$S(x_c, x_t) = x_c \left(\ln \frac{x_t}{x_c} - \frac{3x_t}{4(1-x_t)} \left(1 + \frac{x_t}{1-x_t} \ln x_t \right) \right).$$

Plugging in the well known parameters, the remaining equation

$$\eta \left(0.6(1 - \rho)A^2 S(x_t) + 427(0.3S(x_c, x_t) - 0.7S(x_c)) \right) A^2 B_K = 0.220$$

is a rather ugly looking hyperbola in the (ρ, η) plane. Similar to the $f_{B_d}^2 B_{B_d}$ factor in B^0 mixing, the factor B_K is difficult to calculate, and has drifted somewhat from 0.9 ± 0.6 a few years ago [7] to 0.7 ± 0.2 in recent theoretical analyses [8].

The final currently interesting constraint on (ρ, η) has been mentioned in passing several times already: measurement of the lepton energy spectrum in B decays above the $b \rightarrow cl\nu$ threshold is interpreted as $b \rightarrow ul\nu$ and thus measures V_{ub} . A combined analysis of the CLEO and ARGUS measurements gives [6] $|V_{ub}/V_{cb}| = 0.08 \pm 0.02$. This is readily written:

$$\rho^2 + \eta^2 = (0.36 \pm 0.09)^2$$

where a significant portion of the error is theoretical. This constraint gives a circle in the (ρ, η) plane centred at $(0, 0)$ with radius 0.36 ± 0.09 .

I hesitate to go beyond the above (ρ, η) constraint formulae since my understanding of the errors on $f_{B_d}^2 B_{B_d}$ and B_K is not impressive; however, it is difficult to get any feeling for what they represent without a graphical representation. I will use the following values for the various parameters:

| | | | |
|---------------------|---|--------------------------------|---------------------|
| m_t | = | 176 ± 13 GeV | (CDF preprint), |
| m_c | = | 1.5 ± 0.2 GeV | (Reference [7]), |
| A | = | 0.83 ± 0.07 | (Patterson in [9]), |
| τ_{B^0} | = | 1.5 ± 0.11 psec | (Reference [6]), |
| τ_d | = | 0.71 ± 0.06 | (Reference [6]), |
| B_K | = | 0.7 ± 0.2 | (Reference [8]), |
| $f_{B_d}^2 B_{B_d}$ | = | $(0.200 \pm 0.030)^2$ GeV 2 | (Reference [8]). |

Note that these last two are “ball-park” numbers inferred from various sources used in a recent review article, and may have optimistic errors. The constraints from $B^0 - \bar{B}^0$ mixing, ϵ , and $|V_{ub}/V_{cb}|$ are plotted in Figure 1.1. The central values from the above parameters are solid lines, and the $\pm 1\sigma$ bounds are dashed (variation is done by inspection of the constraint equations – the dashed lines have each parameter varied by either $+1\sigma$ or -1σ). From this figure, it is apparent that only weak constraints are made. If the errors were increased to $\pm 2\sigma$, the only real surviving constraint is the annular region from $|V_{ub}/V_{cb}|$, together with the requirement from ϵ that $\eta > 0$.

The remaining theoretical uncertainties are unlikely to be significantly reduced. Further progress requires measurements of processes that have large internal $t - d$ contributions, and are theoretically clean. The future of particle physics will have several such experiments; most notably the new B factories at SLAC and KEK will severely constrain the entire CKM matrix. The present has only one good candidate:

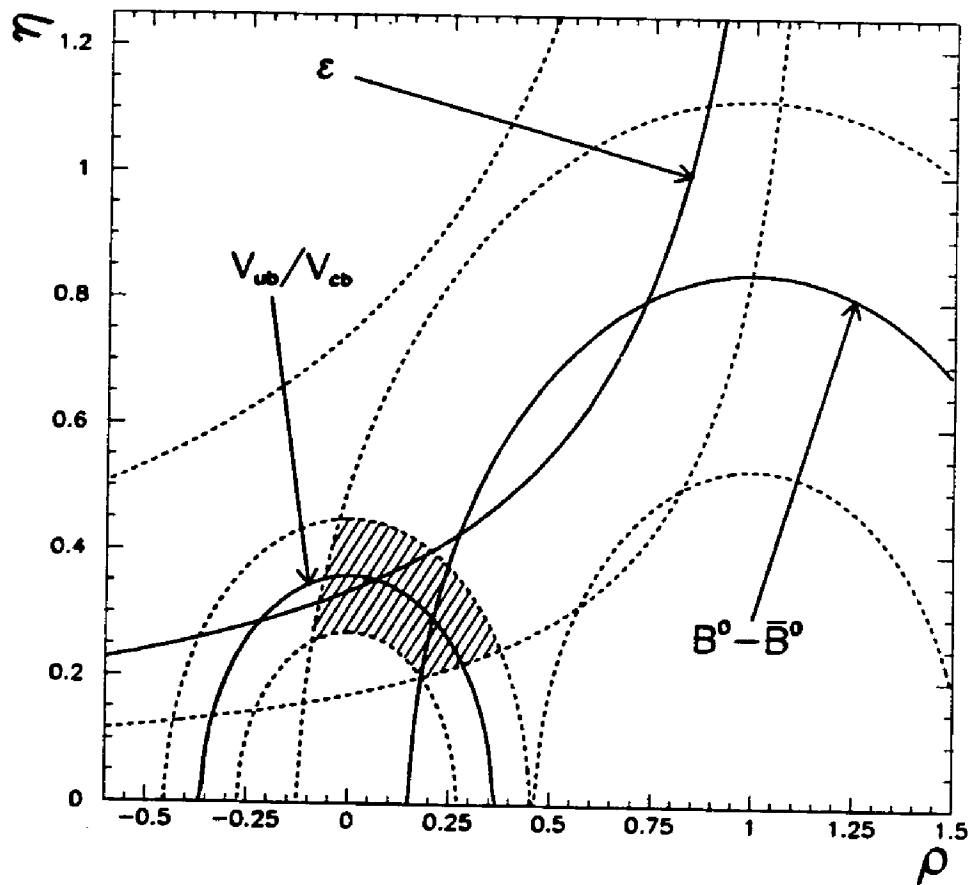
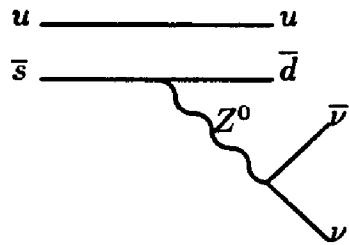


Figure 1.1: Constraints from $B^0 - \bar{B}^0$ mixing, ϵ , and $|V_{ub}/V_{cb}|$ in the (ρ, η) plane. Central values of the various parameters (see text) result in the solid lines, with the $\pm 1\sigma$ values dashed. The allowed region is shaded.

$K^+ \rightarrow \pi^+ \nu \bar{\nu}$.

1.4 The decay $K^+ \rightarrow \pi^+ \nu \bar{\nu}$

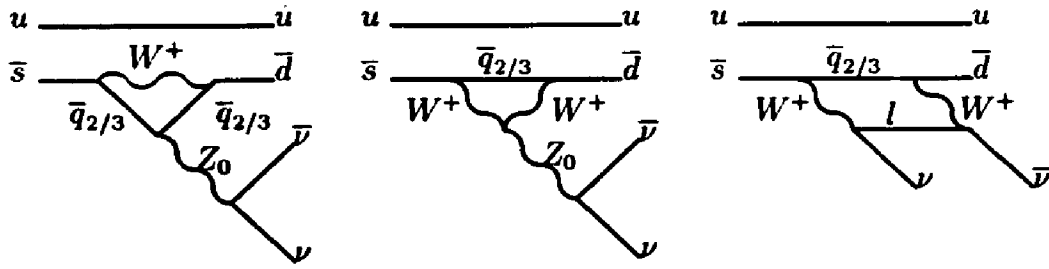
The kaon decay $K^+ \rightarrow \pi^+ \nu \bar{\nu}$ would naively proceed through a first order neutral current from a diagram like



which would be a Flavour Changing Neutral Current (FCNC). Expanding the s and d quarks in the weak basis:

$$J_\mu \propto (V s)^\dagger (V d) = \left(V \begin{pmatrix} 0 \\ 1 \\ 0 \end{pmatrix} \right)^\dagger V \begin{pmatrix} 1 \\ 0 \\ 0 \end{pmatrix} = \begin{pmatrix} V_{us}^* & V_{cs}^* & V_{ts}^* \end{pmatrix} \begin{pmatrix} V_{ud} \\ V_{cd} \\ V_{td} \end{pmatrix} = 0$$

by unitarity. This is just a more explicit form of the neutral current expansion above: unitarity of V_{CKM} forbids first order FCNC's in the Standard Model. At second order, $K^+ \rightarrow \pi^+ \nu \bar{\nu}$ is allowed via two "penguin" and one box diagram



where the u quark is a “spectator.” Again, each of three diagrams occurs for each $q_{2/3} = u, c$ or t . If the u, c and t masses were the same, then the amplitude of each diagram summed over u, c and t would again go as $(Vs)^\dagger (Vd)$, and vanish. In fact, were it not for the different quark masses FCNC’s would be forbidden to *all* orders in the Standard Model. There are several theoretical uncertainties in evaluating the $K^+ \rightarrow \pi^+ \nu\bar{\nu}$ diagrams above. A major one would be uncertainties in the initial and final state hadron wave-functions, but these are removed by normalizing to the observed isospin rotated $K^+ \rightarrow \pi^0 e^+ \nu_e$ mode. The t quark part of $K^+ \rightarrow \pi^+ \nu\bar{\nu}$ is readily calculable [4, 14, 13] and the top quark contribution to the $K^+ \rightarrow \pi^+ \nu\bar{\nu}$ branching ratio for three ν generations is

$$\begin{aligned}\frac{B(K^+ \rightarrow \pi^+ \nu\bar{\nu})}{B(K^+ \rightarrow \pi^0 e^+ \nu_e)} &= \frac{3}{2} \left(\frac{\alpha}{\pi \sin^2 \theta_W} \right)^2 \frac{|V_{ts}^* V_{td}|^2}{|V_{us}|^2} [X(x_t)]^2 \\ &= \frac{3}{2} \left(\frac{\alpha}{\pi \sin^2 \theta_W} \right)^2 A^4 \lambda^8 [(1 - \rho)^2 + \eta^2] [X(x_t)]^2\end{aligned}$$

where A, λ, η and ρ are the Wolfenstein V_{CKM} parameters, and

$$X(x_t) = \frac{x_t}{8} \left(\frac{x_t + 2}{x_t - 1} + \frac{3x_t - 6}{(x_t - 1)^2} \ln x_t \right) \simeq 0.65 x_t^{0.59}$$

with $x_t = m_t^2/m_W^2$. The charm quark contribution is not so readily calculable; however, recent Next-to-Leading-Log QCD calculations [11] have reduced its contribution to the overall $K^+ \rightarrow \pi^+ \nu \bar{\nu}$ branching ratio uncertainty from $\sim 30\%$ to $\sim 7\%$. Inserting $\lambda = 0.22$, $\alpha = 1/128$, $\sin^2 \theta_W = 0.23$, $B(K^+ \rightarrow \pi^0 e^+ \nu_e) = 0.0482$ [6], $X(x_t) \simeq 0.65x_t^{0.59}$ [12], and including the charm contribution yields

$$B(K^+ \rightarrow \pi^+ \nu \bar{\nu}) \simeq 1.97 \times 10^{-11} A^4 x_t^{1.18} [(\rho_0 - \rho)^2 + \eta^2].$$

The parameter ρ_0 contains the c quark contribution,

$$\rho_0 = 1 + \frac{P_0^l}{A^2 X(x_t)}$$

and is technically lepton dependent through the parameter P_0^l . Typically, $\rho_0 \sim 1.2 - 1.6$ (see [11, 12] for the details). Including all uncertainties, $B(K^+ \rightarrow \pi^+ \nu \bar{\nu})$ is certainly in the range $(0.2 - 5) \times 10^{-10}$ and most-likely within $(0.3 - 3) \times 10^{-10}$. Aside from the t quark mass, the major uncertainties are simply the V_{CKM} parameters A , ρ and η .⁶

Referring to the above expression for $B(K^+ \rightarrow \pi^+ \nu \bar{\nu})$ in terms of the V_{CKM} elements a measurement of $K^+ \rightarrow \pi^+ \nu \bar{\nu}$ can be interpreted as a measurement of $|V_{td}|$, which will have errors due to $|V_{ts}|$, m_t , and the measurement error on $B(K^+ \rightarrow \pi^+ \nu \bar{\nu})$ itself (the intrinsic theoretical uncertainties in the charm sector contribute $\Delta V_{td}/V_{td} \sim$

⁶A relatively recent theoretical analysis confines $B(K^+ \rightarrow \pi^+ \nu \bar{\nu})$ to $(0.7 - 1.5) \times 10^{-10}$ [8]. Such a restrictive range requires a relatively high value for, and extremely optimistic errors on, the factor $f_{B_d}^2 B_{B_d}$ which is used above to infer $\rho - \eta$ constraints from $B^0 - \bar{B}^0$ mixing. This high value is motivated by recent lattice QCD calculations, and I take them with a grain of salt.

5% [8]). Examination of that equation quickly shows the relative contributions of the different errors. $|V_{ts}|$ is constrained by unitarity to be nearly equal to $|V_{cb}|$, which is measured to about 10% (primarily theoretical error) in B meson decays; the contribution is then $\Delta V_{td}/V_{td} \sim \Delta V_{ts}/V_{ts} \sim \Delta V_{cb}/V_{cb} \sim 15\%$. Assuming the CDF collaboration has seen the top quark, their mass measurement of 176 ± 13 GeV/c² [6] would contribute $\Delta V_{td}/V_{td} \sim 1.2(\Delta m_t/m_t) \sim 12\%$. The error due to $B(K^+ \rightarrow \pi^+ \nu \bar{\nu})$ will be $\Delta V_{td}/V_{td} \sim 1/2(\Delta B/B)$, so to be competitive with the other errors a 20% measurement of $B(K^+ \rightarrow \pi^+ \nu \bar{\nu})$ needs to be made. As the other uncertainties are reduced, clearly a better measurement of $B(K^+ \rightarrow \pi^+ \nu \bar{\nu})$ will be desirable.

Alternatively, $K^+ \rightarrow \pi^+ \nu \bar{\nu}$ can be fit nicely into the geometrical picture in the (ρ, η) plane mentioned before. The above formulae can be written

$$(\rho_0 - \rho)^2 + \eta^2 = \frac{B(K^+ \rightarrow \pi^+ \nu \bar{\nu})}{1.97 \times 10^{-11} A^4 x_t^{1.18}},$$

a circle centred at $(\rho_0, 0)$. The primary remaining intrinsic theoretical uncertainty is left in ρ_0 , but is very small compared to the uncertainties in either B_K or $f_{B_d}^2 B_{B_d}$. This $K^+ \rightarrow \pi^+ \nu \bar{\nu}$ constraint is added to the (ρ, η) plane in Figure 1.3, assuming a perfect measurement of $B(K^+ \rightarrow \pi^+ \nu \bar{\nu}) = 1 \times 10^{-10}$ and using the other parameter ranges as before. A significant part of the apparent $K^+ \rightarrow \pi^+ \nu \bar{\nu}$ uncertainty in the (ρ, η) plane is really due to the residual uncertainty in A (or $V_{ts} \sim V_{cb}$) raised to the fourth power. In fact, $K^+ \rightarrow \pi^+ \nu \bar{\nu}$ is really an extremely clean way of measuring the product $V_{ts}^* V_{td}$, not quite V_{td} itself.

1.5 Unless There's Something Else Out There

The above discussion assumed the Standard Model with three generations of elementary particles throughout. If this is not true, then all bets are off.

The first natural extension to known physics would be the existence of more than three families. All we know about any additional families is that their neutrinos must have $m_\nu > m_Z/2$, charged leptons $m_l > 44 \text{ GeV}/c^2$, and quarks $m_{q_{1/3}} > 85 \text{ GeV}/c^2$. The quark mixing matrix becomes rather uncertain, with 90% confidence levels on the magnitudes of its components (now assuming only unitarity) [6]

$$\left(\begin{array}{cccc} (0.9728, 0.9757) & (0.218, 0.224) & (0.002, 0.005) & \dots \\ (0.180, 0.228) & (0.800, 0.975) & (0.032, 0.048) & \dots \\ (0, 0.13) & (0, 0.056) & (0, 0.9995) & \dots \\ \vdots & \vdots & \vdots & \vdots \\ \vdots & \vdots & \vdots & \vdots \end{array} \right).$$

In addition to losing all constraints on V_{td} and V_{ts} , there will be additional diagrams due to the new $q_{2/3}$ quarks interfering with the u , c and t diagrams with unknown phases. The existence of additional generations could make $B(K^+ \rightarrow \pi^+ \nu \bar{\nu})$ larger, or smaller, or leave it unchanged.

Various extensions to the Standard Model include new particles that could show up as $K^+ \rightarrow \pi^+ X^0$ or $K^+ \rightarrow \pi^+ X^0 X^0$ (if they are light), as well as contributing

internally to loops in additional $K^+ \rightarrow \pi^+ \nu \bar{\nu}$ diagrams. Possible X^0 's are axions, familons, majorons and hyperphotons (see Ref [5] and the references within for an extensive discussion of $K^+ \rightarrow \pi^+ \nu \bar{\nu}$ beyond the Standard Model). Assuming the X^0 does not interact in the detector and it is massless, $K^+ \rightarrow \pi^+ X^0$ would show up as a mono-energetic peak in the π^+ spectrum at the end-point of the $K^+ \rightarrow \pi^+ \nu \bar{\nu}$ spectrum, $K^+ \rightarrow \pi^+ X^0 X^0$ as an enhancement to the apparent $K^+ \rightarrow \pi^+ \nu \bar{\nu}$ branching ratio (possibly with a different π^+ momentum spectrum altogether depending on its coupling), while additional $K^+ \rightarrow \pi^+ \nu \bar{\nu}$ diagrams would interfere with the known ones much like additional quark families. Except for the direct $K^+ \rightarrow \pi^+ X^0$ search, our philosophy will be to assume the Standard Model is correct, measure the CKM parameters, and see if a consistent picture is formed.

It is rather unlikely that the *actual* CKM matrix, defined as the transformation between mass and electroweak eigenstates, is not unitary; as mentioned above, this is built into the very basic nature of the renormalizable local gauge theories that are believed to describe all interactions. What we really do, then, is to measure its *apparent* parameters to the highest possible precision in different processes. If new physics from a higher energy scale contributes to these processes in different ways, V_{CKM} will appear non-unitary; this is an important part of the program of the near future of particle physics. The errors on the current measurements of the CKM parameters are largely theoretical (due to hadronic uncertainties in extracting the

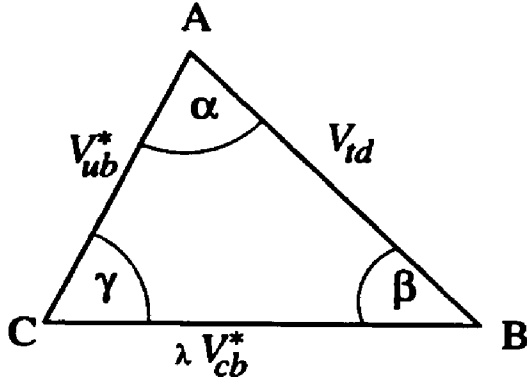


Figure 1.2: The prototype unitarity triangle. $K^+ \rightarrow \pi^+ \nu \bar{\nu}$ and tree-level B decays measure the length of its sides, while CP violation in the B system will measure the angles α , β , and γ .

electroweak physics from strongly interacting particles) and will likely not be reduced without measurements of new, cleaner, processes like $K^+ \rightarrow \pi^+ \nu \bar{\nu}$.

It is worth mentioning how $K^+ \rightarrow \pi^+ \nu \bar{\nu}$ will fit in with results from the new B -factories. Consider unitarity applied to the first and third columns of V_{CKM} :

$$V_{ud} V_{ub}^* + V_{cd} V_{cb}^* + V_{td} V_{tb}^* = 0.$$

Now set $V_{ud} \simeq V_{tb} \simeq 1$ and $V_{cd} \simeq -\lambda$:

$$V_{ub}^* + V_{td} = \lambda V_{cb}^*.$$

This is usually represented as the familiar “unitarity triangle” of Figure 1.2. It is better related to the previous discussion by also setting $V_{cb} \simeq \lambda^2 A$, $V_{ub} \simeq \lambda^3 A(\rho - i\eta)$ and $V_{td} \simeq \lambda^3 A(1 - \rho - i\eta)$ and rescaling the triangle sides. It can then be put directly in the (ρ, η) as in Figure 1.3.

The emphasis at the B -factories will be to use CP violation in B decays to measure

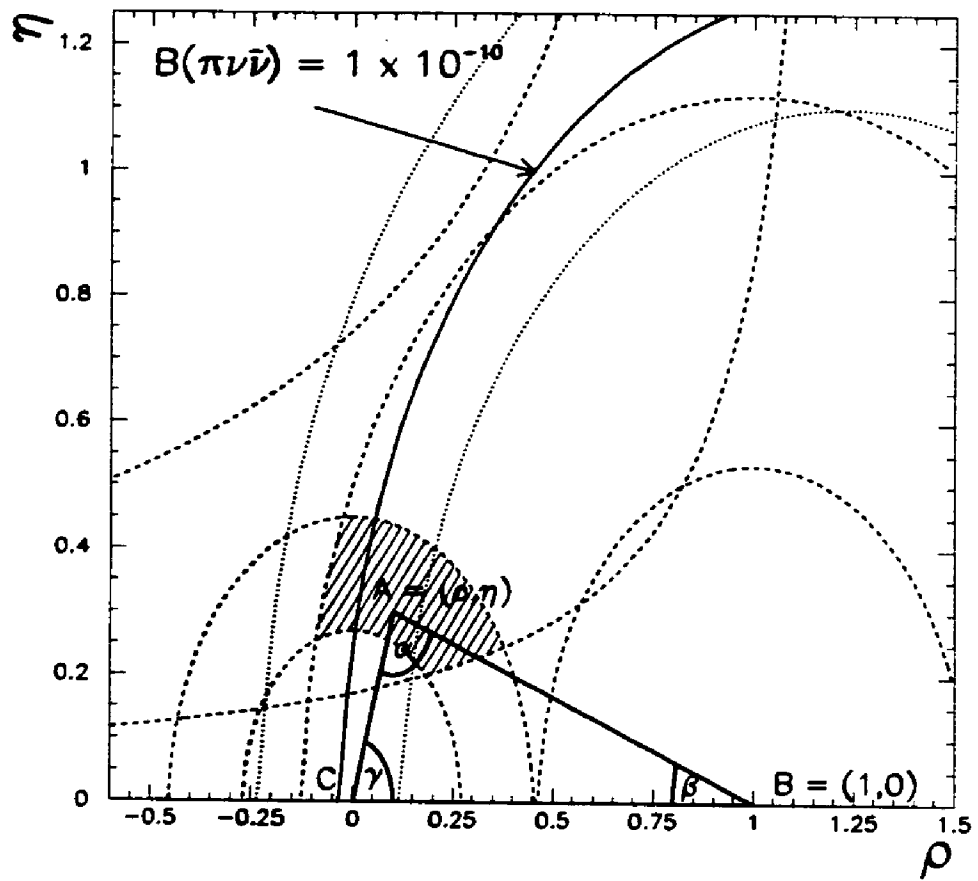


Figure 1.3: A hypothetical perfect $K^+ \rightarrow \pi^+ \nu \bar{\nu}$ measurement of $B = 1 \times 10^{-10}$ superimposed onto the (ρ, η) plane constraints, along with the unitarity triangle. The solid line is the $K^+ \rightarrow \pi^+ \nu \bar{\nu}$ allowed curve for the central parameter values, and the dotted lines are the $\pm 1\sigma$ bounds.

the angles inside this triangle. Consider, for example, the decay $B_d^0 \rightarrow \pi^+ \pi^-$ by first defining the time dependent partial widths:

$$\Gamma(t) = \Gamma(t; B_d^0 \rightarrow \pi^+ \pi^-)$$

$$\bar{\Gamma}(t) = \Gamma(t; \bar{B}_d^0 \rightarrow \pi^+ \pi^-),$$

and then form the CP-violating asymmetry

$$A(t) = \frac{\Gamma(t) - \bar{\Gamma}(t)}{\Gamma(t) + \bar{\Gamma}(t)}.$$

It is straightforward to show that

$$\begin{aligned} A(t) &= \sin(\Delta m_B t) \sin(2 \arg(V_{ud} V_{ub}^* V_{tb} V_{td}^*)) \\ &\simeq \sin(\Delta m_B t) \sin(2 \arg(V_{ub}^* V_{td}^*)) \\ &= \sin(\Delta m_B t) \sin(2\alpha) \end{aligned}$$

where α is the angle from the unitarity triangle in Figures 1.2 and 1.3. The new B factories will run on the $\Upsilon(4S)$ resonance as CESR does now. Unlike CESR, they can measure t by measuring the distance the B^0 travels, since the new asymmetric machines will produce the $\Upsilon(4S)$ in flight.

In addition to α , the new facilities will measure β (with $B_d^0 \rightarrow \psi K_S$) and with luck γ (eg. $B^\pm \rightarrow D K^\pm, D \rightarrow K^+ K^-$) and hopefully some other unitarity angles as well. These angles can all be affected by physics beyond the Standard Model. $K^+ \rightarrow \pi^+ \nu \bar{\nu}$, along with tree-level B semileptonic decays, measures lengths of the triangle sides.

In contrast to $K^+ \rightarrow \pi^+ \nu\bar{\nu}$, these tree level process are relatively insensitive to new physics [10], so any contributions to $K^+ \rightarrow \pi^+ \nu\bar{\nu}$ will hopefully keep the triangle from closing and signal the presence of new physics.

1.6 Current Experimental Status

Searching for $K^+ \rightarrow \pi^+ \nu\bar{\nu}$ has a long history. Its absence was one of the definitive tests of the non-existence of Flavour Changing Neutral Currents, and $K^+ \rightarrow \pi^+ X^0$ was one of the principal search modes for the axion. With our 1989 data set, Experiment 787 at Brookhaven National Lab established 90% upper confidence limits based upon no observed events:

$$B(K^+ \rightarrow \pi^+ \nu\bar{\nu}) \leq 7.5 \times 10^{-9}$$

$$B(K^+ \rightarrow \pi^+ X^0) \leq 1.7 \times 10^{-9}$$

For $K^+ \rightarrow \pi^+ \nu\bar{\nu}$, the corresponding single event sensitivity of 3×10^{-9} is from $10 - 100 \times$ the expected Standard Model branching ratio. Our desired 30% measurement of $B(K^+ \rightarrow \pi^+ \nu\bar{\nu})$ will require about 10 events, so we must increase our sensitivity by a factor of around 100 – 1000, depending on the value of the actual

branching ratio. Our 89-91 data set has been the subject of a complete analysis, leading to the preliminary result $B(K^+ \rightarrow \pi^+ \nu\bar{\nu}) \leq 3.7 \times 10^{-9}$ (90% CL). In addition to the desire within the collaboration to have an independent analysis, a number of improvements to our basic detector calibration methods and analysis software indicate that significant improvements in our sensitivity with reduced levels of background should be possible. This thesis is an effort to extract the highest possible sensitivity from the combined E787 89-91 data set.

Chapter 2

The E787 Experiment

The E787 detector has been extensively described elsewhere, including a review article [19], two previous Princeton theses [20, 21], and a University of Victoria thesis [22]. Accordingly, this chapter will only briefly outline the experiment, providing enough essential details of each detector element to understand this analysis.

2.1 Overview

The experimental signature for $K^+ \rightarrow \pi^+ \nu\bar{\nu}$ or $K^+ \rightarrow \pi^+ X^0$ seems straightforward: no other K^+ decay produces only a single π^+ and no other observable products. There are, however, several K^+ decay modes to a single charged particle, including the two principal modes $K^+ \rightarrow \mu^+ \nu_\mu$ and $K^+ \rightarrow \pi^+ \pi^0$. Table 2.1 lists the known modes having a π^+ or μ^+ in the final state with their maximum charged particle momentum, along with $K^+ \rightarrow \pi^+ \nu\bar{\nu}$ and the hypothetical $K^+ \rightarrow \pi^+ X^0$ (massless X^0).

| K^+ Decay Mode | Branching Fraction | End Point (MeV/c) |
|------------------------|-----------------------------|-------------------|
| $\mu^+ \nu_\mu$ | 0.635 | 236 |
| $\pi^+ \pi^0$ | 0.212 | 205 |
| $\pi^+ \pi^+ \pi^-$ | 0.056 | 125 |
| $\pi^0 \mu^+ \nu_\mu$ | 0.032 | 215 |
| $\pi^+ \pi^0 \pi^0$ | 0.017 | 133 |
| $\mu^+ \nu_\mu \gamma$ | 5.5×10^{-3} | 236 |
| $\pi^+ \nu \bar{\nu}$ | $(0.3 - 3) \times 10^{-10}$ | 227 |
| $\pi^+ X^0$ | - | 227 |

Table 2.1: Decay mode branching ratios and end points for K^+ decays with a final state μ^+ or π^+ , along with the rare decay modes of interest.

The kinematic spectra of the important modes are shown in Figure 2.1; the details of this spectrum are worth noting since they will drive the entire experiment. $K^+ \rightarrow \mu^+ \nu_\mu$, with a branching ratio of 64%, has a monochromatic μ^+ peak at 236 MeV/c. $K^+ \rightarrow \pi^+ \pi^0$, with a branching ratio of 21%, has a mono-chromatic π^+ peak at 205 MeV/c. To aid in background suppression, our search will take place away from these two modes. Two regions are of potential interest: above and below the $K^+ \rightarrow \pi^+ \pi^0$ peak. The region below the peak is rather difficult; principally, nuclear interactions of the π^+ with any material in an experiment can down-shift it to lower momentum, and this background is difficult to overcome [23]. The region above the $K^+ \rightarrow \pi^+ \pi^0$ peak and below the $K^+ \rightarrow \mu^+ \nu_\mu$ peak has been the traditional searching ground for $K^+ \rightarrow \pi^+ \nu \bar{\nu}$, and E787 is designed to look at this kinematic region.

We're looking for a one in 10 billion process hiding between two peaks of order

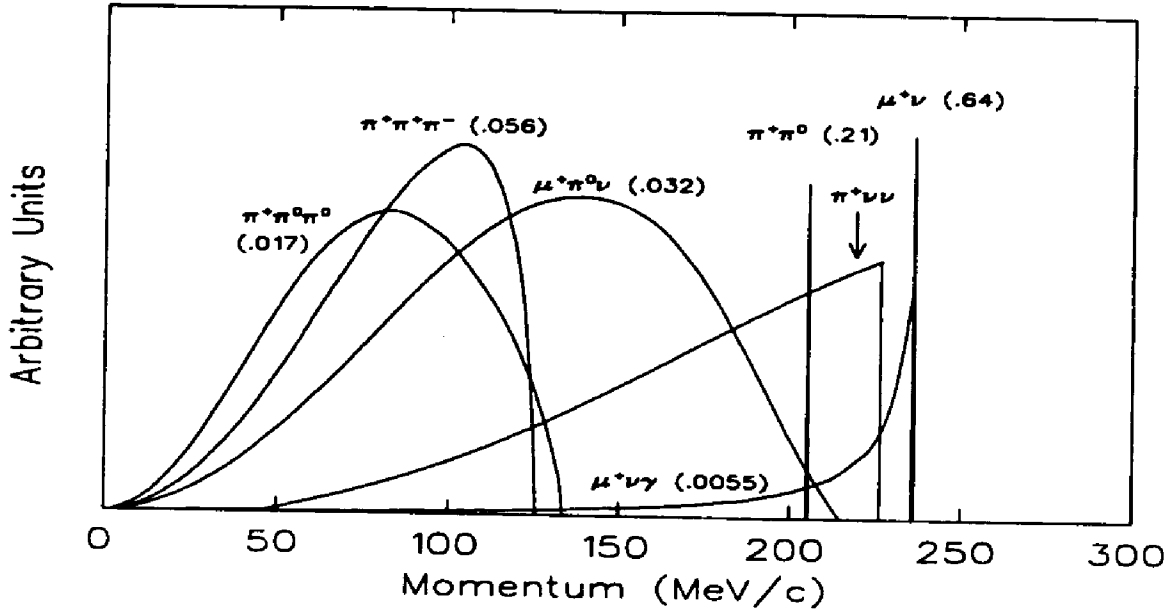


Figure 2.1: Common K^+ Decay mode spectra, along with $K^+ \rightarrow \pi^+\nu\bar{\nu}$.

unity, so clearly a great deal of background rejection is needed. The basic design of any experiment to measure $K^+ \rightarrow \pi^+\nu\bar{\nu}$ must include:

- Good K^+ identification.
- High charged track finding efficiency and kinematic resolution in the K^+ rest frame, requiring a single pion track with momentum between the $K^+ \rightarrow \pi^+\pi^0$ and $K^+ \rightarrow \mu^+\nu_\mu$ peaks.
- Particle identification capable of rejecting the μ^+ 's from the $K^+ \rightarrow \mu^+\nu_\mu$, $K^+ \rightarrow \mu^+\nu_\mu\gamma$, and $K^+ \rightarrow \pi^0\mu^+\nu_\mu$ decays.
- Sufficient hermeticity of photon detection to veto photons from $K^+ \rightarrow \pi^+\pi^0$ ($\pi^0 \rightarrow \gamma\gamma$), $K^+ \rightarrow \pi^0\mu^+\nu_\mu$, and $K^+ \rightarrow \mu^+\nu_\mu\gamma$ decays.

Since the expected branching ratio is very small, a large number of K^+ decays must be observed. With 100% efficiency, around 10^{11} kaon decays would be needed to measure a Standard Model branching ratio; in practice, we are going to need more like $10^{13\text{--}14}$ K^+ decays. Also, the above requirements will ultimately demand a sophisticated experiment with a significant amount of information per event (“event size”). This leads to the somewhat more mundane requirements:

- High rate capability, so the measurement can be made in a finite amount of time.
- Fast trigger capable of enormous online rejection of the dominant backgrounds with high efficiency, along with a sophisticated acquisition system for handling large amounts of data.

The redundant kinematics and triggering requirements drove the first major design decision of E787. In order to achieve enough background rejection, good kinematic resolution with negligible tails is needed in the K^+ rest frame. The solution adopted was to make the kaon frame the lab frame (i.e. stop the K^+). A traditional “in-flight” experiment would measure only particle momentum in the kaon rest frame. Working with a stopped kaon makes range, energy and momentum all useful. Using range in addition to momentum has an added advantage: since muons are more penetrating than pions, the effective separation between the $K^+ \rightarrow \pi^+\pi^0$ and $K^+ \rightarrow \mu^+\nu_\mu$ peaks is increased. In the online trigger, the first-order range measurement uses the fact

that all kaons stop in nearly the same location, and uses fast logic which simply determines the detector element in which the π^+ stopped. This decision can be made in only a few 10's of nsec.

Working with a stopped K^+ is not a panacea and many problems are introduced into the experiment. Since we must necessarily start with a K^+ beam, to get a stopped kaon we must first slow it down. This requires passing the kaon through material, which causes losses from nuclear interactions. This material also provides scattering centres for beam pions, which can potentially chase the kaon into the detector and scatter into our fiducial volume faking a $K^+ \rightarrow \pi^+$ decay. The kaon decay products are at relatively low energy and are quite susceptible to interactions (multiple scattering of π^+ or μ^+ , nuclear interactions of π^+ , and even photo-nuclear interactions of μ^+) adding tails to our kinematic measurements. The photons from the π^0 decay in $K^+ \rightarrow \pi^+\pi^0$ have similarly low energies (as low as 20 MeV), and can be lost entirely in any detector dead material. These considerations lead to a set of revised detector constraints, which are the foundation of E787:

- Low energy, pure, K^+ beam which can be stopped with a minimum of material.
- Good beam kaon identification, and very good beam pion detection.
- Active, highly segmented K^+ stopping target for clean K^+ and π^+ tracking, and good timing insuring the K^+ really came to a complete stop.

- Absolute minimum of detector dead material.
- Redundant measurements of the π^+ momentum.
- Hermetic photon detection for π^0 rejection.
- Redundant μ^+ veto system.

A 3-D perspective view of the E787 detector is shown in Figure 2.2 along with a detailed side-view in Figure 2.3. The detector elements are detailed below. For this description and the following analysis, the z axis is defined such that the K^+ beam travels from $-z$ to $+z$, the $+y$ axis is vertically up, and the x axis is defined to form a right-handed coordinate system with y and z . θ is then the normal polar angle, and ϕ is the azimuthal angle from the x axis in the xy plane.

2.2 The K^+ Beam Instrumentation.

24 GeV protons from the Brookhaven National Laboratory Alternating Gradient Synchrotron (BNL AGS) bombarded our primary production target producing kaons, pions, and many shorter-lived particles. The kaons were transported down the LEST I beam line, which had a single stage electrostatic separator to purify the kaon beam; when it reached the spectrometer, the beam $K : \pi$ ratio was about 1 : 3 with a beam momentum of about 800 MeV/c. This momentum provides a compromise among kaon production cross-section, losses during transport, and stopping the kaons, resulting

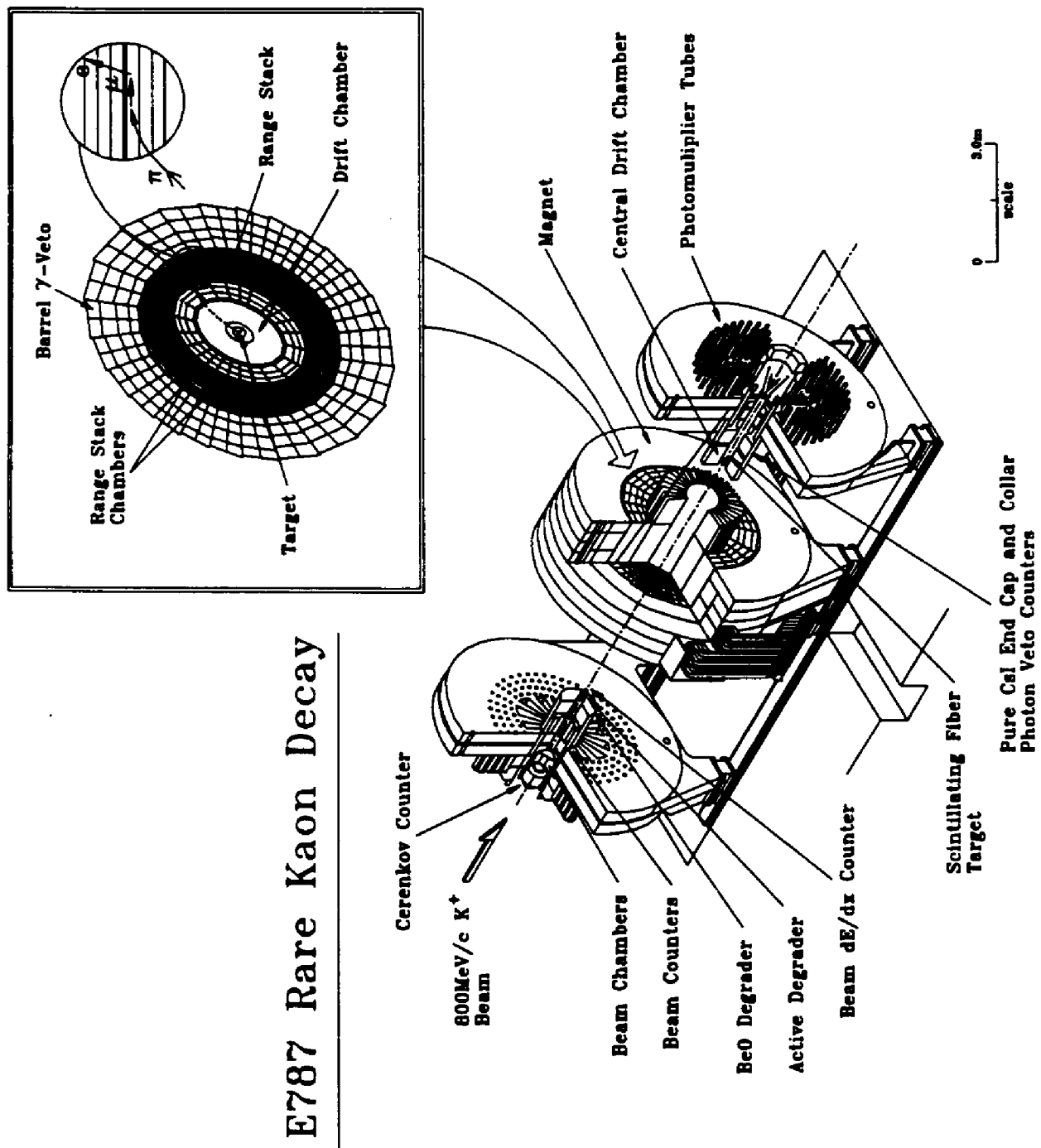


Figure 2.2: 3-D Perspective view of the E787 detector.

2.2. The K^+ Beam Instrumentation.

34

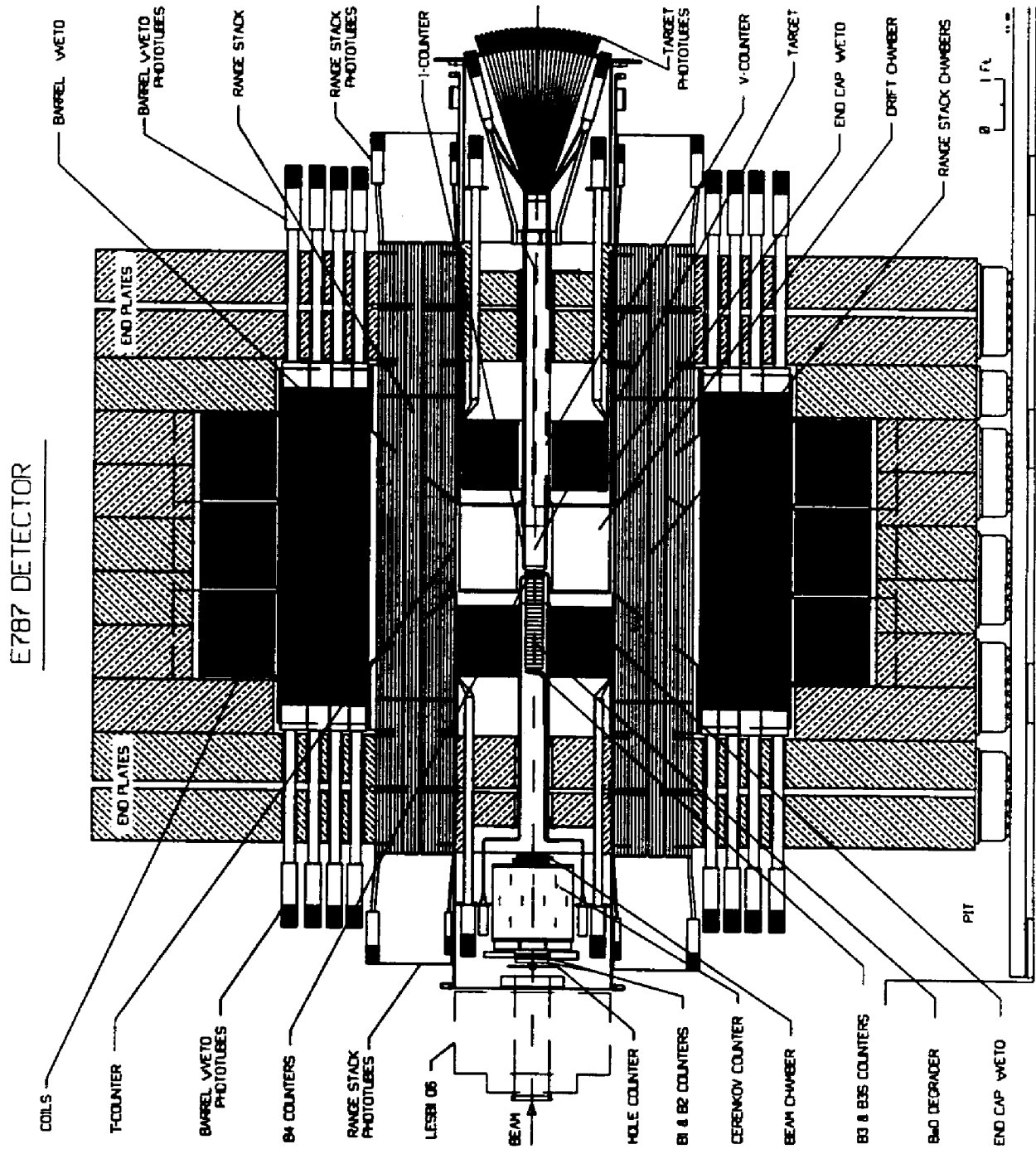


Figure 2.3: Side view of the E787 detector.

in a maximum number of stopped kaons in the detector per AGS proton. The first detector element is the Čerenkov Counter, which gives a positive K^+ tag used both in the trigger and offline analysis (\check{C}_K). The counter also gives a separate tag for beam pions (\check{C}_π), which is used in the offline analysis. The primary Čerenkov signal used in this analysis is a time-to-digital converter (TDC), which reports both the time that the counter fired (TDC pulse leading edge) and amount of time we were dead to secondary (or even tertiary) beam particles (TDC pulse width).

Immediately downstream of the Čerenkov is a 3-plane beam wire chamber (BWPC). This chamber is used to insure that one and only one beam K^+ enters the detector, and no extra beam K^+ or π^+ is present at the apparent kaon decay time. Principally, it is used to reject pions missed by \check{C}_π .

After the BWPC, the beam passes through a BeO degrader, which slows down kaons (and any pions) so they can stop in the target. The degrader also absorbs the residual protons in the beam.

A Pb-Glass Čerenkov counter was added to the degrader for the 1991 run. While it was intended primarily as a γ -catcher for $K^+ \rightarrow \pi^+ \nu \bar{\nu}$ search *below* the $K^+ \rightarrow \pi^+ \pi^0$ peak, in this analysis it is principally used for extra beam pion rejection. A somewhat more sophisticated analysis of this counter is used: it is viewed by a number of phototubes, and a combined tube multiplicity and hit time analysis is used.¹

¹This same power is available to the primary \check{C}_K and \check{C}_π Čerenkov, but was not found to be needed.

After the degrader the beam passes through a two-plane hodoscope (the B4 counter), parallel fingers of scintillator read out by phototubes. In 1989 and 1990, separate TDC channels on each finger are used to look for a second beam particle by searching for extra clusters in the counter. In 1991, transient digitizers (TD's) on the separate fingers were used for this second particle cluster search. The TD's sample the phototube pulse heights every 2 nsec, permitting good timing measurements and a complete pulse-shape analysis; in particular, the TD's are very useful for looking for a second pulse just after a primary one. If a beam pion is present but doesn't form a clear second cluster, it may have hit the same fingers as the kaon; a fit of the kaon pulse is performed using the TD data, searching for such a second pulse. Each B4 finger also has an analog-to-digital (ADC) channel, which are used for dE/dX -based particle identification.

In the 1989 and 1990 runs, a single scintillator slab instrumented with a TD was placed just before the stopping-target. This was a simpler arrangement to work with, and was used for the double-pulse fit mentioned for the B4 counter in 1991. It was only the absence of the B4T counter in 91 (removed because it didn't fit after the lead-glass counter was added) that made the hodoscope analysis necessary that year. B4T also had an ADC channel used for dE/dX -based particle identification.

2.3 The K^+ Stopping Target

After the beam instrumentation, the kaons enter, lose energy, and come to a stop in the kaon stopping target (just the target or TG from now on). The target was a bundled set of 379 active scintillating fibres² lying parallel to the z axis. The beam kaons run roughly parallel to the fibres as they stop, usually hitting only a few fibres and depositing several tens of MeV in each. When a kaon decays, the $K^+ \rightarrow \pi^+ \nu \bar{\nu}$ trigger (see below) requires a resulting charged track running roughly perpendicular to the z axis. After emerging from the kaon fibres, this track deposits a few MeV (typically < 5 MeV) in each target fibre it passes through. The target is surrounded with set of six 0.635 cm thick scintillators called the I-counters (IC), forming a hexagonal shell around the target with roughly the same z length as the target. The IC's are used both to confine the kaon to the target and to measure the pion time in the trigger delayed coincidence requirement.³ The readout of the target consists of a TDC channel on each target fibre and IC for timing, and an ADC channel on each fibre and each IC used for the pion total energy measurement and dE/dX for particle identification and vetoing overlapping photons.

²The target actually has many more fibres than this. The true circular fibres are bundled and glued into triangle-shaped clusters, which are assembled into the full target. Each of these clusters is read out with one phototube, with a total of 379 target channels. I will refer to each of these triangular bundles as a “fibre” from now on.

³The term “delayed coincidence” will be used repeatedly. Online, a signal from \tilde{C}_K is *delayed* and then required to be in *coincidence* with a signal from an I-counter. Effectively, this condition vetoes events with the IC hit at the same time as the \tilde{C}_K , which might have come from a kaon decay-in-flight.

2.4 The Drift Chamber

After leaving the target, the π^+ is tracked with a precision “Jet” type drift chamber (DC). The entire experiment is enclosed in a magnet, producing a 10 kGauss uniform field throughout the entire active detector. The chamber is instrumented with one TDC channel per wire to measure ionization electron drift times, which give us the π^+ distance of closest approach to each wire. The π^+ loses very little energy in the drift chamber gas, so its path is nearly circular; by fitting this circle, we measure the pion’s transverse momentum. The chamber has five layers of 6-wire cells, two of which are “stereo” (layers 2 and 4). Including the stereo layers in the fit gives us the complete π^+ momentum vector, along with accurate tracking useful for event reconstruction in the target and range stack subsystems.

2.5 The Range Stack

The π^+ passes from the drift chamber into a stack of 21 radial layers of scintillator, segmented into 24 azimuthal sectors (the RS). To simplify the detector design and reduce the number of channels, the range stack is read out as 15 effective layers. Physical layers 2-5 become layer *A* or just the *A*-counter, layers 6-8 become the *B*-counter, and layers 9-10 become the *C*-counter. The π^+ loses energy and eventually stops in the range stack. The first layer of the range stack (called the trigger-counters

or T-counters) are shorter than the rest (about 50 cm long) and define the solid angle E787 will accept online. Each range stack scintillator has a phototube on each end. The signal from each end is instrumented with an ADC (used for the total energy measurement and dE/dX particle ID) and a TD. While the TD is used to measure time, more importantly it samples each tube pulse-height every 2 nsec giving detailed pulse-shape information. This signal is used to identify the stopping π^+ , the $\pi^+ \rightarrow \mu^+$ decay, and finally the $\mu^+ \rightarrow e^+$ decay for every event. The power of the TD's is displayed in Figure 2.4 (from [18]), showing a complete $\pi^+ \rightarrow \mu^+ \rightarrow e^+$ sequence for a pion stopping in the range stack. Online, $\pi^+ \rightarrow \mu^+$ is tagged with a simple pulse height to area ratio cut. Offline, a complete fit is performed to insure a $\pi^+ \rightarrow \mu^+$ decay occurred. This is our most important $K^+ \rightarrow \mu^+ \nu_\mu$ rejection tool.

Two multi-wire proportional chambers (the RSPC's) are also imbedded in the range stack (just after layers 10 and 14) and are used for the π^+ range measurement. Delay line readout schemes are used to convert the π^+ 's ϕ and z into times, with a compact 4 TDC channels used per chamber.

2.6 The γ -Veto

E787 has two dedicated photon veto systems: the barrel (BV) and the end caps (EC's). Both are alternating layers of lead and scintillator. The two endcaps fit just inside the range stack, one upstream and the other downstream of the drift chamber.

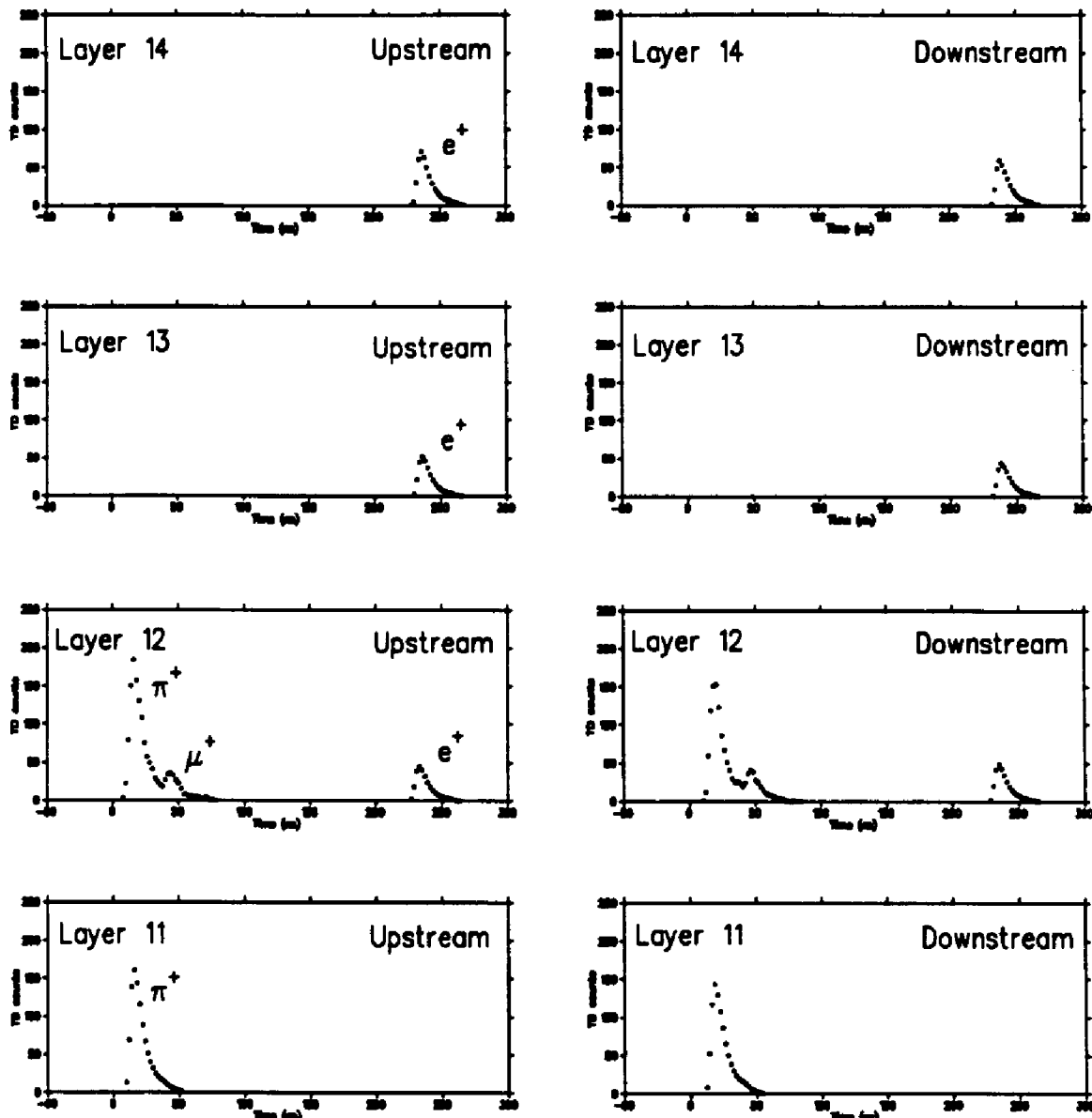


Figure 2.4: Transient digitizer data showing a complete $\pi^+ \rightarrow \mu^+ \rightarrow e^+$ sequence for a pion passing through layer 11 and stopping in layer 12. About 40 nsec later it decayed into a muon which stayed in layer 12. 220 nsec later, the muon decayed into a positron, which penetrates deeper into the range stack.

Each has 24 modules read out by phototubes. The barrel veto surrounds the entire range stack, just inside the magnet coils. At its thinnest, it is about 14 radiation lengths of material. The 48 barrel veto azimuthal scintillator sectors are read out as 4 radial layers, with a phototube viewing each end of each sector/layer. Each barrel veto and endcap tube is read out with one TDC and one ADC channel, and in the offline analysis we search for (and veto on) photons which might have come from a $K^+ \rightarrow \pi^+ \pi^0$. In addition to this dedicated γ -veto, the entire E787 detector is, as much as possible, sensitive to photons with a minimum of “dead material”; in particular, the range stack is about one radiation length of material, so about 1/3 of all photons will convert before the barrel veto. Essentially, we try to veto any event with unaccounted for energy that occurs at the same time as the π^+ .

2.7 The $K^+ \rightarrow \pi^+ \nu \bar{\nu}$ Trigger

By design, many of the signals from the above detector components are also available sufficiently quickly to be used in the online trigger. While it can be regarded more properly as the first stage of the analysis, for continuity it is described here.

2.7.1 Level 0 Trigger

This is the earliest and fastest trigger level, using only the discriminated phototube signals from various detector elements. The trigger front-end electronics calculates

a set of conditions called “trigger bits,” which are available to individual “trigger boards” for making the actual trigger decisions. The $K^+ \rightarrow \pi^+ \nu \bar{\nu}$ level 0 trigger selects a beam K^+ that decays at rest to a charged product that penetrates into the middle of the range stack; it is defined as

$$KT \cdot IC \cdot DC \cdot (T \cdot A) \cdot B_{CT} \cdot \overline{(19_{CT} + 20_{CT} + 21_{CT})} \cdot \overline{(BV + ECM + ECP)}.$$

where

KT : K^+ from beam enters the target ($\dot{C}_K \cdot B4 \cdot E_{TG}$),

IC : Struck I-counter,

DC : Delayed coincidence between IC and \dot{C}_K ,

$T \cdot A$: RS Layers T and A coincidence within one sector,

X_{CT} : RS layer X hit in the $T \cdot A$ or first two clockwise sectors,

BV : BV energy sum > 5 MeV

ECM : Upstream EC energy sum > 10 MeV

ECP : Downstream EC energy sum > 10 MeV

In words, the level 0 trigger first requires a beam kaon pass through the beam instrumentation and enter the target. The kaon must decay into a charged particle that strikes the I-counter more than about 2 nsec after the kaon stopped. The charged track must enter the range stack, but not penetrate into the outer three layers, and there must not be coincident energy in the barrel or endcap photon veto.

2.7.2 Level 1 Refined Range and Hextant Veto

The level 0 trigger range measurement is the simple stopping layer based determination, which does not account for the π^+ range in the target or its “dip angle” ($\cos \theta_z$). At this point, the trigger is dominated by $K^+ \rightarrow \mu^+ \nu_\mu$, which can be removed with a better range measurement. In the level 1 refined range trigger, the level 0 determined stopping layer is digitized into a 4-bit binary number, a selected RSPC end-to-end time based Z measurement is digitized into another 4-bits, and the number of struck target elements is measured by using a 4-bit flash ADC with a discriminator multiplicity sum output. These 12 bits are used to address a memory lookup unit (MLU) as the level 1 refined range pass/fail condition.

Another hole in the level 0 trigger is that about 1/3 of the $K^+ \rightarrow \pi^+ \pi^0$ photons convert in the range stack and don’t penetrate to the photon veto. To partially compensate for this the range stack energy is summed into “hextants” (4 sectors each), which are separately discriminated into 6 hextant-bits. These are used in an MLU to accept only events with either a single or two adjacent hextants hit, rejecting events with an range stack γ cluster well separated from the π^+ track.

2.7.3 Level 1.5 Energy Trigger

After the level 1 trigger, most of the events are still $K^+ \rightarrow \mu^+ \nu_\mu$. Further rejection is achieved using an online measurement of the charged track energy. After imposing a

single $T \cdot A$ requirement, all raw ADC information from the $T \cdot A$ and two immediately clockwise sectors is summed.⁴ The raw target ADC counts from all fibres under 2 MeV are added.⁵ Events are cut if they have total energy above about 130 MeV.

2.7.4 Online TD $\pi^+ \rightarrow \mu^+$ Finder

Still more online muon rejection is achieved by inspecting the TD pulse in the Level 0 determined stopping counter. The offline analysis will become quite involved. Online, we simply calculate the pulse height to pulse area (H/A) ratio, and cut events with either end inconsistent with a $\pi^+ \rightarrow \mu^+$ decay. The $\pi^+ \rightarrow \mu^+$ decay chain adds extra area to the pulse without affecting its height, so most muons show up with an abnormally high H/A and can be cut. The easiest way for a μ^+ to fake a $\pi^+ \rightarrow \mu^+$ decay is for its $\mu^+ \rightarrow e^+$ decay to occur early. Since the electron usually has more energy than the $\pi^+ \rightarrow \mu^+$ muon, most of these event are removed by imposing a minimum allowed H/A as well.

2.8 Monitor Triggers

Simultaneously with the $K^+ \rightarrow \pi^+ \nu\bar{\nu}$ data, several prescaled “monitor” triggers are taken as well. Data from these triggers are used extensively for various detector

⁴The range stack phototube voltages are adjusted to make the calibration (ADC counts per MeV) uniform, except for the T and A layers. These are appropriately scaled in the sum.

⁵The range stack is calibrated to 16 counts/MeV \times 2 ends = 32 counts/MeV, while the target is set at about 22 counts/MeV. This mis calibration is not corrected for.

calibration tasks, and are relied upon heavily for the sensitivity calculation performed in chapter 4. For reference, the important ones are mentioned here.

The $K_{\mu 2}(1)$ ⁶ trigger is defined as

$$KT \cdot (T \cdot A) \cdot B_{CT} \cdot (19_{CT} + 20_{CT} + 21_{CT}).$$

This trigger selects events with a beam kaon that deposits energy in the target, and a charged track that penetrates to the outer part of the range stack. It is dominated by the $K^+ \rightarrow \mu^+ \nu_\mu$ decay mode, and is used to isolate samples of this mode for various acceptance calculations and a branching ratio normalization (chapter 4).

The $K_{\pi 2}(1)$ ⁷ trigger is defined as

$$KT \cdot (T \cdot A) \cdot B_{CT} \cdot \overline{(19_{CT} + 20_{CT} + 21_{CT})},$$

which is identical to the level 0 $K^+ \rightarrow \pi^+ \nu \bar{\nu}$ trigger except for the delayed coincidence and photon veto. It is predominantly a mixture of $K^+ \rightarrow \pi^+ \pi^0$ and $K^+ \rightarrow \mu^+ \nu_\mu$ decays. While it can be used as a source of muons that stop in the allowed $K^+ \rightarrow \pi^+ \nu \bar{\nu}$ stopping layers, in this analysis it will only be used to select $K^+ \rightarrow \pi^+ \pi^0$ samples for a background study (chapter 3), acceptance calculations (chapter 4), and a $K^+ \rightarrow \pi^+ \pi^0$ branching ratio measured used to check the $K^+ \rightarrow \pi^+ \nu \bar{\nu}$ analysis (chapter 4).

The π scat trigger is defined as

$$C_\pi \cdot B4 \cdot E_{TG} \cdot IC \cdot DC \cdot (T \cdot A) \cdot B_{CT} \cdot \overline{(20_{CT} + 21_{CT})} \cdot \overline{(BV + ECM + ECP)}.$$

⁶The decay $K^+ \rightarrow \mu^+ \nu_\mu$ is commonly referred to as $K_{\mu 2}$.

⁷The decay $K^+ \rightarrow \pi^+ \pi^0$ is commonly referred to as $K_{\pi 2}$.

The first three terms duplicate the KT requirement from $K^+ \rightarrow \pi^+ \nu \bar{\nu}$ but use the pion, instead of kaon, Čerenkov. The beam pion is required to scatter from the target into the detector by inverting the delayed coincidence. This sample is used as a source of pions populating the full $K^+ \rightarrow \pi^+ \nu \bar{\nu}$ stopping region in the range stack, useful particularly for the TD acceptance calculation (chapter 4).

2.9 The Data

Events which passed the complete trigger were written to magnetic tape. From the 89, 90, and 91 runs, we took the equivalent of around 300 8mm (roughly half full) Exabyte tapes per year, for a total of about a tera byte of data.

Chapter 3

The Offline Analysis

3.1 Offline Software

Basic offline event handling and reconstruction was done with the E787 software framework **KOFIA** version 1.6, and monte carlo event simulation by **UMC** version 4.0.

The extensively used **KOFIA** is useful for reading data tapes and files, unpacking the raw detector information (TDC bits, ADC counts etc.), parsing and calibrating the information (with calibrations done by sub-system experts), and filling user-friendly fortran common blocks with this massaged data for analysis. **KOFIA** also contains software for subsystem reconstruction (eg. target reconstruction, drift chamber track fitting, range stack track finding) and some analysis tasks (eg. searching for photons at π^+ time throughout the detector) which typically evolved during previous analyses and may be used at a user's own peril.

UMC has evolved from the monte carlo software written originally to design E787. Again, it has evolved along with various analyses, and now includes a complete simulation of the online trigger and event writing for later analysis of UMC data with KOFIA; however, it does not represent some details of the detector geometry perfectly, and must be used with caution. The K^+ beam stopping distribution, accidental distributions in the target, and resolutions important to the trigger are measured with data and inserted into the simulation. For the most part, it only includes detector resolution effects in the trigger simulation, so users must measure and simulate most energy, time, and position resolutions in the offline analysis. UMC simulates electromagnetic interactions, normal ionization energy loss, multiple scattering, and particle decay quite accurately. It does a fair job with π^+ nuclear interactions. Despite some investigation, it is unknown how well it does with some rare processes (particularly photo-nuclear interactions and the subsequent nuclear de-excitations) which may be important to our backgrounds.

3.2 Basic Track Reconstruction and Kinematic Calculations

The full analysis is rather involved, and will be described in several steps. First, I will simply walk through the reconstruction of a single event, describing the steps

qualitatively.

Event reconstruction starts with a search for tracks in the drift chamber. The hits in each drift chamber super-layer are first matched up locally to form track segments, and the segments are pieced together to form lists of hit positions which probably came from a single track. Since the energy loss in the drift chamber is small, the 3 dimensional trajectory of a charged drift chamber track in the detector magnetic field will be nearly helical, or a circle in the $x - y$ plane and a straight line in $z - \phi_{CT}$ space (ϕ_{CT} is the “phase-angle,” which is the angle in the $x - y$ plane using the track’s centre of curvature as the origin). The drift chamber track fit is broken into these two pieces: the $x - y$ positions from the hits in the axial super-layers 1, 3, and 5 are fit to a circle, and the z positions from the hits in the stereo super-layers 2 and 4 are fit to a straight line in $z - \phi_{CT}$. The analysis uses the resulting drift chamber momentum for the kinematic cuts, and well as the detailed tracking information for aiding reconstruction in the target, I-counters, and range stack.

Working outward, the range stack is searched for likely tracks, which are matched-up with the drift chamber tracks. The analysis requires exactly one DC-RS track match. The range stack chambers along the track are then searched for hits giving precise $z - \phi$ positions (this ϕ refers the azimuthal angle in normal detector coordinates centred at the detector origin). Using the drift chamber track extrapolation to the range stack entrance as an additional point, the range in the range stack up to the

entrance of the stopping counter is calculated with a very simple “connect-the-dots” algorithm (with a correction for the track curvature). The range is then corrected for the energy deposited in the stopping layer using an integration of the Bethe-Bloch equation.

The transient digitizers on the range stack counters along the charged track are used to measure the range stack track time. This is our best measurement of kaon decay time, and is used throughout the analysis as a reference time for photon and secondary beam particle searches.

Now working inward, we extrapolate the drift chamber track back through the hexagonal I-counter array, and use it to select likely hit IC's and to estimate its range in the IC's. The energy in the struck IC's is summed for the I-counter energy measurement, and their times are averaged for an I-counter time measurement.

The drift chamber track is also extrapolated back into the target, and used for selecting candidate kaon and pion target tracks. Essentially, a “swath” is drawn around the drift chamber track extrapolation in the target, the first likely kaon cluster (a set of fibres with large energy depositions near $t = 0$) in the swath is selected, and the kaon energy and time is recorded. A maximum likelihood analysis is used to classify all struck “non-kaon” fibres in the swath as either “pion” or “non-pion” fibres. This analysis will accept events with no pion fibres only if the kaon apparently decayed outwards at the target edge. If there are apparent pion fibres, their energy

and average time are recorded and used in the subsequent analysis (if no valid target pion time is found, the I-counter time is defined to be the target pion time). During target reconstruction, any struck fibres near the pion time which are not classified as pion hits are nominated as photon candidates (from a possible $K^+ \rightarrow \pi^+\pi^0$ conversion in the target), and used in the later analysis.

The energy from the target, I-counter, and range stack is summed to give the total charged track energy measurement, which is corrected for losses in the RSPC's, and range stack and drift chamber dead material. The target, I-counter, and range stack range is summed for the total range measurement, which is also corrected for drift chamber dead material. The total charged track momentum measurement consists of the DC momentum, plus a correction for energy loss in the target and I-counter. Two versions of the total momentum are calculated: one corrects the drift chamber momentum with TG+IC energy, the other with TG+IC range. The target range corrected momentum was found to offer slightly higher $K^+ \rightarrow \pi^+\nu\bar{\nu}$ acceptance for the same rejection (inferred in the background studies), and was chosen for the total momentum measurement.

To better define the event, the beam counters and chamber are searched both for a K^+ beam track near the target kaon time, and for a possible secondary beam track near the range stack track time. If a second track is found in the beam system, the event will be vetoed since it may have come from a beam pion scattering from the

target into the range stack faking a $K^+ \rightarrow \pi^+$ decay.

The entire detector is searched for any extra activity occurring near the time of the range stack track, which may have come from photons from a $K^+ \rightarrow \pi^+\pi^0$ decay. The barrel and endcap photon veto systems are particularly important, but the rest of the range stack, I-counters, V-counters, beam counters, and target are also used. Since photon conversions may occur in elements also hit by the charged track (“overlap”), anomalously high energy along the track in the target, I-counter, or range stack will also cause the event to be vetoed.

The range stack transient digitizers observing the stopping counter are used to insure a good $\pi^+ \rightarrow \mu^+$ candidate is present (recall Figure 2.4). The TD pulse shapes are carefully calibrated for each end of each counter, and the shape is fit to the TD data in the stopping counter. The fit must be consistent with a pion stop, some delay, and then a $\pi^+ \rightarrow \mu^+$ decay. The analysis also requires that the μ^+ decays into an e^+ at a later time, which strongly suppresses the background from a stopping muon with an early $\mu^+ \rightarrow e^+$ faking a $\pi^+ \rightarrow \mu^+$ decay. Additionally, any extra activity in the range stack near the apparent pion decay time could have come from an early $\mu^+ \rightarrow e^+$ and may cause the event to be cut.

If the range stack or drift chamber pattern recognition routines were confused so that spurious hits were included, or if the charged track underwent a very hard scatter in the range stack, the measured track kinematics are almost arbitrary; fortunately,

there is enough redundant track information available to diagnose such pathologies.

The extrapolation from the drift chamber into the range stack, along with the pattern of range stack hits, z positions from end-to-end times in the range stack counters, RSPC-measured positions, and energy deposited in the stopping counter, severely constrain the π^+ track in the range stack. This information is fit to find the most likely track momentum and direction at the range stack entrance, along with detailed track information in the range stack (including energy deposited in each range stack layer and the track stopping position). The event is cut if the fit quality is bad. It is also removed if the energy measurements in the range stack layers are inconsistent with the energies expected from the fit (possibly caused by a hard scatter from a $K^+ \rightarrow \mu^+ \nu_\mu$ muon or an overlapping $K^+ \rightarrow \pi^+ \pi^0$ photon), or if the track may have entered the range stack support structure.

3.2.1 Kinematic Scaling

After the event reconstruction, adjustments are made to various kinematic quantities for both data and monte carlo for our final total range, energy, and momentum measurements. Since the monte carlo does not include energy resolution effects, the range stack energy and target energy and times for UMC generated data are first smeared using the software and calibrations from Roy, based on measured detector-element photo-electron yields.

| Year | Target Scale Factor s |
|------|-------------------------|
| 1989 | 0.9322 |
| 1990 | 0.7775 |
| 1991 | 0.9850 |

Table 3.1: Target energy scale factors, the slopes from linear fits to energy vs. visible target energy expected from range. The correction for 1990 data is particularly large.

Inconsistencies in the target energy calibration makes rescaling necessary for data. Before it is used in the total energy measurement, the target energy for data is linearly scaled:

$$E_{\text{TG}}^{\text{new}} = E_{\text{TG}}/s$$

with the scale factors, s listed in Table 3.1. The factors were measured by a fit to visible energy vs. visible energy expected from target range. The correction is particularly large for 1990 data.

The momentum, energy, and range peaks for $K^+ \rightarrow \mu^+ \nu_\mu$ and $K^+ \rightarrow \pi^+ \pi^0$ still do not precisely agree with the true values, nor does data agree in central value or width with monte carlo. The disagreement with the true values is probably not harmful; event selection and resolution effects bias our samples somewhat. The disagreement between data and monte carlo is, however, potentially serious. We use UMC to calculate our kinematic selection efficiencies, so it must represent the data well. The total energy, range, and momentum are adjusted with a simple linear scaling to make the measured $K^+ \rightarrow \pi^+ \pi^0$ and $K^+ \rightarrow \mu^+ \nu_\mu$ peaks in both data and UMC line up with the

true values, and an additional smearing term is added when analyzing UMC data.

The kinematics adjustments made for data are

$$P_{\text{tot}}^{\text{new}} = aP_{\text{tot}} + b$$

$$E_{\text{tot}}^{\text{new}} = aE_{\text{tot}} + b$$

$$R_{\text{tot}}^{\text{new}} = aR_{\text{tot}} + b$$

and for KOFIA analyzed UMC data

$$P_{\text{tot}}^{\text{new}} = aP_{\text{tot}}(1 + \sigma G) + b$$

$$E_{\text{tot}}^{\text{new}} = a(E_{\text{tot}} + \sigma G) + b$$

$$R_{\text{tot}}^{\text{new}} = a(R_{\text{tot}} + \sigma G) + b$$

where G is a unit gaussian random number. The various scaling and smearing factors are listed in Tables 3.2 and 3.3, and $K^+ \rightarrow \pi^+\pi^0$ and $K^+ \rightarrow \mu^+\nu_\mu$ peak positions and resolutions for data and monte carlo before and after rescaling are presented in Table 3.4. Sample fits for 1991 data and reconstructed Monte Carlo after rescaling are shown in Figures 3.1 and 3.2 for $K^+ \rightarrow \pi^+\pi^0$ and $K^+ \rightarrow \mu^+\nu_\mu$ respectively.

| | | 1989 | 1990 | 1991 |
|-----|------------------|-------------|-------------|-------------|
| a | P_{TGE} | 1.0030 | 0.9867 | 0.9899 |
| b | | 3.14 MeV/c | 5.24 MeV/c | 2.90 MeV/c |
| a | P_{TGR} | 1.0302 | 1.0302 | 1.0232 |
| b | | -3.78 MeV/c | -4.91 MeV/c | -5.13 MeV/c |
| a | E | 0.9288 | 0.9268 | 0.9152 |
| b | | 10.85 MeV | 10.68 MeV | 11.45 MeV |
| a | R | 1.0239 | 1.0248 | 1.0270 |
| b | | -0.92 cm | -0.89 cm | -0.91 cm |

Table 3.2: Kinematic scale factors for data.

| | | 1989 | 1990 | 1991 |
|----------|------------------|-------------|-------------|-------------|
| a | P_{TGE} | 0.9964 | 0.9964 | 0.9964 |
| b | | 1.67 MeV/c | 1.67 MeV/c | 1.67 MeV/c |
| σ | | 0.0202 | 0.0182 | 0.0178 |
| a | P_{TGR} | 1.0096 | 1.0096 | 1.0096 |
| b | | -1.43 MeV/c | -1.43 MeV/c | -1.43 MeV/c |
| σ | | 0.0189 | 0.0168 | 0.0174 |
| a | E | 0.9984 | 0.9984 | 0.9984 |
| b | | 1.32 MeV | 1.32 MeV | 1.32 MeV |
| σ | | 0.747 | 1.124 | 1.702 |
| a | R | 1.0426 | 1.0426 | 1.0426 |
| b | | -1.81 cm | -1.81 cm | -1.81 cm |
| σ | | 0.438 | 0.330 | 0.264 |

Table 3.3: Kinematic scale factors and smearing for UMC.

| Quantity | Year | $K^+ \rightarrow \pi^+\pi^0$ | | | $K^+ \rightarrow \mu^+\nu_\mu$ | | |
|---------------------|----------------|------------------------------|----------|-----|--------------------------------|----------|-----|
| | | Peak | σ | % | Peak | σ | % |
| Momentum (MeV/c) | 1989 Raw Data | 202.8 | 4.9 | 2.4 | 232.3 | 6.5 | 2.8 |
| | Corrected Data | 205.2 | 5.1 | 2.5 | 235.5 | 6.7 | 2.8 |
| | Raw UMC | 204.2 | 3.7 | 1.8 | 234.7 | 4.0 | 1.7 |
| | Corrected UMC | 205.1 | 5.2 | 2.5 | 235.5 | 6.5 | 2.8 |
| | 1990 Raw Data | 202.8 | 4.9 | 2.4 | 233.4 | 6.2 | 2.6 |
| | Corrected Data | 205.1 | 4.7 | 2.3 | 235.5 | 6.3 | 2.7 |
| | Raw UMC | 204.2 | 3.7 | 1.8 | 234.8 | 3.8 | 1.6 |
| | Corrected UMC | 205.2 | 4.8 | 2.3 | 235.5 | 6.0 | 2.4 |
| | 1991 Raw Data | 202.8 | 4.9 | 2.4 | 235.2 | 6.2 | 2.6 |
| | Corrected Data | 205.0 | 4.9 | 2.4 | 235.7 | 6.2 | 2.7 |
| | Raw UMC | 204.2 | 3.7 | 1.8 | 234.7 | 4.0 | 1.7 |
| | Corrected UMC | 205.2 | 5.0 | 2.4 | 235.3 | 6.0 | 2.6 |
| True Value | | 205.14 | | | 235.53 | | |
| Energy (MeV) | 1989 Raw Data | 105.2 | 3.7 | 3.5 | 152.5 | 3.8 | 2.5 |
| | Corrected Data | 108.5 | 3.4 | 3.1 | 152.5 | 3.6 | 2.4 |
| | Raw UMC | 107.4 | 3.3 | 3.1 | 151.4 | 3.5 | 2.3 |
| | Corrected UMC | 108.6 | 3.4 | 3.1 | 152.5 | 3.6 | 2.4 |
| | 1990 Raw Data | 105.6 | 3.7 | 3.5 | 153.0 | 4.1 | 2.7 |
| | Corrected Data | 108.5 | 3.4 | 3.1 | 152.5 | 3.8 | 2.5 |
| | Raw UMC | 107.4 | 3.3 | 3.0 | 151.4 | 3.5 | 2.3 |
| | Corrected UMC | 108.6 | 3.4 | 3.1 | 152.5 | 3.7 | 2.4 |
| | 1991 Raw Data | 106.1 | 4.0 | 3.8 | 154.1 | 4.5 | 2.9 |
| | Corrected Data | 108.8 | 4.0 | 3.7 | 152.5 | 4.4 | 2.9 |
| | Raw UMC | 107.4 | 3.3 | 3.1 | 151.4 | 3.5 | 2.3 |
| | Corrected UMC | 108.5 | 4.0 | 3.7 | 152.5 | 3.9 | 2.6 |
| True Value | | 108.55 | | | 152.48 | | |
| Range (cm) | 1989 Raw Data | 30.6 | 1.2 | 3.9 | 54.0 | 2.3 | 4.3 |
| | Corrected Data | 30.4 | 1.2 | 4.1 | 54.4 | 2.4 | 4.4 |
| | Raw UMC | 30.9 | 1.1 | 3.4 | 53.9 | 2.3 | 4.2 |
| | Corrected UMC | 30.4 | 1.2 | 4.1 | 54.4 | 2.4 | 4.4 |
| | 1990 Raw Data | 30.5 | 1.2 | 3.9 | 53.9 | 2.5 | 4.6 |
| | Corrected Data | 30.4 | 1.2 | 3.9 | 54.4 | 2.5 | 4.6 |
| | Raw UMC | 30.9 | 1.1 | 3.5 | 53.9 | 2.3 | 4.2 |
| | Corrected UMC | 30.4 | 1.2 | 3.9 | 54.4 | 2.4 | 4.4 |
| | 1991 Raw Data | 30.5 | 1.1 | 3.6 | 53.8 | 2.3 | 4.3 |
| | Corrected Data | 30.4 | 1.2 | 3.8 | 54.4 | 2.4 | 4.4 |
| | Raw UMC | 30.9 | 1.1 | 3.4 | 53.9 | 2.3 | 4.2 |
| | Corrected UMC | 30.4 | 1.2 | 3.8 | 54.4 | 2.4 | 4.4 |
| True Value | | 30.37 | | | 54.34 | | |

Table 3.4: Peak positions and widths (from gaussian fits with no background) before and after corrections for both data and UMC. Momentum is correct with TG+IC Range.

| Cut Name | Description |
|-----------|---|
| ISKCODE | Require successful event reconstruction |
| PICER | Veto beam pions at the RS charged track time with C_π |
| PISCAT_BW | Veto second beam particle in the beam wire chamber |
| B4DEDX | K^+ particle ID and photon veto in B4 hodoscope |
| B4TDEDX | K^+ particle ID and photon veto in B4T counter (89,90) |
| PISCAT_B4 | Veto second beam particle in B4 hodoscope (91) |
| PIHODO_B4 | Veto second beam particle in B4 hodoscope (89,90) |
| B4TFIT | Veto overlapping beam particle in B4 hodoscope (89,90) |
| PBGLASS | Veto beam pions or photons at the RS charged track time (91) |
| DIPANG | Require $\cos \theta_z$ in detector fiducial volume |
| ZDCOW | Veto charged tracks that may have passed through DC endplate |
| NTRIK | Maximum number of kaon fibres in target |
| TGDCXY | Require good TG/DC track match up |
| ZTGT | Require charged track originate in fiducial target z region |
| TGDCVT | Veto photons in target |
| RTDIF | Remove events with large possible $K^+ - \pi^+$ TG overlap |
| TARGF | Require TG π^+ originate from K^+ cluster |
| EPIMAX | Maximum permitted pion fibre energy |
| TGDEDX | Veto photons in TG with a $\pi^+ dE/dX$ cut |
| EIC | Veto photons in I-counter with a maximum energy cut |
| EKZ | Veto low kaon TG energy but high apparent stopping z |

Table 3.5: Part 1: the complete list of the offline cuts.

3.3 Offline Cuts

Every cut used in this analysis is listed in Table 3.5 (in two parts), and the following sections contain a detailed description of each cut. Non-experts may just refer to this table, and skip to the background studies in Section 3.4.

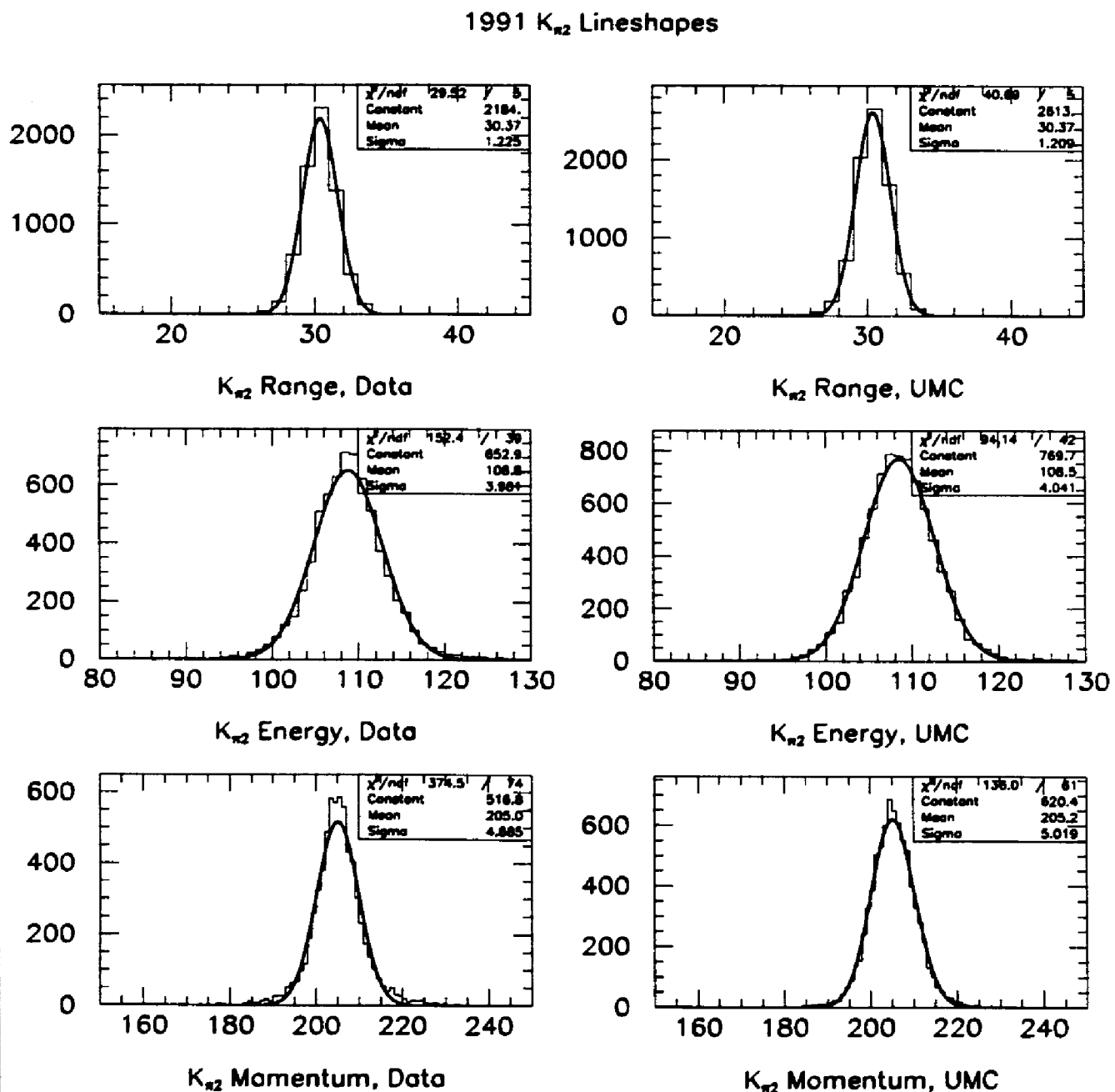


Figure 3.1: Range, energy, and momentum peaks for data and reconstructed monte carlo from 1991.

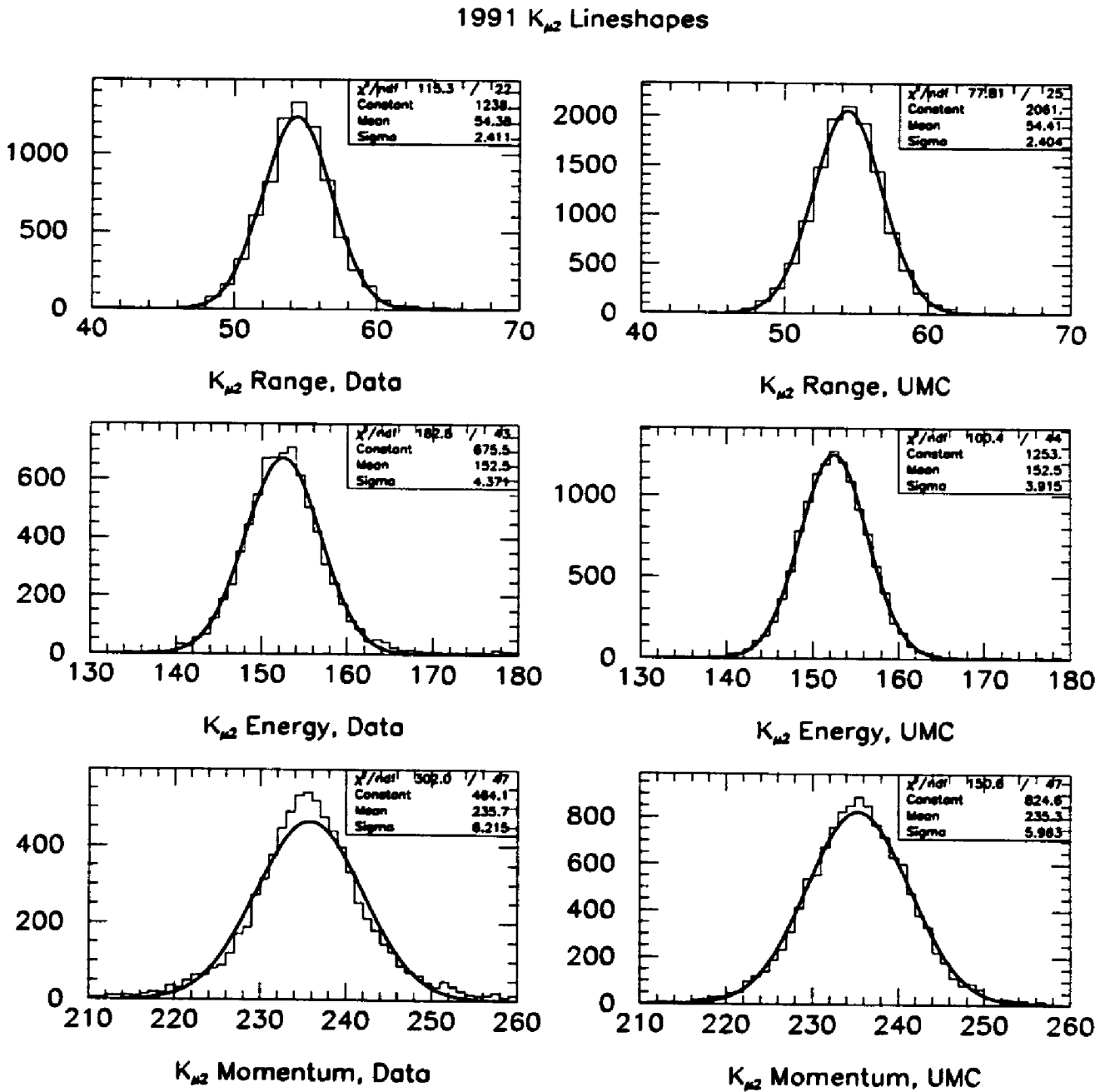


Figure 3.2: Range, energy, and momentum peaks for data and reconstructed monte carlo from 1991.

| Cut Name | Description |
|-----------|---|
| PRPAT | Pattern cut on RS track targeting overlapping photons |
| NSECRS | Maximum of 3 RS sectors on track |
| RNGMOM(2) | Demand DC momentum and RS range consistent with pion |
| CHIRF | Cut events with inconsistent RS track information |
| ZFRF | Require track stop in RS fiducial z region |
| RSDEDX | Cut events inconsistent with $\pi^+ dE/dX$ in RS |
| LAY14 | Cut events whose charged track apparently stopped in RSPC |
| PNNSTOP | Require π^+ stopping layer from 11-18 inclusive |
| DELC | Force kaon decay at rest |
| TIMCON | Cut events with apparent kaon or pion timing anomalies |
| FITPI | Require successful TD $\pi^+ \rightarrow \mu^+$ pulse fit in stopping counter |
| TDACC | Tighter TD quality cut on $\pi^+ \rightarrow \mu^+$ fit signature |
| TDDFA | TD discriminant function separation of pions from muons |
| ELEC_V5 | Demand $\mu^+ \rightarrow e^+$ signature from stopping counter |
| ELVETO | Veto events with extra RS activity at $\pi^+ \rightarrow \mu^+$ time |
| TDFOOL | Veto apparent $\mu^+ \rightarrow e^+$ hiding under RS track at $\pi^+ \rightarrow \mu^+$ time |
| RSHEX | Permit only one hit counter in stopping TD channel |
| TMUBV | Veto on BV activity near stopping sector at $\pi^+ \rightarrow \mu^+$ time |
| TMUADC | Cut events with $\pi^+ \rightarrow \mu^+$ after end of ADC gate |
| STOP_HEX | Require agreement of online and offline stopping hextant/layer |
| GAMVET | Veto on photons in RS, BV, EC, IC, and VC |
| BOX | Range, energy and momentum in fiducial region |

Table 3.5: Part 2: the complete list of the offline cuts, continued.

3.3.1 Reconstruction

Reconstruction is loosely defined as finding reasonable data in the major subsystems that might have come from a single charged track. The cuts are mostly made on software return codes, with no tuning (reconstruction cuts are built into the software – they return only a pass/fail condition). The major additions to the reconstruction are the **ICRNGE** routine from Roy (slightly polished by Livescu) for the I-counters, and the **SWATH**[26] routine from Ardebili for the target. **SWATH** was modified to calculate some useful quantities for later target cuts, and to default to the I-counter pion time for its photon search if no target pion fibres are found.

- **ISKCODE:** The basic reconstruction, including the total momentum, energy and range calculation, is handled with a routine from Meyers called **SETUP_KINE** which returns the code **ISKCODE**. This analysis requires successful event reconstruction, **ISKCODE = 0**. This corresponds to successful target setup (**IFAIL = 0** insures good target data, and **IQUAL ≤ 1** guarantees that either a good $K \rightarrow \pi^+$ candidate is present or that a K candidate is present at the target edge, and the pion travelled outwards into the I-counter striking no non-kaon fibres), successful DC decoding and track fit, one and only one DC/RS track match-up, and a good time found by the **TRKTIM** routine.

3.3.2 Beam line Elements

A good $K^+ \rightarrow \pi^+ \nu \bar{\nu}$ event should have a single beam K^+ at the same time as the apparent target kaon cluster, and no activity at the apparent π^+ time. One of the important backgrounds to $K^+ \rightarrow \pi^+ \nu \bar{\nu}$ is an undetected or misidentified beam pion scattering from the target into the range stack, faking a $K^+ \rightarrow \pi^+$ decay. These will be called “ π scats” from now on. π scats should have a beam track at the apparent $K^+ \rightarrow \pi^+$ decay time.

The beam line cuts were tuned in the course of the π scat background studies described in Section 3.4.1. Various distributions for probable π scats were compared to the distributions for $K^+ \rightarrow \mu^+ \nu_\mu$ events, and the cuts were mostly set by eye. The beam wire chamber is analyzed with the **PISCAT_BW** routine from Roy, modified to handle time offsets in both the kaon and secondary beam particle searches. The lead glass counter from 1991 is analyzed with the **TCEREN** code and calibration from Konaka. In 1991, a new routine called **PISCAT_B4** uses the TD’s for the full B4 hodoscope analysis. Individual hits are matched-up in space and time to form probable clusters, and a multi-pulse fit is performed in each finger struck by the kaon looking for an obscured second beam particle. In 1989 and 1990, the B4 hodoscope TD’s were not well behaved, making the time matchup needed for clustering impossible. The clustering was instead done with the new **PISCAT_HODO** routine using the TDC’s and ADC’s, while the B4T counter was used for the double pulse search. To compensate for the

| Year | Half Window (nsec) | Time Offset (nsec) |
|------|-----------------------|-----------------------|
| 1989 | 7.5 | -2.7 |
| 1990 | 5.0 | -1.0 |
| 1991 | 5.0 | 2.5 |

Table 3.6: Č_π Cut half window and time offset $t_{RS} - t_{C_\pi}$.

absence of the lead glass counter in 1989 and 1990, a dE/dX cut in the B4T counter was added.

- PICER: Our first defence against beam pions is the dedicated pion Čerenkov counter. Veto events with a Č_π TDC leading edge in an offset window around TRS. This is our best beam pion cut. Windows and offsets are listed in Table 3.6.
- PISCAT_BW: The BWPC is used to insure that the K^+ is the only beam particle in the event. PISCAT_BW first looks for a kaon cluster at the target kaon time in the beam wire chamber, which is excluded from the search. It then searches the BWPC for a cluster near TRS. Cut events if PISCAT_BW found a BWPC cluster with average time within Δt of $TRS + t_{\text{off}}$ (see Table 3.7).
- B4DEDX: When they exit the degrader, beam pions are still nearly minimum ionizing and leave about 2 MeV in the B4 hodoscope, while kaons deposit around 5 MeV. Additionally, extra beam particles or photons typically leave more energy than a kaon. Cut events with $E_{B4} < 4$ MeV or $E_{B4} > 20$ MeV.

| Year | Δt (nsec) | t_{off} (nsec) |
|------|----------------------|----------------------------|
| 1989 | 15 | 4.9 |
| 1990 | 10 | 3.5 |
| 1991 | 10 | 0.0 |

Table 3.7: BWPC Cut half window and time offset.

- **B4TDEDX:** Even after the B4DEDX cut, there is still a signature for events with beam pions entering the target. In 1989 and 1990, cut events with $E_{B4T} < 1.25 \text{ MeV}$ or $E_{B4T} > 10 \text{ MeV}$.
- **PISCAT_B4:** Good events have one cluster in the B4 hodoscope at the target kaon time, and no activity at the kaon decay time. Extra beam particles exiting the degrader will usually leave a second cluster in the B4 hodoscope, or pile-up under the primary kaon and leave a double-pulse signature in the kaon fingers. In 1991, the individual B4 hodoscope finger TD channels are calibrated with a time offset and an error reflecting each finger's time resolution for seeing a beam π^+ scatter into the range stack. PISCAT_B4 forms hit clusters in the hodoscope, including an estimate of the cluster time resolution σ . Events are cut if no K^+ cluster is found, or if there is a cluster whose time is within 3σ of TRS. If no secondary cluster is found, perform a pulse-fit in each finger in the K^+ cluster and cut the event if any fit has a bad single pulse fit ($\log \chi^2_{\text{fit}} > 2$) and a large double-pulse-fit second pulse ($E_{\text{fit}} > 10 \text{ TD counts}$) within 6 nsec of TRS.

- PIHODO_B4: In 1989 and 1990, problems with the TD's made the PISCAT_B4 cluster analysis impossible. The PISCAT_HODO routine also forms clusters in the beam hodoscopes, but uses the TDC's rather than TD's for timing. In 1989 and 1990 this cut is used with B4TFIT to replace the PISCAT_B4 cut used in 1991. Events are cut if no K^+ cluster is found in B4, or if a second cluster is found the B4 hodoscope within 5 nsec of TRS.
- B4TFIT: The PIHODO_B4 cut lacks the TD double-pulse rejection of 91 PISCAT_B4 cut. While TD problems made it impossible to match up the times of the hodoscope fingers for clustering, individual TD channels still show the double pulse signature. Rather than using the hodoscope, in 1989 and 1990 the B4T counter is present in every event. In 1989 and 1990, run FITPI in the B4T counter and cut events with a bad single pulse fit ($\log \chi^2_{\text{fit}} > 1.8$) and a large double pulse fit second pulse ($E_{\text{fit}} > 10$ TD counts) within 6 nsec of TRS.
- PBGLASS: With the B4T counter missing in 91, similar beam pion rejection to the B4TDEDX cut is obtained with the Pb-Glass Čerenkov installed that year. Using a 6 nsec half window around TRS, cut events with lead-glass tube multiplicity > 2 .

3.3.3 Drift Chamber

The KOFIA DC_TRACK routine is used for the drift chamber fits. Anomalies in the data led to a major new drift chamber calibration effort, done mostly by Meyers. Complete new drift chamber TDC time offsets and wire staggers are used, along with a systematic global TDC time offset which improves the momentum resolution. There were additional anomalies in the drift chamber momentum, causing asymmetries in the $\cos \theta_z$ dependence of the total momentum and causing the $K^+ \rightarrow \pi^+ \pi^0$ background to strongly favour stopping in the downstream half of the detector. At the suggestion of Shoemaker, a study was undertaken to use these asymmetries and extrapolations from the drift chamber to the range stack chambers to determine if the relative z from the two stereo layers was consistent; in fact, serious discrepancies were found, and the relative z calibrations for drift chamber layers 2 and 4 were adjusted to remove it. In previous analyses, a $|\cos \theta_z|$ -dependent correction to the drift chamber momentum was used. Since this correction was almost certainly just removing a selection bias in the calibration samples, it is not used here. In 1989, the drift chamber suffered from serious HV problems; flaws in the existing offline patching software and calibration were finally fixed for this analysis.

The DIPANG and ZDCOW cuts help to constrain the charged track into our fiducial region. They are basically inherited from previous analyses ($\theta_{\text{dip}} = \sin^{-1} \cos \theta_z$).

- DIPANG: Cut events with $|\theta_{\text{dip}}| > 30^\circ$. Together with the T-counter requirement in the trigger, this defines the charged track solid angle accepted.
- ZDCOW: It may be just barely possible for a charged track to clip the drift chamber endplate and still be accepted in the analysis. Use a TRKPOS extrapolation to find the track z position at the drift chamber outer radius. Cut events with $|z_{\text{dcrs}}| > 25$ cm.

3.3.4 Kaon Stopping Target

In addition to event reconstruction, the target is used for additional π scat rejection, as well searching for overlapping photons from a $K^+ \rightarrow \pi^+\pi^0$ decay. While most of these analyses used to be done with various separate routines, now it is all built into SWATH. Except for the energy rescaling mentioned above, the standard target calibration was used. The target cuts were set either in the π scat or $K^+ \rightarrow \pi^+\pi^0$ background studies described in Sections 3.4.1 and 3.4.3. They are similar to cuts used in previous analyses.

- NTRIK: Typical kaons strike only a few target fibres. Photons from a relatively early $K^+ \rightarrow \pi^+\pi^0$ decay can convert in the target, and their fibres mistakenly added to the kaon cluster. Cut events with more than 10 target Kaon fibres hit.
- TGDCXY: Primarily a TG-DC match-up diagnostic, this cut is largely obsolete with the new SWATH target reconstruction software. Use TRKPOS to extrapolate

drift chamber track to the target edge and compare to **SWATH**'s target peripheral xy position. Cut if match-up worse than 3 cm.

- ZTGT: π scats appear to come from a fairly uniform target z position distribution (including positions outside the target), while real $K^+ \rightarrow \pi^+$ decays are concentrated in the target centre. Use **TRKPOS** to extrapolate drift chamber track to target edge. Cut if $z_{\text{dctg}} < -12$ cm or $z_{\text{dctg}} > 14$ cm.
- TGDCVT: Photons from $K^+ \rightarrow \pi^+\pi^0$ can convert inside the target, showing up as extra energy at the charged track time. **SWATH** nominates non-pion target fibres at **TIMEPI** as γ candidates, recording the number of candidate fibres, N_γ , and total candidate energy, E_γ . Cut if $E_\gamma > 5$ MeV, or if $E_\gamma > 2$ MeV and $N_\gamma > 1$.
- RTDIF: If the pion from a $K^+ \rightarrow \pi^+\pi^0$ decay travels along an extended kaon track in the target, its target range uncertainty can be very large and we can mistakenly infer too large a target range and put the pion into our $K^+ \rightarrow \pi^+\nu\bar{\nu}$ fiducial region. **SWATH** estimates the error in the target pion range, RTDIF. Cut if RTDIF > 1.5 cm.
- TARGF: If a beam kaon is lost in the target, a beam pion can scatter from the target into the RS faking a $K^+ \rightarrow \pi^+$ decay. This pion will usually have some separation from the kaon. Cut if separation between nearest K^+ and π^+ target

fibres is > 1 cm.

- EPIMAX: Photons that convert in the target can overlap the pion track, but usually deposit relatively high energy in the pion fibres. Permit a maximum pion target fibre energy of 5 MeV.
- TGDEXD: Target photon conversions can also be spread out over several fibres, not pushing any one fibre above 5 MeV but making the apparent pion energy in the target inconsistent with its observed range. Additionally, an enhancement was noticed for $K^+ \rightarrow \pi^+\pi^0$ events with large total range measurements that had anomalously small target energy deposition for the apparent target range. Use the SWATH pion range R_{TG} and pion energy E_{TG} . Cut events with $E_{TG} > 25$ MeV or $R_{TG} > 10$ cm. Also cut events with $E_{TG} > 5$ MeV/cm R_{TG} . If the target range is > 3 cm, cut events with $E_{TG} < 17/7$ MeV/cm R_{TG} . This cut was set using $K^+ \rightarrow \pi^+\pi^0$ events in the peak, “high-energy,” and “high-range” tails, described in the $K^+ \rightarrow \pi^+\pi^0$ background study (Section 3.4.3). The cut is sketched in Figure 3.3.
- EIC: Photons can also overlap the charged track in the I-counter. Cut if total I-counter energy on the charged track is > 4 MeV.
- EKZ: The K^+ can enter the target and undergo a charge-exchange interaction forming a K^0 . If the interaction occurs near the target front face, the K^0 can

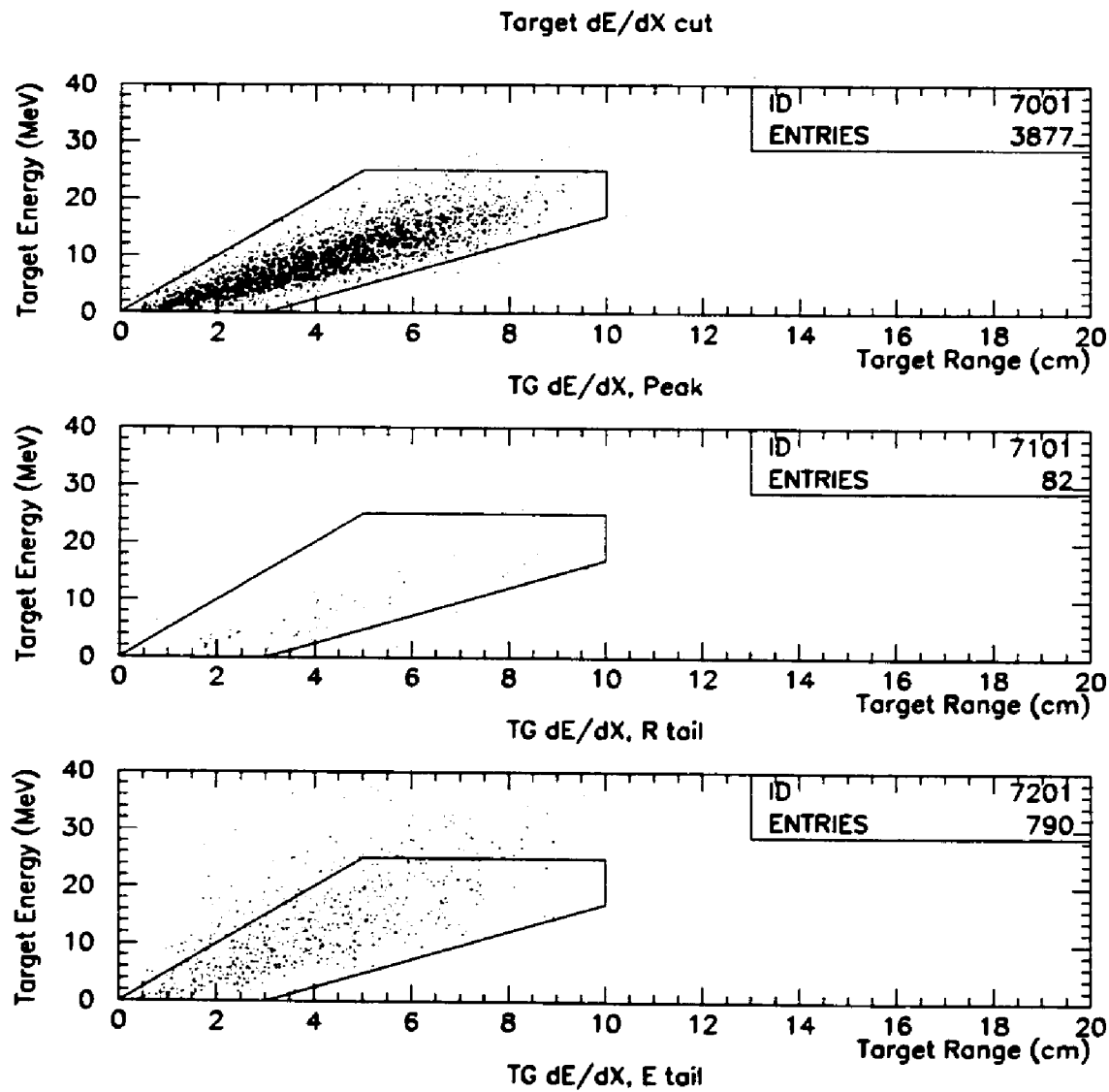


Figure 3.3: The target dE/dX cut for $K^+ \rightarrow \pi^+\pi^0$ pions in the $K^+ \rightarrow \pi^+\nu\bar{\nu}$ data after the Pass 1 photon cuts. The top plot is for events in the peak, centre is for pions with typical $K^+ \rightarrow \pi^+\pi^0$ total energy but a high total range measurement, and the bottom is for pions with typical $K^+ \rightarrow \pi^+\pi^0$ total range but a high energy.

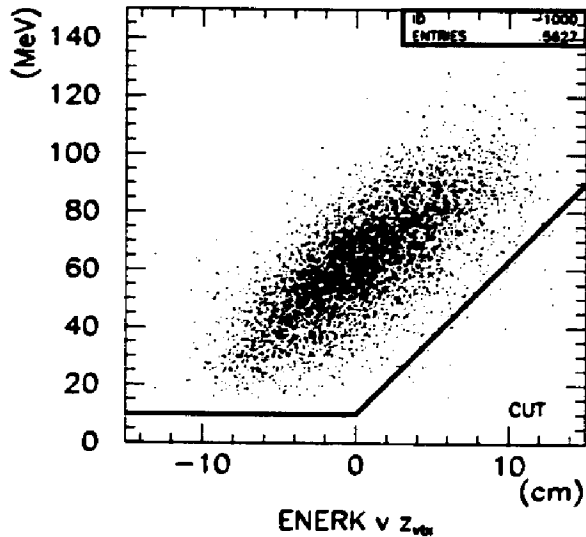


Figure 3.4: Target kaon energy vs. drift chamber extrapolated kaon decay position for 1990 $K^+ \rightarrow \mu^+\nu_\mu$ monitor triggers.

travel in the z direction for about 2 nsec and decay as a K_L^0 near the far end of the target. The apparent kaon cluster should have relatively low energy (ENERK), while the drift chamber track extrapolation to the vertex should suggest a relatively high z position (z_{vtx}). Cut events with target kaon energy $\text{ENERK} < 10 \text{ MeV}$, or $\text{ENERK} < (80/15 \text{ MeV/cm } z_{\text{vtx}} + 10 \text{ cm})$. The cut is sketched in Figure 3.4.

3.3.5 Range Stack Track Analysis

There were a number of problems and anomalies present in the standard range stack software and calibrations, which were at least partially fixed for this analysis. The range stack energy calibration for 1989 data had never been completed, and was

redone (mostly by Livescu [27]). The RSPC calibration had not been pursued in detail since the 1988 data. Ito noticed serious chamber-to-chamber z mismatches contributing to $K^+ \rightarrow \mu^+ \nu_\mu$ background, and Livescu completely redid the RSPC z calibration [24]. In the 1991 data, an error in the RSPC $\phi - z$ time matchup calibration used for hit selection caused the inner chamber in sector 22 to never be accepted by the range routines, costing a full 4% of the 1991 acceptance in [18]. It was fixed for this analysis.

On the software side, the standard range routines use a drift chamber track extrapolation to select RSPC hit candidates, which was found to cause tails in the range measurement correlated with mismeasured drift chamber momentum. Since most spurious RSPC hits come from after-pulsing following a real hit, the earliest candidate hit was chosen instead. Also, if no matching RSPC $\phi - z$ hit was found, the range routines used to default to a DC-based “dead-reckoning” algorithm. Since it is quite common for a ϕ hit to be present even if the z hit is missed, this led to a significant under-utilization of the available information for these events, and I suspect that this one feature caused the $K^+ \rightarrow \mu^+ \nu_\mu$ and $K^+ \rightarrow \pi^+ \pi^0$ kinematic tails to favour events with missing RSPC z hits. The range routines were modified to allow the RSPC ϕ position to be used in the range calculation, even if no z hit was found.

The range stack TD-based track time, TRS, is calculated by the `TRKTIM` routine from Meyers. This time is used directly as the pion time when searching TD-instrumented channels for photons or accidental hits. When comparing to TDC based times, however, a complication noticed by Meyers [25] exists. In 1989 and 1990, the TD's use the B4T counter as a reference time, while the TDC stop is generated by the "beam strobe." Using different references significantly worsens the time resolution when comparing TD-based to TDC-based times, which is a particular problem in our photon veto. For 1990 data, this is easy to correct since the beam strobe is actually put into a TD channel. As was done in previous analyses, the 1990 TD-based times are corrected using the `TCORR` code and calibration from Roy. In 1989 data, however, the beam strobe itself is not in the TD's, but the kaon Čerenkov signal (which nominally sets the beam strobe timing) is. A complete run-by-run time calibration of the TD \bar{C}_K time was performed, and for each event the TD \bar{C}_K channel is searched for a candidate pulse. If one is found, it is used to correct TRS when using it as a TDC reference; otherwise, the best B4T pulse is found and used instead.

The standard range routines take a minimalist approach to the range calculation by using just enough information to exactly calculate the range (DC track extrapolation to the range stack entrance, RSPC hit positions, stopping layer radius, and energy in the stopping layer), and discarding the extra information that over-constrains the track (RS sector crossing positions and the z position in each range

stack counter from end-to-end timing). While for good tracks this merely costs a little bit of range resolution, it can completely miss severe problems in the pathological tracks that make up our backgrounds. These include pattern recognition mistakes (which included spurious hits in the calculation) and very hard scatters in the range stack. For this analysis, a first attempt has been made to use all of the available information to assign a range stack track quality, and to yield detailed results about the track trajectory and energy deposition for later cuts.

The major addition to the previous range stack analysis is a new range stack track fitter, RPRFIT, which works as follows. A hypothetical track (specified by the $z - \phi$ position and three momentum coordinates at the fixed range stack inner radius) is propagated through the range stack with UMC. A χ^2 variable is calculated, using the DC_TRACK position extrapolation to the range stack entrance (2 coordinates), RS sector crossings (2 coordinate per crossing), range stack TD end-to-end-time-based z positions (1 coordinate per layer hit), and ADC-based stopping counter energy (1 measurement). The error on each term in the χ^2 is measured with π scat monitor data. Varying the track parameters, the CERN minimization routine MINUIT is used to find the best track fit.

- PRPAT: Overlapping photons near the range stack charged track often show up with bad apparent range stack track topologies. The PRPAT routine essentially walks forward along the range stack track, counting the number of times it

crosses into each sector. Bad topologies often show up as multiple apparent crossings into a sector. Cut events with more than one crossing into any sector.

- **NSECRS:** Real $K^+ \rightarrow \pi^+ \nu\bar{\nu}$ pions almost never hit more than three range stack sectors. While some $K^+ \rightarrow \mu^+ \nu_\mu$ events might hit four sectors, primarily apparent four sector range stack tracks are caused by overlapping photons or accidentals. Cut any event with more than three total sectors on the charged track.
- **RNGMOM(2):** A muon of a given momentum has a longer range than a pion of the same momentum. The **RNGMOM** routine uses drift chamber momentum and range stack range to calculate a confidence level of an event being a pion (C_π) or a muon (C_μ). Cut if $C_\pi < 0.01$ or $C_\pi < C_\mu$.
- **CHIRF:** If an inconsistent set of information was used for the range calculation, or if a charged track has a very hard scatter, its range stack range measurement is almost arbitrary and its fit χ^2 becomes bad. Require $\chi^2_{\text{rprfit}}/\text{dof} < 20$.
- **ZFRF:** $K^+ \rightarrow \mu^+ \nu_\mu$ muons that pass through the range stack support structure can undergo catastrophic energy loss, and have apparent range and energy in the $K^+ \rightarrow \pi^+ \nu\bar{\nu}$ fiducial region. Cut events with **RPRFIT** stopping z position $> z_{\text{rprfit}}^{\text{max}}$ (Table 3.8). The cuts are shown in Figure 3.5.
- **RSDEDX:** $K^+ \rightarrow \mu^+ \nu_\mu$ muons that undergo a hard scatter in the range stack

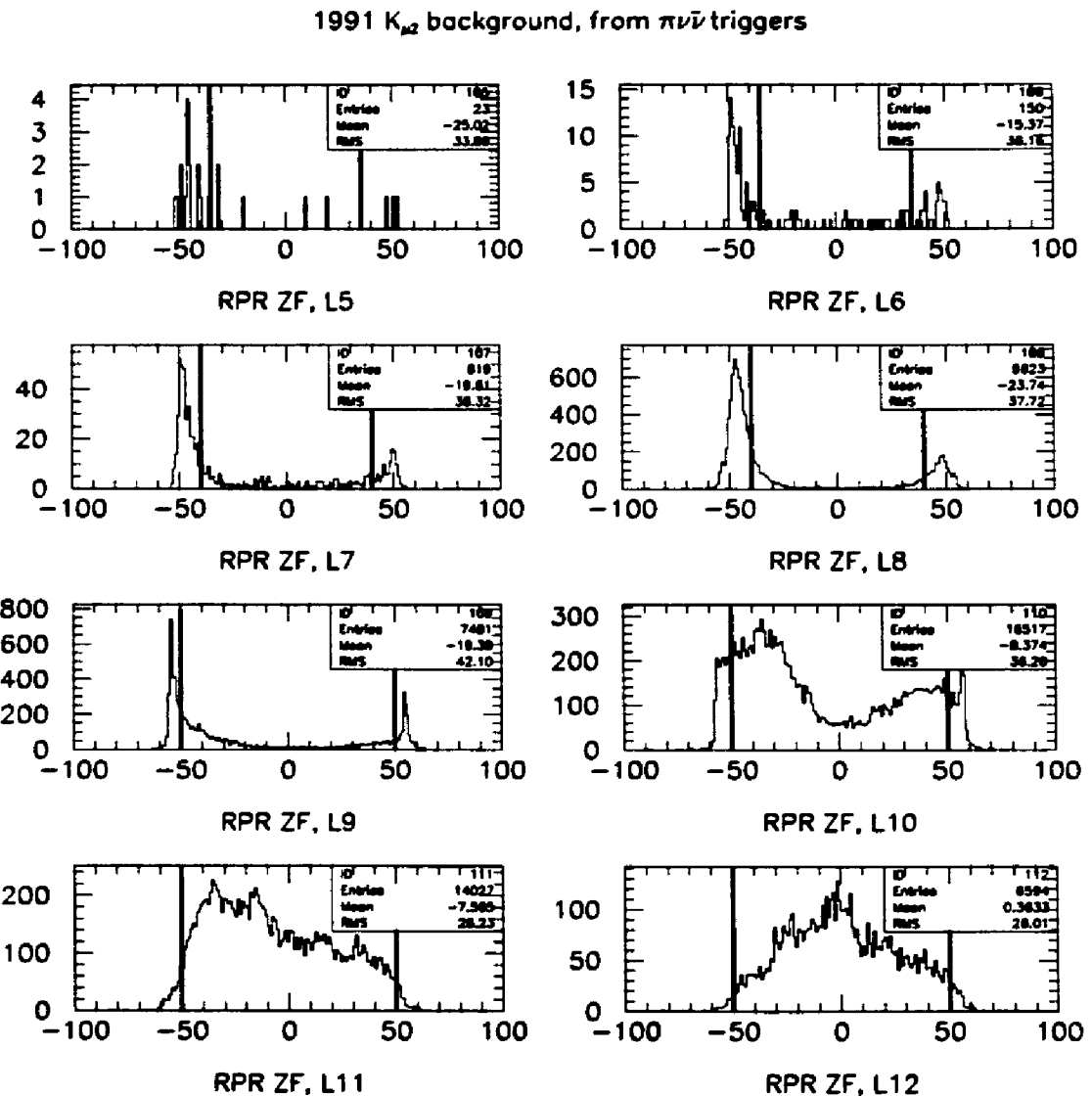


Figure 3.5: The RS stopping z cut, ZFRF. The plots are labeled with effective RS layer, corresponding to physical layers 11-21. Events with high stopping $|z|$ are cut.

| Stopping Layer | z_{rprfit}^{\max} (cm) |
|----------------|------------------------------------|
| 11 | 35 |
| 12 | 35 |
| 13 | 40 |
| 14 | 40 |
| 15 | 50 |
| 16 | 50 |
| 17 | 50 |
| 18 | 50 |

Table 3.8: Maximum allowed RPRFIT stopping position.

scintillator also tend to leave at least one counter with anomalously high energy.

$K^+ \rightarrow \pi^+\pi^0$ photons that convert on top of the charged track will typically leave a number of counters with slightly high energy. Use the energy deposited in each range stack layer, E_i , and the energy expected from RPRFIT, E_i^{rprfit} , to form

$$\chi^2_{\text{RSDEDX}} = \sum_{i=1}^{\text{STLAY}-1} \left(\frac{E_i - E_i^{\text{rprfit}}}{\sigma_i} \right)^2,$$

with σ_i (Table 3.9) measured empirically from residual distributions with π scats.

Require $\chi^2_{\text{RSDEDX}}/(\text{STLAY} - 1) < 2$. This cut is illustrated in Figure 3.6 for $K^+ \rightarrow \mu^+\nu_\mu$ background events. Note that, rather than a particle ID cut, it really targets non-gaussian depositions of extra energy.

- LAY14: $K^+ \rightarrow \mu^+\nu_\mu$ muons can stop in the outer range stack chambers, or even use the gap in the scintillator left for the chambers to escape into the range stack

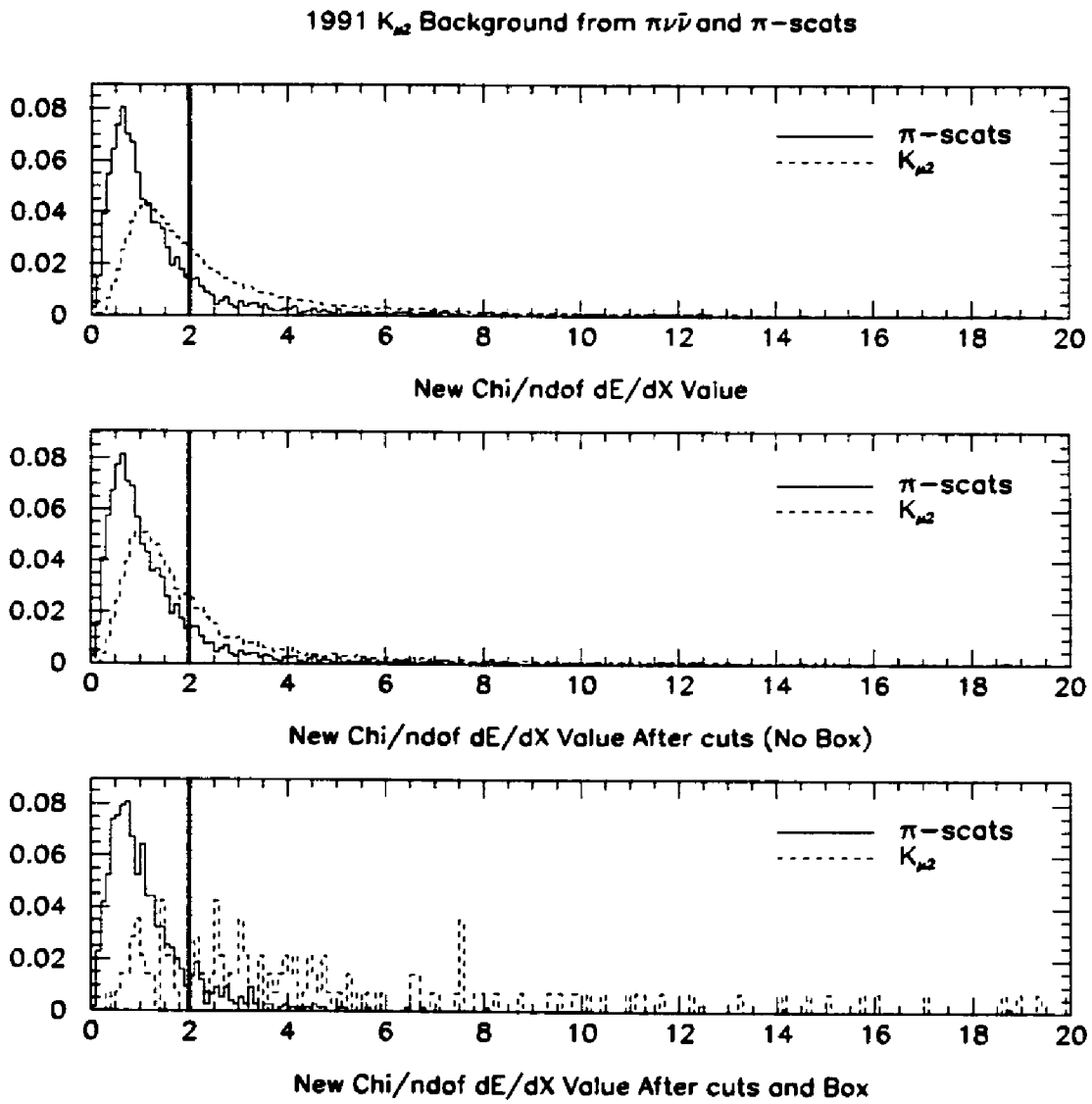


Figure 3.6: Range stack $dE/dX \chi^2$ per degree of freedom. Pions from the π scat trigger are solid lines, and $K^+ \rightarrow \mu^+ \nu_\mu$ background events from the background study in Section 3.4.2 are dashed. The distributions are normalized to unit area, and there are numerous overflows in the $K^+ \rightarrow \mu^+ \nu_\mu$ sample. The top plot is all events passing the $K^+ \rightarrow \mu^+ \nu_\mu$ background “setup” (see the $K^+ \rightarrow \mu^+ \nu_\mu$ background study, Section 3.4.2), the centre is events passing everything except the box, and the bottom is for events in the box.

| Layer i | σ_i (MeV) |
|-----------|---------------------|
| T | 0.5357 |
| A | 2.071 |
| B | 1.830 |
| C | 1.624 |
| 11 | 1.161 |
| 12 | 1.143 |
| 13 | 1.163 |
| 14 | 1.189 |
| 15 | 1.304 |
| 16 | 1.730 |
| 17 | 1.978 |

Table 3.9: RSDEDX σ 's used in χ^2_{RSDEDX} calculation.

support structure. Many of these events appear to stop in range stack layer 14, but also have a hit in the outer RSPC layer (between layers 14 and 15). We cut any event that appears to stop in layer 14 with a hit in the outer RSPC in the stopping sector, or in the sector immediately clockwise of the stopping sector.

- PNNSTOP: A good range measurements requires that the charged track have at least one range stack chamber hit, so it must penetrate beyond layer 10. Since $K^+ \rightarrow \pi^+ \nu \bar{\nu}$ and $K^+ \rightarrow \pi^+ X^0$ almost never make it beyond layer 18, we veto events that hit the outer three range stack layers in the online trigger. Offline, require stopping layer between 11 and 18 inclusive.

3.3.6 Delayed Coincidence and Timing Consistency Checks

The various timing cuts were tuned in the π scat background study described in Section 3.4.1, targeting beam pions that scatter from the target into the range stack.

The delayed coincidence¹ also suppresses kaon decay in flight; since we depend on the monochromatic $K^+ \rightarrow \pi^+\pi^0$ and $K^+ \rightarrow \mu^+\nu_\mu$ charge track energies for much of our rejection, any boost from a moving kaon could put $K^+ \rightarrow \pi^+\pi^0$ and $K^+ \rightarrow \mu^+\nu_\mu$ into the $K^+ \rightarrow \pi^+\nu\bar{\nu}$ fiducial region.

- DELC: The delayed coincidence requirement attempts to force the K^+ to decay at rest, or $t_\pi > t_K$. The cuts employed are: target TIMEPI - TIMEK > 2 nsec; if TIMEPI was I-counter based, TIMEPI - TIMEK > 4 nsec; TRKTIM found TRS > TG TIMEK; TRS > B4 hodoscope TDC-based kaon time; TRS > 0.
- TIMCON: The easiest way to fool DELC is for one or more of the time measurements to be wrong, so a set of timing consistency checks are made. The cuts are: TIMEK > -5 nsec and TIMEK < 3 nsec; the \bar{C}_K -based kaon time must be within 5 nsec of TIMEK; a valid TIMEPI (either target or I-counter based) must be found; $|TIMEPI-TRS| \leq 5$ nsec.

¹Recall section 2.3: a signal from the kaon is *delayed*, and then required to be in *coincidence* with a pion signal, selecting kaon decays at rest. Online, we use \bar{C}_K for the kaon and the I-counter for the pion. Offline, we use the target for the kaon, and either the target or the I-counters for the pion.

3.3.7 TD Particle Identification

Our most powerful muon rejection tool is the requirement of the complete $\pi^+ \rightarrow \mu^+ \rightarrow e^+$ decay sequence in the stopping counter using the transient digitizers (recall Figure 2.4). The $\pi^+ \rightarrow \mu^+$ analysis centres around the FITPI routine from Marlow. Using an empirically determined pulse shape for each range stack counter, FITPI uses MINUIT to fit the information to both a single-pulse and double-pulse hypothesis. A systematic run-by-run and counter-by-counter calibration of the pulse-shapes was performed, fixing serious variations and apparent electronics reflection problems. The error term used in the fit was empirically calibrated for pulse-height, the shape corrected for the TD end-to-end-time-based z position, and a flat background term was added to the fit. Some important FITPI output variables and derivatives are summarized in Table 3.10.

Most of the details of the TD $\pi^+ \rightarrow \mu^+ \rightarrow e^+$ cuts are inherited from previous analyses. The major difference is that, with the improved software and systematic pulse shape calibration used in this analysis, the basic TD rejection is higher and less work is needed afterwards. The TDACC chisquare cut mostly works on the different measurements of the $\pi^+ \rightarrow \mu^+$ z position in the stopping counter, including both pion and muon end-to-end time and pulse height ratios. The discriminant function analysis (DFA) is directly inherited from Turcot [17]. Various versions of one and two dimensional cuts were tried (including the “FITPI2” and “FITPI3” cuts out of

| Variable Name | Definition |
|--------------------|--|
| C_μ^i, C_π^i | Single and double pulse fit quality for end i |
| PROD | Combined fit quality $C_\mu^1/C_\pi^1 \times C_\mu^2/C_\pi^2$ |
| t_π^i | Calibrated pion time from double pulse fit for end i |
| t_μ^i | Time of $\pi^+ \rightarrow \mu^+$ decay (relative to t_π^i) for end i |
| E_π^i | Pion fit energy in TD counts for end i |
| E_μ^i | Muon fit energy in TD counts for end i |
| DTPI | $t_\pi^1 - t_\pi^2$ |
| DTMU | $t_\mu^1 - t_\mu^2$ |
| TMUAV | $(t_\mu^1 + t_\mu^2)/2$ |
| EMUT | $\sqrt{E_\mu^1 \times E_\mu^2}$ |
| EMUMIN | $\min(E_\mu^1, E_\mu^2)$ |
| ZPI | $\log_{10}(E_\pi^1/E_\pi^2)$ |
| ZMU | $\log_{10}(E_\mu^1/E_\mu^2)$ |
| ZMUT | DTPI + DTMU |

Table 3.10: Some FITPI output variables and derivatives.

[16]), but the DFA consistently gives higher acceptance for a given rejection. The major difference is that the software and calibration upgrades greatly reduced the “tail-fluctuation” part of the background, and only one DFA for all pion lifetimes (TMUAV) was found to be useful. The other noteworthy feature here is that the RSHEX cut has been expanded; events with multiple counters hit in the stopping TD channel are impossible to fit reliably, and are simply cut outright.

A slightly modernized version of Akerib’s **ELVETO3** software is used to search the range stack for extra activity at the pion decay time, possibly caused by an early $\mu^+ \rightarrow e^+$ decay or accidentals correlated with a fake $\pi^+ \rightarrow \mu^+$. The **EV5** routine uses the TD’s for the $\mu^+ \rightarrow e^+$ search. **EV5** was slightly modified to accept an external

| i | x_i | \bar{x}_i | | | σ_i | | |
|-----|------------------------------|-------------|----------|-----------|------------|--------|--------|
| | | 1989 | 1990 | 1991 | 1989 | 1990 | 1991 |
| 1 | DTMU (nsec) | 0.04401 | 0.01600 | -0.01144 | 1.136 | 1.098 | 1.144 |
| 2 | EMUT (counts) | 171.1 | 151.1 | 152.4 | 25.61 | 24.13 | 26.43 |
| 3 | z_{dc}^{nsec} -ZMUT (nsec) | 0.2646 | -0.01228 | 0.02386 | 1.909 | 1.187 | 1.248 |
| 4 | ZPI-ZMU | -0.001250 | -0.01404 | -0.006578 | 0.3207 | 0.3362 | 0.3538 |

Table 3.11: Variable central values and sigmas used in the TDACC χ^2 . The quantity z_{dc}^{nsec} is the expected stopping range stack z position based on a DC track extrapolation calibrated in nsec of end-to-end-time.

end-to-end-time-based pion stopping z position, which is used to help its electron search.

- FITPI: The FITPI routine must successfully fit a $\pi^+ \rightarrow \mu^+$ double pulse signature in the TD channels containing the two ends of the offline stopping counter, using its default $\pi^+ \rightarrow \mu^+$ selection criteria.
- TDACC: Real $\pi^+ \rightarrow \mu^+$ decays have a well defined signature that match in energy and time at both ends. The variable

$$\chi^2_{tdacc} = \sum_{i=1}^4 \left(\frac{x_i - \bar{x}_i}{\sigma_i} \right)^2$$

(with x_i defined, \bar{x}_i and σ_i listed in Table 3.11) has a good χ^2 behaviour which shows separation between real pions and accidentals. Converting it into a confidence level, C , for a χ^2 with 4 degrees of freedom, cut events with $C < 0.01$.

| i | x_i | w_i | | |
|-----|--------------------------|----------|----------|----------|
| | | 1989 | 1990 | 1991 |
| 1 | log PROD | 0.63397 | 0.69510 | 0.31969 |
| 2 | EMUT (MeV) | -0.00261 | -0.01739 | -0.00132 |
| 3 | log $C_\mu^1 C_\mu^2$ | 0.77033 | 0.71742 | 0.92792 |
| 4 | ELASTRS (MeV) | -0.06779 | -0.03731 | -0.18844 |
| 5 | $\min(E_\mu^1, E_\mu^2)$ | 0.00795 | 0.02112 | 0.03538 |
| - | F_0 | 4.8891 | 4.0820 | 3.3035 |

Table 3.12: Variables, weights, and pion offsets for DFA. The quantity ELASTRS is the stopping counter energy.

- TDDFA: Further $K^+ \rightarrow \mu^+ \nu_\mu$ rejection is required. Following the pioneering (for E787) work of [17], a discriminant function analysis is used. π scat triggers were used for the pion training sample. $K^+ \rightarrow \mu^+ \nu_\mu$ events surviving all the other TD cuts in the background study were used for the muon training sample.

The “Fisher variable” F is calculated:

$$F = \sum_{i=1}^5 w_i x_i - F_0$$

with weights (w_i), variables (x_i) and offsets (F_0 , used to centre pion distributions at zero) in Table 3.12. The Fisher variable distribution for $K^+ \rightarrow \mu^+ \nu_\mu$ background surviving the rest of the TD analysis and π scats for 1989 data is shown in Figure 3.7. We cut events with $F < -1$.

- ELEC_V5: An easy way for a muon to fake a $\pi^+ \rightarrow \mu^+$ sequence is for the $\mu^+ \rightarrow e^+$ decay to occur early, with the electron leaving about 3 MeV in the stopping counter. This background is suppressed by requiring an apparent

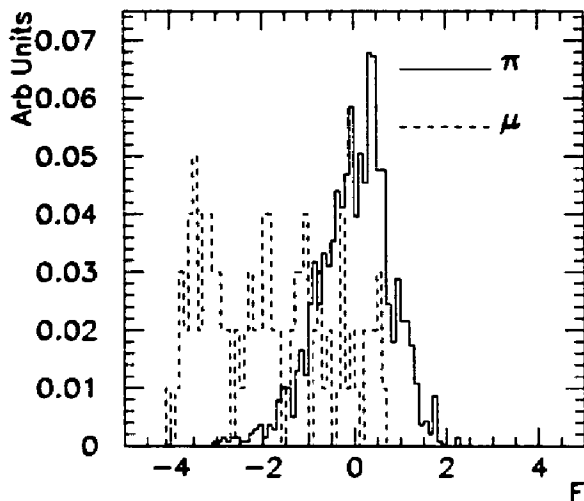


Figure 3.7: The Fisher variable, F , for 1989 $K^+ \rightarrow \mu^+ \nu_\mu$ background events passing the rest of the TD analysis from the $K^+ \rightarrow \mu^+ \nu_\mu$ background study (Section 3.4.2), plotted along with pions from π scats after the same cuts. Cut events with $F < -1$.

$\mu^+ \rightarrow e^+$ decay to occur at a later time in the stopping counter using the EV5 routine. A good electron candidate must have at least two counters hit in a 3 sector by 5 layer region centred by the stopping counter, with at least one hit either in the stopping counter, or the same sector and ± 1 layer.

- ELVETO: If the apparent $\pi^+ \rightarrow \mu^+$ was really an early $\mu^+ \rightarrow e^+$ the electron will almost always deposit energy outside the stopping counter. Additionally, if the $\pi^+ \rightarrow \mu^+$ decay sequence was really caused by an accidental, there is usually other range stack activity associated with that accidental. ELVETO3 searches for hits in the range stack TD's near in time to TMUAV. It classifies hits as being on the charged track (excluding the prompt pulses), near the

charged track (± 1 sector of the stopping counter, all layers), or remote from the charged track (everything else). Cut events with any ELVETO3 found extra hits at TMUAV either on or near the charged track, or more than one extra hit in the entire range stack at TMUAV.

- TDFOOL: If an early electron was missed by ELVETO it may be hiding under the range stack track, but this should be visible as a double pulse signature in charged track struck counters other than the stopping counter. Looping back from the stopping counter along the range stack track, FITPI is run in the two counters preceding the stopping counter having unique TD channels. Certain default FITPI cuts which have been tuned for $\pi^+ \rightarrow \mu^+$ are not applied. Cut if either counter has bad relative single/double pulse fits at both ends ($\chi_1^2/\chi_2^2 > 4$), and average second pulse fit time from the double pulse fit (called TMUAV for the stopping counter fit) within 5 nsec of the real TMUAV.
- RSHEX: The range stack TD's are multiplexed into "hextants" of four sectors per layer. In addition to giving 4 counters for a possible accidental faking the $\pi^+ \rightarrow \mu^+$ to hit instead of one, slight differences in pulse shape and counter-to-counter timing make any pulse shape fit unreliable. Use the ADC's to cut events with more than one hit in the stopping TD channel.
- TMUBV: Accidental faking the $\pi^+ \rightarrow \mu^+$ signature are often correlated with nearby activity in the barrel veto. Search the barrel veto for hits within ± 3 RS

sectors of the stopping sector. Cut the event if there's a hit within 8 nsec of TRS+TMUAV.

- TMUADC: $K^+ \rightarrow \mu^+ \nu_\mu$ events passing the TD cuts preferentially occur at very large TMUAV. Turcot hypothesized that this is caused by $\mu^+ \rightarrow e^+$ decays after the end of the ADC gate, which can fake the $\pi^+ \rightarrow \mu^+$ but not be preferentially removed by the level 1.5 energy trigger. Require that the FITPI average muon time TMUAV < 75 nsec.
- STOP_HEX: Online stopping hextant/layer must agree with offline stopping hextant/layer.

3.3.8 INTIME γ Veto

The offline analysis searches throughout the detector for possible photons from a $K^+ \rightarrow \pi^+ \pi^0$ decay, principally using the INTIME routine from Meyers for the BV, EC, RS, IC and VC subsystems. INTIME first searches each subsystem element for any ADC energy, and classifies the energy as “prompt” if that element has a hit with a time inside a user-specified window. It returns the total prompt energy in each subsystem.

The photon veto cuts were set by inspection of energy and time distributions of $K^+ \rightarrow \pi^+ \pi^0$ events from the $K^+ \rightarrow \pi^+ \nu\bar{\nu}$ data and $K_{\mu 2}(1)$ monitor samples during the $K^+ \rightarrow \pi^+ \pi^0$ background study described in Section 3.4.3. The photon veto

energy thresholds were set by plotting prompt energy using fairly narrow time windows (about ± 1 nsec) around TRS, and extending the cut downwards in energy while $K^+ \rightarrow \pi^+\pi^0$ events from $K^+ \rightarrow \pi^+\nu\bar{\nu}$ data showed a distinct excess over $K_{\mu 2}(1)$ monitors (Figure 3.8). The energy threshold was frozen, and then the time windows were set by plotting the time of the hit nearest TRS with energy above the threshold, again looking for an excess of $K^+ \rightarrow \pi^+\pi^0$ over $K_{\mu 2}(1)$ (Figure 3.9). While I make no promises of optimization,² in the model that our final background of interest is due to isolated low-energy photons, this scheme seems fairly robust.

The survivors of the full Pass 3 γ veto were scrutinized in some detail looking for events passing the analysis with a significant signal in the other INTIME energy categories. In particular, it was hoped that either the barrel veto or range stack would show a significant number of events with large, early pulses indicating that part of our γ inefficiency was due to early accidentals obscuring the prompt pulse leading edges (such losses might have been recoverable using the transient digitizers). No substantial excess was observed. Another INTIME category looks for counters with ADC energies but no associated hit times, which would indicate problems with the TDC's or TD's. No significant excess was observed here either. It has been recently observed that another category of interest is hits with times but no corresponding energy, possibly due to problems in the ADC or its readout. This was investigated by examining data

²Reference [18] attempted a sort of optimized analysis, but it was my experience that the method used there was not entirely successful. That analysis left a hole for small prompt pulses in the endcaps.

| Subsystem | Δt (nsec) | t_{off} (nsec) | E_{thresh} (MeV) |
|-----------|----------------------|----------------------------|------------------------------|
| RS | 3.5 | 1.5 | 0.5 |
| BV | 4.5 | 2.5 | 0.2 |
| EC | 5.0 | 0.0 | 1.0 |
| IC | 3.0 | 0.0 | 1.0 |
| VC | 5.0 | 2.0 | 1.0 |

Table 3.13: INTIME half window, time offset, and prompt energy thresholds.

in the $K^+ \rightarrow \pi^+\pi^0$ peak surviving the full analysis. There is no apparent prompt time signature in the TDC's (BV and EC) or TD's (RS) in counters with no ADC energy, so problems in the ADC's do not apparently contribute significantly to the photon-veto inefficiency.

- GAMVET: The routine INTIME adds up all the energy in a subsystem (RS, BV, EC, IC or VC) with a hit within Δt of $\text{TRS}+t_{\text{off}}$. Events are cut if this “prompt energy” is above the relevant subsystem dependent thresholds E_{thresh} (Table 3.13). Note that the cuts used here completely include the Pass 1 cuts [18].

3.3.9 Kinematics

The final kinematic “box” cuts are made using the rescaled kinematic quantities described in Section 3.2.1. P_{tot} is corrected for energy loss in the target with target range. I started with the cuts used in the 89 analysis [16], but extended the lower edge

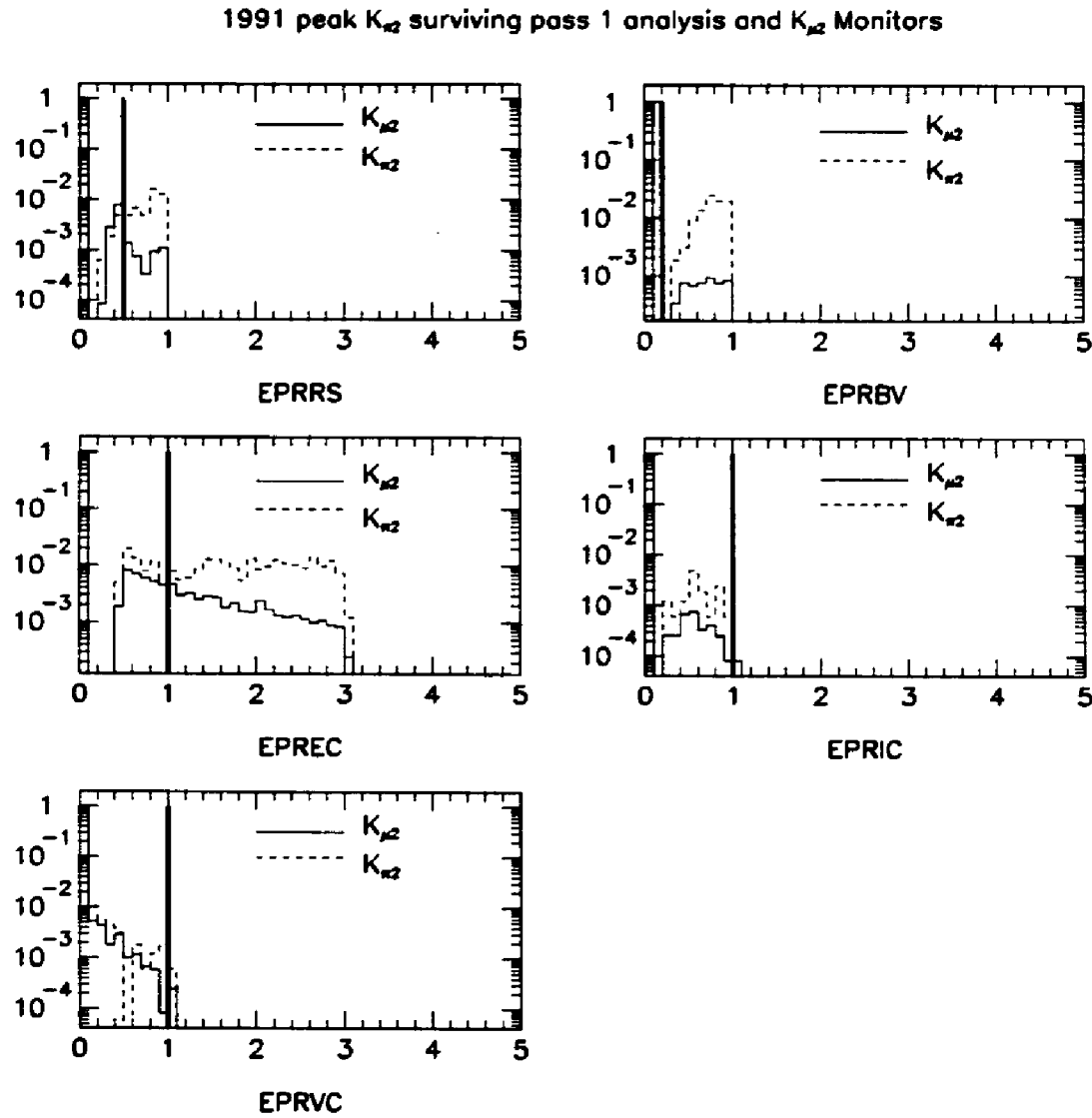


Figure 3.8: The final photon veto, part 1: the energy threshold. After applying the full Pass 1 photon veto, the prompt energy in each sub-system in narrow time windows around TRS is plotted for residual $K^+ \rightarrow \pi^+ \pi^0$ in the $K^+ \rightarrow \pi^+ \nu \bar{\nu}$ data and $K_{\mu 2}(1)$ monitors. The energy threshold is set by inspection of these distributions, shown with solid lines in the plots for the RS, BV, EC, IC, and VC. The energy cuts off on the high side due to photon veto applied at Pass 1.

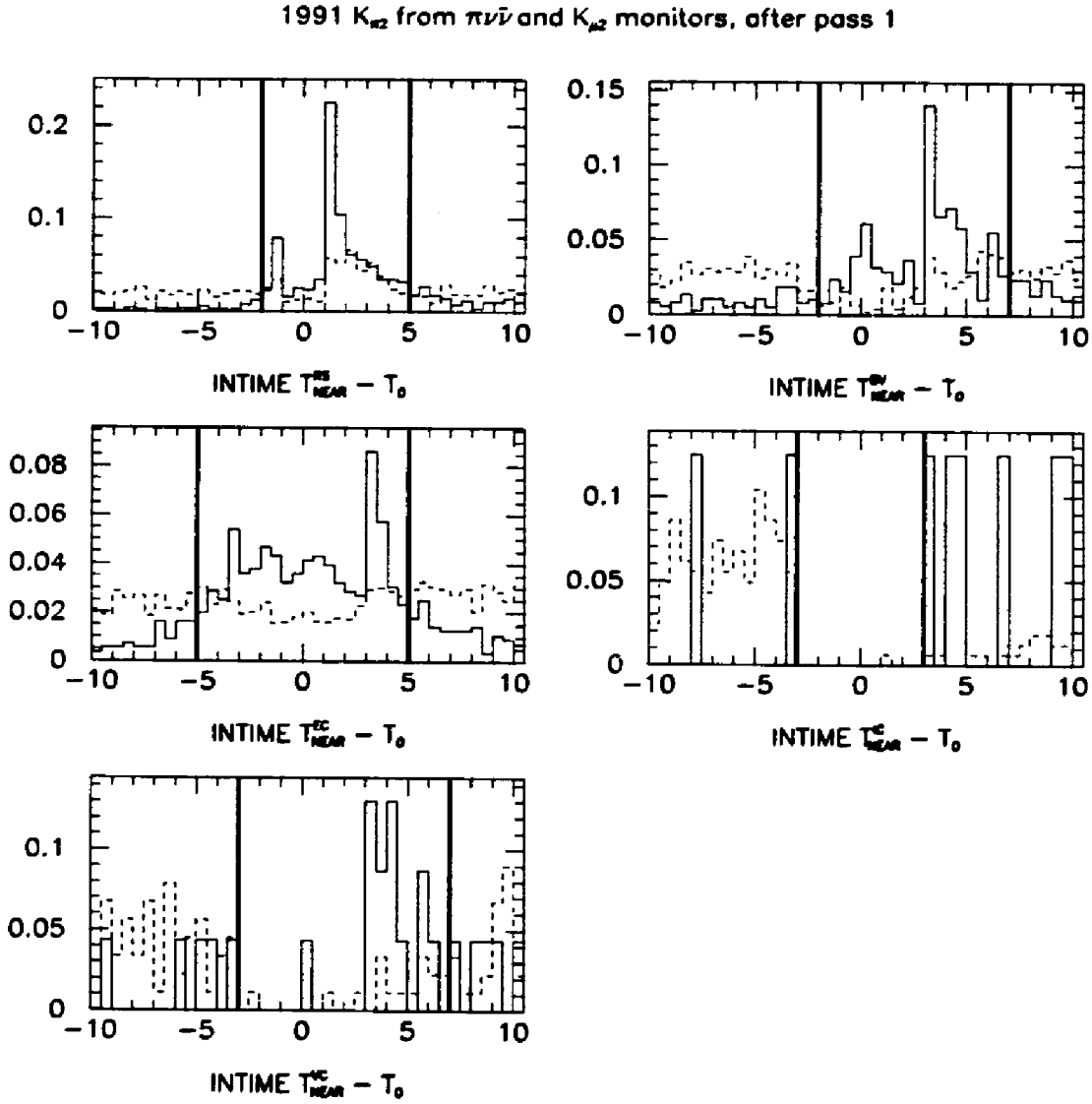


Figure 3.9: The final photon veto, part 2: the INTIME time windows. Using the energy threshold found above, the time of the hit nearest TRS with energy above threshold in each subsystem is plotted, and the time window is set by eye. The distributions are made after the full Pass 1 γ -veto, which makes the “notch” near $t = 0$ corresponding the Pass 1 windows. $K^+ \rightarrow \pi^+\pi^0$ lines are solid, and $K^+ \rightarrow \mu^+\nu_\mu$ lines are dashed.

of the range cut up to 34 cm during the $K^+ \rightarrow \pi^+ \pi^0$ background study (Section 3.4.3), reducing the expected background level from < 0.41 to < 0.14 events at the 90% confidence level.

- PBOX: Require $211 \text{ MeV}/c \leq P_{\text{tot}}^{\text{new}} \leq 243 \text{ MeV}/c$.
- EBOX: Require $115 \text{ MeV} \leq E_{\text{tot}}^{\text{new}} \leq 135 \text{ MeV}$
- RBOX: Require $34 \text{ cm} \leq R_{\text{tot}}^{\text{new}} \leq 40 \text{ cm}$

3.4 Background Studies

If the $K^+ \rightarrow \pi^+ \nu \bar{\nu}$ branching ratio truly appears at the level expected in the Standard Model, at most a handful of events will be observed. This will require a “zero-background” analysis, achieving a factor of a 100 billion in background suppression, leading to the cuts listed in the previous section. Now, suppose the analysis is almost done, but an event or two has survived. It is likely that one of the cuts available could be adjusted slightly, or a new cut invented, to remove the event with a negligible loss of sensitivity, even if that event is a real $K^+ \rightarrow \pi^+ \nu \bar{\nu}$. This argument can lead to the conclusion that one would have *no* sensitivity for seeing a few real events.

This possibility of analysis bias has led to the conclusion that the cuts must be established by making dead-reckoning predictions of the background levels without detailed scrutiny of surviving candidate events. Once the cuts are established, the

analysis is run and any survivors scrutinized in detail. If they do not appear to be $K^+ \rightarrow \pi^+ \nu\bar{\nu}$ because, for example, each sits at the edge of several cuts, an unbiased branching ratio limit must still be calculated assuming they are signal. One can hope that any survivors will, however, appear to be $K^+ \rightarrow \pi^+ \nu\bar{\nu}$ and be called a discovery.

Based on the experience of previous E787 studies, I expected three principal backgrounds to be severe problems in this analysis: π scats, $K^+ \rightarrow \mu^+ \nu_\mu$ and $K^+ \rightarrow \pi^+ \pi^0$. The above cuts were tuned during the studies described here to give an expectation of significantly less than one surviving event for each of these processes. These dead-reckoning background predictions are tricky. In this analysis, the studies attempt to factor the rejections of groups of cuts into independent, uncorrelated sets, and assume the combined rejection of the sets is the product of the separate rejections. In practice, it is essentially impossible to find uncorrelated sets, so some conservatism and common sense will be required. A prototype background study is sketched in Figure 3.10. While the studies are described in complete detail in the following sections, the expected background levels are listed in Table 3.14 for reference.

Previous E787 studies have also considered other background processes; in particular, the “charge exchange” process in which a K^+ enters the target but interacts with a carbon nucleus to form a neutral kaon is worrisome. About 1/2 of these K^0 ’s will decay as a K_S^0 (with a lifetime of 0.089 nsec) and be vetoed by the delayed coincidence cuts. The other 1/2 will decay as a K_L^0 ($\tau = 51.7$ nsec), which we may accept. About

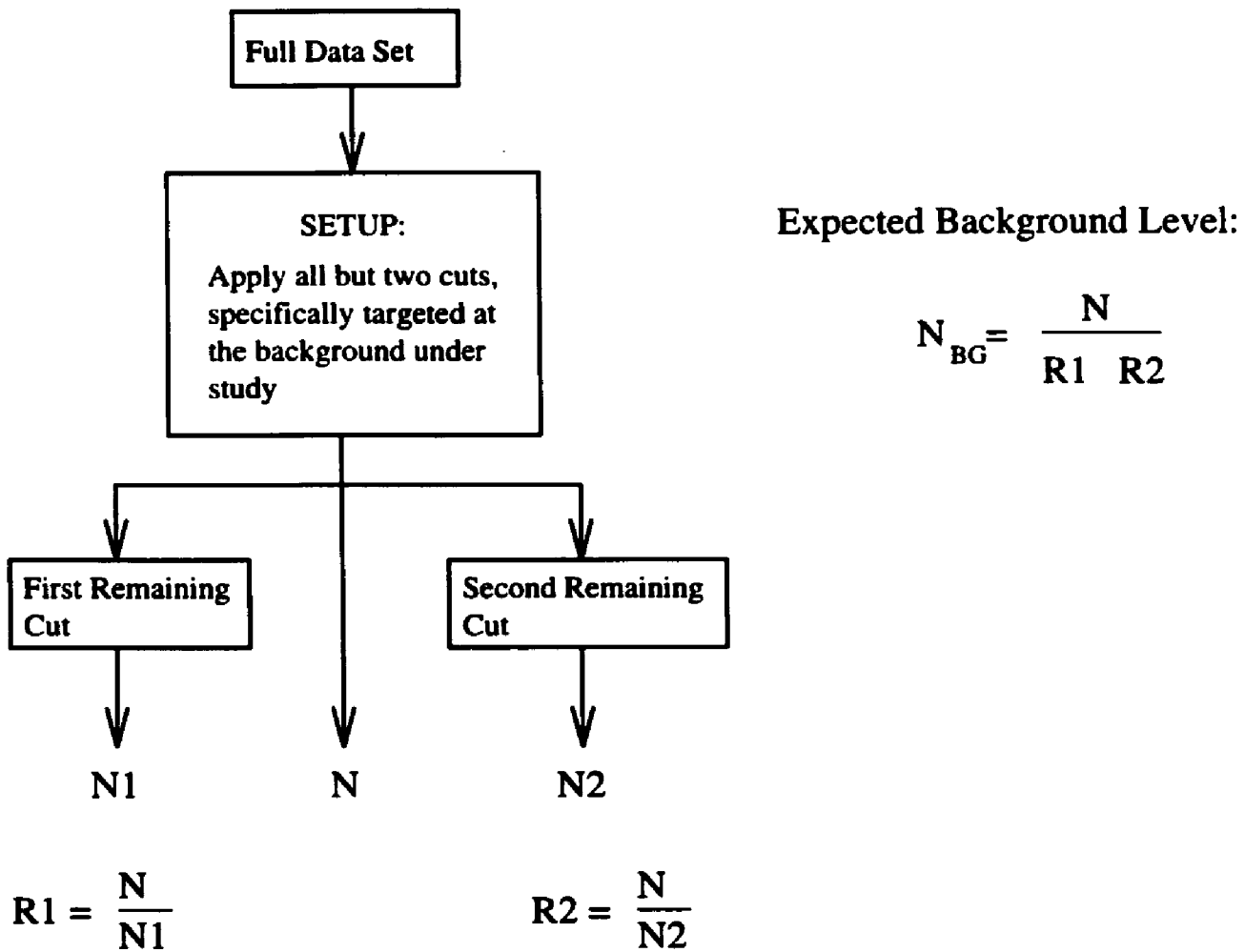


Figure 3.10: A prototype background study. The full $K^+ \rightarrow \pi^+ \nu\bar{\nu}$ data set is analyzed with all but two selected cuts. These cuts should have high rejections for the background under study, and be uncorrelated. Using this technique of factoring the rejections of multiple cuts allows estimates of less than one expected event to be inferred from the study.

| Background | Number of Survivors Expected |
|---------------------------------|---------------------------------|
| Two-beam-particle π scat | < 0.04 events, 90% CL |
| One-beam-particle π scat | < 0.03 events, 90% CL |
| $K^+ \rightarrow \mu^+ \nu_\mu$ | 0.12 ± 0.02 events. |
| $K^+ \rightarrow \pi^+ \pi^0$ | < 0.14 events, 90% CL |

Table 3.14: Summary of the background study results arrived at in the following sections. The π scat background is split into two parts: the “two-beam-particle” background is defined to have a second beam particle in coincidence with the range stack time TRS, while the “one-beam-particle” background does not.

1/3 of the K_L^0 decays will be via the semileptonic $K_L^0 \rightarrow \pi^+ \mu^- \bar{\nu}_\mu$ or $K_L^0 \rightarrow \pi^+ e^- \bar{\nu}_e$ modes, with π^+ endpoints inside our fiducial region (216 and 229 MeV/c respectively). If we miss the lepton, our only defence is that the K_L^0 must travel for about 2 nsec before it decays, and thus its decay products will be separated from the target K^+ cluster which may cause the event to be vetoed. Obviously, the slower the K_L^0 is moving the smaller this separation will be, so our background level is critically dependent on the (poorly known) low energy charge exchange cross-section.

A number of studies were conducted in the past, mostly by Kitching and Marlow (with Wright and Jeffrey). Their conclusion was that this background is likely not a severe problem at current sensitivity levels *unless* our understanding of the low energy charge exchange cross-section is in error. Recent studies have not made any attempt to address this fundamental problem with the old estimates. They were not repeated here because I had no desire to perform the same calculation, with

its potentially very large and completely correlated theoretical error, again. While reviewing this analysis, however, Bryman and Konaka correctly pointed out that the previous analysis of this data [18] had at least one cut with potential rejection for the charge exchange background. Part of their target “principal components analysis” (TGPCA) includes a consistency check on the target kaon energy and drift chamber extrapolated kaon stopping z position. The TGPCA cut had been considered during the studies of the π scat and $K^+ \rightarrow \pi^+\pi^0$ backgrounds, but it was not found to have any rejection and was not used; however, to avoid the possibility of having this background sneak back in, the EKZ cut described in Section 3.3.4 was added before performing the final Pass 3 analysis. This cut targets events with low kaon cluster energy but an apparently large kaon stopping z position, which is the particularly worrisome regime for the charge exchange background. After completing the final analysis, it was re-run without the EKZ cut; no events survived the full analysis without this cut either.

3.4.1 π scats

If a beam pion enters the target, it can scatter into the range stack and be mistaken for a π^+ from a $K^+ \rightarrow \pi^+\nu\bar{\nu}$ decay. Various cuts have rejection for such events, especially the beam and target analyses. The “setup” stage of the π scat study consists of all

| Cut |
|-----------|
| PICER |
| PISCAT.BW |
| PBGLASS |
| B4DEDX |
| B4TDEDX |
| DELC |
| TGDCXY |
| TGDCVT |
| RTDIF |
| TARGF |
| NTRIK |
| ZTGT |
| EPIMAX |
| TGDEDX |
| EIC |

Table 3.15: Cuts removed from analysis for π scat study setup. The PBGLASS cut was used only in 1991, while B4TDEDX was used only for 1989 and 1990.

cuts except those list in Table 3.15, resulting in 2819, 4591 and 10067³ events in 1989, 1990 and 1991 respectively.

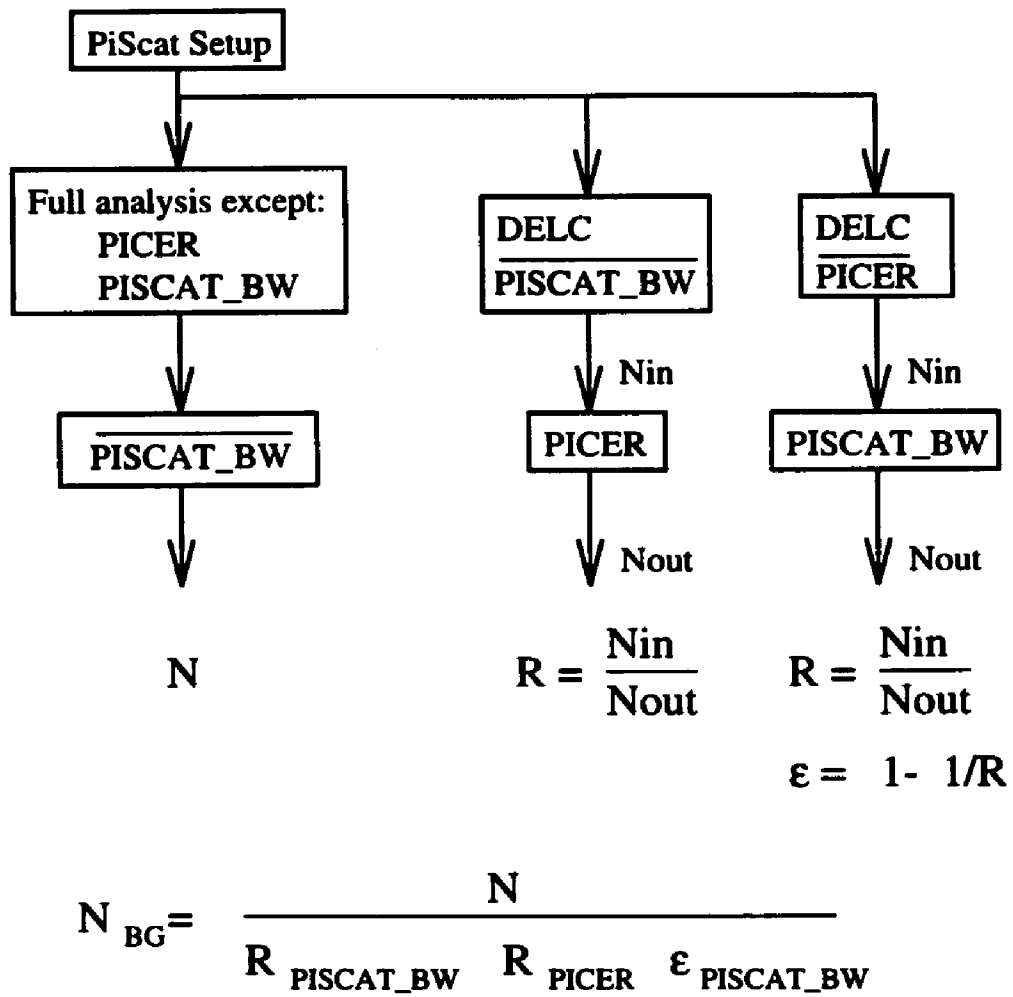
The π scat study setup leaves a sample with significant contamination from other processes; in particular, a substantial portion of our $K^+ \rightarrow \pi^+\pi^0$ rejection is obtained with the veto on overlapping photons built into the target analysis. Because of this problem, a selection step is added to the π scat study. The selection involves “inverting” an analysis cut with large π scat rejection, by selecting the events which it would fail. This sample is used to evaluate the rejection of the remaining cuts,

³The π scat “setup” in 1991 mistakenly also removed the PISCAT.B4 and TIMCON cuts, both of which have rejections correlated with the PISCAT.BW cut. While this resulted in more events, the PISCAT.BW rejection inferred for 1991 is likely too good.

while the rejection (and background sample selection efficiency) of the primary cut is separately measured.

Two types of π scats are considered at this point, called “two-beam-particle” and “one-beam-particle” π scats. In the first, a beam kaon enters the detector satisfying the online and offline \check{C}_K requirement, but is lost downstream of the Čerenkov counter. This kaon may have entered the target, forming a kaon cluster. A beam pion follows the kaon, scattering in the target, mimicking a $K^+ \rightarrow \pi^+$ decay. The two best cuts available against this “ $K - \pi$ ” background are PICER (which should find the beam pion) and PISCAT_BW (which should find the any second beam particle). A variant on this background is when a second beam kaon enters the detector and decays or interacts producing a pion downstream of the Čerenkov counter; our best defence against this “ $K - K$ ” background is the PISCAT_BW cut. By measuring the pion Čerenkov efficiency for all events that have two beam wire chamber tracks, both the $K - \pi$ and $K - K$ backgrounds are naturally included in this one measurement.

The two-beam-particle study is outlined in Figure 3.11. The study assumes that the beam wire chamber and pion Čerenkov rejections can be factored from the analysis and measured separately. Two-beam-particle events are selected by inverting the PISCAT_BW cut, requiring that a second beam particle enter the detector near TRS. The full remaining analysis, except for the PISCAT_BW and PICER cuts, is applied to this sample, and the number of survivors is counted. The PISCAT_BW cut rejection

Figure 3.11: Two-beam-particle π scat study.

(and background selection efficiency of the inverted cut) is measured with a sample from the π scat setup data by inverting the PICER cut, requiring a beam pion near TRS. The PICER rejection is measured for events in the π scat setup sample passing the inverted PISCAT-BW cut. The various rejection estimates and sample selection are summarized in Table 3.16.

A combined 3 year two-beam-particle estimate can be inferred from the table.

| Cut | 1989 | | | 1990 | | | 1991 | | |
|---------------|-----------------|------------------|---------|-----------------|------------------|---------|-----------------|------------------|------------|
| | N _{in} | N _{out} | R | N _{in} | N _{out} | R | N _{in} | N _{out} | R |
| PICER | 145 | 2 | 72 ± 50 | 58 | 2 | 29 ± 20 | 3462 | 190 | 18.2 ± 1.3 |
| PISCAT_BW | 145 | 12 | 12 ± 3 | 60 | 5 | 12 ± 5 | 3236 | 98 | 33 ± 3 |
| Selection (N) | 1 | | | 1 | | | 2 | | |

Table 3.16: Sample selection and rejection estimates for the two-beam-particle background study. In 1991, the several cuts were inadvertently not used in “setup” stage of the PICER and PISCAT_BW rejection measurements, resulting in increased statistics but possibly with a sample not representative of the background. “Selection” refers to the inverted PISCAT_BW cut described in the text, resulting in N survivors in the figure.

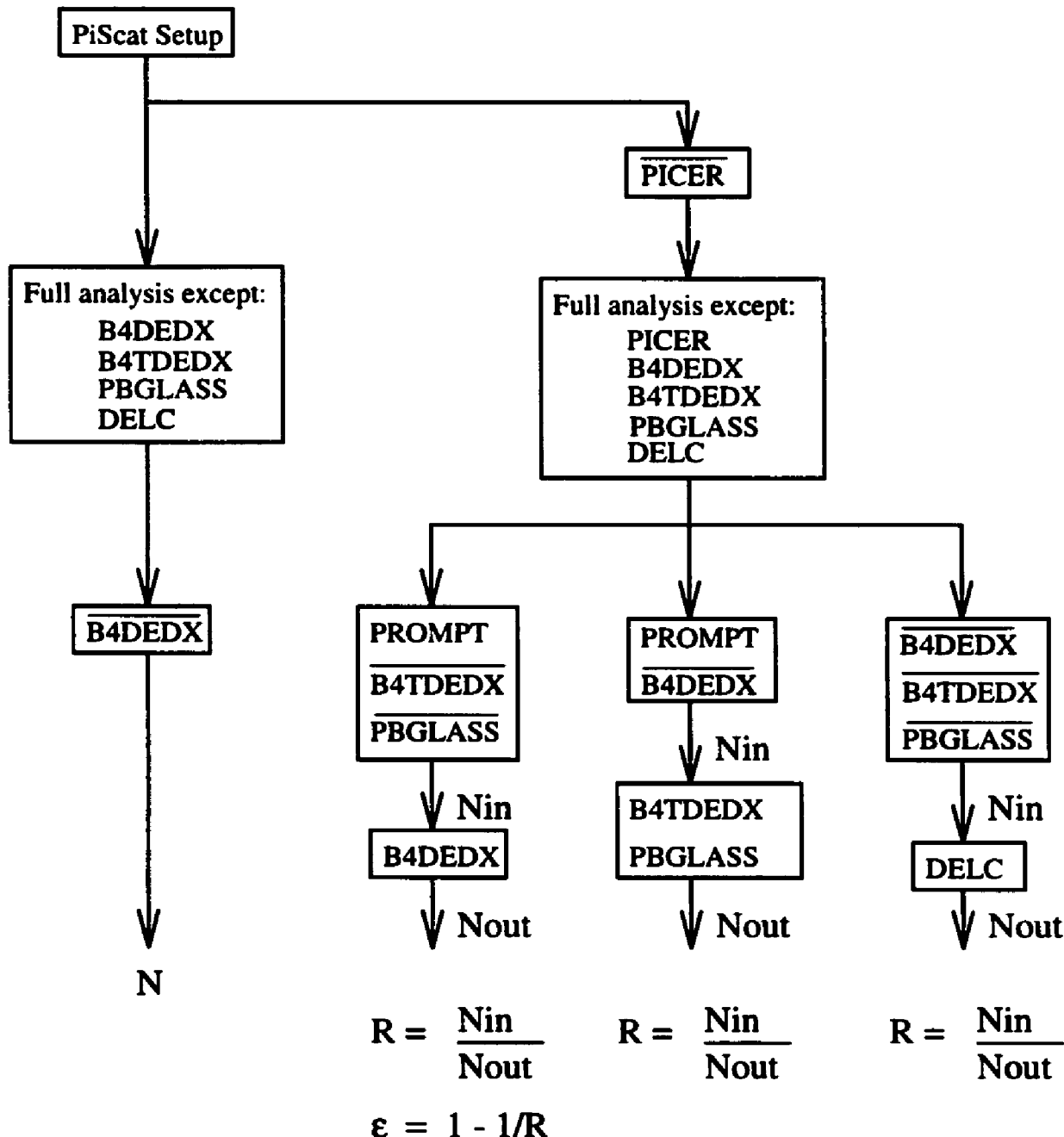
Summed over all years, 4 events survive the inverted PISCAT_BW selection. The PICER rejection is barely consistent over all three years – for a conservative estimate, I picked the smallest value, $R_{\text{PICER}} = 18$. I believe an error in the 1991 study may have made the PISCAT_BW rejection artificially good, so I used the common value of $R_{\text{PISCAT_BW}} = 12$ from 1989 and 1990, corresponding to a selection efficiency for the inverted cut of $\epsilon = 1 - 1/R = 0.92$. Now, using the standard poisson statistics technique for setting confidence limits, 7.99 expected events has a 10% chance of fluctuating down to 4 or less events in a given experiment. So, a conservative upper bound on the two-beam-particle π scat background for 1989-1991 is

$$N_{\text{BG}}^{2-\text{beam}} < \frac{7.99}{\epsilon_{\text{sel}} R_{\text{PICER}} R_{\text{PISCAT_BW}}} = \frac{7.99}{(0.92)(18)(12)} = 0.04 \text{ events, 90\%CL.}$$

The other type of π scat background considered here is when a *single* beam kaon interacts or decays downstream of the Čerenkov leaving a single π^+ to scatter in the

target, satisfying both the kaon and pion requirements in the target. Our best defence against this background is the DELC cut (which forces the kaon to stop for around 2 nsec before we accept the event), along with the B4DEDX, B4TDEDX (in 1989 and 1990) and PBGLASS (in 1991) cuts, which all veto isolated pions entering the target.

The one-beam-particle study is outlined in Figure 3.12. The study assumes that the rejections of the beam counters that tag isolated pions entering the target can be factored, along with the delayed-coincidence (kaon stopping) requirement. First, events with a single beam pion entering the target are selected by inverting the B4DEDX cut. The full remaining analysis except for the B4DEDX, B4TDEDX, PBGLASS, and DELC cuts is applied, and the number of survivors counted. The rejection of these cuts is measured by returning to the π scat setup data, and selecting a sample with a beam pion using the inverted PICER cut. The B4DEDX cut rejection (and selection efficiency of the inverted cut) is measured by taking this sample, requiring the target pion time be within 2 nsec of the target kaon time (called “PROMPT” in the figure), and inverting either the B4TDEDX cut (in 1989 and 1990) or the PBGLASS cut (1991). The B4TDEDX (or PBGLASS) and DELC cut rejections were similarly measured. The various rejection estimates and sample selection are summarized in Table 3.17.



$$N_{BG} = \frac{N}{\epsilon_{B4DEDX} R_{B4DEDX} R_{B4TDEDX} R_{PBGLASS} R_{DELC}}$$

Figure 3.12: One-beam-particle π scat study. PROMPT requires that the target TIMEPI be within 2 nsec of TIMEK.

| Cut | 1989 | | | 1990 | | | 1991 | | |
|-----------------|-----------------|------------------|---------|-----------------|------------------|---------|-----------------|------------------|-----------|
| | N _{in} | N _{out} | R | N _{in} | N _{out} | R | N _{in} | N _{out} | R |
| B4DEDX | 29 | 3 | 9.7 ± 5 | 40 | 6 | 6.7 ± 2 | 103 | 14 | 7.4 ± 2 |
| B4TDEDX/PBGLASS | 44 | 15 | 3 ± 1 | 41 | 6 | 7 ± 3 | 117 | 5 | 3.4 ± 1.5 |
| DELC | 160 | 0 | > 70 | 202 | 0 | > 88 | 31 | 1 | > 8 |
| Selection (N) | 11 | | | 15 | | | 20 | | |

Table 3.17: Sample selection and rejection estimates for the one-beam-particle background study. “Selection” refers to the inverted B4DEDX cut, resulting in N survivors in the figure.

A combined 1989-1991 estimate of the one-beam-particle background can be inferred from the table. A total of 46 events survive the inverted B4DEDX cut selection. The B4DEDX cut rejection was consistent for the 3 years and the variance-weighted average is $R_{\text{B4DEDX}} = 7.2$, corresponding to a selection efficiency for the inverted cut of 86%. The B4TDEDX/PBGLASS cut rejections are similar in all 3 years; I used the lowest number, $R_{\text{B4T/PBG}} = 3$. The DELC rejection is harder to measure, since only 1 selected event passed the cut. Using poisson statistics, I set a 90% lower limit on the rejection: $R_{\text{DELC}} > 393/3.89 = 101$. So, an upper bound on the one-beam-particle background for 1989-1991 is

$$N_{\text{BG}}^{\text{1-beam}} = \frac{N}{\epsilon_{\text{sel}} R_{\text{B4DEDX}} R_{\text{B4T/PBG}} R_{\text{DELC}}} < \frac{46}{(0.86)(7.2)(3)(101)} = 0.03 \text{ events, 90\% CL.}$$

3.4.2 $K^+ \rightarrow \mu^+ \nu_\mu$

A muon from the favoured $K^+ \rightarrow \mu^+ \nu_\mu$ decay should appear at higher energy and range than any pion from $K^+ \rightarrow \pi^+ \nu\bar{\nu}$ and fail the box cut. In addition, a muon of a given momentum should have longer range than a pion with that momentum, and be cut by the RNGMOM cut. There are several ways a muon can appear in the box. If the muon undergoes a hard scatter down-shifting its energy in the target, its range, energy, and momentum could all be in the box; however, it should still appear to be a μ^+ to RNGMOM and be cut. If it undergoes a hard scatter in the range stack, its total momentum should appear at relatively high $P_{\text{tot}}^{\text{new}}$; unfortunately, our resolution compared to the momentum separation of the $K^+ \rightarrow \mu^+ \nu_\mu$ peak from $K^+ \rightarrow \pi^+ X^0$ makes this cut only marginally useful.⁴ The muon might have come from the related $K^+ \rightarrow \mu^+ \nu_\mu \gamma$ decay and started out with lower momentum. In that case, we have some rejection with the photon veto, and RNGMOM should still be effective.

Even if they manage to pass the kinematic cuts, muons should still not exhibit the $\pi^+ \rightarrow \mu^+$ decay sequence in the transient digitizers, although there are several ways a muon can fake the $\pi^+ \rightarrow \mu^+$ decay.

- A large muon stopping pulse can have a “tail fluctuation” on its trailing edge, which can appear much like a stopping pion with a $\pi^+ \rightarrow \mu^+$ decay. These fluctuation fakes usually appear smaller than a real $\pi^+ \rightarrow \mu^+$ pulse, and at

⁴The $K^+ \rightarrow \mu^+ \nu_\mu$ peak sits at 236 MeV/c, while the upper PBOX cut used in this analysis is 243 MeV/c, or about 1σ above the peak.

early apparent pion lifetimes; this background has become rather small with the FITPI upgrades used in this analysis.

- A random “accidental” pulse in the stopping counter within a few pion lifetimes of the stopping pulse can also look exactly like a $\pi^+ \rightarrow \mu^+$ pulse. Most of the accidentals appear at energies lower than the 4 MeV associated with the $\pi^+ \rightarrow \mu^+$ decay, and they will not in general appear at the same z position in the counter (measured with end-to-end time); these are targeted by the TDACC cut.
- The muons also decay into electrons via the three-body $\mu^+ \rightarrow e^+$ decay and the e^+ can leave the same 4 MeV in the stopping counter as the $\pi^+ \rightarrow \mu^+$ muon, providing another mechanism for a $K^+ \rightarrow \mu^+ \nu_\mu$ to get by the TD cuts. While a real $\pi^+ \rightarrow \mu^+$ muon deposits energy outside the stopping counter only rarely, the $\mu^+ \rightarrow e^+$ electron does so almost always so we veto on any such energy with ELVETO. Also, if the muon faked the $\pi^+ \rightarrow \mu^+$ with a $\mu^+ \rightarrow e^+$ decay, it will not undergo the normal $\mu^+ \rightarrow e^+$ decay expected later. Requiring the $\mu^+ \rightarrow e^+$ decay with the ELEC_V5 cut provides additional muon rejection.

The $K^+ \rightarrow \mu^+ \nu_\mu$ background study is outlined in Figure 3.13. The setup stage comprised the full analysis except the cuts listed in Table 3.18. Essentially, it is assumed that the kinematic and TD rejections are uncorrelated, so they are factored into two separate measurements. The full analysis except for the TD cuts is applied

| Kinematic Cuts | TD Cuts |
|----------------|---------|
| DIPANG | FITPI |
| ZDCOW | TDACC |
| RNGMOM2 | TDDFA |
| CHIRF | ELEC_V5 |
| ZFRF | ELVETO |
| RSDEDX | TDFOOL |
| LAY14 | RSHEX |
| RBOX | TMUBV |
| EBOX | TMUADC |
| PBOX | - |

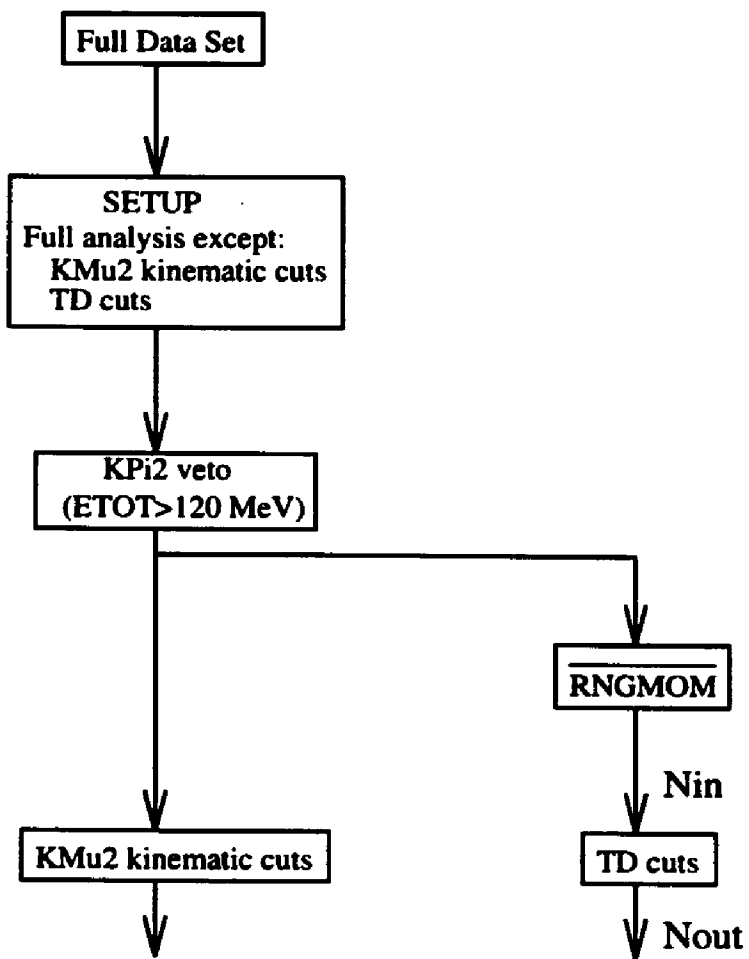
Table 3.18: $K^+ \rightarrow \mu^+ \nu_\mu$ kinematic and TD cuts removed from setup.

to all the data, and the number of surviving events is counted. The TD rejection is measured for events surviving the $K^+ \rightarrow \mu^+ \nu_\mu$ setup. We divide the number of kinematic survivors by the TD rejection to arrive at the background estimate.

The numerical results from the $K^+ \rightarrow \mu^+ \nu_\mu$ background study for all three years are presented in Table 3.19. The resulting estimate for the number of $K^+ \rightarrow \mu^+ \nu_\mu$ background events expected for all 3 years is

$$N_{\text{BG}}^{K^+ \rightarrow \mu^+ \nu_\mu} = 0.12 \pm 0.02 \text{ events.}$$

This study was performed before the $K^+ \rightarrow \pi^+ \pi^0$ study, and before much of the final target and photon veto analysis was optimized, and before a final set of upgrades to the drift chamber and RSPC code and calibrations was performed. If part of the cut inefficiency was due to these problems, this estimate could be overly pessimistic; however, there has also been some suggestion that the TD rejection for muons *inside*

 N

$$R = \frac{N_{in}}{N_{out}}$$

$$N_{BG} = \frac{N}{R}$$

Figure 3.13: $K^+ \rightarrow \mu^+ \nu_\mu$ background study outline. The inverted RNGMOM cut was not applied to 1990 data, because a version of RNGMOM was applied at Pass 1.

| TD rejection | | | | | | | | | | | | | | | | | |
|---|------------------|--------------------|-----------------|------------------|-------------------|-----------------|------------------|----------------|--|--|--|--|--|--|--|--|--|
| 1989 | | | 1990 | | | 1991 | | | | | | | | | | | |
| N _{in} | N _{out} | R | N _{in} | N _{out} | R | N _{in} | N _{out} | R | | | | | | | | | |
| 5273 | 24 | 220 ± 45 | 56601 | 42 | 1348 ± 208 | 55392 | 41 | 1351 ± 210 | | | | | | | | | |
| Kinematic Survivors | | | | | | | | | | | | | | | | | |
| 10 | | 62 | | | 35 | | | | | | | | | | | | |
| Year-by-year background estimates | | | | | | | | | | | | | | | | | |
| 0.0455 ± 0.014 | | 0.0458 ± 0.006 | | | 0.026 ± 0.004 | | | | | | | | | | | | |
| Total $K^+ \rightarrow \mu^+ \nu_\mu$ background estimate | | | | | | | | | | | | | | | | | |
| 0.12 ± 0.02 | | | | | | | | | | | | | | | | | |

Table 3.19: Numerical results of the $K^+ \rightarrow \mu^+ \nu_\mu$ background studies. A local version of the ELVETO cut (Section 3.3.7) was applied in the 1989 Pass 1, reducing both the number surviving the kinematic selection and TD rejection.

the range, energy, and momentum box is worse by about a factor of 4 than for events “above-the-box.”⁵ Since the TD rejection is essentially measured with events above-the-box, such a direct correlation between the kinematic and TD cuts would ruin the study completely. Of the 83 events that passed the TD cuts in the 1990 and 1991 TD rejection measurement, 5 appeared to be $K^+ \rightarrow \mu^+ \nu_\mu$ events in the box. The sample had started with 2032 events in the box, so the TD rejection inferred is indeed 3.3 ± 1 worse than the dominant above-the-box sample.

It is possible that a correlation exists causing a reduced TD rejection for box events; however, selecting the sample in the box without using the rest of the kinematic cuts yields pathological events which are specifically targeted by the rest of the that analysis (LAY14, ZFRF, RSDEDX, CHIRF, etc). In my judgement, it is more

⁵Akira Konaka, personal communication.

| Year | # Survivors $R_{\text{tot}}^{\text{new}} > 40 \text{ cm}$, No TD | TD Rejection | # Predicted $R_{\text{tot}}^{\text{new}} > 40 \text{ cm}$ | # Observed $R_{\text{tot}}^{\text{new}} > 40 \text{ cm}$ |
|-------|--|-----------------|--|---|
| 1989 | 66 | 220 ± 45 | 0.30 ± 0.06 | 0 |
| 1990 | 571 | 1348 ± 208 | 0.42 ± 0.07 | 1 |
| 1991 | 234 | 1351 ± 210 | 0.17 ± 0.03 | 1 |
| total | - | - | 0.89 ± 0.09 | 2 |

Table 3.20: Cross check of the $K^+ \rightarrow \mu^+ \nu_\mu$ study, by predicting the number of surviving events after inverting the RBOX cut.

likely that selecting the events that predominantly fail the rest of the range stack analysis lowers the apparent TD rejection, rather than a direct correlation with the box itself. There are insufficient statistics in this sample to explore further correlations, and this study continues to assume that the TD and kinematic rejections are uncorrelated.

As a cross-check of the $K^+ \rightarrow \mu^+ \nu_\mu$ background estimate, we define a control sample of events passing the complete analysis except RBOX, requiring $R_{\text{tot}}^{\text{new}} > 40 \text{ cm}$. This does not completely address a possible kinematic-TD correlation since these events are by definition not “in-the-box,” but at least they do pass every other kinematic cut including EBOX. This control study is summarized in Table 3.20, and the agreement between predicted and observed events is good. Summed over all 3 years, a background of 0.89 ± 0.09 events is predicted and two events are observed.

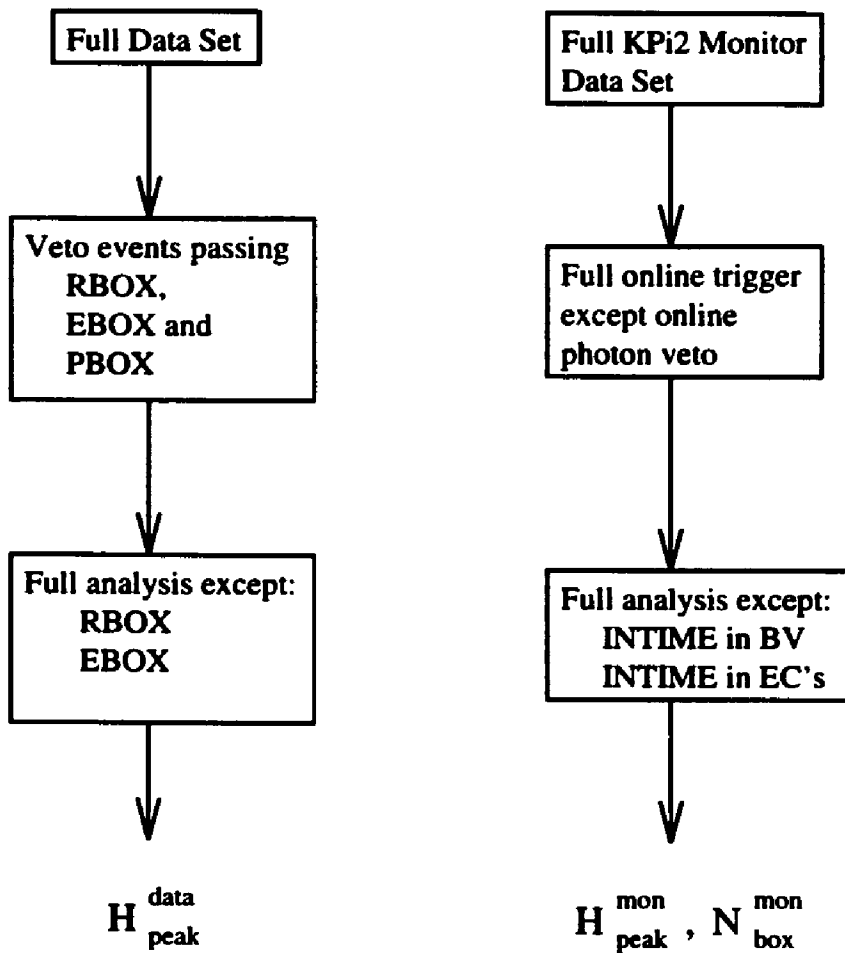
3.4.3 $K^+ \rightarrow \pi^+\pi^0$

If the kaon decays to $\pi^+\pi^0$, the pion should appear below the $K^+ \rightarrow \pi^+\nu\bar{\nu}$ box cut in range, energy, and momentum. The event should also be vetoed by finding one or both photons from the $\pi^0 \rightarrow \gamma\gamma$ decay. The $K^+ \rightarrow \pi^+\pi^0$ background study assumes that the kinematic rejection and photon veto is independent, and proceeds as outlined in Figure 3.14. After removing any events in the box, the full analysis except for the RBOX and EBOX cuts is applied to the data (the PBOX cut is applied), and the “size” of the $K^+ \rightarrow \pi^+\pi^0$ peak is measured. The size of the peak is measured by fitting a gaussian curve to the range, $R_{\text{tot}}^{\text{new}}$, of the entire sample, and the fitted peak height is called the “peak height.” Using the separate $K^+ \rightarrow \pi^+\pi^0$ monitor trigger data⁶ the full analysis except the BV and EC photon veto, RBOX and EBOX is applied (the PBOX is applied), and the ratio of the number of events in the box to the $K^+ \rightarrow \pi^+\pi^0$ peak height is measured. This ratio is multiplied by the $K^+ \rightarrow \pi^+\pi^0$ peak height after the full $K^+ \rightarrow \pi^+\nu\bar{\nu}$ analysis to give the $K^+ \rightarrow \pi^+\pi^0$ background estimate.

The numerical results of the $K^+ \rightarrow \pi^+\pi^0$ study are summarized in Table 3.21. Summed over 1989-1991, the expected level of $K^+ \rightarrow \pi^+\pi^0$ background is:

$$N_{\text{BG}}^{K^+ \rightarrow \pi^+\pi^0} < 0.14 \text{ events at the 90\% CL.}$$

⁶Two types of $K^+ \rightarrow \pi^+\pi^0$ monitor data are taken, both of which are used in this study. By examining the online trigger bits stored with the data, the full $K^+ \rightarrow \pi^+\nu\bar{\nu}$ trigger except for the online photon veto is required as part of the sample selection.



$$N_{\text{BG}} = H_{\text{peak}}^{\text{data}} \cdot \frac{N_{\text{box}}^{\text{mon}}}{H_{\text{peak}}^{\text{mon}}}$$

Figure 3.14: $K^+ \rightarrow \pi^+\pi^0$ background study outline.

| Year | $H_{\text{peak}}^{\text{mon}}$ | $N_{\text{box}}^{\text{33cm}}$ | $N_{\text{box}}^{\text{mon}}$ | $H_{\text{peak}}^{\text{data}}$ | $N_{\text{BG}}^{\text{33cm}}$ 90% CL | N_{BG} 90% CL |
|-------|--------------------------------|--------------------------------|-------------------------------|---------------------------------|---|---------------------------|
| 1989 | 636.8 | 2 | 0 | 40.40 | 0.25 | 0.11 |
| 1990 | 399.3 | 1 | 0 | 38.54 | 0.38 | 0.22 |
| 1991 | 475.1 | 0 | 0 | 14.69 | 0.29 | 0.29 |
| Total | 1511.2 | 3 | 0 | 93.63 | 0.41 | 0.14 |

Table 3.21: Numerical results of the $K^+ \rightarrow \pi^+\pi^0$ background studies. The “33cm” entries refer to a range box cut with a lower bound of 33 cm which was considered for this analysis, but replaced with a 34 cm cut based on this study.

Of all the backgrounds to $K^+ \rightarrow \pi^+\nu\bar{\nu}$ in E787, $K^+ \rightarrow \pi^+\pi^0$ has proved in the past to be the most difficult to predict. It has been hypothesized that correlations between the photon veto and kinematic measurements make the “peak-to-box” ratio overly optimistic. The potential for correlation is obvious. If a $K^+ \rightarrow \pi^+\pi^0$ passes the full photon veto, both photons were lost. One place for a photon to hide is on top of the charged track, which would add energy to the track and possibly hurt reconstruction affecting the range measurement. In the kinematic study, the barrel veto and endcap veto cuts are relaxed. This gives the photons a place to escape without hiding under the charged track, so this sample might be cleaner than the final data. As a cross-check of the $K^+ \rightarrow \pi^+\pi^0$ study the number of events in the “high range tail” ($100 \text{ MeV} < E_{\text{tot}}^{\text{new}} < 115 \text{ MeV}$ and $R_{\text{tot}}^{\text{new}} > 33 \text{ cm}$) and “high energy tail” ($28 \text{ cm} < R_{\text{tot}}^{\text{new}} < 33 \text{ cm}$ and $E_{\text{tot}}^{\text{new}} > 115 \text{ MeV}$) were separately predicted. These predictions can be directly compared to the $K^+ \rightarrow \pi^+\nu\bar{\nu}$ data after the full analysis, which is summarized in Table 3.22. The agreement is rather good, lending

| Year | N ^{mon} HighR | N ^{Expected} HighR | N ^{Observed} HighR | N ^{mon} HighE | N ^{Expected} HighE | N ^{Observed} HighE |
|-------|---------------------------|--------------------------------|--------------------------------|---------------------------|--------------------------------|--------------------------------|
| 1989 | 33 | 2.0 | 0 | 29 | 1.8 | 2 |
| 1990 | 16 | 1.0 | 0 | 42 | 2.6 | 4 |
| 1991 | 19 | 1.2 | 1 | 52 | 3.2 | 2 |
| Total | 68 | 4.2 | 1 | 123 | 7.6 | 7 |

Table 3.22: Cross check of the $K^+ \rightarrow \pi^+\pi^0$ study, by predicting the number of events expected in the “High Range” ($100 \text{ MeV} < E_{\text{tot}}^{\text{new}} < 115 \text{ MeV}$ and $R_{\text{tot}}^{\text{new}} > 33 \text{ cm}$) and “High Energy” ($28 \text{ cm} < R_{\text{tot}}^{\text{new}} < 33 \text{ cm}$ and $E_{\text{tot}}^{\text{new}} > 115 \text{ MeV}$) tails of the $K^+ \rightarrow \pi^+\pi^0$ peak. The agreement is fairly good.

some confidence to the actual background prediction itself. Any remaining undetected pathological correlation would have to affect range and energy together (thus putting events into the box) without affecting either the range or energy tails separately.

An additional check of the $K^+ \rightarrow \pi^+\pi^0$ background study is made by running the full analysis, but vetoing only in the final range/energy/momentum box. Up to this point, the inverted RBOX cut had assumed a 33 cm lower range cut. Since the final box is set at 34 cm, the region $33 \text{ cm} < R_{\text{tot}}^{\text{new}} < 34 \text{ cm}$ is not in the signal region, but has still not yet been examined. From Table 3.21, < 0.41 events were expected in this region at the 90% confidence level. No events are observed.

3.5 The $K^+ \rightarrow \pi^+ \nu\bar{\nu}$ Search

3.5.1 Pass 1

This analysis starts from the existing “Pass 1” output described in [18]. Pass 1 started with the entire set of $K^+ \rightarrow \pi^+ \nu\bar{\nu}$ triggers written to tape, applying basic event reconstruction and minimal analysis to reduce the primary data set to a more manageable size. The most important Pass 1 cuts are the default FITPI TD analysis and a loose photon-veto. Since much of the software and subsystem calibrations have improved in the meantime, this creates the minor annoyance of maintaining some older and obsolete versions of code and calibrations (successful target reconstruction with the TARBNK routine was required in 1989 and 1990, default FITPI in all three years, a TD $\pi^+ \rightarrow \mu^+$ after-burner called CHITD was used in 1989 and 1991, and Turcot’s ELVETO_V4 was used in 1989), which must be included in the acceptance calculation. Pass 1 represented a major undertaking by the entire collaboration; it was not repeated for this analysis because the acceptance losses caused in Pass 1 (measured in Chapter 4) are small. The Pass 1 analysis is summarized in Table 3.23.

3.5.2 Pass 2

Pass 2 took the full Pass 1 output sample, and applied much of the final analysis to reduce the data set further. The complete Pass 2 analysis for all three years is

| Cut | Description | 1989 | 1990 | 1991 |
|---------|--------------------------|------|------|------|
| TARGET | TG reconstruction | yes | yes | no |
| DC.FIT | DC reconstruction | yes | yes | yes |
| NTRK_RS | One DC/RS track match | yes | yes | yes |
| P_DC | $P_{DC} < 270$ Mev/c | yes | yes | yes |
| TRKTIM | Find RS time | yes | no | yes |
| TICTG | Find TG or IC time | yes | no | no |
| DIPANG | $\cos\theta_z$ cut | yes | yes | yes |
| RNGMOM0 | Light range-momentum cut | no | yes | no |
| PREFIT | Single pulse TD fit | yes | yes | no |
| INTIME | RS, BV, EC photon veto | yes | yes | yes |
| DCTG_XY | TG/DC track match | yes | yes | no |
| TRSTG | TG/RS pion time matchup | yes | no | no |
| FITPI | Default FITPI cut | yes | yes | yes |
| TMUAV | TMUAV > 8 nsec | yes | no | no |
| CHITD | TD after-burner cut | yes | no | yes |
| ELVETO | Local region ELVETO cut | yes | no | no |

Table 3.23: Summary of the various Pass 1 analyses from 89-91 data.

summarized in Table 3.24. After Pass 2, the entire data set was stored in three disk files, one per year.

3.5.3 Pass 3

Pass 3 applies the remaining analysis to the Pass 2 survivors, and is detailed in Table 3.25. As part of the Pass 3 analysis, the software checks for the appearance of duplicate runs. These are typically caused by mistakes in tape handling or hardware problems during Pass 1, and since Pass 3 is the first time a single analysis job sees the entire span of runs for each year most book-keeping tasks are deferred to here. The analysis will only analyze data from a run once, and the first cut applied at Pass 3, “GOOD_RUN,” removes any events associated with duplicate runs. This identical run selection will be used for the kaon flux determination in Chapter 4. The final range/energy spectrum after the total momentum cut is in Figure 3.15.

The final kinematic region (the BOX) was not inspected for signal until 19 June 1995. No candidate events are observed.

| Description | 1989 | | 1990 | | 1991 | |
|-------------|---------------------|-----------|---------------------|-----------|---------------------|-----------|
| | N _{passed} | Rejection | N _{passed} | Rejection | N _{passed} | Rejection |
| Pass 1 | 138024 | - | 504640 | - | 667945 | - |
| ISKCODE | 128067 | 1.08 | 468022 | 1.08 | 486127 | 1.37 |
| PNNSTOP | 127891 | 1.00 | 465312 | 1.01 | 482020 | 1.01 |
| STOP_HEX | 127448 | 1.00 | 461471 | 1.01 | 474642 | 1.02 |
| DIPANG | 113585 | 1.12 | 366919 | 1.26 | 398724 | 1.19 |
| EIC | 99268 | 1.14 | 337287 | 1.09 | 351972 | 1.13 |
| PICER | 68608 | 1.45 | 274723 | 1.23 | 265434 | 1.33 |
| PISCAT_BW | 59535 | 1.15 | 244839 | 1.12 | 232432 | 1.14 |
| B4DEDX | 57643 | 1.03 | 239156 | 1.02 | 223719 | 1.04 |
| PISCAT_B4 | - | - | - | - | 200576 | 1.12 |
| PBGLASS | - | - | - | - | 180999 | 1.11 |
| B4TDEDX | 57526 | 1.02 | 236135 | 1.01 | - | - |
| B4TFIT | 53068 | 1.08 | 216945 | 1.09 | - | - |
| PIHODO_B4 | 48941 | 1.08 | 198982 | 1.09 | - | - |
| TGDCXY | 48888 | 1.00 | 198657 | 1.00 | 180433 | 1.00 |
| ZTGT | 48470 | 1.01 | 197723 | 1.00 | 178959 | 1.01 |
| TGDCVT | 21345 | 2.23 | 131708 | 1.50 | 128484 | 1.39 |
| RTDIF | 21255 | 1.00 | 131365 | 1.00 | 127744 | 1.01 |
| TARGF | 20338 | 1.05 | 127092 | 1.03 | 123881 | 1.03 |
| TGDDEX | 18215 | 1.12 | 97092 | 1.31 | 105465 | 1.17 |
| EPIMAX | 18149 | 1.00 | 96859 | 1.00 | 104801 | 1.01 |
| NTRIK | 17853 | 1.02 | 96270 | 1.01 | 103773 | 1.01 |
| GAMVETP1 | 14299 | 1.25 | 70741 | 1.36 | 85312 | 1.22 |
| PRPAT | 12338 | 1.16 | 57932 | 1.22 | 68975 | 1.24 |
| NSECRS | 11880 | 1.04 | 54462 | 1.06 | 66697 | 1.03 |
| DELC | 8642 | 1.37 | 45305 | 1.20 | 45221 | 1.47 |
| TIMCON | 7993 | 1.08 | 43091 | 1.05 | 44565 | 1.02 |
| RNGMOM(2) | 5199 | 1.54 | 29699 | 1.45 | 14702 | 3.03 |
| ZDCOW | 5149 | 1.01 | 29348 | 1.01 | 14347 | 1.02 |
| FITPI | 4885 | 1.05 | 18717 | 1.57 | 11302 | 1.27 |
| ELVETO | 3961 | 1.23 | 6683 | 2.80 | 3095 | 3.65 |
| ELEC_V5 | 3095 | 1.28 | 4804 | 1.39 | 2170 | 1.43 |
| RSHEX | 2965 | 1.04 | 4083 | 1.18 | 2036 | 1.07 |
| TMUBV | 2906 | 1.02 | 4083 | 1.02 | 2004 | 1.02 |
| TMUADC | 2805 | 1.04 | 3890 | 1.05 | 1938 | 1.03 |
| Pass 2 | 2805 | 49.21 | 3890 | 129.73 | 1938 | 344.66 |

Table 3.24: The Pass 2 analysis. During Pass 1, under certain conditions no photon veto was applied. The cut GAMVETP1 forces the re-application of the full Pass 1 photon veto.

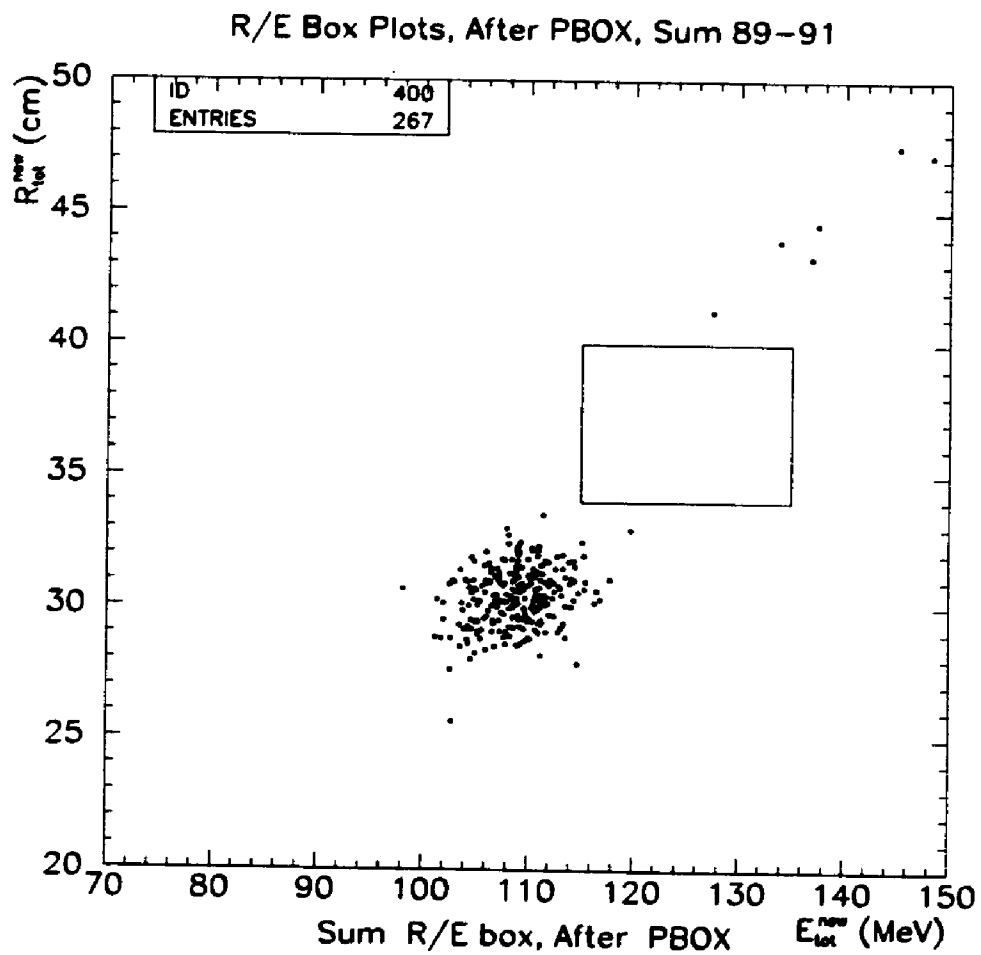


Figure 3.15: The final range/energy spectrum after the total momentum cut. The range/energy box is overlaid. No events are observed in the final sample.

| Description | 1989 | | 1990 | | 1991 | |
|-------------|---------------------|-----------|---------------------|-----------|---------------------|-----------|
| | N _{passed} | Rejection | N _{passed} | Rejection | N _{passed} | Rejection |
| Pass 2 | 2805 | - | 3890 | - | 1938 | - |
| GOOD_RUN | 2708 | - | 3876 | - | 1938 | - |
| EKZ | 2684 | 1.01 | 3828 | 1.01 | 1922 | 1.01 |
| GAMVET | 1102 | 2.44 | 1529 | 2.50 | 693 | 2.77 |
| CHIRF | 1092 | 1.01 | 1514 | 1.01 | 690 | 1.01 |
| ZFRF | 1020 | 1.07 | 1402 | 1.08 | 645 | 1.07 |
| LAY14 | 1014 | 1.01 | 1381 | 1.02 | 642 | 1.01 |
| RSDEXD | 831 | 1.22 | 1102 | 1.25 | 512 | 1.25 |
| TDFOOL | 830 | 1.00 | 1100 | 1.00 | 512 | 1.00 |
| TDACC | 813 | 1.02 | 1028 | 1.07 | 501 | 1.02 |
| TDDFA | 737 | 1.10 | 895 | 1.15 | 379 | 1.32 |
| BOX | 0 | - | 0 | - | 0 | - |

Table 3.25: The Pass 3 analysis. The GOOD_RUN cut removes events from duplicate runs, and is used consistently during the scaler counting in Chapter 4.

Chapter 4

The Sensitivity

While generating the list of cuts from chapter 3 was an arduous process, figuring out what they do to a typical $K^+ \rightarrow \pi^+ \nu\bar{\nu}$ decay is at least as challenging. Starting with a large sample of $K^+ \rightarrow \pi^+ \nu\bar{\nu}$ decays, every cut in the list will remove some events. This is an acceptance loss, and all the losses must be properly added up in order to translate a number of observed events into a physically interesting branching ratio or limit. One problem is that a candidate event might be removed by several cuts, and an attempt to separately add up the losses from each cut may result in multiple-counting. For example, suppose a beam pion really entered the detector at about the same time a $K^+ \rightarrow \pi^+ \nu\bar{\nu}$ decay occurred. That event could be cut by most of the beam and target cuts, as well as some of the photon veto cuts. The trick is to count each acceptance loss exactly once.

If the monte carlo were a perfect detector simulation, the task would be fairly simple. A sample of $N_0 K^+ \rightarrow \pi^+ \nu\bar{\nu}$ events could be generated, run through the online

trigger simulation and offline analysis, and the number of survivors N counted. The acceptance would then be simply be N/N_0 . This simulation would have to include a perfect representation of the entire detector geometry, every physics process (multiple scattering, energy loss, nuclear interactions, etc.), instrumentation and resolution effects for each channel of each sub-system in the detector. It would also have to have a perfect K^+ beam representation including accidental beam K^+ and π^+ particle distributions and rates, as well as a complete simulation of random accidental rates throughout the detector. Of course, resolutions and accidental rates vary with time and intensity, and this would have to be accounted for as well.

Since this perfect simulation is somewhat impractical, a different strategy will be employed. UMC will be used only to measure the acceptance of cuts that depend critically on the kinematics of $K^+ \rightarrow \pi^+ \nu\bar{\nu}$ itself. This includes the online trigger fiducial volume cuts (I-counter, $T \cdot A$, level 1 refined range), offline total range, energy, and momentum box cuts, the dip angle cut, and stopping position cuts. The trigger acceptance will be called A_{trig} (Section 4.1.1), and the basic offline “fiducial region” factor will be A_{umc} (Section 4.1.2). The other effects which depend critically on the π^+ kinematics are losses due to pion nuclear interactions and decay-in-flight. While decay-in-flight is relatively easy to simulate, nuclear interaction losses are harder and will remain one of the largest systematic errors in the acceptance. This factor will be included by measuring the ratio of the acceptance with decay-in-flight and nuclear

interactions enabled in UMC to the acceptance with them disabled. Call this factor A_{midif} (Section 4.1.3).

With the UMC-based factors in hand, the other cuts are broken into groups with common acceptance losses, which will be measured with data from minimum-bias “monitor” triggers. The three triggers used are $K_{\mu 2}(1)$, $K_{\pi 2}(1)$ and π scat, which were mentioned in Section 2.8 and are described in detail in [20]. Basically, $K_{\mu 2}(1)$ are events with a beam kaon and a charged track that penetrates deeply into the range stack, $K_{\pi 2}(1)$ have a beam kaon and a charged track penetrating into the middle of the range stack, and π scats have a beam pion with a charged track that penetrates somewhere into the range stack. These monitor triggers are evenly distributed throughout the data-taking period, and naturally account for instrumentation effects, resolutions, intensities and accidental rates.

First, the efficiency for reconstructing events with one charged track from a K^+ decay travelling from the target to the range stack is measured. This is rather tricky, since it requires some event selection *without* any reconstruction. It is done with events from the $K_{\mu 2}(1)$ trigger, using only the highly efficient RS_TRK code for selection (a small correction for RS_TRK losses is made later). Events with RS energy consistent with $K^+ \rightarrow \mu^+ \nu_\mu$ are selected and reconstructed with the full drift chamber, range stack, and target analysis. Failures are counted as reconstruction losses, yielding the factor A_{recon} (Section 4.2.1).

The next step is to select $K^+ \rightarrow \mu^+ \nu_\mu$ events, and measure the losses due to extra beam particles, accidentals, and any cuts not dependent on particle type. This will be done in two parts. First, we select $K^+ \rightarrow \mu^+ \nu_\mu$ decays at rest by applying the online and offline delayed coincidence cuts, and requiring that the measured μ^+ range, energy, and momentum be consistent with a $K^+ \rightarrow \mu^+ \nu_\mu$ decay. This sample is used to measure the acceptance of the full online and offline photon veto, post-reconstruction target analysis, beam analysis, and losses due to accidentals in the online trigger. Call this factor $A_{K\mu_2}$ (Section 4.2.2). The loss due to accidentals causing an outer RSPC hit vetoing the event with the LAY14 cut, $A_{\text{LAY14}}^{\text{acc}}$ (Section 4.2.3), is measured with the survivors. Second, select $K^+ \rightarrow \mu^+ \nu_\mu$ events with the full beam and target analysis and with a tight kinematic box cut requiring that the muon has range, energy, and momentum consistent with a $K^+ \rightarrow \mu^+ \nu_\mu$ decay. This sample is assumed to be $K^+ \rightarrow \mu^+ \nu_\mu$ decays at rest, and is used to measure the online and offline delayed coincidence and timing consistency cuts acceptance, A_{DC} (Section 4.2.4).

The remaining cuts require pion samples for the efficiency measurement. π scat triggers have a similar range stack stopping distribution to $K^+ \rightarrow \pi^+ \nu\bar{\nu}$ candidates. π scats that stop in range stack layers 11-18 are used for the FITPI and related TD cut acceptance, A_{TD} (Section 4.3.1). The cuts which depend critically on having pions with typical range, energy, and momentum in the drift chamber and range stack are evaluated by selecting π scat events from the $K^+ \rightarrow \pi^+ \nu\bar{\nu}$ data with a hit

in \check{C}_π near TRS. After applying the box and TD cuts, the efficiency of RNGMOM, RSDEDX, and CHIRF cuts are measured for each stopping layer, and weighted by the UMC-based $K^+ \rightarrow \pi^+ \nu \bar{\nu}$ (or $K^+ \rightarrow \pi^+ X^0$) stopping layer distribution to give $A_{\pi scat}$ (Section 4.3.2).

Target cuts dependent on a $K^+ \rightarrow \pi^+$ decay cannot be measured with π scats, so a sample of $K^+ \rightarrow \pi^+ \pi^0$ events from the $K_{\pi 2}(1)$ trigger is selected. A range, energy, and momentum $K^+ \rightarrow \pi^+ \pi^0$ box is applied. This sample is used to measure the acceptance of TGDEDX and EPIMAX, $A_{K_{\pi 2}}$ (Section 4.4.1). An item not yet accounted for is the level 1.5 energy trigger. This acceptance is measured by using the $K^+ \rightarrow \pi^+ \pi^0$ peak as a model of a π^+ “delta function” in energy in the detector, measuring the efficiency for an effective level 1.5 energy cut and convolving the efficiency over the final UMC $K^+ \rightarrow \pi^+ \nu \bar{\nu}$ energy spectrum for the acceptance $A_{L1.5}$ (Section 4.4.2).

The probability of an event with a stopped K^+ decay to $\pi^+ \nu \bar{\nu}$ surviving the analysis is then

$$A_{\text{tot}} = A_{\text{trig}} \times A_{\text{umc}} \times A_{\text{nidif}} \times A_{\text{recon}} \times A_{K_{\mu 2}} \times A_{L14}^{\text{acc}} \times A_{\text{DC}} \times A_{\text{TD}} \times A_{\pi scat} \times A_{K_{\pi 2}} \times A_{L1.5}.$$

The remaining step is to determine the number of decays of stopped K^+ 's that were eligible to fire the $K^+ \rightarrow \pi^+ \nu \bar{\nu}$ trigger. This number is broken into two pieces. First, the number of beam kaons that deposit energy in the B4 hodoscope and target (this was called KT in the $K^+ \rightarrow \pi^+ \nu \bar{\nu}$ trigger) when the detector was “live”

(KT_{live}) is counted and called $N_{KT_{live}}$ (Section 4.5). Secondly, the fraction, f_S , of $N_{KT_{live}}$ that yielded a stopped K^+ decay in the target is measured with a simple $K^+ \rightarrow \mu^+ \nu_\mu$ branching ratio analysis (Section 4.6). This f_S factor may also include any extra normalization factors (eg. small dead-time accounting errors or imperfect detector simulation effects) common to the $K^+ \rightarrow \pi^+ \nu\bar{\nu}$ analysis. The $K^+ \rightarrow \pi^+ \nu\bar{\nu}$ sensitivity becomes

$$S = f_S \times N_{KT_{live}} \times A_{tot}.$$

To cross-check that no gross errors are present a $K^+ \rightarrow \pi^+ \pi^0$ branching ratio measurement is performed (Section 4.7). The result (0.205 ± 0.008) agrees well with the expected value (0.2116 ± 0.0014). This particularly checks that the UMC-based nuclear interaction calculation and the TD $\pi^+ \rightarrow \mu^+$ fitting acceptance are not badly in error.

The bulk of the rest of this chapter contains the complete details of each part of the sensitivity calculation. While this should be of interest to experts, casual readers will probably want to skip to the last section of this chapter where the results are assembled and summarized.

4.1 The UMC-based acceptance measurements

The monte carlo simulation software UMC is run using a K^+ stopping distribution measured with $K^+ \rightarrow \mu^+ \nu_\mu$ data, as described in [16]. The beam-line instrumentation is not simulated. The kaon is required to stop, and it is forced to decay into $K^+ \rightarrow \pi^+ \nu\bar{\nu}$ (or $K^+ \rightarrow \pi^+ X^0$ with massless X^0). The π^+ is propagated until it comes to rest with decay-in-flight and nuclear interactions disabled. The online level 0 and level 1 triggers are simulated, and the number of events passed by each trigger section is recorded and used for the trigger acceptance. The events passing the trigger simulation are written to a file.

The file produced by UMC is read by the KOFIA analysis program. Where possible, all the cuts whose acceptance is evaluated with $K_{\mu 2}(1)$ and $K_{\pi 2}(1)$, but *not* π scat triggers,¹ are applied.

Additional cuts just for UMC data are applied:

- UFATE: Require that the pion stops without interacting or decaying.
- USTMED: Require that the pion stops in scintillator.
- USTOP_HEX: Require the offline stopping hextant and layer agree with the true stopping hextant and layer.

¹The π scats will be used for the RNGMOM, RSDEDX, and CHIRF acceptance. To get a sample of pions from π scats typical of $K^+ \rightarrow \pi^+ \nu\bar{\nu}$ produced pions, the box cut will be applied. It is therefore necessary to calculate A_{umc} with UMC $K^+ \rightarrow \pi^+ \nu\bar{\nu}$ without those cuts applied.

Since the A_{TD} acceptance calculation will assume that the π^+ stopped in scintillator and that KOFIA found the correct TD channel (range stack hextant and layer), these represent losses which must be accounted for here. Note that the UFATE cut only removes events when nuclear interactions and decay-in-flight are enabled in the simulation. The offline fiducial volume cuts are then applied, and the acceptance measured. The complete process is repeated with both nuclear interactions and decay-in-flight enabled, and the resulting acceptance loss is treated as a separate item. The complete UMC-based acceptance calculation is sketched in Figure 4.1.

4.1.1 The online trigger, A_{trig}

With reference to Figure 4.1, the UMC-based trigger acceptance is not exactly the $K^+ \rightarrow \pi^+ \nu \bar{\nu}$ trigger survival fraction. The reason is that several of the factors depend critically on the details of the trigger timing or chamber efficiencies, and will be measured separately with data. A_{trig} is defined to *not* include these items – they are part of $A_{K_{\mu 2}}$. The trigger efficiency factors derived from UMC are extracted from the UMC trigger summary statistics and listed in Table 4.1 for $K^+ \rightarrow \pi^+ \nu \bar{\nu}$ and Table 4.2 for $K^+ \rightarrow \pi^+ X^0$. Since the errors on the different components of A_{trig} are strongly correlated, the error is approximated by using the number of KT 's generated by UMC and the total number of trigger simulation survivors.

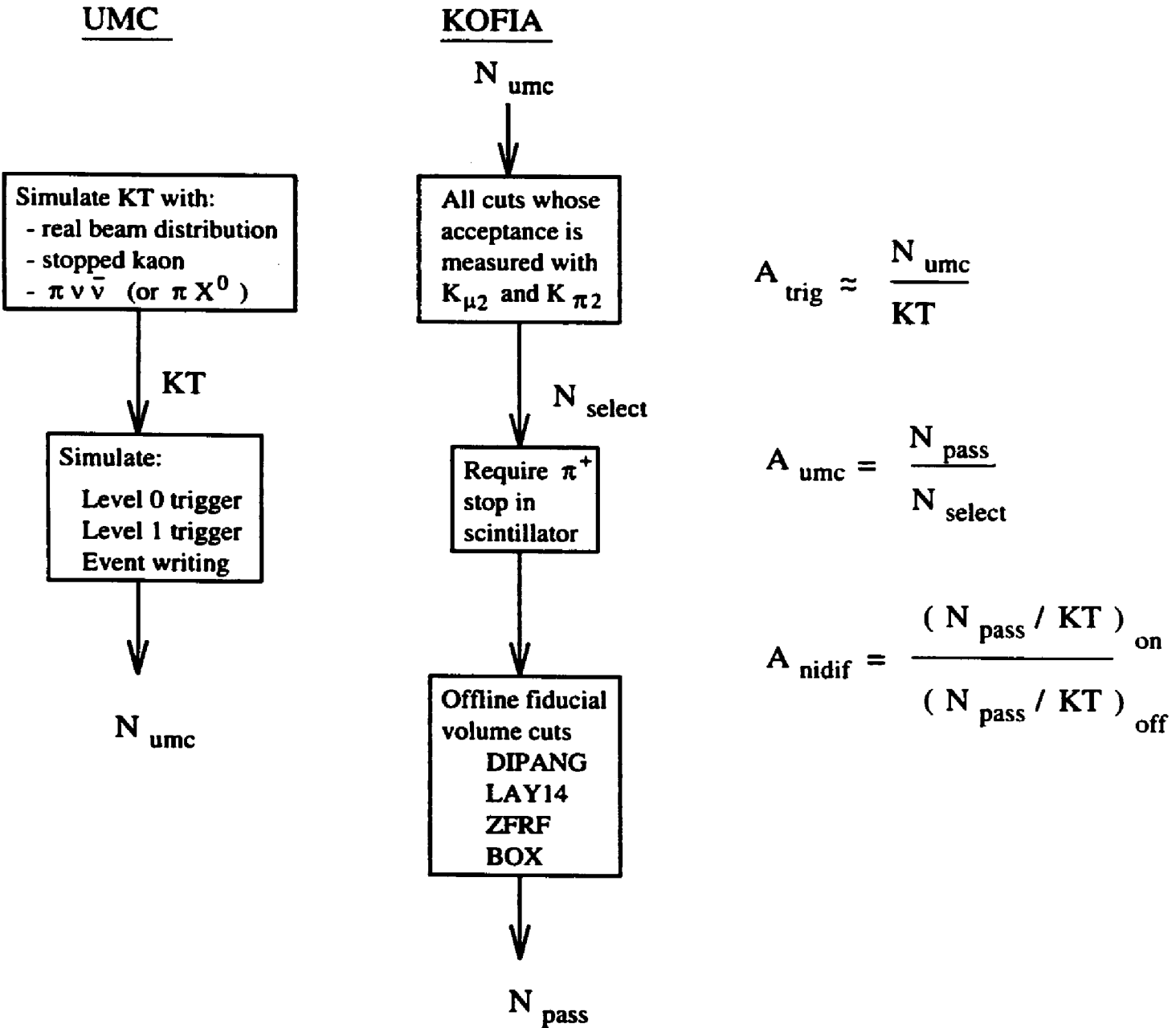


Figure 4.1: The UMC-based acceptance calculations.

| Requirement | Quantity | 1989 | 1990 | 1991 |
|-------------------|---------------------|----------------------|----------------------|----------------------|
| $T \cdot A$ | N_{exam} | 190334 | 190747 | 190122 |
| | N_{passed} | 77654 | 78350 | 77555 |
| | A | 0.408 ± 0.001 | 0.411 ± 0.001 | 0.408 ± 0.001 |
| Layer B | N_{exam} | 77654 | 78350 | 77555 |
| | N_{passed} | 64466 | 65102 | 64431 |
| | A | 0.830 ± 0.001 | 0.831 ± 0.001 | 0.831 ± 0.001 |
| μ veto | N_{exam} | 63962 | 64874 | 64067 |
| | N_{passed} | 63950 | 64865 | 64049 |
| | A | 0.9998 ± 0.00005 | 0.9999 ± 0.00005 | 0.9997 ± 0.00007 |
| Reach Layer 11 | N_{exam} | 63950 | 64865 | 64049 |
| | N_{passed} | 35538 | 36296 | 35717 |
| | A | 0.556 ± 0.002 | 0.560 ± 0.002 | 0.558 ± 0.002 |
| Level 1 MLU | N_{exam} | 32966 | 33628 | 33042 |
| | N_{passed} | 32109 | 32725 | 32038 |
| | A | 0.974 ± 0.001 | 0.973 ± 0.001 | 0.9696 ± 0.0009 |
| A_{trig} | | 0.183 ± 0.001 | 0.186 ± 0.001 | 0.183 ± 0.001 |

Table 4.1: UMC-based $K^+ \rightarrow \pi^+ \nu \bar{\nu}$ trigger acceptance factors.

| Requirement | Quantity | 1989 | 1990 | 1991 |
|-------------------|---------------------|-----------------------|-----------------------|-----------------------|
| $T \cdot A$ | N_{exam} | 190353 | 190735 | 190279 |
| | N_{passed} | 85460 | 86091 | 86273 |
| | A | 0.449 ± 0.001 | 0.451 ± 0.001 | 0.453 ± 0.001 |
| Layer B | N_{exam} | 85460 | 86091 | 86273 |
| | N_{passed} | 85456 | 86089 | 86268 |
| | A | 0.99995 ± 0.00002 | 0.99998 ± 0.00002 | 0.99994 ± 0.00003 |
| μ veto | N_{exam} | 84789 | 85775 | 85758 |
| | N_{passed} | 84321 | 85380 | 85204 |
| | A | 0.9944 ± 0.0003 | 0.9954 ± 0.0002 | 0.9935 ± 0.0003 |
| Reach Layer 11 | N_{exam} | 84321 | 85380 | 85204 |
| | N_{passed} | 84124 | 85209 | 85021 |
| | A | 0.9977 ± 0.0002 | 0.9980 ± 0.0002 | 0.9979 ± 0.0002 |
| Level 1 MLU | N_{exam} | 77391 | 78384 | 78185 |
| | N_{passed} | 69320 | 70167 | 68292 |
| | A | 0.896 ± 0.001 | 0.895 ± 0.001 | 0.873 ± 0.001 |
| A_{trig} | | 0.399 ± 0.001 | 0.401 ± 0.001 | 0.393 ± 0.001 |

Table 4.2: UMC-based $K^+ \rightarrow \pi^+ X^0$ trigger acceptance factors.

| Cut | 1989 | | 1990 | | 1991 | |
|------------------|---------------------|-------|---------------------|-------|---------------------|-------|
| | N _{passed} | A | N _{passed} | A | N _{passed} | A |
| Selection | 26001 | - | 26703 | - | 25693 | - |
| UFATE | 26001 | 1.000 | 26703 | 1.000 | 25693 | 1.000 |
| USTMED | 25347 | 0.975 | 26035 | 0.975 | 25033 | 0.974 |
| USTOP_HEX | 25191 | 0.994 | 25860 | 0.993 | 24868 | 0.993 |
| DIPANG | 24389 | 0.968 | 25209 | 0.975 | 24205 | 0.973 |
| LAY14 | 24389 | 1.000 | 25209 | 1.000 | 24205 | 1.000 |
| NSECRS | 24389 | 1.000 | 25209 | 1.000 | 24205 | 1.000 |
| ZFRF | 23569 | 0.966 | 24310 | 0.964 | 23390 | 0.966 |
| BOX | 8432 | 0.358 | 8798 | 0.362 | 8326 | 0.356 |
| A_{umc} | 0.324 ± 0.003 | | 0.329 ± 0.003 | | 0.324 ± 0.003 | |

Table 4.3: UMC-based fiducial volume acceptance for $K^+ \rightarrow \pi^+ \nu \bar{\nu}$.

4.1.2 The offline fiducial region cuts, A_{umc}

Again with reference to Figure 4.1, the UMC-based acceptance of the fiducial region cuts is summarized for $K^+ \rightarrow \pi^+ \nu \bar{\nu}$ in Table 4.3 and $K^+ \rightarrow \pi^+ X^0$ in Table 4.4. While only the overall A_{umc} factor is used, each cut is listed for personal and public edification in the tables.²

4.1.3 Nuclear interactions and decay-in-flight, A_{nidi}

Finally, the nuclear interaction and decay-in-flight losses are estimated by applying the full analysis to UMC generated data with both enabled, and comparing to the

²The LAY14 cut is discussed in the $K^+ \rightarrow \mu^+ \nu_\mu$ section below.

| Cut | 1989 | | 1990 | | 1991 | |
|------------------|---------------------|-------|---------------------|-------|---------------------|-------|
| | N _{passed} | A | N _{passed} | A | N _{passed} | A |
| Selection | 56989 | - | 58109 | - | 55503 | - |
| UFATE | 56989 | 1.000 | 58109 | 1.000 | 55503 | 1.000 |
| USTMED | 54746 | 0.961 | 55781 | 0.960 | 53352 | 0.961 |
| USTOP_HEX | 54431 | 0.994 | 55432 | 0.994 | 53058 | 0.994 |
| DIPANG | 52200 | 0.959 | 53588 | 0.967 | 51274 | 0.966 |
| LAY14 | 52197 | 1.000 | 53587 | 1.000 | 51268 | 1.000 |
| NSECRS | 52197 | 1.000 | 53587 | 1.000 | 51268 | 1.000 |
| ZFRF | 50958 | 0.976 | 52236 | 0.975 | 50009 | 0.975 |
| BOX | 41490 | 0.814 | 43178 | 0.827 | 41639 | 0.833 |
| A_{umc} | 0.728 ± 0.002 | | 0.743 ± 0.002 | | 0.750 ± 0.002 | |

Table 4.4: UMC-based fiducial volume acceptance for $K^+ \rightarrow \pi^+ X^0$.

acceptance with both disabled:

$$A_{\text{nudif}} = \frac{(N_{\text{pass}}/N_{KT})_{\text{on}}}{(N_{\text{pass}}/N_{KT})_{\text{off}}}.$$

The KOFIA analysis on the UMC samples generated with nuclear interactions and decay-in-flight enabled is summarized in Table 4.5 and Table 4.6, and the acceptance calculations are done in Table 4.7 and Table 4.8 for $K^+ \rightarrow \pi^+ \nu \bar{\nu}$ and $K^+ \rightarrow \pi^+ X^0$ respectively. While not apparent from the tables, the dominant losses due to nuclear interactions and decay-in-flight occur at the trigger level. After the full nuclear interactions and decay-in-flight simulation, the range vs. energy spectra before and after the PBOX cut are shown for $K^+ \rightarrow \pi^+ \nu \bar{\nu}$ in Figure 4.2 and for $K^+ \rightarrow \pi^+ X^0$ in Figure 4.3.

| Cut | 1989 | | 1990 | | 1991 | |
|-----------|---------------------|-------|---------------------|-------|---------------------|-------|
| | N _{passed} | A | N _{passed} | A | N _{passed} | A |
| Selection | 16924 | - | 15831 | - | 15635 | - |
| UFATE | 15614 | 0.923 | 15189 | 0.959 | 14983 | 0.958 |
| USTMED | 15433 | 0.988 | 14792 | 0.974 | 14602 | 0.975 |
| USTOP_HEX | 15103 | 0.979 | 14631 | 0.989 | 14428 | 0.988 |
| DIPANG | 14602 | 0.967 | 14270 | 0.975 | 14092 | 0.977 |
| LAY14 | 14307 | 0.980 | 14021 | 0.983 | 13845 | 0.982 |
| NSECRS | 14307 | 1.000 | 14021 | 1.000 | 13845 | 1.000 |
| ZFRF | 14028 | 0.980 | 13778 | 0.983 | 13574 | 0.980 |
| BOX | 4026 | 0.287 | 4316 | 0.313 | 4153 | 0.306 |

Table 4.5: UMC-based nuclear interactions and decay-in-flight analysis for $K^+ \rightarrow \pi^+ \nu\bar{\nu}$.

| Cut | 1989 | | 1990 | | 1991 | |
|-----------|---------------------|-------|---------------------|-------|---------------------|-------|
| | N _{passed} | A | N _{passed} | A | N _{passed} | A |
| Selection | 30952 | - | 28925 | - | 27871 | - |
| UFATE | 28273 | 0.913 | 27684 | 0.957 | 26589 | 0.954 |
| USTMED | 27794 | 0.983 | 26586 | 0.961 | 25539 | 0.961 |
| USTOP_HEX | 26949 | 0.970 | 26185 | 0.985 | 25178 | 0.986 |
| DIPANG | 25739 | 0.955 | 25274 | 0.965 | 24244 | 0.963 |
| LAY14 | 25339 | 0.984 | 24932 | 0.986 | 23841 | 0.983 |
| NSECRS | 25339 | 1.000 | 24932 | 1.000 | 23841 | 1.000 |
| ZFRF | 24909 | 0.983 | 24577 | 0.986 | 23646 | 0.992 |
| BOX | 18600 | 0.747 | 19969 | 0.813 | 19331 | 0.818 |

Table 4.6: UMC-based nuclear interactions and decay-in-flight analysis for $K^+ \rightarrow \pi^+ X^0$.

| Condition | Quantity | 1989 | 1990 | 1991 |
|--------------------|-------------------|-------------------|-------------------|-------------------|
| NIDIF off | N_{KT} | 190334 | 190747 | 190122 |
| | N_{pass} | 8432 | 8798 | 8326 |
| NIDIF on | N_{KT} | 190076 | 190655 | 190030 |
| | N_{pass} | 4026 | 4316 | 4153 |
| A_{nidif} | | 0.478 ± 0.004 | 0.491 ± 0.009 | 0.499 ± 0.009 |

Table 4.7: $K^+ \rightarrow \pi^+ \nu \bar{\nu}$ nuclear interaction and decay-in-flight acceptance. The errors are purely statistical, and the true errors due to uncertainties in the nuclear interaction simulation are likely somewhat larger.

| Condition | Quantity | 1989 | 1990 | 1991 |
|--------------------|-------------------|-------------------|-------------------|-------------------|
| NIDIF off | N_{KT} | 190353 | 190735 | 190279 |
| | N_{pass} | 41490 | 43178 | 41639 |
| NIDIF on | N_{KT} | 190182 | 190697 | 190050 |
| | N_{pass} | 18600 | 19969 | 19331 |
| A_{nidif} | | 0.449 ± 0.004 | 0.463 ± 0.004 | 0.465 ± 0.004 |

Table 4.8: $K^+ \rightarrow \pi^+ X^0$ nuclear interaction and decay-in-flight acceptance. The errors are purely statistical, and the true errors due to uncertainties in the nuclear interaction simulation are likely somewhat larger.

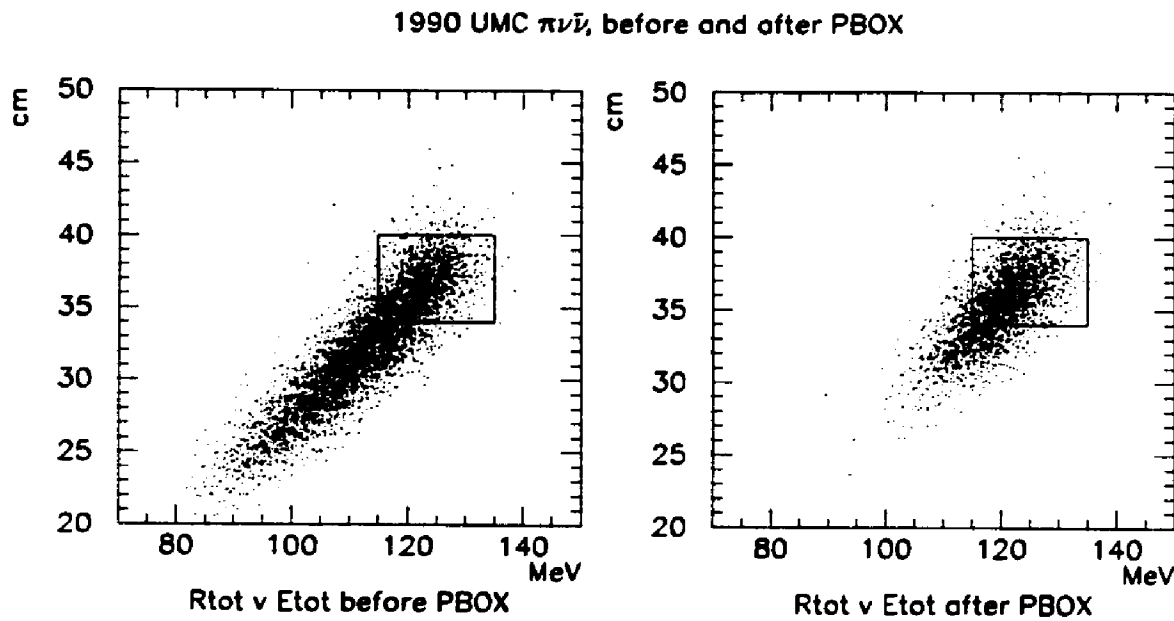


Figure 4.2: Range vs. Energy spectra for $K^+ \rightarrow \pi^+ \nu\bar{\nu}$, before and after the PBOX cut, showing the RBOX/EBOX cuts, using the nuclear interactions and decay-in-flight enabled sample.

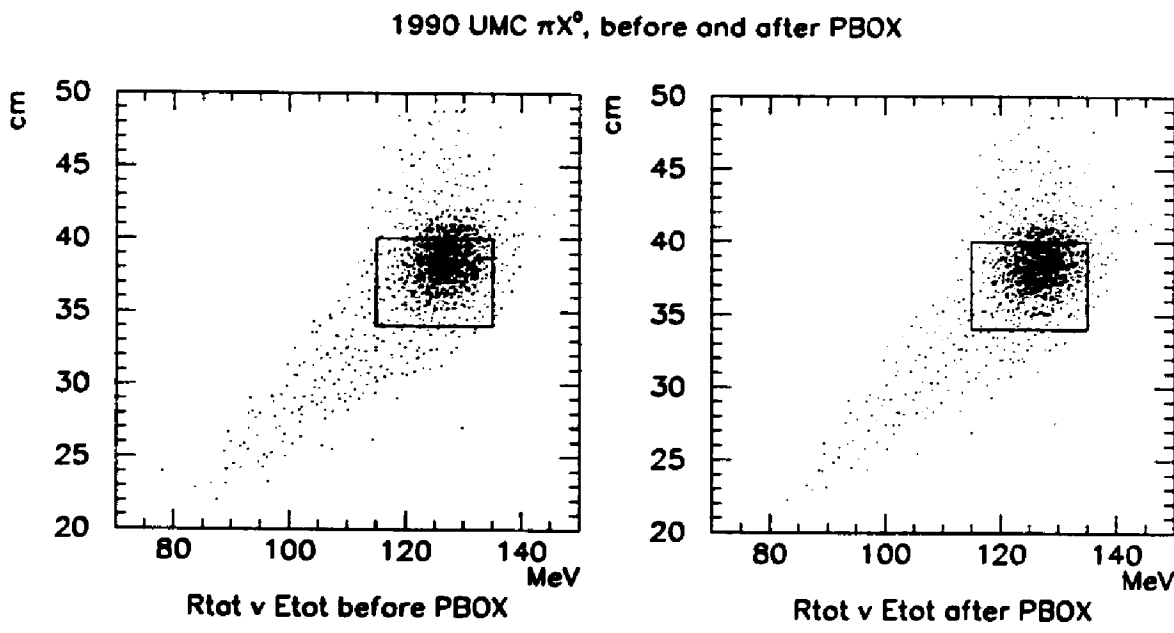


Figure 4.3: Range vs. Energy spectra for $K^+ \rightarrow \pi^+ X^0$, before and after the PBOX cut, showing the RBOX/EBOX cuts, using the nuclear interactions and decay-in-flight enabled sample.

4.2 $K^+ \rightarrow \mu^+ \nu_\mu$ based measurements

The $K_{\mu 2}(1)$ triggers taken simultaneously with the data are further “prescaled” by a factor of 3 to yield a convenient sample for acceptance calculations. Many $K^+ \rightarrow \mu^+ \nu_\mu$ produced muons stop in the BV, causing a mis-measurement of the range and energy. To allow for clean energy and range measurements for later selection, events with any hits in the outermost range stack layer are first removed by inspection of the online trigger bits stored with the data. The various acceptance calculations performed with these monitors are shown in Figure 4.4.

4.2.1 Reconstruction losses, A_{recon}

Since most selection techniques require some reconstruction first, measuring the reconstruction efficiency itself is tricky. This is done with minimal selection on $K_{\mu 2}(1)$ triggers. First, the online delayed coincidence requirement is applied to select kaon decays at rest. The highly efficient RS-TRK routine is run, and the range stack energy E_{RS} of the track closest to 130 MeV (typical $K^+ \rightarrow \mu^+ \nu_\mu$ energy deposited in the range stack) is recorded. This range stack energy, called ETRKKM2, is plotted in Figure 4.5 for all 1990 $K_{\mu 2}(1)$ triggers, $K_{\mu 2}(1)$ triggers after the online delayed coincidence, and $K_{\mu 2}(1)$ triggers after the online delayed coincidence and outer RS layer veto. Several selection methods attempt to use this energy to select $K^+ \rightarrow \mu^+ \nu_\mu$ events, and measure the efficiency of the ISKCODE reconstruction analysis.

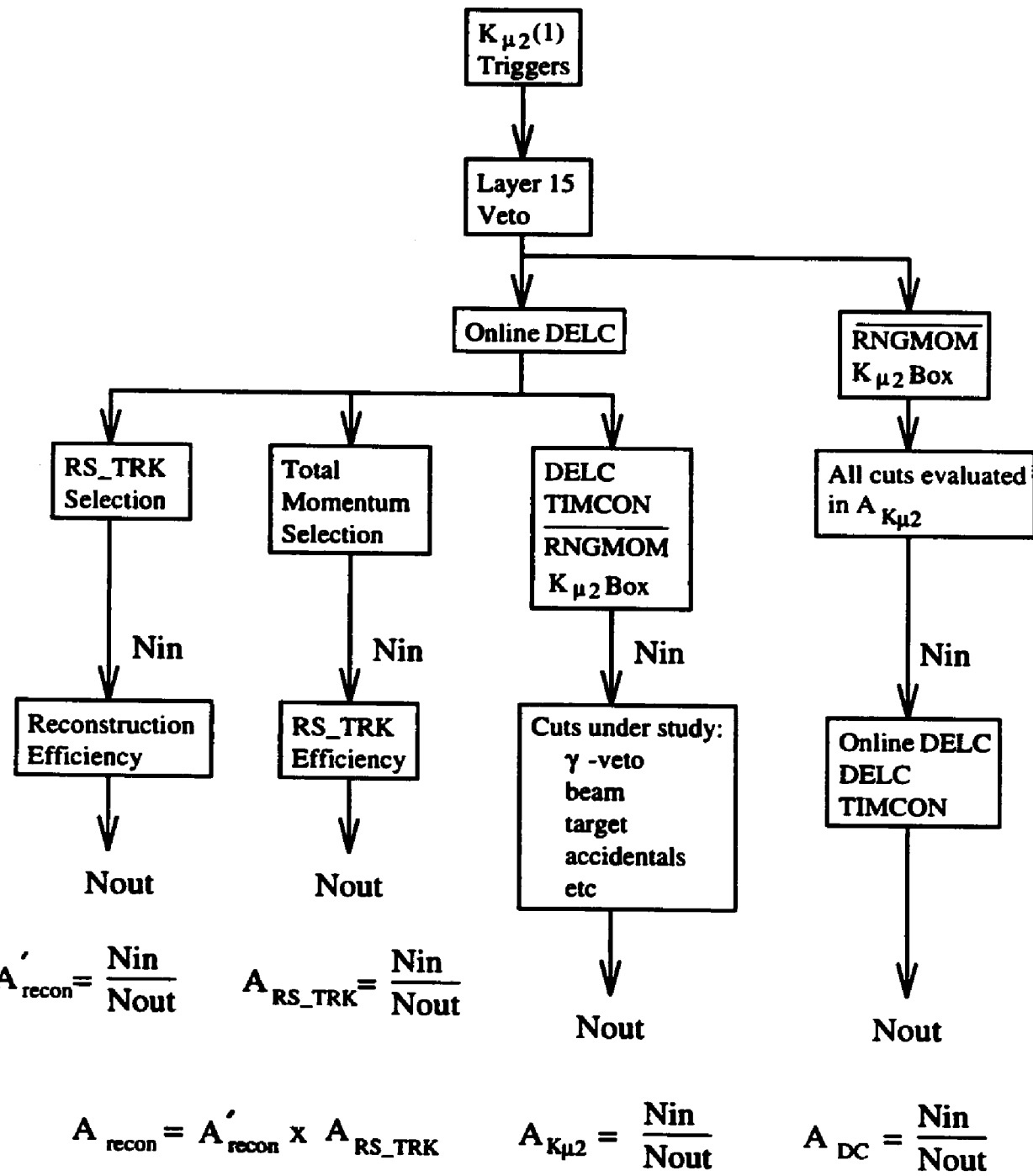


Figure 4.4: The $K^+ \rightarrow \mu^+ \nu_\mu$ based acceptance calculations. The “layer 15 veto” refers to effective layer 15, which is the outer RS layer (physical layer 21).

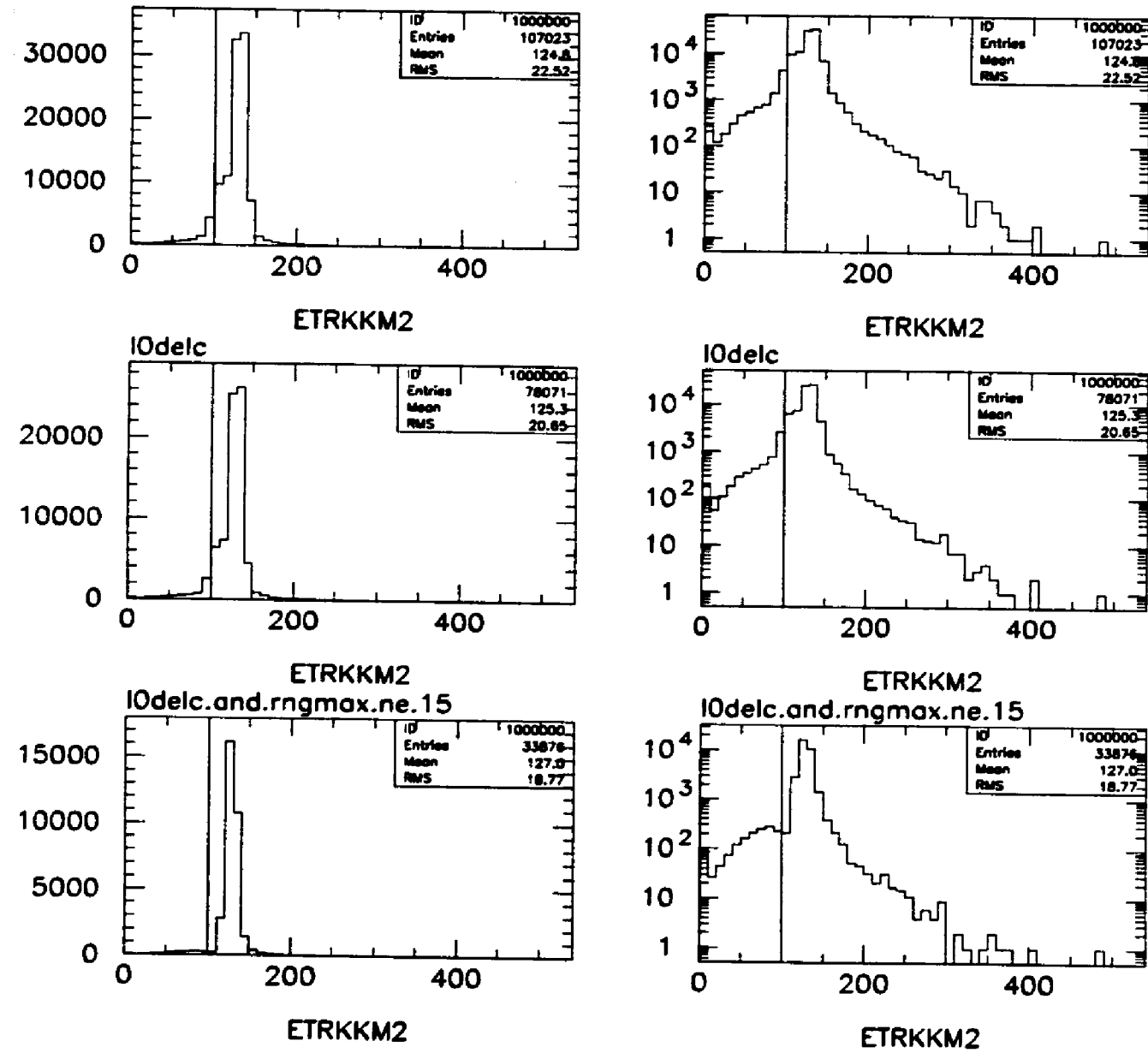
1990 $K_{\mu 2}(1)$, no setup cuts

Figure 4.5: The RS energy of the track found by RS_TRK nearest 130 MeV for all 1990 $K_{\mu 2}(1)$ triggers (top), plus the online delayed coincidence (middle), plus a veto on the outer RS layer (bottom), plotted on linear (left) and log (right) scales. The final reconstruction efficiency measurement will assume that all events above 100 MeV (the vertical line) are reconstructible.

- Method 1: Assume that all events passing the online delayed coincidence, L0DELC, are reconstructible. This is likely pessimistic, since a lost beam kaon together with appropriate accidentals can fire the trigger, but not be reconstructible.
- Method 2: Assume the events passing L0DELC with $E_{RS} > 100$ MeV are good events. I believe this is the fairest method.
- Method 3: Assume that events passing L0DELC with $100 \text{ MeV} < E_{RS} < 160 \text{ MeV}$ are good events. This is likely optimistic, since real events with large overlapping accidentals (possibly including a complete second track) may not be counted.
- Method 4: Count events passing L0DELC before and after reconstruction using a gaussian fit of data with $100 \text{ MeV} < E_{RS} < 160 \text{ MeV}$, calling the gaussian fitted area the number of events. This “peak-to-peak” method is closest to the method used in previous analyses, but I suspect it is too optimistic. It seems likely that events with correctly measured charged track energy will have higher reconstruction efficiency than an average event. Since events that fail reconstruction are effectively gone forever, losses must be counted here.

The various results for method 1-4 are summarized in Table 4.9 to Table 4.12 respectively. As expected, method 1 gives the lowest efficiency and method 4 gives

| ISKCODE | Description | 1989 | | 1990 | | 1991 | |
|---------------------|---------------|---------------------|-------|---------------------|-------|---------------------|-------|
| | | N _{passed} | A | N _{passed} | A | N _{passed} | A |
| - | Selection | 30849 | - | 33876 | - | 18076 | - |
| 3 | DC_DECODE | 30814 | 0.999 | 33650 | 0.993 | 18053 | 0.999 |
| 4 | DC_TRACK | 26550 | 0.862 | 32416 | 0.963 | 17290 | 0.958 |
| 5 | 1 RS-DC Match | 25936 | 0.977 | 31494 | 0.972 | 16685 | 0.965 |
| 1 | TG Fail | 25932 | 1.000 | 31491 | 1.000 | 16684 | 1.000 |
| 2 | TG Quality | 24885 | 0.960 | 30272 | 0.961 | 16113 | 0.966 |
| 6 | TRKTIM | 24881 | 1.000 | 30237 | 0.999 | 16094 | 0.999 |
| A'_{recon} | | 0.807 ± 0.002 | | 0.893 ± 0.002 | | 0.890 ± 0.002 | |

Table 4.9: Reconstruction efficiency method 1: assume all $K_{\mu 2}(1)$ events passing the online delayed coincidence are reconstructible.

the highest efficiency. Since I think that they should bound the true value, I will call the difference of method 1 and 4 2σ , and use method 2 as the reconstruction efficiency.

The reconstruction efficiency must be corrected for the basic inefficiency in the RS_TRK selection algorithm itself. Returning to the sample of $K_{\mu 2}(1)$ events passing the online delayed coincidence and outer RS layer veto above, we select events with $221 \text{ MeV}/c < P_{\text{tot}}^{\text{new}} < 251 \text{ MeV}/c$, and run RS_TRK to measure the efficiency with a simple counting method, summarized in Table 4.13. Note that $A_{\text{RS_TRK}}$ does not merely measure the fraction of momentum-selected events that are reconstructed with RS_TRK, but rather the fraction of momentum-selected events that are reconstructed with RS_TRK *and* have $E_{\text{RS}} > 100 \text{ MeV}/c$. This self-consistent definition of

| ISKCODE | Description | 1989 | | 1990 | | 1991 | |
|---------------------|---------------|---------------------|-------|---------------------|-------|---------------------|-------|
| | | N _{passed} | A | N _{passed} | A | N _{passed} | A |
| - | Selection | 29681 | - | 32405 | - | 17218 | - |
| 3 | DC_DECODE | 29654 | 0.999 | 32210 | 0.994 | 17197 | 0.999 |
| 4 | DC_TRACK | 25615 | 0.864 | 31134 | 0.967 | 16529 | 0.961 |
| 5 | 1 RS-DC Match | 25143 | 0.982 | 30462 | 0.978 | 16066 | 0.972 |
| 1 | TG Fail | 25139 | 1.000 | 30459 | 1.000 | 16065 | 1.000 |
| 2 | TG Quality | 24177 | 0.962 | 29334 | 0.963 | 15554 | 0.968 |
| 6 | TRKTIM | 24176 | 1.000 | 29305 | 0.999 | 15538 | 0.999 |
| A'_{recon} | | 0.815 ± 0.002 | | 0.904 ± 0.002 | | 0.902 ± 0.002 | |

Table 4.10: Reconstruction efficiency method 2: assume $K_{\mu 2}(1)$ events passing the online delayed coincidence and with $E_{RS} > 100$ MeV are reconstructible.

| ISKCODE | Description | 1989 | | 1990 | | 1991 | |
|---------------------|---------------|---------------------|-------|---------------------|-------|---------------------|-------|
| | | N _{passed} | A | N _{passed} | A | N _{passed} | A |
| - | Selection | 29221 | - | 31806 | - | 16799 | - |
| 3 | DC_DECODE | 29194 | 0.999 | 31617 | 0.994 | 16780 | 0.999 |
| 4 | DC_TRACK | 25262 | 0.865 | 30601 | 0.968 | 16179 | 0.964 |
| 5 | 1 RS-DC Match | 24835 | 0.983 | 30010 | 0.981 | 15775 | 0.975 |
| 1 | TG Fail | 24831 | 1.000 | 30007 | 1.000 | 15774 | 1.000 |
| 2 | TG Quality | 23907 | 0.963 | 28953 | 0.965 | 15296 | 0.970 |
| 6 | TRKTIM | 23906 | 1.000 | 28924 | 0.999 | 15280 | 0.999 |
| A'_{recon} | | 0.818 ± 0.002 | | 0.909 ± 0.002 | | 0.910 ± 0.002 | |

Table 4.11: Reconstruction efficiency method 3: assume $K_{\mu 2}(1)$ events passing the online delayed coincidence and with $100 \text{ MeV} < E_{RS} < 160 \text{ MeV}$ are reconstructible.

| ISKCODE | Description | 1989 | | 1990 | | 1991 | |
|---------------------|---------------|---------------------|-------|---------------------|-------|---------------------|-------|
| | | N _{passed} | A | N _{passed} | A | N _{passed} | A |
| - | Selection | 27671 | - | 30018 | - | 15913 | - |
| 3 | DC_DECODE | 27646 | 0.999 | 29834 | 0.994 | 15896 | 0.999 |
| 4 | DC_TRACK | 23927 | 0.865 | 28980 | 0.971 | 15341 | 0.965 |
| 5 | 1 RS-DC Match | 23632 | 0.988 | 28574 | 0.986 | 15059 | 0.982 |
| 1 | TG Fail | 23630 | 1.000 | 28573 | 1.000 | 15059 | 1.000 |
| 2 | TG Quality | 22827 | 0.966 | 27613 | 0.966 | 14620 | 0.971 |
| 6 | TRKTIM | 22826 | 1.000 | 27585 | 0.999 | 14606 | 0.999 |
| A'_{recon} | | 0.825 ± 0.002 | | 0.919 ± 0.002 | | 0.918 ± 0.002 | |

Table 4.12: Reconstruction efficiency method 4: Using the events from method 3, use the area of a gaussian fit to E_{RS} to count the events (the actual fit is a gaussian plus flat background).

A_{RS_TRK} already results in an efficiency slightly lower than the value quoted in previous analyses. In fact, for a self-consistent “peak-to-peak” reconstruction efficiency measurement such as the above method 4 or the ones used in [16] and [18], A_{RS_TRK} could be defined as the fraction of momentum-selected events that have a successfully reconstructed RS_TRK track actually in the gaussian part of the energy peak. While this only makes a percent or-so difference for 1989-1991 data, it might be a significant effect in future E787 analyses using data taken at higher rates. The issue is whether $K^+ \rightarrow \pi^+ \nu\bar{\nu}$ events reconstructed with incorrect RS energies represent a loss, and if this loss is counted in any other place. The method used here is the most conservative approach.

Combining A'_{recon} from method 2 above with A_{RS_TRK} gives the complete reconstruction efficiency, summarized in Table 4.14. Note that it is assumed that the

| Description | 1989 | | 1990 | | 1991 | |
|---------------|---------------------|--------|---------------------|--------|---------------------|-------|
| | N _{passed} | A | N _{passed} | A | N _{passed} | A |
| Selection | 21703 | - | 26848 | - | 14208 | - |
| RS_TRK | 21608 | 0.9956 | 26651 | 0.9927 | 14115 | 0.993 |
| A_{RS_TRK} | 0.9956 ± 0.0004 | | 0.9927 ± 0.0005 | | 0.9935 ± 0.0007 | |

Table 4.13: The RS_TRK algorithm efficiency. The “RS_TRK” entry is the number of events that pass the momentum-selection that are reconstructed by RS_TRK with $E_{RS} > 100$ MeV/c.

| Quantity | 1989 | 1990 | 1991 |
|---------------|---------------------|---------------------|---------------------|
| A_{RS_TRK} | 0.9956 ± 0.0004 | 0.9927 ± 0.0005 | 0.9935 ± 0.0007 |
| A'_{recon} | 0.815 ± 0.01 | 0.904 ± 0.01 | 0.902 ± 0.01 |
| A_{recon} | 0.811 ± 0.01 | 0.898 ± 0.01 | 0.897 ± 0.01 |

Table 4.14: The final reconstruction efficiency calculation.

reconstruction efficiency is the same for $K^+ \rightarrow \mu^+ \nu_\mu$ and $K^+ \rightarrow \pi^+ \nu\bar{\nu}$; since this efficiency will be used below in both the flux normalization factor f_S and A_{tot} , it will cancel in the $K^+ \rightarrow \pi^+ \nu\bar{\nu}$ sensitivity calculation. It is measured primarily as a consistency check.

4.2.2 Photon veto, beam, target, and accidental losses, $A_{K_{\mu 2}}$

With reconstruction in hand, muons can be selected using an inverted RNGMOM cut and a tight range, energy, and momentum box around the $K^+ \rightarrow \mu^+ \nu_\mu$ peak. After first applying DELC and TIMCON to truly force kaon decays at rest, various photon veto, accidental losses, and beam cut efficiencies are measured as outlined

in Figure 4.4 and summarized in Table 4.15. The offline cuts applied correspond to the definitions from Chapter 3. The online cuts are applied by examining the trigger bits stored with the data, except for the Level 0 μ veto (from Section 2.7.1, events are vetoed if the charged track hits any of the outer 3 range stack layers). This cut is simulated with a special routine, `L0_MUVETO`, which uses the transient digitizers to construct the online trigger information, but looking 6 sectors clockwise of the stopping sector.

4.2.3 Accidental losses in the LAY14 cut, $A_{\text{L14}}^{\text{acc}}$

LAY14 cuts events with a charged track that stops just before the outer range stack chamber with a hit in the chamber in the stopping, or immediately clockwise, sector. There are three potential losses from this cut. A real $K^+ \rightarrow \pi^+ \nu\bar{\nu}$ pion can appear to stop in layer 14, but actually enter the chamber. These pions will either stop in the chamber (or possibly layer 15 with very little energy loss), and that loss is built into the USTMED and USTOP_HEX contributions to the A_{umc} measurement. Secondly, the electron (or possibly the muon) from the $\pi^+ \rightarrow \mu^+ \rightarrow e^+$ decay chain can cause a hit in the RSPC within the time window used in the hit selection. This loss is included in the A_{nidi} measurement.³ Finally, an accidental can cause a hit in

³UMC actually stores all RSPC hits, including those from late electrons which cause hits outside of the RSPC unpacking time window used for data. When applying the LAY14 cut to UMC generated data, an effective time-window matching that used for data is applied. It is not clear to me how this loss was accounted for in previous analyses, since by default nearly 1/2 of all layer 14 stops should have been cut in the A_{nidi} measurement, which apparently did not happen.

| Description | 1989 | | 1990 | | 1991 | |
|-----------------------|---------------------|-------|---------------------|-------|---------------------|-------|
| | N _{passed} | A | N _{passed} | A | N _{passed} | A |
| Selection | 9886 | - | 11709 | - | 5843 | - |
| GAMVET (RS) | 9466 | 0.958 | 11100 | 0.948 | 5468 | 0.936 |
| GAMVET (BV) | 9287 | 0.981 | 10855 | 0.978 | 5355 | 0.979 |
| GAMVET (EC) | 8554 | 0.921 | 9732 | 0.897 | 4678 | 0.874 |
| GAMVET (IC) | 8504 | 0.994 | 9698 | 0.997 | 4654 | 0.995 |
| GAMVET (VC) | 8468 | 0.996 | 9660 | 0.996 | 4608 | 0.990 |
| Level 0 γ veto | 8226 | 0.971 | 9262 | 0.959 | 4408 | 0.957 |
| Level 0 μ veto | 8210 | 0.998 | 9248 | 0.998 | 4398 | 0.998 |
| Level 1 RR Setup | 7285 | 0.887 | 8076 | 0.873 | 3707 | 0.843 |
| Level 1 Hextant Setup | 7183 | 0.986 | 7981 | 0.988 | 3648 | 0.984 |
| Level 0 1 T · A | 7175 | 0.999 | 7964 | 0.998 | 3643 | 0.999 |
| NTRIK | 7087 | 0.988 | 7903 | 0.992 | 3582 | 0.983 |
| TGDCXY | 7084 | 1.000 | 7902 | 1.000 | 3582 | 1.000 |
| TGDCVT | 6842 | 0.966 | 7689 | 0.973 | 3413 | 0.953 |
| ZTGT | 6820 | 0.997 | 7676 | 0.998 | 3408 | 0.999 |
| ZDCOW | 6783 | 0.995 | 7646 | 0.996 | 3401 | 0.998 |
| RTDIF | 6771 | 0.998 | 7638 | 0.999 | 3395 | 0.998 |
| TARGF | 6669 | 0.985 | 7464 | 0.977 | 3332 | 0.981 |
| EIC | 6453 | 0.968 | 7382 | 0.989 | 3253 | 0.976 |
| PRPAT | 6148 | 0.953 | 6930 | 0.939 | 3056 | 0.939 |
| PISCAT_BW | 5802 | 0.944 | 6379 | 0.920 | 2874 | 0.940 |
| PISCAT_B4 | - | - | - | - | 2739 | 0.953 |
| PIHODO_B4 | 5473 | 0.943 | 5983 | 0.938 | - | - |
| B4TFIT | 5419 | 0.990 | 5760 | 0.963 | - | - |
| B4DEDX | 5379 | 0.993 | 5695 | 0.989 | 2690 | 0.982 |
| B4TDEDX | 5378 | 1.000 | 5653 | 0.993 | - | - |
| PBGLASS | - | - | - | - | 2622 | 0.975 |
| PICER | 5316 | 0.988 | 5631 | 0.996 | 2618 | 0.998 |
| Pass 1 Target | 5309 | 0.999 | 5622 | 0.998 | - | - |
| EKZ | 5273 | 0.993 | 5569 | 0.991 | 2607 | 0.996 |
| $A_{K_{\mu 2}}$ | 0.533 ± 0.005 | | 0.476 ± 0.005 | | 0.446 ± 0.007 | |

Table 4.15: The basic $K^+ \rightarrow \mu^+ \nu_\mu$ efficiency measurement.

| Quantity | 1989 | 1990 | 1991 |
|-------------------------------|-------------------|-------------------|-------------------|
| N_{exam} | 5316 | 5631 | 2618 |
| N_{passed} | 5104 | 5349 | 2468 |
| L14 fraction | 0.160 ± 0.005 | 0.172 ± 0.006 | 0.166 ± 0.006 |
| $A_{\text{L14}}^{\text{acc}}$ | 0.994 ± 0.007 | 0.991 ± 0.008 | 0.990 ± 0.008 |

Table 4.16: Accidental losses in the LAY14 cut for $K^+ \rightarrow \pi^+ \nu\bar{\nu}$.

one of these chambers. This loss was recently pointed out by Meyers, and was not accounted for in previous analyses using similar cuts. It is included here as a separate “line-item.”

The survivors of the $A_{K_{\mu 2}}$ measurement from Table 4.15 are used to look for accidental chamber hits. The identical software used to look for RSPC hits for the LAY14 cut is used to look for hits in the two chambers on the opposite side of the detector.⁴ This is weighted by the fraction of the full $K^+ \rightarrow \pi^+ \nu\bar{\nu}$ (or $K^+ \rightarrow \pi^+ X^0$) simulation surviving the complete analysis that stopped in layer 14. The measurement is summarized for $K^+ \rightarrow \pi^+ \nu\bar{\nu}$ in Table 4.16, and for $K^+ \rightarrow \pi^+ X^0$ in Table 4.17.

⁴Ito pointed out a potential problem with this method. While any losses correlated with the photon veto and beam analysis are naturally accounted for using the $A_{K_{\mu 2}}$ survivors, the tight photon veto cuts applied on the opposite side of the detector might make the accidental rate there atypically small; however, the 250 nsec time windows used in the RSPC hit unpacking are quite large compared to the effective photon veto windows of a few nsec, so this effect should be very small.

| Quantity | 1989 | 1990 | 1991 |
|-------------------------------|-------------------|-------------------|-------------------|
| N_{exam} | 5316 | 5631 | 2618 |
| N_{passed} | 5104 | 5349 | 2468 |
| L14 fraction | 0.199 ± 0.003 | 0.218 ± 0.003 | 0.210 ± 0.003 |
| $A_{\text{L14}}^{\text{acc}}$ | 0.992 ± 0.004 | 0.989 ± 0.004 | 0.988 ± 0.005 |

Table 4.17: Accidental losses in the LAY14 cut for $K^+ \rightarrow \pi^+ X^0$.

| Description | 1989 | | 1990 | | 1991 | |
|-----------------|---------------------|-------|---------------------|-------|---------------------|-------|
| | N_{passed} | A | N_{passed} | A | N_{passed} | A |
| Selection | 7693 | - | 7874 | - | 3536 | - |
| Level 0 DELC | 6350 | 0.825 | 6502 | 0.826 | 2987 | 0.845 |
| DELC | 5942 | 0.936 | 6158 | 0.947 | 2845 | 0.952 |
| TIMCON | 5629 | 0.947 | 5850 | 0.950 | 2718 | 0.955 |
| A_{DC} | 0.732 ± 0.005 | | 0.743 ± 0.005 | | 0.769 ± 0.008 | |

Table 4.18: Delayed coincidence and related acceptances.

4.2.4 Delayed coincidence and related losses, A_{DC}

Using same inverted RNGMOM and $K^+ \rightarrow \mu^+ \nu_\mu$ box cuts, along with all of the cuts evaluated in $A_{K_{\mu 2}}$ above, a clean sample of kaon decays at rest is selected without any timing cuts. This sample is used to measure the delayed coincidence and related acceptances as outlined in Figure 4.4 and summarized in Table 4.18. This measurement assumes that all events passing this selection are from kaon decays at rest (Figure 4.6). As with the reconstruction efficiency, A_{DC} is common to both the acceptance A_{tot} and flux normalization f_S , and need not have been explicitly measured.

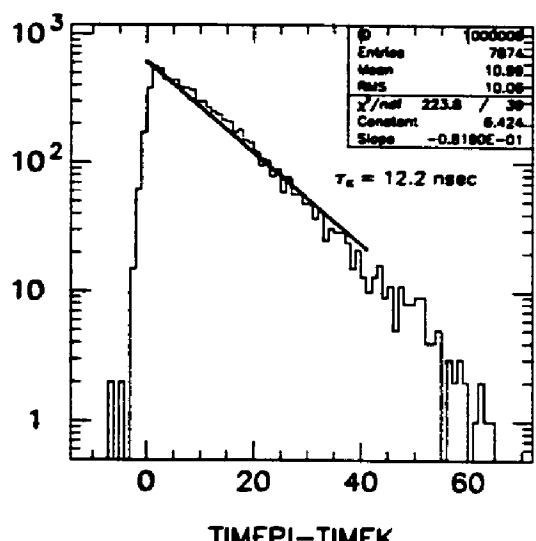


Figure 4.6: Target TIMEPI-TIMEK for the 1990 $K_{\mu 2}(1)$ selected sample used to measure the delayed coincidence efficiency. The sample has no significant decay-in-flight contamination. TIMEPI-TIMEK is fit to an exponential from 0 to 40 nsec resulting in a kaon lifetime $\tau_K = 12.2 \pm 0.2$ nsec, in good agreement with the accepted value of 12.371 ± 0.0029 nsec.

4.3 π scat measurements

Events with a beam π^+ scattering from the target into the range stack are used for drift chamber and range stack efficiency measurements.

4.3.1 TD $\pi^+ \rightarrow \mu^+$ fitter and related losses, A_{TD}

Extracting the efficiency of the TD $\pi^+ \rightarrow \mu^+$ fitter and related cuts is not straightforward. The UMC-based measurements have already accounted for decay-in-flight and nuclear interaction losses. Here, we just want to measure the TD fitter efficiency for pions which did not decay or interact before they came to a rest. Selecting such events for use in a “counting method” is almost impossible. Instead, the “area” method invented in [15] will be used.

The dominant efficiency loss of the $\pi^+ \rightarrow \mu^+$ fitting algorithm is the loss at early decay times, when the muon pulse is not separated from the pion stopping pulse. The area method first assumes that all efficiency loss occurs at early $\pi^+ \rightarrow \mu^+$ decay times. A sample of pions from the π scat trigger stopping in the allowed $K^+ \rightarrow \pi^+ \nu \bar{\nu}$ range stack stopping layers are used. Events from the π scat trigger are typically quite messy, so a set of range stack clean-up cuts are first applied to give a sample resembling typical pions from a $K^+ \rightarrow \pi^+$ decay. The selection cuts used are listed in Table 4.19. In addition to cuts from the $K^+ \rightarrow \pi^+ \nu \bar{\nu}$ analysis, the RNGMOM3 cut listed uses DC momentum and RS range to achieve almost complete μ^+ rejection.

| Cut | Description |
|------------|--|
| HEXCUT | Online hextant veto from $K^+ \rightarrow \pi^+ \nu \bar{\nu}$ trigger |
| PNNSTOP | RS Stopping layer 11-18 inclusive |
| GAMVET(RS) | RS part of the INTIME γ -veto |
| RNGMOM3 | Tight kinematic muon veto in RS |
| ISKCODE | same as $K^+ \rightarrow \pi^+ \nu \bar{\nu}$ analysis |
| DIPANG | same as $K^+ \rightarrow \pi^+ \nu \bar{\nu}$ analysis |
| PRPAT | same as $K^+ \rightarrow \pi^+ \nu \bar{\nu}$ analysis |

Table 4.19: Selection cuts applied to π scat triggers for the TD efficiency calculation.

For each selected event, the TD fitting code **FITPI** is run in the offline stopping counter, and the pion decay times (TMUAV) are recorded. The TMUAV distribution is then fit to a single exponential, and the total area under the curve is assumed to be the number of π^+ decays. This area includes pions which decayed too early to be properly fit, the major source of inefficiency. The ratio of the area under the curve, N_A , to the number of pions successfully fit, N_P , is the basic area method efficiency. It is essential to restrict the range of the TMUAV area method fits. At low TMUAV, the **FITPI** efficiency drops precipitously. At very high TMUAV, the probability of a real $\pi^+ \rightarrow \mu^+$ decay is small, and accidental fakes of $\pi^+ \rightarrow \mu^+$ become relatively more probable. This is illustrated in Figure 4.7, where the pion lifetime is fit with the equation

$$N = (a/\tau)e^{-t/\tau}$$

with the 2 parameters a and τ left free. With 1 nsec bins, a is just total number of pions from the area under the curve, and τ is the pion lifetime. After fixing the

fit range between 20 nsec and 75 nsec, the pion lifetime is fixed at 26.03 nsec, and the fit is redone with only a free, to extract $N_A = a$. Given the large arbitrary fit range effects, a more realistic error on N_A is estimated by comparing its variation over reasonable fit ranges.

A_{area} must be corrected for any residual FITPI inefficiency that doesn't occur at early TMUAV. This correction is performed by skimming one in 25 FITPI failures and hand-scanning them, looking for missed $\pi^+ \rightarrow \mu^+$ decays by eye. To allow unambiguous identification of the $\pi^+ \rightarrow \mu^+$ decay, only decays after one pion lifetime are used in the correction. Calling the number of apparent $\pi^+ \rightarrow \mu^+$ decays found in the FITPI failure sample N_H , the correction to N_A is $\Delta N_A = 25 \times e \times N_H$, resulting in the complete area method TD efficiency

$$A_{\text{area}} = \frac{N_P}{N_A + \Delta N_A}.$$

A final correction is made for $\pi^+ \rightarrow \mu^+$ muons that escape from the stopping counter, depositing too little energy in the stopping counter to pass the default FITPI cuts. Turcot points out in [18] that outward going muon escapes will usually leave enough energy in the next RS layer to extend the apparent track, which is already counted in the UMC measurements. His self-consistent estimate is $\epsilon_{\text{escape}} = 0.982$. The basic TD area method efficiency is sketched in Figure 4.8, and the complete calculation of A_{tdfit} is summarized in Table 4.20.

Using the FITPI survivors from the area method, a simple counting method is

2 Parameter Fits in Different Ranges.

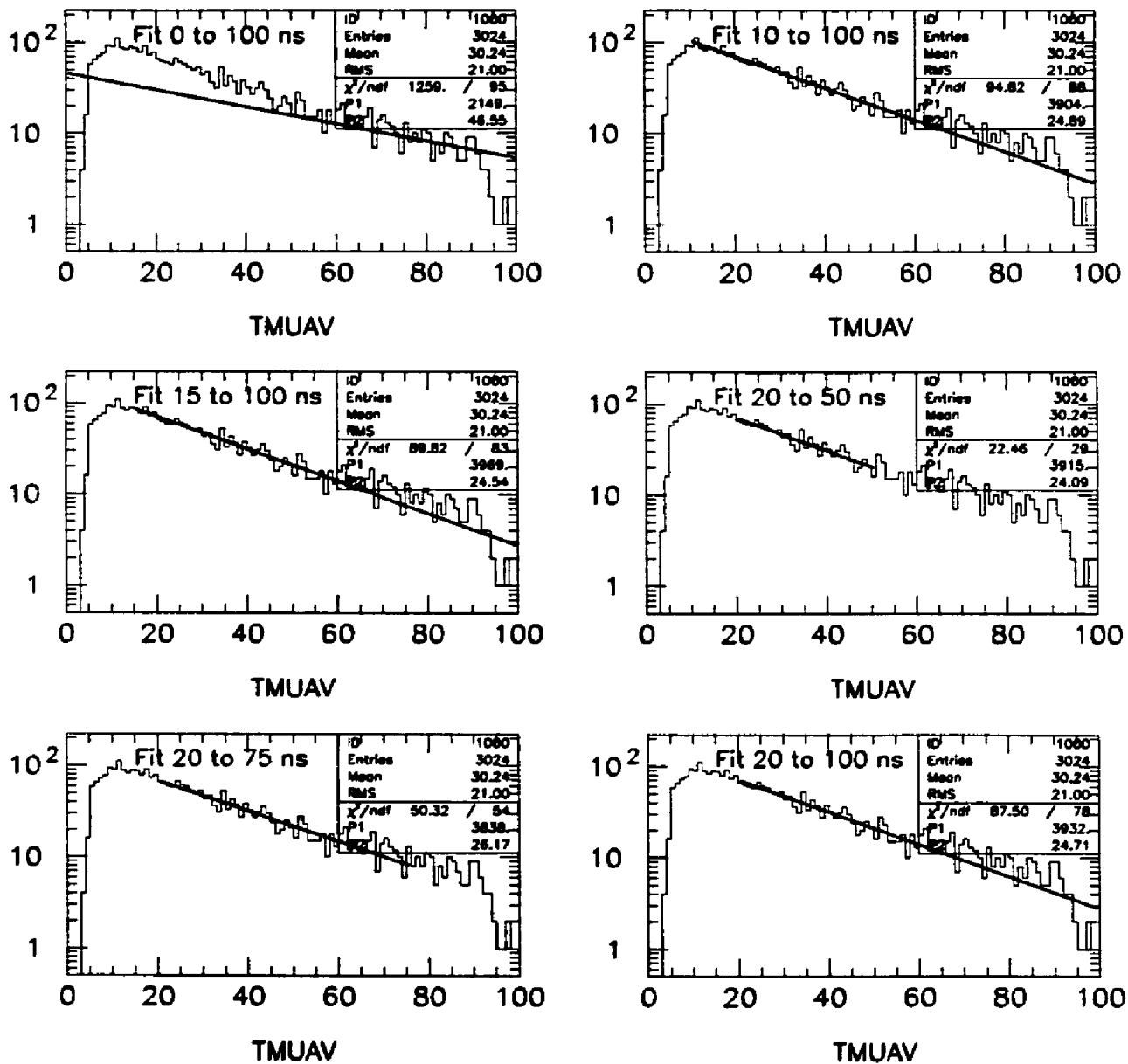


Figure 4.7: Pion lifetime fits over various fit ranges for 1990 data. The parameter “P2” is the τ_π (in nsec) fit result, and changes significantly with different fit ranges. Zero-bins are included in the fit.

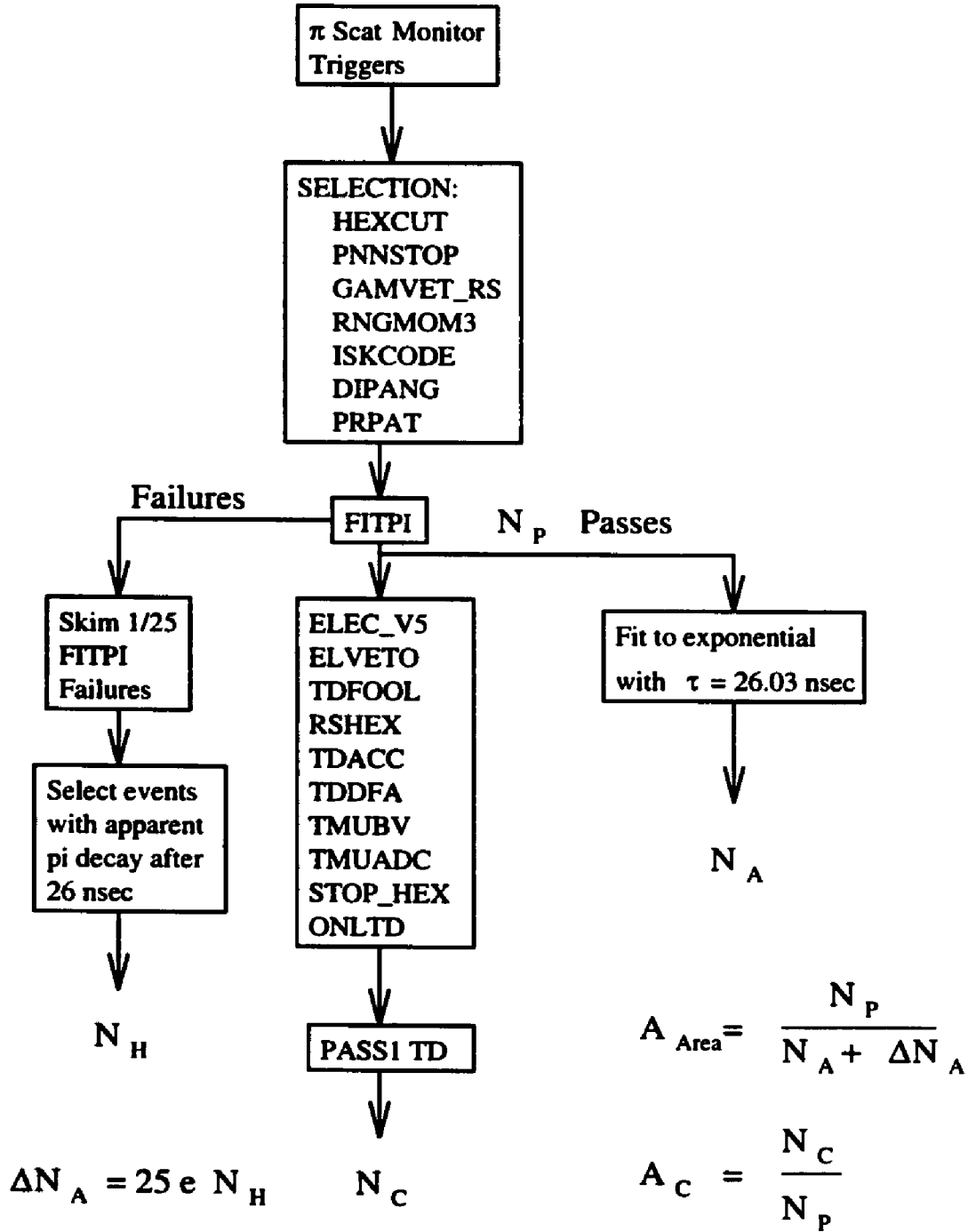


Figure 4.8: The TD fitter acceptance calculation.

| Quantity | 1989 | 1990 | 1991 |
|----------------------------|------------------|------------------|------------------|
| N_P | 1416 | 3024 | 3076 |
| N_A | 1640 ± 40 | 3847 ± 60 | 3926 ± 100 |
| Prescale | 25 | 25 | 25 |
| N_H | 3 | 4 | 6 |
| ΔN_A | 203.9 ± 118 | 271.8 ± 136 | 407.7 ± 166 |
| ϵ_{escape} | 0.982 | 0.982 | 0.982 |
| A_{tdfit} | 0.754 ± 0.05 | 0.721 ± 0.03 | 0.697 ± 0.03 |

Table 4.20: The TD fitter efficiency, A_{tdfit} .

used to measure the efficiency of the remaining $\pi^+ \rightarrow \mu^+ \rightarrow e^+$ cuts, including the online TD cut ONLTD. This calculation of A_C is also sketched in Figure 4.8, and is summarized in Table 4.21. Since significant upgrades were performed to the TD fitting software and calibration for this analysis, A_C also includes the effect of re-running the TD analysis used in Pass 1 [18].

The combined acceptance of the complete TD and related $\pi^+ \rightarrow \mu^+$ cuts is $A_{\text{TD}} = A_{\text{tdfit}} \times A_C$, calculated in Table 4.22.

4.3.2 Tracking losses in the range stack, $A_{\pi\text{scat}}$

For the remaining analysis in the range stack, it is essential to select pions with kinematics typical of $K^+ \rightarrow \pi^+ \nu \bar{\nu}$. π scat triggers can be messy, and the π^+ can have almost arbitrary energy. Turcot [18] also points out a particular problem with mis-timed ADC gates in the 1989 data, making them difficult to work with. Instead of using the π scat trigger, a sample of pions is selected by requiring a coincidence

| Description | 1989 | | 1990 | | 1991 | |
|---------------|---------------------|-------|---------------------|-------|---------------------|-------|
| | N _{passed} | A | N _{passed} | A | N _{passed} | A |
| Selection | 1416 | - | 3024 | - | 3076 | - |
| ELEC_V5 | 1170 | 0.826 | 2602 | 0.860 | 2543 | 0.827 |
| ELVETO | 1008 | 0.862 | 2286 | 0.879 | 2217 | 0.872 |
| TDFOOL | 1007 | 0.999 | 2285 | 1.000 | 2216 | 1.000 |
| RSHEX | 988 | 0.981 | 2212 | 0.968 | 2135 | 0.963 |
| TDACC | 932 | 0.943 | 2071 | 0.936 | 2037 | 0.954 |
| TDDFA | 806 | 0.865 | 1783 | 0.861 | 1593 | 0.782 |
| TMUBV | 796 | 0.988 | 1750 | 0.981 | 1552 | 0.974 |
| TMUADC | 766 | 0.962 | 1692 | 0.967 | 1509 | 0.972 |
| STOP_HEX | 745 | 0.973 | 1635 | 0.966 | 1479 | 0.980 |
| ONLTD | 710 | 0.953 | 1470 | 0.899 | 1447 | 0.978 |
| Pass 1 PREFIT | 710 | 1.000 | 1470 | 1.000 | - | - |
| Pass 1 FITPI | 707 | 0.996 | 1447 | 0.984 | 1438 | 0.994 |
| Pass 1 CHITD | 700 | 0.990 | - | - | 1415 | 0.984 |
| Pass 1 TMUAV | 693 | 0.990 | - | - | - | - |
| A_C | 0.489 ± 0.013 | | 0.479 ± 0.009 | | 0.460 ± 0.009 | |

Table 4.21: The acceptance of the remaining TD cuts, A_C . ONLTD is the online $\pi^+ \rightarrow \mu^+$ finder described in chapter 2.

| Quantity | 1989 | 1990 | 1991 |
|--------------------|-------------------|-------------------|-------------------|
| A_{tdfit} | 0.754 ± 0.05 | 0.721 ± 0.03 | 0.697 ± 0.03 |
| A_C | 0.489 ± 0.013 | 0.479 ± 0.009 | 0.460 ± 0.009 |
| A_{TD} | 0.369 ± 0.026 | 0.345 ± 0.015 | 0.321 ± 0.015 |

Table 4.22: The complete TD $\pi^+ \rightarrow \mu^+$ cuts acceptance.

| Cut | Description |
|------------|--|
| PICER | Require \check{C}_π hit near TRS (Table 3.6) |
| GAMVET(RS) | RS part of the INTIME γ -veto |
| ISKCODE | same as $K^+ \rightarrow \pi^+ \nu \bar{\nu}$ analysis |
| STOP_HEX | same as $K^+ \rightarrow \pi^+ \nu \bar{\nu}$ analysis |
| DIPANG | same as $K^+ \rightarrow \pi^+ \nu \bar{\nu}$ analysis |
| PRPAT | same as $K^+ \rightarrow \pi^+ \nu \bar{\nu}$ analysis |
| FITPI | same as $K^+ \rightarrow \pi^+ \nu \bar{\nu}$ analysis |
| ELEC_V5 | same as $K^+ \rightarrow \pi^+ \nu \bar{\nu}$ analysis |
| ELVETO | same as $K^+ \rightarrow \pi^+ \nu \bar{\nu}$ analysis |
| TDFOOL | same as $K^+ \rightarrow \pi^+ \nu \bar{\nu}$ analysis |
| RSHEX | same as $K^+ \rightarrow \pi^+ \nu \bar{\nu}$ analysis |
| TDACC | same as $K^+ \rightarrow \pi^+ \nu \bar{\nu}$ analysis |
| TDDFA | same as $K^+ \rightarrow \pi^+ \nu \bar{\nu}$ analysis |
| TMUBV | same as $K^+ \rightarrow \pi^+ \nu \bar{\nu}$ analysis |
| TMUADC | same as $K^+ \rightarrow \pi^+ \nu \bar{\nu}$ analysis |
| RBOX | same as $K^+ \rightarrow \pi^+ \nu \bar{\nu}$ analysis |
| EBOX | same as $K^+ \rightarrow \pi^+ \nu \bar{\nu}$ analysis |
| PBOX | same as $K^+ \rightarrow \pi^+ \nu \bar{\nu}$ analysis |

Table 4.23: Selection cuts applied to $K^+ \rightarrow \pi^+ \nu \bar{\nu}$ triggers for the DC/RS efficiency calculation, $A_{\pi scat}$

between \check{C}_π and TRS in the $K^+ \rightarrow \pi^+ \nu \bar{\nu}$ trigger itself. This sample was derived from the Pass 1 output data using the selection cuts lists in Table 4.23.

Before measuring the RS analysis efficiency, pions must be required to have kinematics typical of $K^+ \rightarrow \pi^+ \nu \bar{\nu}$. The total range-energy distribution for 1990 π scat pions from the $K^+ \rightarrow \pi^+ \nu \bar{\nu}$ data is shown in Figure 4.9. Clearly, many of the pions do not have kinematics typical of signal candidates, and some selection is desired.

We really need to know the efficiency of the RS analysis for pions “in-the-box;” however, since the box cut efficiency is calculated with UMC and the efficiency of the

RS analysis is energy dependent, there is a danger here of either under-counting or double-counting losses. For example, previous analyses have typically applied the RS analysis to the UMC data before measuring the box efficiency, but also used some kinematic selection of the π scat pions before the RS analysis efficiency measurement. $K^+ \rightarrow \pi^+ \nu \bar{\nu}$ events which fail both the RS analysis and the kinematic selection were not counted as a loss. Since these cuts are strongly correlated, I believe that technique yielded an optimistic assessment of the overall acceptance. The method used here is to measure the UMC-based box efficiency without the RS analysis, and then to measure the RS analysis efficiency only for pions in-the-box. The obvious problem with this method is the uncertainty resulting from the target analysis for π scats. Using a subjective judgment of typical target charged track kinematic errors for π scats, an error is assigned to this $A_{\pi\text{scat}}$ efficiency by varying the RBOX by ± 1 cm, EBOX by ± 3 MeV, and PBOX by ± 6 MeV/c.

Because the track kinematics affect the the RS analysis efficiency, it will vary with pion stopping layer. For reference, the $A_{\pi\text{scat}}$ efficiency is first calculated assuming stopping layer independence, so that the separate cuts can be readily examined, summarized in Table 4.24.

The final $A_{\pi\text{scat}}$ acceptance is calculated by measuring it in each stopping layer, and weighting by the stopping layer distribution for $K^+ \rightarrow \pi^+ \nu \bar{\nu}$ (and $K^+ \rightarrow \pi^+ X^0$) surviving the complete UMC analysis with nuclear interactions and decay-in-flight

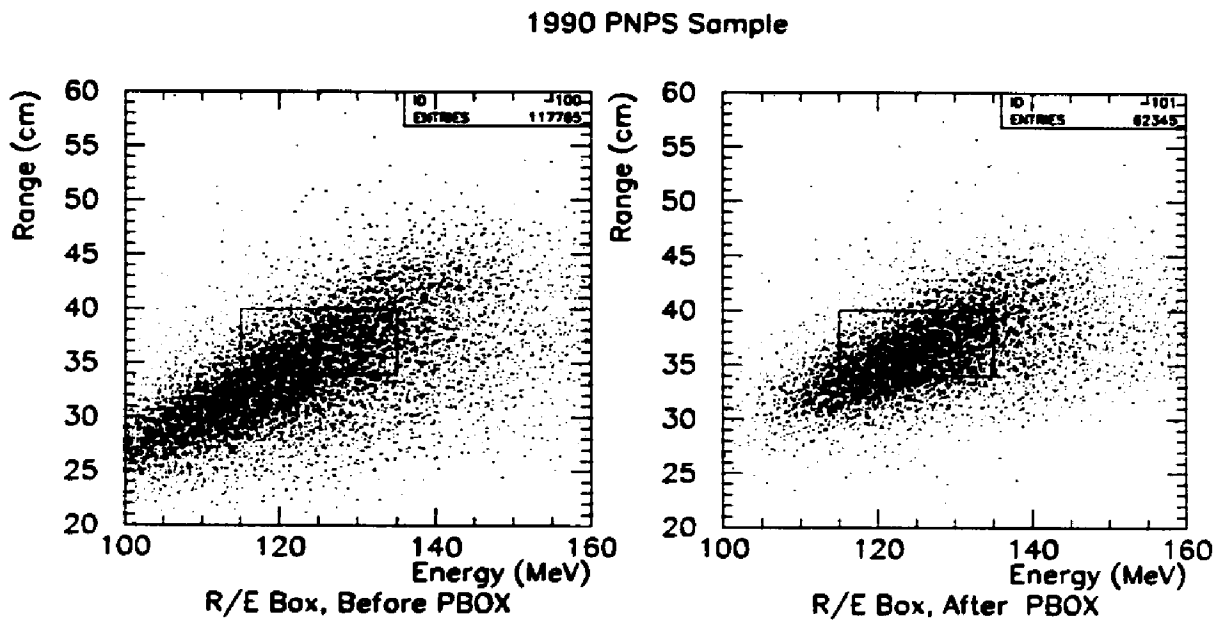


Figure 4.9: Total range vs. energy distributions for π scats from the $K^+ \rightarrow \pi^+ \nu\bar{\nu}$ trigger, before and after the PBOX cut. The range-energy box is overlaid. The sample in-the-box is used for the $A_{\pi\text{scat}}$ efficiency measurement.

| Description | 1989 | | 1990 | | 1991 | |
|-----------------------|---------------------|-------|---------------------|-------|---------------------|-------|
| | N _{passed} | A | N _{passed} | A | N _{passed} | A |
| Selection | 4197 | - | 5060 | - | 7028 | - |
| RNGMOM(2) | 4115 | 0.980 | 5009 | 0.990 | 7011 | 0.998 |
| RSDEDX | 3603 | 0.876 | 4348 | 0.868 | 6085 | 0.868 |
| CHIRF | 3586 | 0.995 | 4336 | 0.997 | 6067 | 0.997 |
| $A'_{\pi\text{scat}}$ | 0.854 ± 0.005 | | 0.857 ± 0.005 | | 0.865 ± 0.004 | |

Table 4.24: The acceptance of the RS analysis, assuming stopping layer independence.

| Description | 1989 | 1990 | 1991 |
|----------------------|------------------|------------------|------------------|
| Nominal box | 0.850 | 0.873 | 0.883 |
| bigger box | 0.837 | 0.856 | 0.869 |
| smaller box | 0.861 | 0.876 | 0.890 |
| $A_{\pi\text{scat}}$ | 0.850 ± 0.01 | 0.873 ± 0.01 | 0.883 ± 0.01 |

Table 4.25: The acceptance of the RS analysis weighted by $K^+ \rightarrow \pi^+ \nu\bar{\nu}$ stopping layer distribution. Error is inferred by varying the box cut used for selection as described in the text.

| Description | 1989 | 1990 | 1991 |
|----------------------|------------------|------------------|------------------|
| Nominal box | 0.875 | 0.893 | 0.904 |
| bigger box | 0.866 | 0.874 | 0.889 |
| smaller box | 0.889 | 0.906 | 0.907 |
| $A_{\pi\text{scat}}$ | 0.875 ± 0.01 | 0.893 ± 0.01 | 0.904 ± 0.01 |

Table 4.26: The acceptance of the RS analysis weighted by $K^+ \rightarrow \pi^+ X^0$ stopping layer distribution. Error is inferred by varying the box cut used for selection as described in the text.

enabled. The final $K^+ \rightarrow \pi^+ \nu\bar{\nu}$ $A_{\pi\text{scat}}$ is summarized in Table 4.25, and $K^+ \rightarrow \pi^+ X^0$ is summarized in Table 4.26.

A comment is in order about the higher value of $A_{\pi\text{scat}}$ for $K^+ \rightarrow \pi^+ X^0$ than for $K^+ \rightarrow \pi^+ \nu\bar{\nu}$. The RNGMOM acceptance is actually somewhat *lower* for $K^+ \rightarrow \pi^+ X^0$, but this is more than compensated for by the RSDEDX cut. The latter is a cut on the simple χ^2/dof , and is less efficient for smaller stopping layer events because they have fewer degrees of freedom. In retrospect, since this is a rather well behaved χ^2 , it is possible a better cut would have been on the confidence level inferred from the

χ^2 instead.

4.4 $K^+ \rightarrow \pi^+\pi^0$ measurements

4.4.1 Particle-type dependent losses in the target, $A_{K_{\pi 2}}$

Since π scats are messy in the target, they cannot be used to measure the acceptance of target particle-type dependent cuts. Instead, $K^+ \rightarrow \pi^+\pi^0$ events are selected from the $K_{\pi 2}(1)$ monitor trigger. To avoid double-counting losses, the following selection is used:

- Full online and offline delayed coincidence and timing cuts.
- All cuts evaluated with $K^+ \rightarrow \mu^+\nu_\mu$ except the online and offline γ veto in the RS, BV, and EC's.
- The full TD $\pi^+ \rightarrow \mu^+ \rightarrow e^+$ package
- $K^+ \rightarrow \pi^+\pi^0$ box cut in range, energy and momentum
- DIPANG
- PNNSTOP (only use stopping layers 11-18)

The acceptance calculation is in Table 4.27. Using the above selection, this acceptance could still be systematically low due to overlapping photons in the target; however, since $A_{K_{\pi 2}}$ is measured to be essentially unity, this was ignored.

| Description | 1989 | | 1990 | | 1991 | |
|--------------|---------------------|-------|---------------------|-------|---------------------|-------|
| | N _{passed} | A | N _{passed} | A | N _{passed} | A |
| Selection | 770 | - | 382 | - | 397 | - |
| TGDEDX | 767 | 0.996 | 377 | 0.987 | 394 | 0.992 |
| EPIMAX | 767 | 1.000 | 377 | 1.000 | 393 | 0.997 |
| $A_{K\pi_2}$ | 0.996 ± 0.002 | | 0.987 ± 0.006 | | 0.990 ± 0.005 | |

Table 4.27: The pion dependent target cuts, $A_{K\pi_2}$.

4.4.2 Level 1.5 energy trigger, $A_{L1.5}$

The final item in the acceptance calculation is the online level 1.5 energy cut. Several methods have been used in the past, using different models of RS energy resolution and effective online calibrations. Thanks to those heroic efforts [15, 16, 18], it is now well known that the acceptance is both very high and does not vary significantly using these different measurement methods. Accordingly, here I will use the simplest one.

The level 1.5 energy trigger cuts those events with more than 17024 ADC counts. For the $K^+ \rightarrow \pi^+ X^0$ acceptance, we use the $K^+ \rightarrow \pi^+\pi^0$ peak as a model of an energy delta function in the detector, and scale the level 1.5 cut using the nominal calibration of 128 counts/MeV and the 18.5 MeV separation between $K^+ \rightarrow \pi^+ X^0$ and $K^+ \rightarrow \pi^+\pi^0$ to an effective cut for $K^+ \rightarrow \pi^+\pi^0$'s:

$$\text{Effective Level 1.5 cut} = 17024 - 128 \times 18.5 = 14656 \text{ counts.}$$

We are interested only in the efficiency for pions that end up in our energy box, so we first apply an effective upper EBOX cut of $E < 135 \text{ MeV} - 18.5 \text{ MeV} = 116.5 \text{ MeV}$.

The selection applied to $K_{\pi 2}(1)$ triggers was:

- Full online plus offline delayed coincidence and timing cuts.
- DIPANG
- Online HEXTANT cut
- Beam cuts
- Target cuts
- Offline γ veto in the RS
- RNGMOM, RSDEDX
- LAY14, PRPAT, ZFRF, ZDCOW
- Full TD package

Following the notation of [16],

$$A_{L1.5} = \frac{(\# \text{ in spectrum}) - (\# \text{ failing EBOX}) - (\# \text{ failing L1.5})}{(\# \text{ in spectrum}) - (\# \text{ failing BOX})} = \frac{N_A}{N_A + N_C},$$

using the definitions of Figure 4.10.

The various factors for the $K^+ \rightarrow \pi^+ X^0$ efficiency are summarized in Table 4.28.

For $K^+ \rightarrow \pi^+ \nu\bar{\nu}$, the efficiency of the level 1.5 energy cut should be higher since the typical pion energy is lower than for $K^+ \rightarrow \pi^+ X^0$. The efficiency is calculated

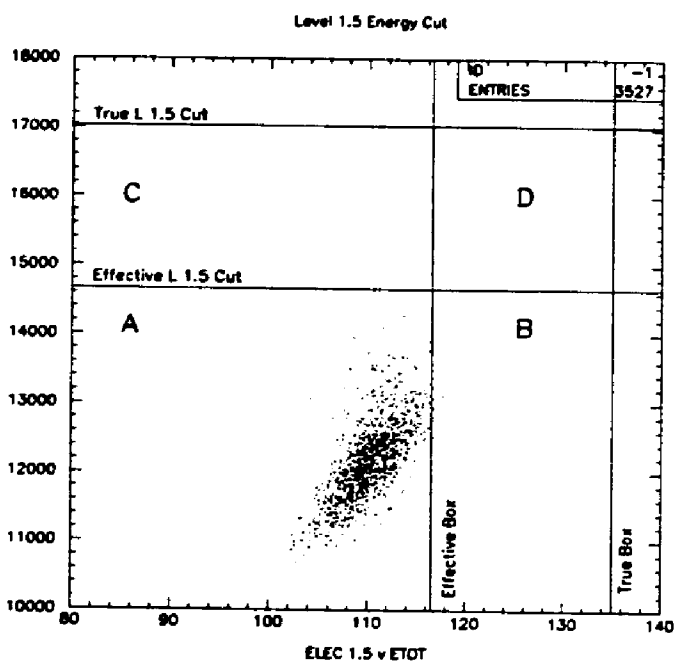


Figure 4.10: Regions in the level 1.5 energy trigger efficiency calculation.

| Description | 1989 | 1990 | 1991 |
|-------------|-------------------|-------------------|-------------------|
| $N_A + N_C$ | 3454 | 428 | 495 |
| N_A | 3401 | 423 | 489 |
| $A_{L1.5}$ | 0.985 ± 0.002 | 0.988 ± 0.005 | 0.988 ± 0.005 |

Table 4.28: The $K^+ \rightarrow \pi^+ X^0$ level 1.5 trigger efficiency measurement.

| Description | 1989 | 1990 | 1991 |
|-------------|-------------------|-------------------|-------------------|
| $A_{L1.5}$ | 0.996 ± 0.002 | 0.993 ± 0.005 | 0.994 ± 0.001 |

Table 4.29: The $K^+ \rightarrow \pi^+ \nu\bar{\nu}$ level 1.5 trigger efficiency measurement.

in 1 MeV bins of true pion energy. The first bin is identical to the $K^+ \rightarrow \pi^+ X^0$ calculation above. In the second bin, the above procedure is repeated, but the effective box is moved up by 1 MeV to 117.5 MeV, the effective level 1.5 cut is moved up by 128 counts to 14784 counts, and the efficiency is re-measured. This procedure is iterated to give the level 1.5 efficiency in bins of true pion energy, with the first 1 MeV-wide bin centred at the $K^+ \rightarrow \pi^+ \nu\bar{\nu}$ end-point, the second bin centred 1 MeV below the end-point, and so-on. The bin weights are the number of UMC generated $K^+ \rightarrow \pi^+ \nu\bar{\nu}$ events surviving the full analysis, using the true pion energies of the sample with nuclear interactions and decay-in-flight enabled in the simulation. The efficiency for $K^+ \rightarrow \pi^+ \nu\bar{\nu}$ is summarized in Table 4.29.

4.5 The beam kaon flux, N_{KTlive}

The unit of beam kaon flux, the KT , was defined in the online trigger as $\dot{C}_K \cdot B4 \cdot E_{TG}$; that is, a beam kaon with coincident energy in the B4 hodoscope and the target. Correcting for the online trigger dead-time results in $KTlive$, which is counted in scaler modules and read out with the data as “scaler records”. In principle, KOFIA counts

these records for us, and the value can simply be looked up directly in the offline analysis; in practice, adding up the number of $KTlive$'s requires some care.

There are a number of things that can go wrong with the $KTlive$ accounting:

- Data can be split up with events from a single run going to multiple output files, but with all the scaler records going to all the output files. This is a particular problem when analyzing 1989 data, where a large fraction of $K^+ \rightarrow \pi^+ \nu\bar{\nu}$ data is only available in this form. When these data files are later recombined, the same scaler records show up multiple times. For the later analysis and accounting, it is important to note that these runs were recombined sequentially, so that data from a given run is encountered in multiple sequential files, and then the next run is found in the next set of files, and so-on. The right thing to do with this data is to analyze all the events, but to only count the scaler records from any given run once. In the original 1989 analysis [16], Akerib handled this by building a data-base of $KTlive$'s for each run, and only counting $KTlive$'s once per run. To the best of my knowledge, no one except Akerib ever counted the 1989 $K^+ \rightarrow \pi^+ \nu\bar{\nu}$ $KTlive$'s, since any KOFIA-based scheme yields about 35% more apparent kaon flux than his measured 1.75×10^{11} .
- Known hardware problems make us exclude some data from the analysis. For example, in 1990 a number of runs from the beginning of the year were excluded due to a bug in the online data-compaction software. Used with caution, KOFIA

is able to handle this by excluding these runs entirely from the analysis. In 1989, a number of runs interspersed throughout the year were excluded due to a hardware problem in the TD system. KOFIA has no capacity for handling this case, although Akerib's scheme permitted him to exclude these bad runs from his count by selectively removing them from his data-base, while also excluding the data from these runs from the analysis.

- Runs can be accidentally included multiple times in the analysis, usually due to operator-error while handling data. Sometimes, the full run appears twice, but it is also possible for the full run to appear once while a partial copy of it appears the second time (presumably, this was caused by problems while running Pass 1). Usually, these multiple copies of a given run are separated by data from other runs. Counting the $KTlive$'s for a given run only once fixes this problem too, but in this case the data from the multiple occurrences of the run should not be analyzed.
- It is not uncommon for an end-of-file (EOF) mark to appear *inside* a run, put there either in the data acquisition system or in the subsequent data handling. This is equivalent to data from a given run (together with the scaler records associated with only that data) being split off into multiple streams and later recombined sequentially. The correct thing to do in this case is to analyze all the data *and* count all the scaler records. This is extremely common in the

1990 $K^+ \rightarrow \pi^+ \nu \bar{\nu}$ data, and is also present at a smaller level in the 1989 and 1991 data sets. This has the unfortunate effect of breaking Akerib's data-base scheme; since his data base includes one entry per EOF mark, he only counted the number of $KTlive$'s before the anomalous EOF, while analyzing the data from the entire run.

For this analysis, the 1989 $KTlive$ total is counted by returning to Akerib's original data-base, but adjusting the counting method. The scaler records were saved with the data right up to the Pass 3 stage, where the entire year can be stored in one file. In Pass 3, each time the run number changes, the analysis notes that the old run is completed. It will never analyze data with that run number again, but it does record each subsequent occurrence of data with that run number in its log. The entries corresponding to these additional copies of a run are removed from the $KTlive$ data-base by hand. Note that it analyzes data with the same run number on both sides of an EOF mark, which is essential given the state of our data set. The data-base is further modified, removing all entries with the same run number *and* a duplicate $KTlive$ count as another entry. This eliminates the bulk of entries with multiple copies of the same scaler records, although it is possible for anomalies in the record-keeping to include partial copies of the same $KTlive$ records in the data-base, which still must be removed. All remaining duplicate run number entries are examined by hand, by comparing the total number of $KTLive$'s and the apparent Pass 1 rejection

(Akerib recorded the number of survivors of his original 1989 Pass 1 in the data-base) with nearby runs. This comparison allows essentially all duplicates to be reliably removed. Finally, the 1989 $KTlive$ total is counted from the remaining data-base; it is about 1% larger than Akerib's original number, presumably due to including otherwise intact runs containing an internal EOF mark.

For the 1990 and 1991 data sets, a simpler scheme is used. While multiple copies of a given run on the Pass 1 output tapes are not particularly rare, multiple copies of the same scalers in files with different events from the same run is not a significant problem. As with 1989, the analysis notes the run number change and will not analyze data with that run number again. The difference from 89 is that a running scaler total is maintained by adding up the $KTlive$'s every time a record is encountered; by using the same multi-run veto as the analysis, a completely self-consistent count of $KTlive$'s for the data analyzed results. Of course, as with most things, it is necessary to bypass the default KOFIA code to get a good approximation to the right answer.

The resulting beam kaon flux is listed for 1989, 1990, and 1991 data in Table 4.30.

| Year | First Run | Last Run | Number Runs | N_{KTlive} |
|-------|-----------|----------|-------------|-------------------------|
| 1989 | 3728 | 6148 | 1659 | 1.7688×10^{11} |
| 1990 | 6749 | 8429 | 1169 | 2.1178×10^{11} |
| 1991 | 9018 | 10141 | 609 | 1.4554×10^{11} |
| Total | - | - | 3437 | 5.3647×10^{11} |

Table 4.30: The run ranges analyzed, and the kaon flux into the target with the detector “live.”

4.6 The $K^+ \rightarrow \mu^+ \nu_\mu$ branching ratio and kaon stopping fraction, f_s

The $K^+ \rightarrow \mu^+ \nu_\mu$ branching ratio is used for a stopping-flux normalization factor f_s .

The most important factor is the fraction of $KTlive$'s that come to a stop in the target and decay as a K^+ . One third of the $K_{\mu 2}(1)$ monitor triggers spanning the same run ranges as the $K^+ \rightarrow \pi^+ \nu \bar{\nu}$ data are analyzed with the cuts outlined in Table 4.31.

With a 63% branching ratio, $K^+ \rightarrow \mu^+ \nu_\mu$ is easy to select. The trigger already has a severe range cut, requiring that the track penetrate to least to RS layer 19. The full online and offline delayed coincidence and timing cuts are used to insure decays at rest, the beam cuts remove π scats, and the full RS, BV, EC, IC and VC γ -veto cuts insure basic event cleanliness.⁵

The efficiency for a $K^+ \rightarrow \mu^+ \nu_\mu$ decay at rest satisfying the $K_{\mu 2}(1)$ trigger and the

⁵Since the $K^+ \rightarrow \mu^+ \nu_\mu$ branching ratio analysis does not veto events that may have penetrated to the barrel veto, the five BV sectors behind the apparent range stack stopping counter are not used in the offline photon veto.

| Description | 1989 | 1990 | 1991 |
|-------------|---------------------|---------------------|---------------------|
| | N _{passed} | N _{passed} | N _{passed} |
| Prescale | 94929 | 107023 | 64430 |
| L0DELC | 67894 | 78071 | 43222 |
| ISKCODE | 54287 | 69150 | 38294 |
| DIPANG | 51850 | 66744 | 36946 |
| PICER | 49700 | 64414 | 35790 |
| PISCAT_BW | 43917 | 56733 | 31331 |
| B4DEDX | 43359 | 56012 | 30757 |
| B4TDEDX | 43324 | 55560 | - |
| B4TFIT | 42703 | 53122 | - |
| PISCAT_B4 | - | - | 28969 |
| PBGLASS | - | - | 27963 |
| PIHODO_B4 | 40085 | 49606 | - |
| GAMVET | 32968 | 39346 | 21650 |
| DELCA | 28640 | 35254 | 18792 |
| TIMCON | 26347 | 33108 | 18471 |

Table 4.31: The $K^+ \rightarrow \mu^+ \nu_\mu$ branching ratio analysis.

DIPANG cut is measured with UMC, and summarized in Table 4.32. This efficiency depends on the average range stack scintillator thickness used in the simulation. The RS scintillator thickness was nominally specified as 3/4 inch (1.905 cm) per layer. In previous analyses, using the value 1.95 cm in UMC has been somewhat more popular, but it is unreasonable to assume that the “correct” value is known to better than somewhere near this thickness.⁶ For this analysis, both 1.905 cm and 1.95 cm are tried for the acceptance calculation; the average is used for the f_S measurement, and the difference is used for the (approximately 4%) error.⁷ It is worth emphasizing that, by design, the $K^+ \rightarrow \pi^+ \nu\bar{\nu}$ and $K^+ \rightarrow \pi^+ X^0$ acceptances are essentially independent of small variations of this assumption; unfortunately, since our sensitivity is normalized to the $K^+ \rightarrow \mu^+ \nu_\mu$ branching ratio, it has become dependent on a parameter that we do not know very well.

The $K^+ \rightarrow \mu^+ \nu_\mu$ acceptance also requires a self-consistent measurement of the remaining cuts in the analysis in Table 4.31. The delayed coincidence and timing cut measurement (A_{DC}) should still apply, but a new beam and photon veto acceptance (A_{rest}) must be measured. In Table 4.15, the beam cut acceptance was evaluated after

⁶A brief study was undertaken varying the UMC RS scintillator thickness parameter, and comparing the $K^+ \rightarrow \mu^+ \nu_\mu$ and $K^+ \rightarrow \pi^+ \pi^0$ stopping layer distributions between data and KOFIA reconstructed UMC. The $K^+ \rightarrow \mu^+ \nu_\mu$ ’s favoured about 1.97 cm, while the $K^+ \rightarrow \pi^+ \pi^0$ ’s favoured about 1.91 cm.

⁷It is tempting to reject events that penetrate to the outer RS layer for the branching ratio analysis so that clean range and energy measurements are available for $K^+ \rightarrow \mu^+ \nu_\mu$ selection, as was done in [18]. The variation of the $K^+ \rightarrow \mu^+ \nu_\mu$ acceptance between the 1.905 cm and 1.95 cm RS scintillator assumptions increases to about 10% if such a selection is used. Since that selection is not needed to get a clean $K^+ \rightarrow \mu^+ \nu_\mu$ sample, it is not used here.

| Cut | N _{passed} 1989 | | N _{passed} 1990 | | N _{passed} 1991 | |
|---------------------------------|--------------------------|---------|--------------------------|---------|--------------------------|---------|
| | 1.905 cm | 1.95 cm | 1.905 cm | 1.95 cm | 1.905 cm | 1.95 cm |
| KT | 95083 | 95197 | 95238 | 95310 | 95132 | 95066 |
| Trigger | 36634 | 34895 | 36725 | 35359 | 36480 | 35005 |
| ISKCODE | 35880 | 34166 | 35973 | 34675 | 35732 | 34304 |
| DIPANG | 35195 | 33681 | 35295 | 34191 | 35031 | 33738 |
| $A_{\text{recon}}^{\text{umc}}$ | 0.979 | 0.979 | 0.980 | 0.981 | 0.979 | 0.980 |
| $A_{K_{\mu 2}}^{\text{umc}}$ | 0.370 | 0.354 | 0.371 | 0.359 | 0.368 | 0.355 |
| $A_{K_{\mu 2}}^{\text{umc}}$ | 0.362 ± 0.016 | | 0.365 ± 0.012 | | 0.362 ± 0.013 | |

Table 4.32: The UMC $K^+ \rightarrow \mu^+ \nu_\mu$ analysis efficiency, for assumed range stack layer thicknesses 1.905 cm and 1.95 cm. The total efficiency of the analysis is $A_{K_{\mu 2}}^{\text{umc}}$. The reconstruction efficiency, $A_{\text{recon}}^{\text{umc}}$, for UMC data is the fraction of events passed by ISKCODE, and will be used in the branching ratio calculation below.

the target analysis which is not applied in the $K^+ \rightarrow \mu^+ \nu_\mu$ branching ratio calculation. Since the losses of the beam cuts are strongly correlated with the target losses, a new measurement is required. This was done with the $K_{\mu 2}(1)$ monitor sample used for the $A_{K_{\mu 2}}$ above, but using only the remaining cuts from Table 4.31. The basic reconstruction efficiency A_{recon} should apply here, but it is partially included already in the $A_{K_{\mu 2}}^{\text{umc}}$ factor. For example, when the UMC generated $K^+ \rightarrow \mu^+ \nu_\mu$ sample is analyzed, some events will not be successfully fit by the drift chamber code, and this loss is counted in $A_{K_{\mu 2}}^{\text{umc}}$; however, this loss is already counted in the A_{recon} measurement. This double-counting is removed using the $A_{\text{recon}}^{\text{umc}}$ factor from Table 4.32.

Finally, a consistent measurement of the effective number of KT_{live} 's used for the branching ratio measurement is needed. In principle, the KT_{live} measurement from the $K^+ \rightarrow \pi^+ \nu \bar{\nu}$ analysis can simply be corrected for the monitor trigger prescale

| Quantity | 1989 | 1990 | 1991 |
|---------------------------------------|------------------------|------------------------|------------------------|
| KT_{live} | 1.816×10^{11} | 1.998×10^{11} | 1.266×10^{11} |
| # $K_{\mu 2}(1)$ triggers | 3.749×10^{10} | 4.211×10^{10} | 2.551×10^{10} |
| Triggers analyzed | 94920 | 107023 | 64430 |
| $N_{KT_{\text{live}}}^{\text{equiv}}$ | 459809 | 507912 | 319836 |

Table 4.33: The KT_{live} calculation for the $K^+ \rightarrow \mu^+ \nu_\mu$ branching ratio calculation.

factor, along with any additional offline prescale factor used in sample selection; in practice, the somewhat lax handling of monitor tapes makes it essential to re-measure this by counting the scaler records stored with the data during the branching ratio analysis. The effective number of KT_{live} 's is then

$$N_{KT_{\text{live}}}^{\text{equiv}} = (\# KT_{\text{live}}) \frac{\# \text{ triggers analyzed}}{\# \text{ raw } K_{\mu 2}(1) \text{ triggers}},$$

where the “# KT_{live} ” and “# raw $K_{\mu 2}(1)$ triggers” entries are counted from the scalers stored with the data in the branching ratio analysis, and “# triggers analyzed” is the number of events to enter the branching ratio analysis. This is summarized in Table 4.33. It is worth noting that the inferred $K_{\mu 2}(1)$ prescale factor from this count agrees well with the expected value (131072 from the online trigger prescale factor, times the factor of 3 used offline in all three years).

The $K^+ \rightarrow \mu^+ \nu_\mu$ branching ratio is given by

$$B_{K_{\mu 2}} = \frac{(\# K_{\mu 2})_{\text{anal}}}{f_S N_{KT_{\text{live}}}^{\text{equiv}}} \frac{1}{A_{K_{\mu 2}}^{\text{unc}}} \left(\frac{A_{\text{recon}}^{\text{unc}}}{A_{\text{recon}}^{\text{data}}} \right)_{K_{\mu 2}} \frac{1}{A_{\text{DC}}} \frac{1}{A_{\text{rest}}},$$

| Quantity | 1989 | 1990 | 1991 |
|------------------------------------|-------------------|-------------------|-------------------|
| $(\# K_{\mu 2})_{\text{anal}}$ | 26347 | 33108 | 18471 |
| $B_{K_{\mu 2}}$ | 0.6351 | 0.6351 | 0.6351 |
| $N_{KT\text{live}}^{\text{equiv}}$ | 459809 | 507912 | 319836 |
| $A_{K_{\mu 2}}^{\text{umc}}$ | 0.362 ± 0.016 | 0.365 ± 0.012 | 0.362 ± 0.013 |
| $A_{\text{recon}}^{\text{umc}}$ | 0.979 ± 0.001 | 0.980 ± 0.001 | 0.979 ± 0.001 |
| $A_{\text{recon}}^{\text{data}}$ | 0.811 ± 0.01 | 0.898 ± 0.01 | 0.897 ± 0.01 |
| A_{DC} | 0.732 ± 0.005 | 0.743 ± 0.005 | 0.769 ± 0.008 |
| A_{rest} | 0.609 ± 0.005 | 0.607 ± 0.005 | 0.604 ± 0.006 |
| f_S | 0.675 ± 0.03 | 0.681 ± 0.03 | 0.590 ± 0.02 |

Table 4.34: The f_S calculation. In 1991, changes in the beam instrumentation may be responsible for the lower stopping fraction that year.

which is trivially solved for f_S :

$$f_S = \frac{(\# K_{\mu 2})_{\text{anal}}}{B_{K_{\mu 2}} N_{KT\text{live}}^{\text{equiv}}} \frac{1}{A_{K_{\mu 2}}^{\text{umc}}} \left(\frac{A_{\text{recon}}^{\text{umc}}}{A_{\text{recon}}^{\text{data}}} \right)_{K_{\mu 2}} \frac{1}{A_{\text{DC}}} \frac{1}{A_{\text{rest}}}.$$

The f_S calculation is summarized in Table 4.34.

4.7 The $K^+ \rightarrow \pi^+\pi^0$ branching ratio

The $K^+ \rightarrow \pi^+\pi^0$ branching ratio is measured and used for a cross-check of the TD fitter acceptance calculation and the UMC nuclear interactions simulation. A set of $K_{\pi 2}(1)$ monitors spanning the same run ranges as the $K^+ \rightarrow \pi^+\nu\bar{\nu}$ analysis is used.

The online and offline delayed coincidence and timing cuts are used, along with the beam analysis. The basic FITPI TD $\pi^+ \rightarrow \mu^+$ cut is applied. Since the TD's are only well calibrated in the $K^+ \rightarrow \pi^+\nu\bar{\nu}$ stopping layers, the pions are required to

| Description | 1989 | 1990 | 1991 |
|-------------|---------------------|---------------------|---------------------|
| | N _{passed} | N _{passed} | N _{passed} |
| Prescale | 212952 | 91450 | 145039 |
| LODELC | 129494 | 57729 | 80199 |
| ISKCODE | 95085 | 46589 | 64849 |
| PNNSTOP | 67593 | 32930 | 45482 |
| DIPANG | 58703 | 29179 | 40109 |
| KP2BRBOX | 27126 | 13305 | 18282 |
| PICER | 25962 | 12863 | 17782 |
| PISCAT_BW | 23123 | 11426 | 15713 |
| B4DEDX | 22792 | 11294 | 15409 |
| B4TDEDX | 22779 | 11199 | - |
| PISCAT_B4 | - | - | 14370 |
| PBGLASS | - | - | 13615 |
| PIHODO_B4 | 20783 | 9835 | - |
| DELС | 18227 | 8831 | 11805 |
| TIMCON | 16599 | 8281 | 11578 |
| FITPI | 10439 | 4914 | 7724 |

Table 4.35: The $K^+ \rightarrow \pi^+\pi^0$ branching ratio analysis.

penetrate to at least layer 11. A total range cut ($26 \text{ cm} \leq R_{\text{tot}}^{\text{new}} \leq 34 \text{ cm}$) is used to select $K^+ \rightarrow \pi^+\pi^0$ candidates. The analysis is summarized in Table 4.35.

The $K^+ \rightarrow \pi^+\pi^0$ acceptance calculation is done with UMC, and summarized in Table 4.36. As with the $K^+ \rightarrow \pi^+\nu\bar{\nu}$ analysis, the TD efficiency assumes that the pion was still a π^+ when it stopped. The inefficiencies due to decay-in-flight, nuclear interactions and finding the incorrect stopping counter are measured here using the UFATE, USTMED, and USTOP_HEX cuts.

As with the $K^+ \rightarrow \mu^+\nu_\mu$ measurement, the effective number of $KTlive$'s must be measured for the $K^+ \rightarrow \pi^+\pi^0$ analysis, summarized in Table 4.37. Again, the inferred

| Cut | N _{passed} 1989 | | N _{passed} 1990 | | N _{passed} 1991 | |
|---------------------------------|--------------------------|---------|--------------------------|---------|--------------------------|---------|
| | 1.905 cm | 1.95 cm | 1.905 cm | 1.95 cm | 1.905 cm | 1.95 cm |
| KT | 95039 | 47588 | 47603 | 47659 | 47494 | 47489 |
| Trigger | 34076 | 17122 | 17270 | 17244 | 17028 | 17165 |
| UFATE | 28771 | 14452 | 14631 | 14582 | 14318 | 14603 |
| USTMED | 27404 | 13724 | 13929 | 13920 | 13660 | 13942 |
| ISKCODE | 24823 | 12473 | 12612 | 12688 | 12370 | 12698 |
| PNNSTOP | 17620 | 8465 | 8994 | 8662 | 8711 | 8455 |
| USTOP_HEX | 16831 | 8087 | 8610 | 8238 | 8357 | 8063 |
| DIPANG | 16373 | 7888 | 8412 | 8035 | 8091 | 7870 |
| KP2BRBOX | 16065 | 7775 | 8140 | 7926 | 7947 | 7736 |
| $A_{\text{recon}}^{\text{umc}}$ | 0.906 | 0.909 | 0.905 | 0.911 | 0.906 | 0.911 |
| $A_{K_{\pi 2}}^{\text{umc}}$ | 0.169 | 0.163 | 0.171 | 0.166 | 0.167 | 0.163 |
| $A_{K_{\pi 2}}^{\text{umc}}$ | 0.166 ± 0.006 | | 0.169 ± 0.005 | | 0.165 ± 0.004 | |

Table 4.36: The UMC $K^+ \rightarrow \pi^+\pi^0$ analysis efficiency, for assumed range stack layer thicknesses 1.905 cm and 1.95 cm (the PNNSTOP cut introduces the scintillator thickness dependency). $A_{\text{recon}}^{\text{umc}}$ is the basic reconstruction efficiency for the UMC data.

| Quantity | 1989 | 1990 | 1991 |
|---------------------------------------|------------------------|------------------------|------------------------|
| KT_{live} | 1.761×10^{11} | 1.998×10^{11} | 1.263×10^{11} |
| # $K_{\pi 2}(1)$ triggers | 2.647×10^{10} | 3.011×10^{10} | 1.909×10^{10} |
| Trigger analyzed | 212952 | 91450 | 145039 |
| $N_{KT_{\text{live}}}^{\text{equiv}}$ | 1417137 | 606967 | 959941 |

Table 4.37: The KT_{live} calculation for the $K^+ \rightarrow \pi^+ \pi^0$ branching ratio calculation.

$K_{\pi 2}(1)$ prescale factor agrees with the expected value (20480, 65536 and 131072 online times 6, 5 or 1 offline in 1989, 1990 and 1991 respectively).

The $K^+ \rightarrow \pi^+ \pi^0$ branching ratio is given by

$$B_{K_{\pi 2}} = \frac{(\# K_{\pi 2})_{\text{anal}}}{f_S N_{KT_{\text{live}}}^{\text{equiv}}} \frac{1}{A_{K_{\pi 2}}^{\text{umc}}} \left(\frac{A_{\text{recon}}^{\text{umc}}}{A_{\text{recon}}^{\text{data}}} \right)_{K_{\pi 2}} \frac{1}{A_{\text{DC}}} \frac{1}{A_{\text{rest}}} \frac{1}{A_{\text{tdfit}}}.$$

Normalizing to the $K^+ \rightarrow \mu^+ \nu_\mu$ measurement,

$$B_{K_{\pi 2}} = B_{K_{\mu 2}} \frac{(\# K_{\pi 2})_{\text{anal}}}{(\# K_{\mu 2})_{\text{anal}}} \frac{(N_{KT_{\text{live}}}^{\text{equiv}})_{K_{\mu 2}}}{(N_{KT_{\text{live}}}^{\text{equiv}})_{K_{\pi 2}}} \frac{A_{K_{\mu 2}}^{\text{umc}}}{A_{K_{\pi 2}}^{\text{umc}}} \frac{(A_{\text{recon}}^{\text{umc}}/A_{\text{recon}}^{\text{data}})_{K_{\pi 2}}}{(A_{\text{recon}}^{\text{umc}}/A_{\text{recon}}^{\text{data}})_{K_{\mu 2}}} \frac{(A_{\text{rest}})_{K_{\mu 2}}}{(A_{\text{rest}})_{K_{\pi 2}}} \frac{1}{A_{\text{tdfit}}}.$$

The factor $(A_{\text{rest}})_{K_{\pi 2}}$ is really just the beam analysis, so the ratio $(A_{\text{rest}})_{K_{\mu 2}}/(A_{\text{rest}})_{K_{\pi 2}}$ is the acceptance of the photon veto cuts $A_{\bar{\gamma}}$, which can be directly inferred from the $K_{\mu 2}(1)$ measurements in Table 4.15. A_{tdfit} is the basic FITPI acceptance, from Table 4.20.

Correct treatment of the ratio of reconstruction efficiencies requires more thought.

Define the double ratio R :

$$R = \frac{(A_{\text{recon}}^{\text{umc}}/A_{\text{recon}}^{\text{data}})_{K_{\pi 2}}}{(A_{\text{recon}}^{\text{umc}}/A_{\text{recon}}^{\text{data}})_{K_{\mu 2}}}.$$

| Propagate γ 's | Nuclear Interactions | Decay-in-flight | $A_{\text{recon}}^{\text{umc}}$ |
|-----------------------|----------------------|-----------------|---------------------------------|
| yes | yes | yes | 0.906 ± 0.001 |
| yes | no | no | 0.927 ± 0.002 |
| no | yes | yes | 0.957 ± 0.002 |
| no | no | yes | 0.972 ± 0.002 |

Table 4.38: The KOFIA reconstruction efficiency for UMC $K^+ \rightarrow \pi^+\pi^0$ under various conditions. The range stack scintillator thickness parameter was set to 1.905 cm for all trials. The corresponding $A_{\text{recon}}^{\text{umc}}$ for $K^+ \rightarrow \mu^+\nu_\mu$ is 0.979 ± 0.001

Two strategies have been used in previous analyses. In the original 89 analysis [16], $A_{\text{recon}}^{\text{data}}$ was taken to be equal for $K^+ \rightarrow \pi^+\pi^0$ and $K^+ \rightarrow \mu^+\nu_\mu$, so $R = (A_{\text{recon}}^{\text{umc}})_{K_{\pi 2}} / (A_{\text{recon}}^{\text{umc}})_{K_{\mu 2}} \neq 1$. In Turcot's analysis [18] $R = 1$. Inspection of Tables 4.32 ($(A_{\text{recon}}^{\text{umc}})_{K_{\mu 2}}$) and 4.36 ($(A_{\text{recon}}^{\text{umc}})_{K_{\pi 2}}$) shows that the two strategies yield nearly a 10% difference in the measured $K^+ \rightarrow \pi^+\pi^0$ branching ratio. It is important to understand the reason that $A_{\text{recon}}^{\text{umc}}$ is lower for $K^+ \rightarrow \pi^+\pi^0$ than for $K^+ \rightarrow \mu^+\nu_\mu$. If it is entirely due to the presence of photons, then the $K^+ \rightarrow \mu^+\nu_\mu$ based A_{recon} may still be a good measurement of the reconstruction efficiency for clean, isolated pions from a $K^+ \rightarrow \pi^+$ decay, and may be used in our rare decay acceptance; however, if some component of the lower value of the $K^+ \rightarrow \pi^+\pi^0$ reconstruction efficiency is due to particle type or energy, then A_{recon} from Table 4.14 might not be appropriate for $K^+ \rightarrow \pi^+\nu\bar{\nu}$ at all. This is investigated by reconstructing UMC $K^+ \rightarrow \pi^+\pi^0$ events with various combinations of propagating or dropping photons, and enabling or disabling nuclear interactions, summarized in Table 4.38.

Inspection of the results shows that photons are indeed the biggest effect (about 3%), but nuclear interactions (presumably elastic scattering since the events passed the UFATE cut which is applied before $A_{\text{recon}}^{\text{umc}}$ is measured) are almost as large (about 2%). With both nuclear interactions and photon propagation turned off, the efficiency recovers almost fully to 0.972 ± 0.002 (compared to $A_{\text{recon}}^{\text{umc}} = 0.979 \pm 0.001$ for UMC $K^+ \rightarrow \mu^+ \nu_\mu$), so hopefully there are no large, hidden pion or energy dependent losses.⁸ For $K^+ \rightarrow \pi^+ \nu \bar{\nu}$, there are no photons and the loss due to nuclear interactions is accounted for in A_{nifit} , so A_{recon} from Table 4.14 may still be OK. For the $K^+ \rightarrow \pi^+ \pi^0$ branching ratio measurement, these losses are properly built into $A_{K_{\pi^2}}^{\text{umc}}$ and are not double counted, thus it is appropriate to use $R = 1$ here.

The $K^+ \rightarrow \pi^+ \pi^0$ branching ratio becomes

$$B_{K_{\pi^2}} = B_{K_{\mu^2}} \frac{(\# K_{\pi^2})_{\text{anal}}}{(\# K_{\mu^2})_{\text{anal}}} \frac{(N_{KT\text{live}}^{\text{equiv}})_{K_{\mu^2}}}{(N_{KT\text{live}}^{\text{equiv}})_{K_{\pi^2}}} \frac{A_{K_{\mu^2}}^{\text{umc}}}{A_{K_{\pi^2}}^{\text{umc}}} A_{\gamma} \frac{1}{A_{\text{tdfit}}}.$$

The full $K^+ \rightarrow \pi^+ \pi^0$ branching ratio measurement is summarized in Table 4.39. Averaged over all three years, the measurement is 0.205 ± 0.008 . This agrees well with the accepted value of 0.2116 ± 0.0014 .

4.8 Putting it all together

The complete $K^+ \rightarrow \pi^+ \nu \bar{\nu}$ and $K^+ \rightarrow \pi^+ X^0$ efficiency calculations are summarized in Tables 4.40 and 4.41 respectively. The error on each term is realistic, except for

⁸At least, none present in the simulation.

| Quantity | 1989 | 1990 | 1991 |
|--|-------------------|-------------------|-------------------|
| $B_{K_{\mu 2}}$ | 0.6351 | 0.6351 | 0.6351 |
| (# $K_{\mu 2}$) _{anal} | 26347 | 33108 | 18471 |
| (# $K_{\pi 2}$) _{anal} | 10439 | 4914 | 7724 |
| (N_{KTlive}^{equiv}) _{$K_{\mu 2}$} | 459809 | 507912 | 319836 |
| (N_{KTlive}^{equiv}) _{$K_{\pi 2}$} | 1417137 | 606967 | 959941 |
| $A_{K_{\mu 2}}^{unc}$ | 0.362 ± 0.016 | 0.365 ± 0.012 | 0.362 ± 0.013 |
| $A_{K_{\pi 2}}^{unc}$ | 0.166 ± 0.006 | 0.169 ± 0.005 | 0.165 ± 0.004 |
| A_{γ} | 0.853 ± 0.004 | 0.825 ± 0.004 | 0.789 ± 0.005 |
| A_{tdfit} | 0.754 ± 0.05 | 0.721 ± 0.03 | 0.697 ± 0.03 |
| $B_{K_{\pi 2}}$ | 0.201 ± 0.016 | 0.195 ± 0.012 | 0.220 ± 0.013 |
| Average $B_{K_{\pi 2}}$ | 0.205 ± 0.008 | | |

Table 4.39: The $K^+ \rightarrow \pi^+ \pi^0$ branching ratio measurement. The accepted value is 0.2116 ± 0.0014 , so the measurement is about 3% low (a 0.75σ discrepancy).

the unknown uncertainties in the nuclear interaction simulation implicit in A_{nidif} ; the only bound on that error is the $K^+ \rightarrow \pi^+ \pi^0$ branching ratio measurement.

The sensitivity for the complete analysis is the sum of the sensitivities for the three years of data:

$$S_{tot} = \sum_{89,90,91} S_i = \sum_{89,90,91} (A_{tot} f_S N_{KTlive})_i.$$

The total sensitivity calculation is summarized in Table 4.42 for $K^+ \rightarrow \pi^+ \nu \bar{\nu}$, and Table 4.43 for $K^+ \rightarrow \pi^+ X^0$. In the sensitivity calculation, errors common to f_S and A_{tot} are removed, since they will cancel in the product.

| Factor | 1989 | 1990 | 1991 |
|-------------------------------|----------------------------------|----------------------------------|----------------------------------|
| A_{trig} | 0.183 ± 0.001 | 0.186 ± 0.001 | 0.183 ± 0.001 |
| A_{umc} | 0.324 ± 0.003 | 0.329 ± 0.003 | 0.324 ± 0.003 |
| A_{nivid} | 0.478 ± 0.004 | 0.491 ± 0.009 | 0.499 ± 0.009 |
| A_{recon} | 0.811 ± 0.01 | 0.898 ± 0.01 | 0.897 ± 0.01 |
| $A_{K_{\mu 2}}$ | 0.533 ± 0.005 | 0.476 ± 0.005 | 0.446 ± 0.007 |
| $A_{\text{L14}}^{\text{acc}}$ | 0.994 ± 0.007 | 0.991 ± 0.008 | 0.990 ± 0.008 |
| A_{DC} | 0.732 ± 0.005 | 0.743 ± 0.005 | 0.769 ± 0.008 |
| A_{TD} | 0.369 ± 0.02 | 0.345 ± 0.015 | 0.321 ± 0.015 |
| $A_{\pi \text{scat}}$ | 0.850 ± 0.01 | 0.873 ± 0.01 | 0.883 ± 0.01 |
| $A_{K_{\pi 2}}$ | 0.996 ± 0.002 | 0.987 ± 0.006 | 0.990 ± 0.005 |
| $A_{\text{L1.5}}$ | 0.996 ± 0.002 | 0.993 ± 0.005 | 0.994 ± 0.001 |
| A_{tot} | $(2.77 \pm 0.17) \times 10^{-3}$ | $(2.78 \pm 0.15) \times 10^{-3}$ | $(2.51 \pm 0.15) \times 10^{-3}$ |

Table 4.40: The complete $K^+ \rightarrow \pi^+ \nu \bar{\nu}$ efficiency.

| Factor | 1989 | 1990 | 1991 |
|-------------------------------|----------------------------------|----------------------------------|----------------------------------|
| A_{trig} | 0.399 ± 0.001 | 0.401 ± 0.001 | 0.393 ± 0.001 |
| A_{umc} | 0.728 ± 0.002 | 0.743 ± 0.002 | 0.750 ± 0.002 |
| A_{nivid} | 0.449 ± 0.004 | 0.463 ± 0.004 | 0.465 ± 0.004 |
| A_{recon} | 0.811 ± 0.01 | 0.898 ± 0.01 | 0.897 ± 0.01 |
| $A_{K_{\mu 2}}$ | 0.533 ± 0.005 | 0.476 ± 0.005 | 0.446 ± 0.007 |
| $A_{\text{L14}}^{\text{acc}}$ | 0.992 ± 0.004 | 0.989 ± 0.004 | 0.988 ± 0.005 |
| A_{DC} | 0.732 ± 0.005 | 0.743 ± 0.005 | 0.769 ± 0.008 |
| A_{TD} | 0.369 ± 0.02 | 0.345 ± 0.015 | 0.321 ± 0.015 |
| $A_{\pi \text{scat}}$ | 0.875 ± 0.01 | 0.893 ± 0.01 | 0.904 ± 0.01 |
| $A_{K_{\pi 2}}$ | 0.996 ± 0.002 | 0.987 ± 0.006 | 0.990 ± 0.005 |
| $A_{\text{L1.5}}$ | 0.985 ± 0.002 | 0.988 ± 0.005 | 0.988 ± 0.005 |
| A_{tot} | $(1.30 \pm 0.07) \times 10^{-2}$ | $(1.30 \pm 0.06) \times 10^{-2}$ | $(1.18 \pm 0.06) \times 10^{-2}$ |

Table 4.41: The complete $K^+ \rightarrow \pi^+ X^0$ efficiency.

| Year | A_{tot} | f_S | $N_{KT\text{live}}$ | S_i |
|------------------------------------|----------------------------------|-------------------|-------------------------|---------------------------------|
| 1989 | $(2.77 \pm 0.16) \times 10^{-3}$ | 0.675 ± 0.030 | 1.7688×10^{11} | $(3.308 \pm 0.242) \times 10^8$ |
| 1990 | $(2.78 \pm 0.14) \times 10^{-3}$ | 0.681 ± 0.022 | 2.1178×10^{11} | $(4.015 \pm 0.241) \times 10^8$ |
| 1991 | $(2.51 \pm 0.13) \times 10^{-3}$ | 0.590 ± 0.021 | 1.4554×10^{11} | $(2.155 \pm 0.136) \times 10^8$ |
| $S_{\text{tot}}^{\pi\nu\bar{\nu}}$ | - | - | - | $(9.478 \pm 0.368) \times 10^8$ |

Table 4.42: The complete $K^+ \rightarrow \pi^+ \nu\bar{\nu}$ sensitivity. The errors on A_{tot} and f_S have been adjusted, removing common factors that will cancel in the product.

| Year | A_{tot} | f_S | $N_{KT\text{live}}$ | S_i |
|----------------------------|----------------------------------|-------------------|-------------------------|---------------------------------|
| 1989 | $(1.30 \pm 0.07) \times 10^{-2}$ | 0.675 ± 0.030 | 1.7688×10^{11} | $(1.553 \pm 0.107) \times 10^9$ |
| 1990 | $(1.30 \pm 0.06) \times 10^{-2}$ | 0.681 ± 0.022 | 2.1178×10^{11} | $(1.871 \pm 0.106) \times 10^9$ |
| 1991 | $(1.18 \pm 0.06) \times 10^{-2}$ | 0.590 ± 0.021 | 1.4554×10^{11} | $(1.018 \pm 0.063) \times 10^9$ |
| $S_{\text{tot}}^{\pi X^0}$ | - | - | - | $(4.442 \pm 0.163) \times 10^9$ |

Table 4.43: The complete $K^+ \rightarrow \pi^+ X^0$ sensitivity. The errors on A_{tot} and f_S have been adjusted, removing common factors that will cancel in the product.

Chapter 5

Conclusions

5.1 Establishing Branching Ratio Upper Limits

Given an observation of N events, the branching ratio, B , can be calculated very simply:

$$B = \frac{N}{S_{\text{tot}}}.$$

If no clear signal is observed, a limit on the maximum allowed branching ratio can be set instead. The familiar technique follows directly from the Poisson statistics of observing n events given an expected number of counts, μ :

$$P(n; \mu) = \frac{e^{-\mu} \mu^n}{n!}.$$

With n_0 observed events, a limit at the confidence level α (usually 0.90 or 0.95) is set by solving the equation

$$1 - \alpha = \sum_{n=0}^{n_0} P(n; \mu)$$

for μ . In words, the upper limit on the number of events expected is the value, μ , that has a probability $1 - \alpha$ of resulting in n_0 or less observed events in any given identical experiment. This choice satisfies the classical definition of a confidence level, in the sense that if μ is the true value of the expected number of events in an infinite number of identical experiments, α experiments will observe more than n_0 events and $1 - \alpha$ experiments will observe n_0 or less events.

For no observed events, the limit is determined by solving

$$P(0; \mu) = \frac{e^{-\mu} \mu^0}{0!} = 1 - \alpha.$$

By tradition, we set a 90% confidence level ($1 - \alpha = 0.1$), yielding $\mu = 2.30$. Thus, the 90% confidence level upper limit on the branching ratio becomes

$$B \leq \frac{2.30}{S_{\text{tot}}}.$$

If the error on the sensitivity is well known, it is straightforward to include it in the limit. While there is a relatively recent article on the subject [28], members of E787 should already be familiar with this since the exact form for the inclusion was presented in the discussion of the original 1988 analysis [15]. Following the derivation of that note, the error on the sensitivity can be included by assuming some probability distribution for that error, $f(\eta)$, and then solving (for zero observed events and a 90% confidence level)

$$\bar{P}(0; \mu) = \int_0^\infty f(\eta) P(0; \eta\mu) d\eta = 0.1$$

for μ . For example, if we take $f(\mu)$ to be normally distributed with $\sigma = 10\%$, μ rises from 2.30 to 2.33. Even with a 30% error on the sensitivity, μ only rises to 2.60. The error on the sensitivity quoted in Chapter 4 was about 4%; however, viewing the acceptance calculation somewhat skeptically has led E787 to an error estimate of about 10% on the sensitivity, due in large part to the uncertainties in the nuclear interactions simulation in the monte carlo. Even with this large error inflation, it was argued in the old analyses that inflating 2.30 to 2.33 was not particularly meaningful, and it is not done here.

5.1.1 The $K^+ \rightarrow \pi^+ \nu \bar{\nu}$ Upper Limit

Using the sensitivity from Table 4.42, the upper limit on the $K^+ \rightarrow \pi^+ \nu \bar{\nu}$ branching ratio from this analysis is

$$B(K^+ \rightarrow \pi^+ \nu \bar{\nu}) \leq \frac{2.30}{S_{\text{tot}}^{\pi^+ \nu \bar{\nu}}} = \frac{2.30}{9.478 \times 10^8} = 2.43 \times 10^{-9}.$$

This is a factor of 3.1 improvement over the E787 published 7.5×10^{-9} limit based only on the 1989 data set, and a factor of 1.54 over the preliminary result from the other combined E787 1989-1991 analysis [18].

5.1.2 The $K^+ \rightarrow \pi^+ X^0$ Upper Limit

Using the sensitivity from Table 4.43, the upper limit on the $K^+ \rightarrow \pi^+ X^0$ (with massless X^0) branching ratio from this analysis is

$$B(K^+ \rightarrow \pi^+ X^0) \leq \frac{2.30}{S_{\text{tot}}^{\pi X^0}} = \frac{2.30}{4.442 \times 10^9} = 5.18 \times 10^{-10}.$$

This is a factor of 3.3 improvement over the E787 published 1.7×10^{-9} based on the 1989 data set, and a factor of 1.19 improvement over the preliminary result from the other combined E787 1989-1991 analysis.

5.2 The Future

The 1989, 1990 and 1991 runs represent “Phase I” of E787. The single event sensitivity from this analysis for $K^+ \rightarrow \pi^+ \nu \bar{\nu}$ of 1.06×10^{-9} is a good factor of 2 above the top of the Standard Model allowed range; it is clearly desirable to continue to push this experiment to the maximum possible sensitivity, especially since E787 is the only $K^+ \rightarrow \pi^+ \nu \bar{\nu}$ search for the foreseeable future. Increasing the sensitivity requires increasing the rejection for the various background processes, requiring tighter cuts which would *reduce* our (already less than impressive) acceptance. Instead of simply running the Phase I experiment to its background limit, E787 has undergone a major set of upgrades designed to improve our background rejection capabilities *without* compromising the acceptance, while running at much higher kaon rates to push the

sensitivity ahead in a reasonable time. While not technically part of this analysis, since I spent somewhat more time as a graduate student working on the detector upgrade program than on analysis, it is worth listing the improvements here.

- K^+ beam line: the old LESB I beam line has beam replaced with LESB III, which includes a second stage of electrostatic separation. Instead of running at a $K^+ : \pi^+$ ratio of 1 : 2, LESB III typically runs at 4 : 1. For a fixed beam kaon rate, the beam pion rate is decreased by almost an order of magnitude, greatly reducing the π scat background level. Additionally, the accidental rates in the detector (which dominate our photon-veto losses and TD rejection) have been measured to scale with the total beam particle rate; thus, the greatly increased $K^+ : \pi^+$ ratio will permit higher K^+ rate running without compromising efficiency or rejection.
- K^+ stopping target: a significant part of our charged track energy uncertainty was due the limited light from the target fibres. A completely new stopping target was built by our BNL collaborators, using fibres that yield about a factor of three more scintillation light than the old ones. The new fibres are also square instead of circular, which allows the new target to be a close-packed structure with no dead-material. The new target should help all of our kinematic measurements, which will almost certainly improve our $K^+ \rightarrow \mu^+ \nu_\mu$ and $K^+ \rightarrow \pi^+ \pi^0$ rejection.

- Drift chamber: the resolution of the drift chamber provided the poorest relative separation between the $K^+ \rightarrow \pi^+\pi^0$ and $K^+ \rightarrow \mu^+\nu_\mu$ peaks, giving the weakest-link in our kinematic rejection. A new design, the “Ultra Thin Chamber” (or UTC) is much less massive than the old “Jet Chamber,” whose resolution may have been at least partially limited by multiple scattering. My first major task on E787 was the construction of a prototype of the new chamber; a test in the E787 detector at the end of the 1991 run verified the momentum resolution capability of the UTC design [29]. The final chamber, built by our TRIUMF collaborators, is verified to have a factor of two improvement in momentum resolution over the Jet Chamber. This resolution should improve the $K^+ \rightarrow \pi^+\pi^0$ rejection of the total momentum cut, and may even make it a useful cut for rejecting $K^+ \rightarrow \mu^+\nu_\mu$.
- Demultiplexed range stack: in the Phase I detector the inner range stack layers were optically ganged (recall Section 2.5), resulting in an effective 15 layer RS. Our BNL collaborators separated the inner layers’ readout, which has been verified to yield more total charged track light from the RS, improving the energy resolution.
- Range stack straw chambers: the $K^+ \rightarrow \mu^+\nu_\mu$ background has a large contribution from muons that stop in RS layer 14, which are hypothesized to stop in the outer range stack chambers. Those chambers represented a large fraction

of the dead material seen by charged tracks, and it is concentrated near the stopping region where the particles are heavily ionizing. These chambers are now replaced by a set of 48 straw-tube chambers, which are about a factor of 6 thinner than the old chambers and completely lack any mass concentrations (the old chambers had additional mass concentrations in side-walls and wire-supports). This project was headed by Mark Convery at Princeton, but also involved the majority of my time as a graduate student. The readout electronics system for the new straw chambers is described in Appendix C.

- CsI endcaps: the visible light fraction in the old lead-scintillator endcaps was about 1/3, and EC sampling fluctuations represented a sizable part of our low-energy photon inefficiency. The endcaps have been replaced (by our BNL and new Japanese collaborators) by pure CsI crystals with a sampling fraction of unity; unfortunately, CsI pulses have rather slow trailing edges, so a large early accidental can obscure a small prompt pulse. An integral part of the endcap upgrade is a new CCD-based transient digitizer system (built at TRIUMF), which may allow these obscured pulses to be recovered using a multi-pulse fitting technique similar to our $\pi^+ \rightarrow \mu^+$ tagging in the RS. It is hoped that this will improve our $K^+ \rightarrow \pi^+\pi^0$ rejection considerably.
- Trigger: the online trigger has been completely rebuilt, and the lowest level is now implemented almost entirely in fastbus. This upgrade included moving

the old level 1 refined range and hextant cuts down into level 0, increasing the rejection in the fastest trigger stage. This upgrade allows the trigger to function at a factor of 4 higher beam kaon rate with a slight *decrease* in trigger dead-time. The new level 0 trigger construction was done at Princeton by Ardebili, Ito, Meyers, Marlow, and myself. The old online TD $\pi^+ \rightarrow \mu^+$ finder has also been sped up; our Brookhaven collaborators designed a dedicated application specific integrated circuit that performs this cut, along with a number of other of data formatting and organizational tasks. These upgrades to the trigger permit E787 to run at much higher rates, which is essential if we are to push our sensitivity forward in an acceptable amount of time.

- Data acquisition system: the faster trigger is not quite enough, since we also have to collect the data and write it out to tape. BNL has designed and implemented a completely new data acquisition system, built around a Silicon Graphics mini-computer. This system is now routinely used to write 10 double-density 8 mm tapes (about 4.5 GBytes each) simultaneously, to be compared with the one single-density tape written during most of Phase I.

Our first full Phase II run is just being completed now. In this 1995 run, we will take around 13×10^{11} *KTlive*'s, or about 2.5 times more than our entire Phase I data set.¹ It seems reasonable to expect that our upgrades will provide an additional

¹Actually, since our event size has increased considerably, this is somewhat more than 2.5 times more *data*. In fact, it represents about 25 TeraBytes.

factor of 2.5 in background suppression, so the single event sensitivity could drop to around the 4×10^{-10} range from just this one run alone.

This is really starting to get interesting.

References

- [1] E.D.Commins & P.H.Bucksbaum *Weak interactions of leptons and quarks*, Cambridge University Press (1983)
- [2] C.N.Yang and R.L.Mills **Conservation of Isotopic Spin and Isotopic Gauge Invariance**, *Phys. Rev.* Volume 96, Number 1, 1 October 1954
- [3] Peter Meyers' course notes, Princeton University Physics 529, unpublished
- [4] L.Littenberg and G.Valencia, **Rare and Radiative Kaon Decays** in *Annu. Rev. Nucl. Part. Sci.* (1993) 43:729-792
- [5] J. Hagelin and L. Littenberg, **Rare Kaon Decays** in *Prog. Part. Nucl. Phys.* 23 1 (1989)
- [6] Review of Particle Properties, *Phys. Rev. D*50, Part 1, (1994)
- [7] Claudio O. Dib *Rare K Meson Decays in the case of a Heavy Top Quark*, Stanford University Thesis, April 1990

- [8] A.Buras, M.Lautenbacher, G.Ostermaier, **Waiting for the Top Quark Mass, $K^+ \rightarrow \pi^+ \nu \bar{\nu}$, $B_s^0 - \bar{B}_s^0$ Mixing and CP Asymmetries in B -Decays**, it Technische Universitat Munchen preprint MPI-PH/94-14.
- [9] Proceedings of the XXVII International Conference on High Energy Physics, Glasgow, Scotland, July, 1994.
- [10] A.Buras, **Towards Precise Determination for the CKM Matrix without Hadronic Uncertainties**, it Technische Universitat Munchen preprint MPI-PH/94-57.
- [11] G.Buchalla and A.J.Buras **The rare decays $K^+ \rightarrow \pi^+ \nu \bar{\nu}$ and $K_L^0 \rightarrow \mu^+ \mu^-$ beyond leading logarithms**, *Nuclear Physics* B412:106 (1994)
- [12] G.Buchalla, A.Buras, M.Harlander *Nuclear Physics* B349:1 (1991)
- [13] T.Inami, C.S. Lim, *Prog. Theor. Phys.* 65:297 (1981); erratum 65:1772 (1981)
- [14] A.Buras and M.Harlander, **A Top Quark Story** in *Heavy Flavours* ed. A.J.Buras and M.Linder, World Scientific (1992)
- [15] E787 Technical Note 168: The Princeton Analysis of the $K^+ \rightarrow \pi^+ \nu \bar{\nu}$ Branching Ratio Limit from the 1988 Run, D.Akerib, D.Marlow, and P.Meyers, 11 July 89
- [16] E787 Technical Note 186: The Princeton Analysis of the $K^+ \rightarrow \pi^+ \nu \bar{\nu}$ Branching Ratio Limit from the 1989 Run, D.Akerib, D.Marlow, and P.Meyers, 8 Aug 1990

- [17] E787 Technical Note 234: Application of Multivariate Analysis to Pion Identification and $\pi - \mu$ Separation, Andre S. Turcot, Nov 3 1993
- [18] E787 Technical Note 281: The Search for $K^+ \rightarrow \pi^+ \nu\bar{\nu}$ above the $K^+ \rightarrow \pi^+ \pi^0$ Peak in the 1989-1991 Data Set, Andre S. Turcot, March 2 1994
- [19] A Detector to search for $K^+ \rightarrow \pi^+ \mu^+ \mu^-$, NIM A321 (1992) 129-151
- [20] Mats A. Selen, *Hunting for the Rare Decay $K^+ \rightarrow \pi^+ \mu^+ \mu^-$* , Princeton University *PhD* thesis, January 1989
- [21] Daniel S. Akerib, *A Search for the Rare Decay $K^+ \rightarrow \pi^+ \nu\bar{\nu}$* , Princeton University *PhD* thesis, January 1991
- [22] Andre Spence Turcot , *The Search for the Rare Decay $K^+ \rightarrow \pi^+ \nu\bar{\nu}$* , University of Victoria *PhD* thesis, 1994
- [23] E787 Technical Note 296: Search for $K^+ \rightarrow \pi^+ \nu\bar{\nu}$ below the $K^+ \rightarrow \pi^+ \pi^0$ Peak using 1991 Data, Jean Roy, 3 October, 1994
- [24] E787 Technical Note 259: Range Stack Energy Recalibration for 1989, Karen Livescu, July 7, 1993
- [25] E787 Technical Note 209: Improvements in TDC Timing Resolution, Peter Meyers, July 22, 1991

- [26] E787 Technical Note 228: Target Tracking Using the Drift Chamber Trajectory,
Mehran Ardebili, Dan Marlow, Peter Meyers January 2, 1992
- [27] E787 Technical Note 287: Range Stack Proportional Chamber Recalibration for
1990 and 1991, Karen Livescu, August 8, 1994
- [28] R.D.Cousins and V.L.Highland NIM A320 (1992) 331
- [29] E787 Technical Note 212: The Foil Chamber Prototype, Robert A. McPherson,
Mark R. Convery, Mark M. Ito, Daniel R. Marlow, and William R. Sands, 7 Au-
gust 1991
- [30] *Gas Studies for the E787 Straw Chambers*, C.Denniston, Princeton University
General's Experimental Project, December 1, 1992

Appendix A

The E787 Collaboration

A.1 The E787 collaboration, participating in data taking or analysis for this thesis

S. Adler, M.S. Atiya, I-H. Chiang, J.S. Frank, J.S. Haggerty, T.F. Kycia,
K.K. Li, L.S. Littenberg, A. Sambamurti, A. Stevens, R.C. Strand,
and C. Witzig

Brookhaven National Laboratory

W.C. Louis

Los Alamos National Laboratory

D.S. Akerib, M. Ardebili, M. Convery, M.M. Ito, D.R. Marlow, R.A. McPherson,
P.D. Meyers, M.A. Selen, F.C. Shoemaker, A.J.S. Smith, and J.R. Stone

Joseph Henry Laboratories, Princeton University

A.1. The E787 collaboration, participating in data taking or analysis for this thesis 198

E.W. Blackmore, D.A. Bryman, L. Felawka, P. Kitching, A. Konaka,
Y. Kuno, J.A. Macdonald, T. Nakano, T. Numao, P. Padley, J-M. Poutissou,
R. Poutissou, J. Roy, R. Soluk, and A.S. Turcot

TRIUMF

Appendix B

The Home of the Offline Analysis

B.1 KOFIA

In developing my analysis, I spent a great deal of time examining the software and run scripts of everyone who went before me. While those who come after me will have to do the same, I can at least tell them where to look. The complete analysis lives exclusively on the machine `puhep1.princeton.edu`, a Silicon Graphics UNIX-based computer. The main source code directory for the analysis is `/usr/people/rob/pnn/src`; the Makefile in that directory is used to build the analysis. The range stack track fitter code is `/usr/people/rob/kofia/rprfit`. The (many) routines that were taken and modified from standard KOFIA 1.6 are in `/usr/people/rob/kofia/new`. The analysis modifies KOFIA 1.6 to use the new calibration file management software (CFM) version 2.2, with pointers in `/usr/people/rob/pnn/cfm.db`.

Run scripts are in `/usr/people/rob/pnn/run/89, 90, 91, u89, u90, and u91` for

analyzing real data and UMC generated data from 89, 90, and 91. For example, /usr/people/rob/pnn/run/89/pass3_89 was used to run Pass 3 code on 1989 data. Numerous modified calibration files are located in these “run” directories. All KOFIA command files are in /usr/people/rob/pnn/kcm. The KOFIA analysis is used to produce HBOOK ntuple files, which are analyzed with the various macros in the /usr/people/rob/pnn/paw directory.

B.2 UMC

The main UMC code directory is /usr/people/rob/pnn/umc, although I used almost exclusively the default UMC version 4.0 code (this is the one fringe benefit of being a software czar – if you think the software ought to do something differently, just change it). The main UMC running directories are /usr/people/rob/pnn/umc/89, 90, and 91. All the scripts and UMC parameter files live in those directories.

Appendix C

The Straw Chamber Electronics

C.1 Overview

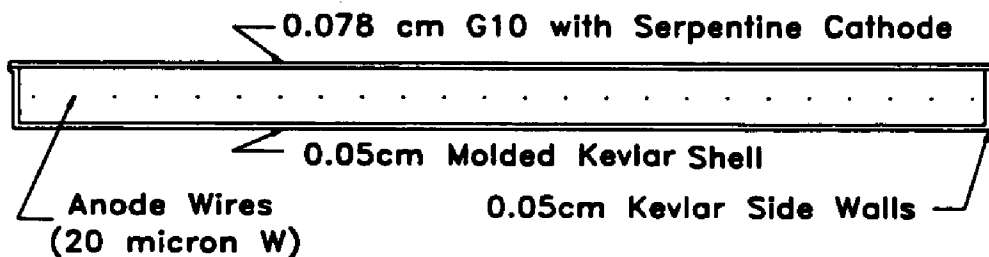
The range stack straw chamber (RSSC) project was an ordeal. They replace the existing range stack chambers, but are much less massive. The inner RSSC's are 2 layers of 24 straws each, and the outer RSSC's are 2 layers of 28 straws each. They are compared to the old chambers in Figure C.1, and a detailed drawing is in Figure C.2. There are a total of 48 chambers, or 2496 straws, currently installed in the E787 experiment.

I defer the worst of it to Mark Convery. Here, without including complete schematics, I will just document the readout electronics.

The chambers are used in the range stack tracking and charged particle range measurement. The standard analysis uses the chamber $z - \phi$ position. Just knowing which straw is hit gives the ϕ coordinate to better accuracy than the old chambers

OLD MWPC (Proportional Mode)

Total Mass: 0.31 g/cm^2



NEW STRAW CHAMBERS (Limited Streamer Mode)

Total Mass: 0.054 g/cm^2

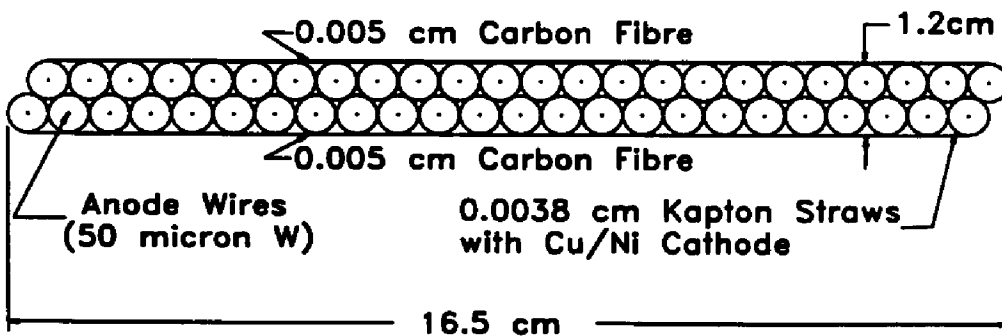


Figure C.1: Comparison of old range stack chambers to new straw chambers.

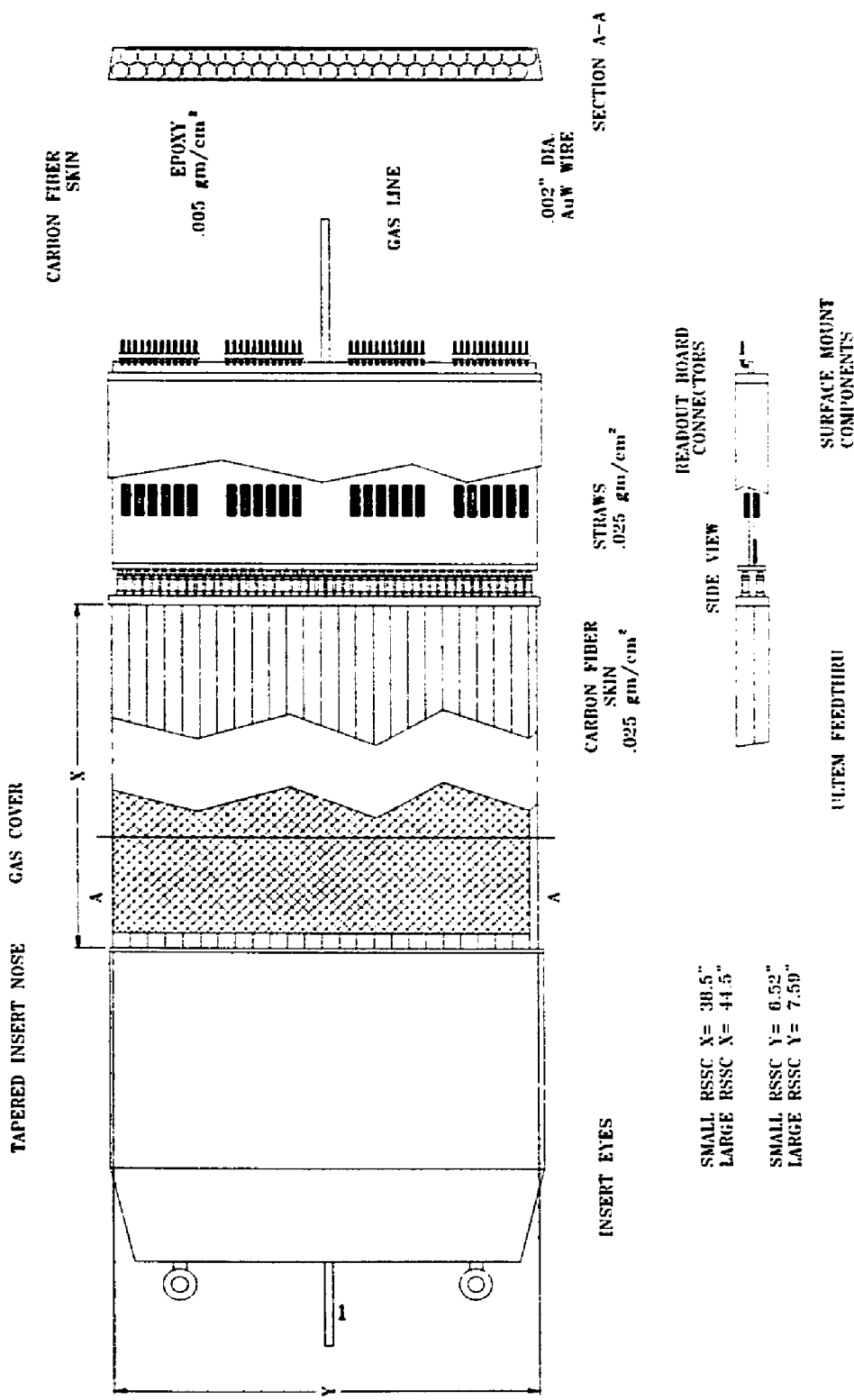


Figure C.2: Detailed view of the new straw chambers, drawn by William Sands, Princeton High Energy Physics group.

(although the new local angle information may also prove useful). The problem is how to get z out of the chambers: we use end-to-end timing. The RSSC readout scheme is sketched in Figure C.3. An important consideration in this readout is that it is essentially impossible to access the chambers for any repairs. Because of that, we elected to mount the minimum possible electronics on the chambers themselves (“Chamber Front End” in the figure); this meant no pre-amplifiers, and also running the analogue signals from the chambers down the shortest possible cables to the external electronics (“Chamber Readout Cards” in the figure), which are mounted on the spectrometer magnet as close as possible to the chambers. Since we need big pulses to make up for the lack of pre-amps, and reproducible pulses to make the end-to-end timing scheme work, the chambers are run in limited-streamer mode. A set of aging test were performed [30], verifying that chambers should outlast the expected lifetime of the experiment even with the large pulse size.

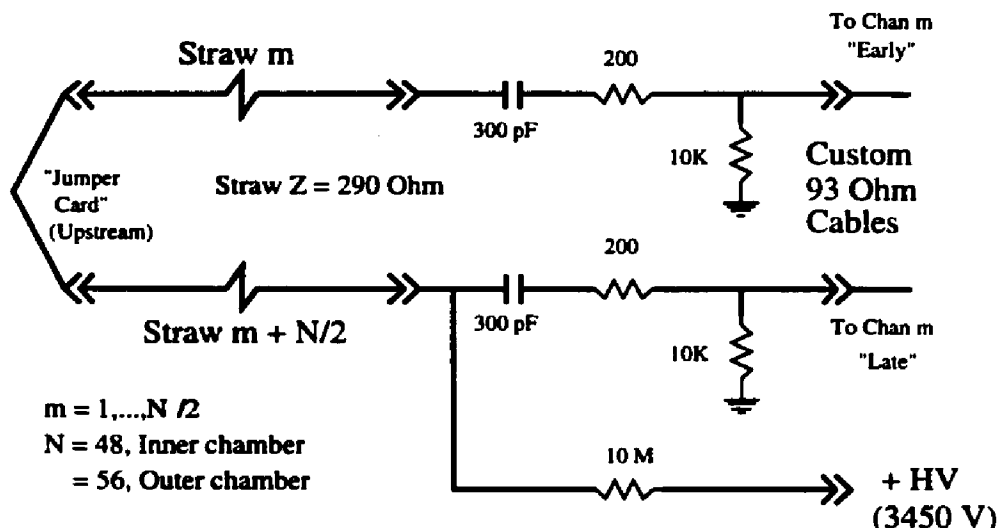
C.2 Front End Electronics

From Figure C.3, it is apparent just how electronically simple the chamber front-end electronics really are. The front-end consists of a single custom 2-layer readout-card, with a daughter board containing a set of sockets that line up with pins connected to the chamber wires that literally plugs into the end of the chamber. This card (like everything else in this project) must take up almost no space, and ultimately becomes

RSSC Electronics Layout

Convery, McPherson
Princeton, 21 Feb 95

Chamber Front End Schematic



Chamber Readout Cards

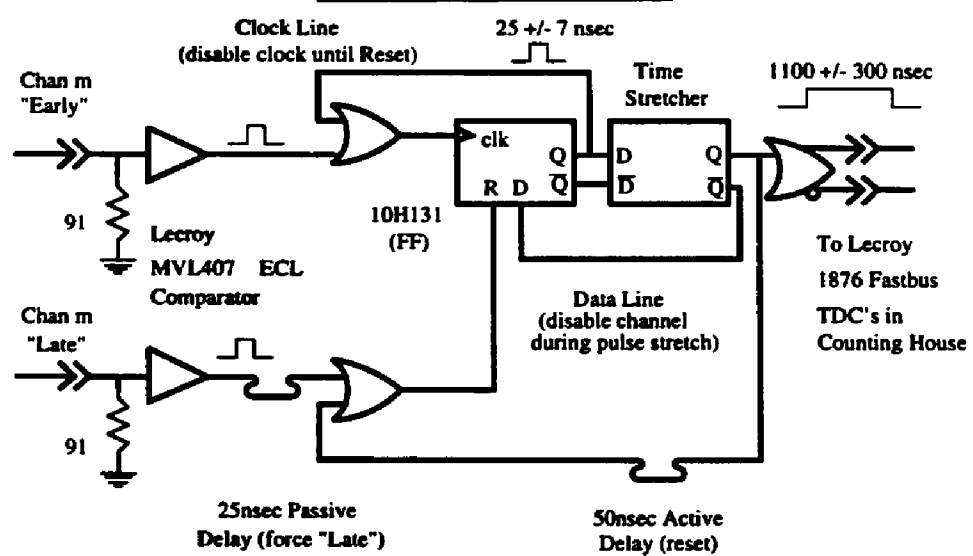


Figure C.3: RSSC readout electronics.

part of the mechanical structure of the chamber itself. I designed all of the boards mounted on the chambers with the Mentor Graphics electronics design tools; they were fabricated by an outside vendor, and assembled at Princeton by Stanley Chidzik and Dick Rabberman. They are made entirely with surface-mount components.

Both because of the severe space constraints and the desire to have the smallest possible separation between the chambers and the external readout, the chambers are read out from only the downstream end. We maintain the end-to-end information by connecting the pairs of straws on the upstream end together using another dedicated card (neighbouring straws are not connected – connected straws are separated by either 12 or 14 straws, for the small or large chambers respectively), reducing the channel count from 2496 straws to 1248 pairs. In our recent 1995 run the single straw rates were about 5 kHz, and since the time stretcher deadtime is about 1 μ sec per hit the pile-up rate is still fairly small (about 1%). The straw walls are held at signal ground through a conductive-epoxy connection from the straws to an aluminum gas-tight end-piece box, which is mechanically connected to the readout-card with small brass bolts. The high voltage is distributed onto a bus on the front-end card, and to each straw pair through a custom $10\text{ M}\Omega$ surface-mount resistor. The signals pass through a custom surface-mount HV blocking capacitor, a resistor to match the straw impedance to the cables, and then through a connector built into the chamber to the cables themselves.

| Description | Manufacturer | Unit Cost | Number per Straw Pair | Cost per Straw Pair |
|--|------------------------------------|-----------|-----------------------|---------------------|
| Custom 10 M Ω Thick Film Resistor SR-1005-4008-25-JWA | Piconics Inc. Tyngsboro MA | \$1.09 | 1 | \$1.09 |
| HV Ceramic 300 pF 5 kV Chip Capacitor WC4113X301KD02 | Wright Capacitors Santa Ana, CA | \$1.21 | 2 | \$2.42 |

Table C.1: Custom surface mount parts for HV distribution and blocking.

The key elements in the front end are the custom surface mount resistors and capacitors used for HV distribution and blocking. While the resistors do not typically hold significant voltage, this custom thick-film elongated surface mount part is able to withstand HV sparks. These two unusual parts used are listed in Table C.1.

C.3 Cables

For our end-to-end time resolution, we want to preserve the largest possible signals at the external electronics. Since the straws themselves are $290\ \Omega$ transmission lines, we use the highest impedance good-quality cable possible. Also, the chambers do not fit into any of the standard multi-conductor cable sizes, so we were led to manufacturing a set of custom $93\ \Omega$ coaxial cables for the project, which was an ordeal in itself (not mine – they were assembled by Dick Rabberman at Princeton). The cables were built into commercially available socket receptacles, and are 16 feet long.

| Description | Manufacturer | Cost per 1000 feet | Length per Straw Pair | Cost per Straw Pair |
|--|---------------------------------|--------------------|-----------------------|---------------------|
| 93 Ω Coax Cable, 30 AWG Type 9393 CXC | Belden | \$124.70 | 32 feet | \$4.00 |
| 5 kV HV Wire 24 Gauge R790-0524 | Rowe Industries Toledo, Ohio | \$300.00 | 2 feet | \$0.60 |

Table C.2: Cables used for custom signal cable assemblies, and HV distribution. Each cable is actually 16 feet long.

The HV supplies are located in the E787 counting house, and one RG58 cable per chamber runs to the detector. The HV and its ground are transferred onto a pair of thin cables capable of holding 5 kV (we typically run the chambers at 3450 Volts). The signal and HV cables used are listed in Table C.2.

C.4 External Electronics

The other half of Figure C.3 shows the chamber readout cards, which are double-height 8-layer custom VME boards mounted into crates built on the main spectrometer magnet. I designed the complete boards at Princeton with the Mentor Graphics electronics design tools; they were fabricated by an outside vendor, costing about \$300 each (just because I have to write this down somewhere, the board has 5518 plated-through holes – I was just learning how to do surface mount). We stuffed and completely tested two boards at Princeton, and then sent the rest (60 total) to

an outside company for production assembly. The interface with the fabrication and assembly companies was handled by Carl Bopp at Princeton. There are 28 channels per board, which reads out either one small or one large chamber. The first active electronics the signals see is a Lecroy MVL407 comparator. After forcing one end of the pair to always come late using a 25 nsec passive delay line, a time difference pulse is formed using a 10H131 ECL flip-flop. Note that the flip-flop clock is disabled while the primary time-difference pulse is being formed (which is absolutely essentially due to internal 10H131 propagation delay anomalies at the time scales we're working), that the channel is disabled while the time stretcher is active, and that the channel is self-resetting if no "late" pulse arrives.

The primary time difference pulse is about 25 ± 7 nsec wide, with our z measurement encoded in that pulse width. We stretch this pulse by about a factor of 45 using a linear "Time Stretcher" circuit, making it about 1100 ± 300 nsec. With a modest 1 nsec resolution on the stretched pulse width, we have 20 psec resolution on the primary pulse width, which would be a 0.3 cm resolution z measurement. In practice, when running the chambers in the experiment we achieve a z resolution a little worse than 1 cm.

The external electronics has two key features. Firstly, we want to be able to set the primary comparator threshold quite low, which requires a quiet circuit board and threshold voltage. To keep the board quiet, in addition to severely bypassing the

power supply voltages, a ceramic $0.01 \mu\text{F}$ bypass capacitor is placed beside every power pin on the entire board. The level is set with a potentiometer on the board front-panel, and is shipped around at $100 \times$ the actual threshold level. It is divided down separately at each comparator input, and a $0.01 \mu\text{F}$ capacitor bypasses each channel's threshold to ground.¹ Since any noise pickup on that long trace is also divided down, the threshold seen by the comparator is quiet. The limitedStreamer pulses have a charge of about 100 pC at the chamber operating point. After the blocking capacitor and cables, they land on the external electronics boards as roughly 100 mV high, 30 nsec wide pulses. We lower the comparator thresholds until the z resolution stops improving, which is typically about 10 mV . For chambers with HV problems the board can go down to $< 5 \text{ mV}$ threshold reliably, recovering some of the lost z resolution. These fast comparators can also have a common-mode transient input current at both inputs (threshold and signal) of the same channel. To keep a reliable relative threshold level, these inputs should see the same impedance when looking back from either the signal or the threshold side. A set of resistors matching the signal termination impedance are added to the threshold lines for this purpose. The comparator signal and threshold schematic is sketched in Figure C.4.

The other key external electronics feature is the linear time stretcher circuit. Its schematic is included in Figure C.5; it was copied in part from a Lecroy time-of-flight

¹After they received the boards and parts, the assembly company phoned back in some state of concern asking "Do you know there are over 300 $0.01 \mu\text{F}$ capacitors on this board?" We were, of course, shocked.

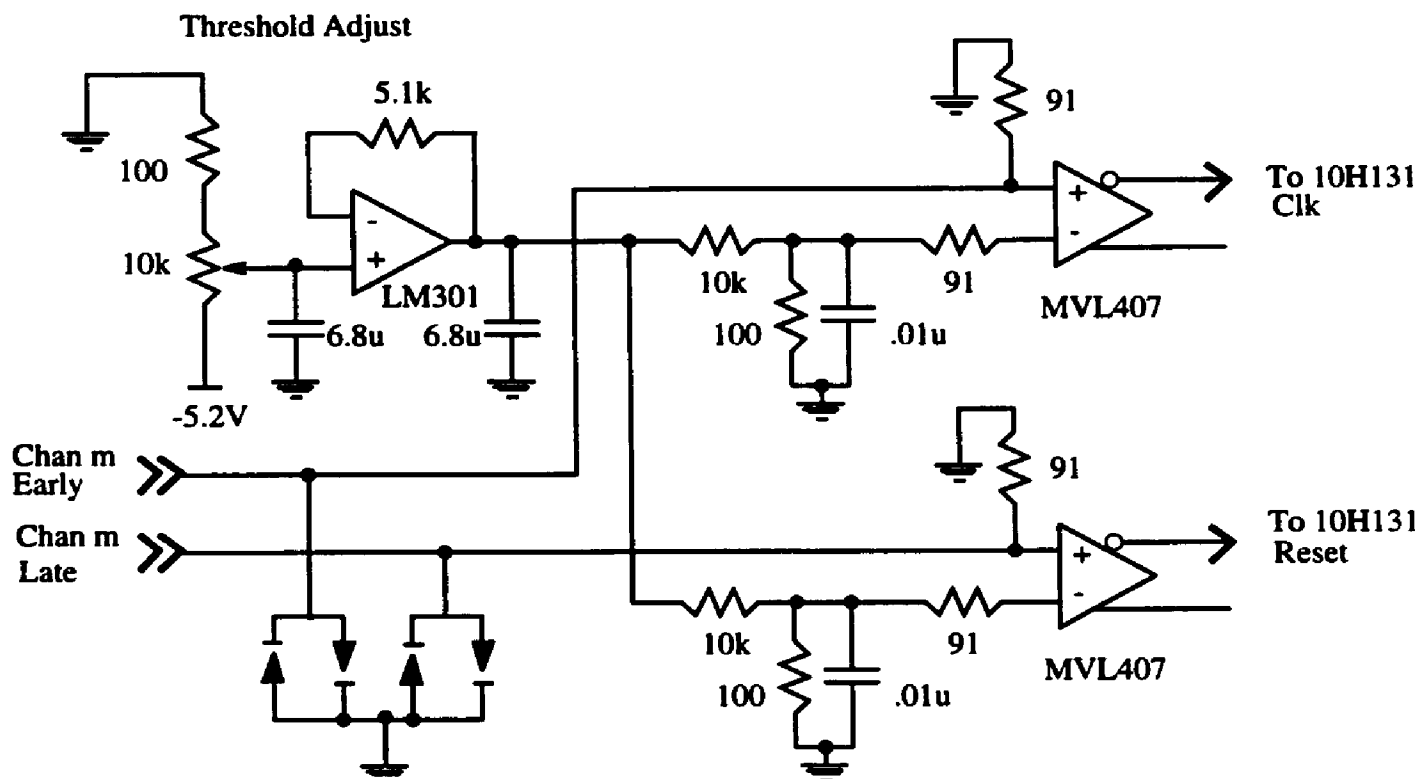


Figure C.4: Comparator threshold adjust and signal path for one straw pair.

| Description | Results |
|-------------------------|--|
| Linearity | Typical deviations from linear fit of ± 20 psec primary pulse width, over a range of 15-35 nsec widths |
| Temperature Variations | Better than ± 2 psec per degree Celsius primary pulse width, 5-35 degree Celsius |
| Power Supply Variations | -2 V supply: 1.5 psec per mV, primary pulse width -5.2 V supply: 0.2 psec per mV, primary pulse width rest: negligible |
| Magnetic Fields | No observable effects in fields up to 200 Gauss. (stray field at electronics racks < 20 Gauss) |

Table C.3: Tests performed end-to-end time readout circuit.

TDC design. The complete readout system underwent a fairly severe set of tests: linearity, temperature variation, power supply voltage variations and magnetic field effects. Several boards received the complete torture treatment, and every channel of every board was subjected to a complete linearity check over its full dynamic range using a semi-automated PC-based system built around a Lecroy 9210 programmable pulse generator and a Lecroy 2277 CAMAC TDC (the “semi” part was handled by Jesse Stone at Princeton). The tests are not fully documented here, but are at least summarized in Table C.3. The key parts used on the external electronics board are listed in Table C.4. The external electronics boards output differential ECL logic pulses, which are run along standard twist-and-flat cables to Lecroy 1876 Fastbus TDC’s in the E787 counting house.

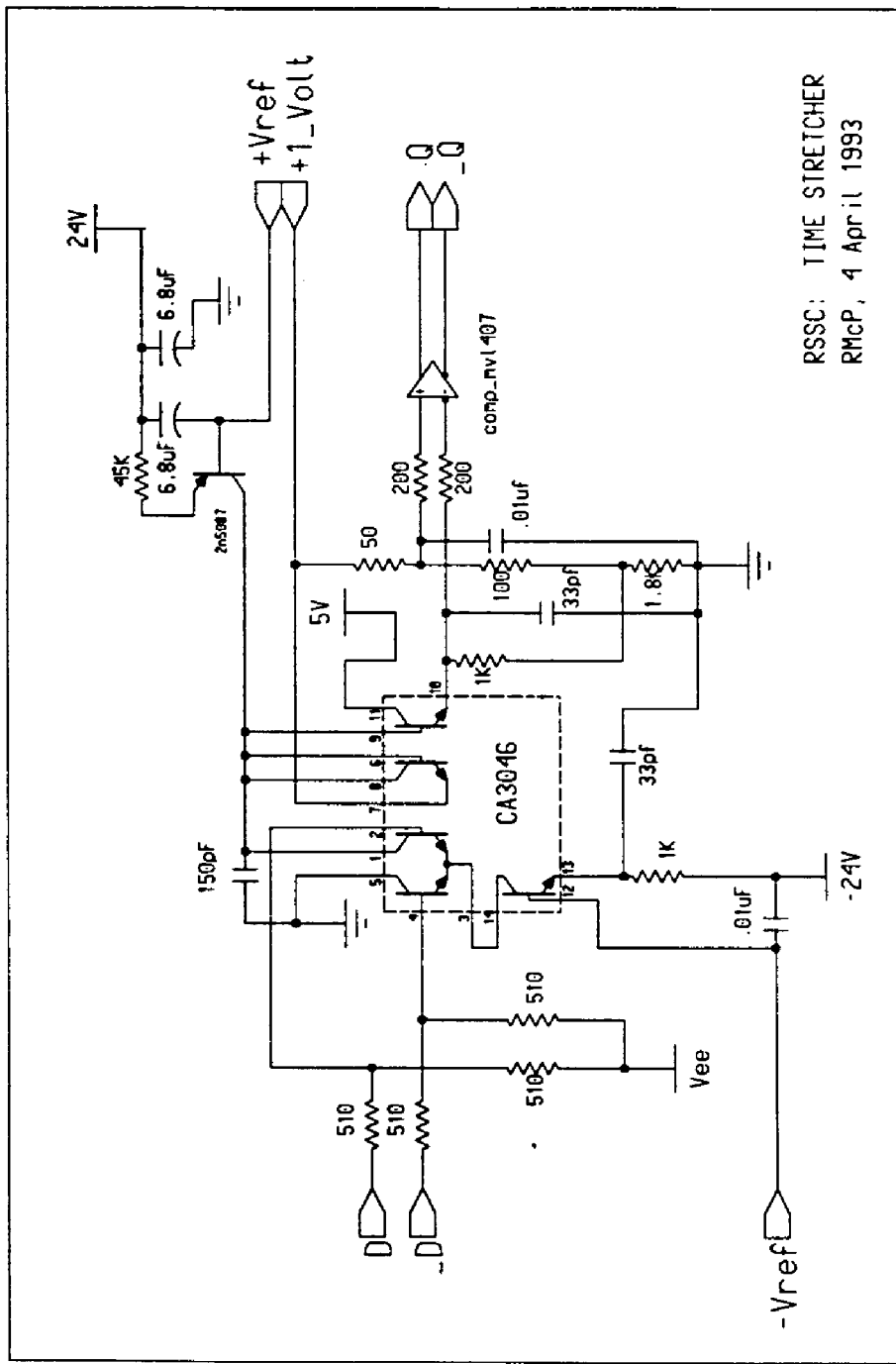


Figure C.5: The time stretcher schematic. The design is adapted from a Lecroy time-of-flight TDC. "Vref" is about 9 volts.

| Description | Manufacturer | Cost per Unit | Units per Straw Pair | Cost per Straw Pair |
|---|--------------------------------------|---------------|----------------------|---------------------|
| High Speed ECL Quad Comparator MVL407 | Lecroy Corp Chestnut Ridge NY | \$12.6 | 3/4 | \$9.75 |
| 25 nsec High Speed Passive 100 Ω Delay Line 1513-25B | Data Delay Devices Clifton, NJ | \$3.99 | 1 | \$3.99 |
| 50 nsec Triple Active ECL 10KH Delay Line MDU-13-50 | Data Delay Devices Clifton, NJ | \$8.23 | 1/3 | \$2.74 |

Table C.4: Key parts used on the external electronics boards.

C.5 Calibration sources

A set of ^{55}Fe calibration sources are built into the RSSC's for calibration and diagnostic purposes. ^{55}Fe decays via electron capture to ^{55}Mn , which de-excites producing a 6 keV K x-ray. If the x-ray is captured in the chamber gas a local ionization avalanche is created, resulting in a pulse resembling one from a charged track in the straw. The ^{55}Fe is deposited on mylar strips, which are glued across the outside of the straw chamber at constant z positions. Each chamber has four such strips, two on each side. Each straw therefore has two ^{55}Fe induced peaks, and each electronics channel (a straw pair) has four. Recent calibration data from the first channel of the inner chamber in RS sector 1 is in Figure C.6, showing the four calibration peaks. A careful monte carlo calculation was made of the efficiency of an individual straw seeing the source, and the activity was dialed to give about 2 Hz per source per straw. This

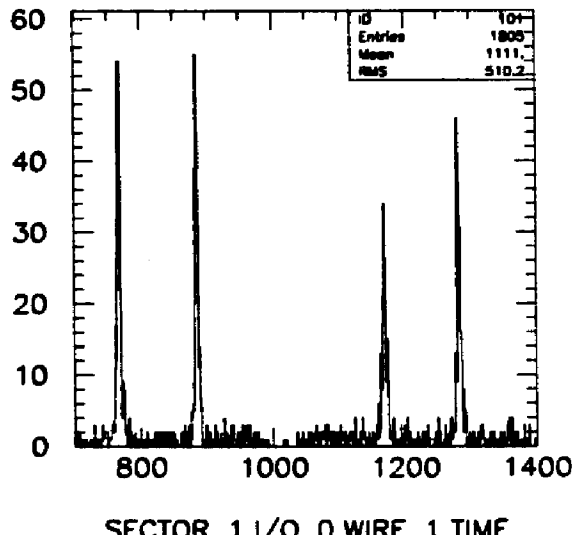


Figure C.6: ^{55}Fe calibration data from the inner straw chamber in RS sector 1, channel 1. There are two peaks per straw, or 4 per channel. The ordinate is counts, and the abscissa is the pulse width in stretched nsec. The complete system has 1248 such channels, or 2496 straws.

activity level does not significantly increase the local chamber aging rate, but allows us to take a good set of calibration data in an hour or two. The sources purchased were 8 inches long \times 0.1 inches wide \times 0.001 inches thick, with an activity of $0.2 \mu\text{Ci}$ ($\pm 20\%$) per sq. inch on one side only, and were cut in length at Princeton to match the chamber width. They were manufactured by ISOTOPE PRODUCTS LABORATORIES, 1800 N. Keystone Street, Burbank, CA 91504, and cost about \$10 each or \$40 per chamber.

C.6 Where, and what, to ground

The system signal ground is located at the main AC power breakers in the E787 counting house. It is run out with the power cables to the DC power supplies in the spectrometer magnet-mounted racks. These racks, power supplies, and the readout VME crates are electrically isolated from the magnet ground. The readout boards get ground from the DC supplies, then the ground runs along the custom signal coax cables to the chambers, and the front end electronics board, chamber aluminum end-boxes, and straw walls are all securely held at signal ground. The chambers are completely electrically isolated from the detector support structure.

The HV ground is carried from the HV power supplies in the counting house along RG58 cables, and then the special thin-wire HV cables, to the chambers. The HV ground lands on the front end electronics board, and is isolated from the signal ground by a $10\text{ k}\Omega$ surface mount resistor.

During (and after) the chamber installation, the various electrical connections were carefully monitored. In particular, the chamber aluminum end-pieces are isolated from the detector support structure by a layer of epoxy paint and a wrapping of Kapton tape. Since the chamber installation was an extremely difficult task, it was difficult to avoid damaging this insulation and shorting the chamber ground to the magnet ground; however, with care and effort, we believe that there are no ground loops present in this system.